

**The Aggregation Behavior of Mixture of
Alkylmethyloxides with Their Protonated
Analogues in Aqueous Solution**

**Dissertation
zur Erlangung des Doktorgrades
der Fakultät Biologie, Chemie und Geowissenschaften
der Universität Bayreuth**

**Yuji Yamashita
aus Japan**

2004

Die experimentellen Arbeiten zur vorliegenden Dissertation wurden in der Zeit von April 2002 bis August 2004 am Lehrstuhl für Physikalische Chemie I der Universität Bayreuth unter der Leitung von Herrn Prof. Dr. em. H. Hoffmann durchgeführt.

Ich danke Herrn Prof. Dr. em. H. Hoffmann an dieser Stelle für die interessante Themenstellung, seine stete Diskussionsbereitschaft sowie seine Vorschläge bei der Durchführung dieser Arbeit.

Ich bedanke mich sehr herzlich bei Herrn Prof. Dr. em. H. Maeda für den freundlichen wissenschaftlichen Austausch bezüglich dieser Arbeit. Er hat mich tiefgreifend unterrichtet und mir zahlreiche neue Aspekte der Materie vorgestellt.

Bei Herrn Prof. Dr. Y. Talmon, Herrn Prof. Dr. M. Ballauff und Herrn Dr. M. Drechsler bedanke ich mich für ihre experimentelle Hilfe. Frau Li Li, Mitarbeiterin von Prof. Dr. M. Ballauff danke ich sehr herzlich für ihre Experimente und den aufschlußreichen Austausch.

Ich danke weiterhin Herrn Prof. Dr. G. Platz und Herrn PD Dr. M. Gradzielski für ihre Diskussionsbereitschaft bzgl. meiner Arbeit und deren experimentelle Hilfe.

Allen Mitarbeitern des Lehrstuhls danke ich für ihre stete Hilfsbereitschaft, die Zusammenarbeit und das angenehme Arbeitsklima. Besonders möchte ich Frau U. Meyer, Herrn K.-H. Lauterbach, Frau C. Bächer und Frau C. Thunig für ihre private und experimentelle Unterstützung danken.

Schließlich möchte ich noch Herrn Dr. S. Mezzato, Herrn V. Daniel und Frau G. Cantea für die experimentelle Hilfe bezüglich der außerhalb meiner Doktorarbeit durchgeführten Projekten danken.

Contents

1 Introduction	1
1.1 Outline	1
1.2 Aim of Study.....	3
2 Theory.....	5
2.1 Micellization	5
2.2 Krafft Temperature.....	6
2.3 Colloidal Forces	7
2.3.1 Van der Waals Forces	7
2.3.2 Electric Double-Layer Forces	8
2.3.3 DLVO Theory	9
2.3.4 Hydration Force	10
2.4 Self-Assembly Structure	10
2.4.1 Formulation of Model for Free Energy	10
2.4.2 Packing Constraints	11
2.4.3 Bilayer Structures.....	12
2.4.4 Interfacial Curvature and Elastic Modulus	13
2.4.5 Worm-Like Micelle.....	15
2.5 Phase Transition.....	15
2.5.1 Concentration-Induced Phase Transition	15
2.5.2 Effects of Additives	16
2.5.3 Temperature-Induced Phase Transition.....	17
2.5.4 Shear-Induced Phase Transition.....	18
3 Experiment.....	21
3.1 Ingredients	21
3.1.1 Surfactants	21
3.1.2 Acids	22
3.1.3 Esters.....	25
3.2 Phase Study.....	25
3.2.1 Single Phases	25
3.2.2 Phase Separation and Tie Line.....	26
3.3 Rheology	26
3.3.1 Newtonian Solution	27
3.3.2 Ideal Elastic Deformation	27
3.3.3 Viscoelastic Fluid.....	27
3.3.3.1 Linear Viscoelasticity.....	27
3.3.3.2 Non-Linear Viscoelasticity	29
3.3.4 Equipments	31

3.4 Surface Tension.....	32
3.4.1 Gibbs Adsorption Isotherm.....	33
3.4.2 Equipments	33
3.5 Interfacial Tension	34
3.5.1 Spinning Drop Method	34
3.5.2 Pendant Drop Method	34
3.5.3 Equipments	35
3.6 Microscope.....	35
3.6.1 Polarized Microscope.....	35
3.6.2 Transmission Electron Microscope.....	36
3.6.2.1 Freeze Fracture.....	37
3.6.2.2 Cryogenic Preparation	37
3.6.3 Equipments	37
3.7 Differential Scanning Calorimetry.....	37
3.7.1 Equipments	39
3.8 Conductometry.....	39
3.8.1 Equipments	39
3.9 pH-Metry	39
3.10 Densimetry	40
3.10.1 Density of Surfactant	40
3.10.2 Equipments	40
3.11 Small Angle X-Ray Scattering.....	40
3.11.1 Interference and Scattering	41
3.11.2 Scattering from Lamellar Structure.....	42
3.11.3 Scalling Law	43
3.11.4 Equipments.....	44
3.12 Dynamic Light Scattering.....	44
3.12.1 Principle	45
3.12.2 Equipments	46

4 C₁₂C₈MAO/HCl System: Influence of Preparation Route on Lyotropic Mesophase 47

4.1 Normal Preparation: Equilibrium Properties	47
4.1.1 Phase Sequence.....	47
4.1.2 pH and Conductivity Measurements.....	50
4.1.3 Rheological Properties of L _α Phase	52
4.1.4 Microscopic Observation	58
4.1.5 Synergism	59
4.1.6 Interlamellar Spacing between the Bilayer	61
4.1.7 Ion Condensation	63
4.2 Thermal Treatment.....	65
4.2.1 Clouding Phenomenon.....	65
4.2.2 Rheological Properties.....	66
4.2.3 Thermal Quantity and Phase Transition.....	69

4.2.4 Microstructure Change.....	71
4.3 Chemical Reaction.....	73
4.3.1 Protonation with Time.....	73
4.3.2 Microscopy	74
4.3.3 Rheological Properties for Non-Sheared Solution.....	75
5 C_xDMAO System: Effect of Counter-Ion on Aggregate Structure	79
5.1 Aggregate Structure and Zero-Shear Viscosity.....	79
5.1.1 C ₁₄ DMAO Micelle.....	79
5.1.2 Protonation of C ₁₄ DMAO	81
5.1.2.1 Micellar Phase.....	81
5.1.2.2 Formation of Lamellar Phase.....	84
5.1.2.3 Hydration and Viscoelasticity	89
5.2 Trifluoro Acetic Acid CF ₃ COOH	94
5.2.1 Viscoelasticity.....	94
5.2.2 Adsorption Properties	97
5.2.3 Activation Energy and Interfacial Tension.....	101
5.2.4 Microstructure Observation	102
5.2.5 Scattering Profile	105
5.3 Concentration Variable.....	106
5.4 Mixing Effect.....	110
5.4.1 CF ₃ COOH/HCOOH.....	110
5.4.2 HClO ₄ /HCOOH	112
5.5 Effect of Hydrocarbon Chain-Length	114
5.5.1 L _α Phase Formation	114
5.5.2 Rheological Parameters and ΔG_{hyd}	116
6 Conclusions	120
7 Zusammenfassung	125
Appendix	131
A.1 Volume Fraction of Hydrophobic Chain	131
References.....	133

Chapter 1

INTRODUCTION

Surfactant is an abbreviation for surface active agent, which literally means active at a surface. In other words, a surfactant is characterized by its tendency to adsorb at surfaces and interfaces. The driving force for a surfactant to adsorb at an interface is to lower the free energy of that phase boundary. This originates from the chemical structure consisting of incompatible functional groups in the identical molecule. They are used to be called “hydrophilic chain” and “hydrophobic chain”, or, “lipophobic chain” and “lipophilic chain”. Thus, the peculiar structure can be affinity to not only water but oil, consequently, enables both components to be intimate with one another.

Colloid science is subject to nano or micron scale. Surfactant solutions are in this scale because of their self-associate feature. The self-associate mechanism has been well explored and defined theoretically and experimentally. However, differing from “Hard matter” such as inorganic material and polymer, the aggregate consisting of molecules is easily deformable and rearranged by physical and chemical factors, therefore, we need to correct further information in order to establish thus “Soft matter”.

In our daily life, we often use surfactants for versatile purposes, for instance, emulsification, detergence, wetting, lubrication and so on. In the scientific fields, moreover, it is well-known that amphiphilic materials are useful for template of mesoporous material,¹ emulsion polymerization,² and drug delivery.³ One can imagine that these properties are applicable for numerous life products. Besides of the industrial materials, it is noteworthy that surfactant would be potentially working out a part of nano technologies.

1.1 OUTLINE

The thermodynamic properties of amphiphiles in solution are controlled by the tendency for the hydrophobic region to avoid contact with the water, which has been termed the *hydrophobic effect*.⁴ This leads to the association of molecules into micelles, which are spherical or elongated structures in which the hydrophobic inner core is shielded from water by the surrounding corona formed from the hydrophilic ends of the molecules. These aggregates form by spontaneous self-assembly at sufficiently high concentrations of amphiphile, above a *critical micelle concentration (CMC)*. The formation of micelles is predominantly an entropic effect, as deduced from comparisons of the contributions of the enthalpy and entropy to the Gibbs free energy of micellization. The enthalpic contribution results partly from the energetically favorable enhancement of interactions between the hydrocarbon chains. The entropic contribution arises from the local structuring of water due to hydrogen bonding. Unassociated hydrocarbon chains break up the hydrogen bonds between water molecules and impose a locally more ordered structure that is entropically unfavorable. Because this disruption of water structure is reduced when micelles are formed, they are entropically favored compared to unassociated molecules.

Colloidal assemblies are stabilized or destabilized by numerous interactions, which we can classify into two interaction forces, *repulsion* and *attraction*. Namely, interaction between dispersions is determined in terms of the balance of van der Waals

force (attractive potential energy) and electrostatic force (repulsive potential energy). This is well-known as *Derjaguin-Landau-Verwey-Overbeek (DLVO) theory*.^{5,6} DLVO theory, in general, applies for considerably low surfactant concentration, especially, for ionic surfactants which have the strong electric hindrance on coagulation. For high concentration solutions, micelles are obliged to approach each other because of the decrease in bulk phase volume. This is energetically disadvantageous. However, if a micellar structure is reconstructed into a long cylindrical micelle, the assemblies can apart more far from one another.

At high concentrations, amphiphiles can self-assemble into *lyotropic liquid crystalline* phases. “Lyotropic” refers to the fact that such phases are built up by amphiphiles as a function of concentration. Lyotropic phases with one-dimensional translational order consisting of bilayers of amphiphiles separated by solvent are called lamellar phases. A two-dimensional structure is formed by rod-like micelles packed in the hexagonal array. Cubic phases are formed by packing micelles into body-centered cubic or face-centered cubic arrays. The bicontinuous cubic phases are more complex structures, where space is partitioned into two continuous labyrinths.

The lamellar liquid crystalline phase is often formed in detergent solutions. When subjected to perturbation, lamellae can curve into closed shell structures called *vesicles*. A vesicle is a hollow aggregate with a shell made from one or more amphiphilic bilayers. A vesicle formed from a single bilayer is termed a *unilamellar vesicle*, while one with a shell of several bilayers is known as a *multilamellar vesicle*, or sometimes an *onion vesicle*. The unilamellar vesicle is sketched in Figure 1.1. Vesicles are usually not in thermodynamic equilibrium. However, they can be kinetically stable for quite long periods. There are many methods to prepare them, which result in different types of vesicles and size distributions. It is well-known that sonication⁷ (exposure to ultrasound) of dilute lamellar phases induces to vesiculation. An alternative method is to disperse vesicle-forming lipids dissolved in a water-miscible organic solvent into an aqueous solvent.⁸ Dialysis⁹ against water of a solution of amphiphile in detergent is also used to prepare uniform vesicles. All of these methods are somewhat hit-and-miss in their ability to deliver the technologically desirable goal of uniform vesicles with a large encapsulation ratio.

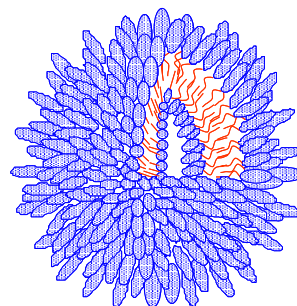


Figure 1.1 Unilamellar Vesicle.

Shear-induced phase transition has been focused on in a few decades. A classical lamellae is ready to transform into vesicles upon addition of shear stress. However certain proper condition (concentration, temperature, ionic strength and so on) permits the vesicle formation. Roux *et al.* had examined it in detail and proposed a *dynamic phase diagram* as a function of shear rate (Figure 1.2).¹⁰ During any procedures of products, shear force must be present purposely or spontaneously. The modified structure by shear force is kinetically stable, while it may retransform to the original structure (equilibrium structure at rest) once shear stress is released from a system. One often encounters quasi-equilibrium vesicles after applied shear, and the vesicles remain stable over a few months ~ more than one year.

Preparation processes of samples influence on the end products. It is used to be called *hysteresis*. Hysteresis is usually referred to a relation between two scalar time-

dependent quantities that cannot be expressed in terms of a single-valued function. In nature hysteresis effects are often caused by phase transitions which are accompanied by abrupt changes of some of the involved physical quantities, as well as by the absorption or release of energy in the form of latent heat. Hysteresis appears in various occasions, for instance, shape memory alloys,¹¹ size-controlled emulsification,¹² vesiculation,¹³ with which irreversible phenomena accompanied are quantified entropically according to the second law of thermodynamics. For the aggregates consisting of the finite numbers of molecules, substantially, hysteresis may be interpreted by a long relaxation time,¹⁴ although the time constant seems to be considerably long.

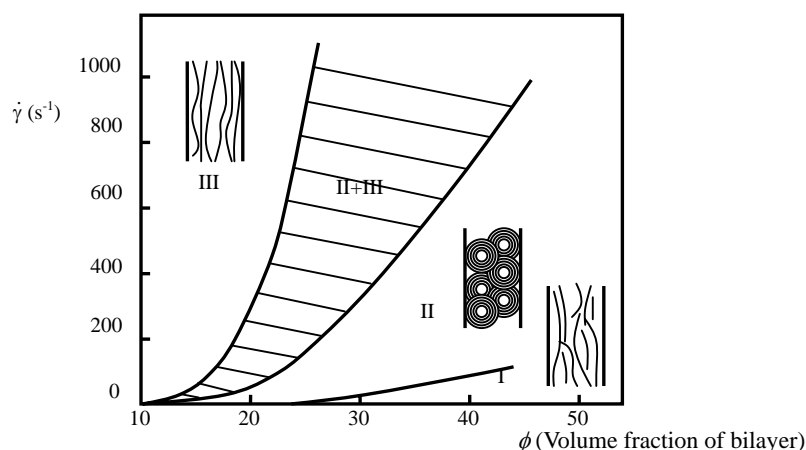


Figure 1.2 Dynamic phase diagram in SDS/pentanol/water/dodecane system.¹⁰

1.2 AIM OF STUDY

The present investigation is divided into two sections in terms of the kind of surfactant used. Firstly, the physicochemical properties and phase behavior in N-Dodecyl-N-Octyl-N-methylaminoxide ($C_{12}C_8MAO$) aqueous system will be focused. This surfactant is in the series of zwitterionic surfactant, and ionic atmosphere on their head group can be manipulated by simple protonation. Such systems thus are assigned to “quasi mixed surfactants system”. Aminoxide surfactants with single alkyl chain have been well elucidated and the protonation degree has significant effects on the associating behavior.¹⁵ The feature is due to the peculiar head group, while chemically different hydrophilic and hydrophobic contributions have not been explored until now. I demonstrate properties of these surfactants in each chapter separately, and their derivative structures are analyzed by means of rheometry, microscopy, conductometry, tensiometry, and scattering techniques.

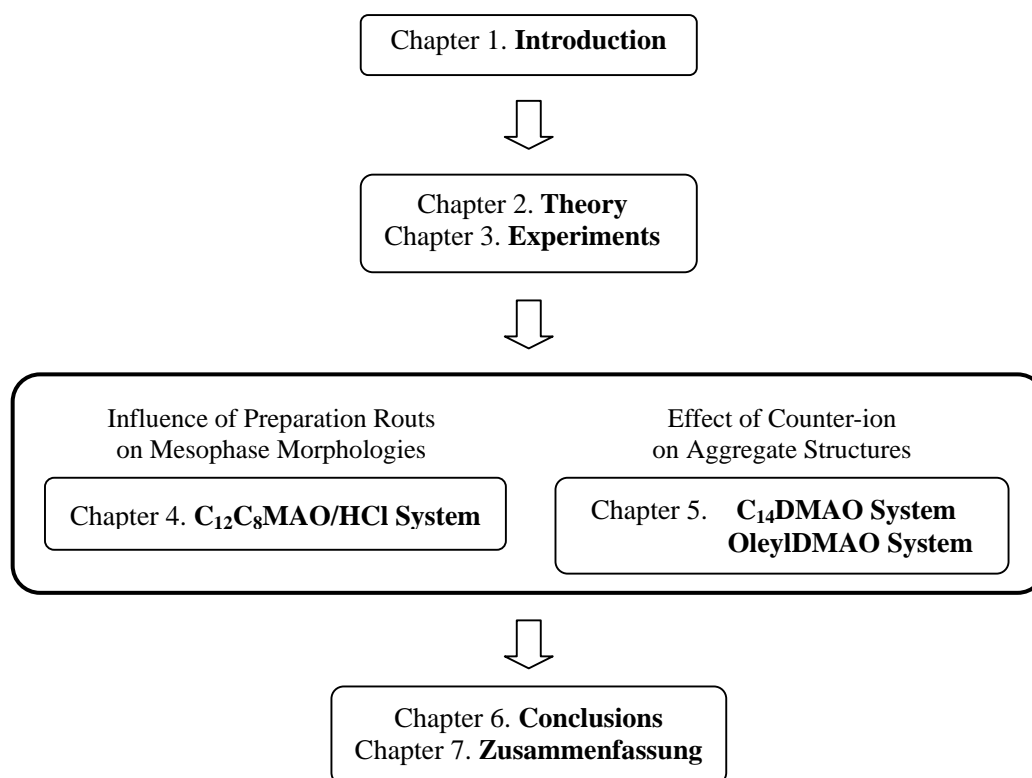
Subsequently, an effect of exposed shear stress on vesiculation is studied using a chemical reaction in both the above systems. As was seen in Figure 1.2, lamellar morphologies are ready to be modified under shearing. Here I compare the static structures at rest between pre-shear and non-shear systems and exhibit the dynamical phase transition in the present systems.

Following the shear history, temperature treatment is investigated in $C_{12}C_8MAO$ system. In the range of moderate protonation, the surfactant solution shows clouding

phenomenon. A cycle of heating and cooling brings about different morphologies. The structure experienced through clouding temperature is identified, and the transformation is interpreted by using thermodynamic quantities.

Finally, effects of counter-ion on the aggregation property are shown in the most conventional aminoxide surfactants, N-tetradecyl-N,N-dimethyl-aminoxide (C_{14} DMAO) and N-oleyl-N,N-dimethyl-aminoxide (OleylDMAO), aqueous solution systems. Various acids composed of different anionic species are served as protonating agent. The counter-ions of ionic surfactants, especially cationic surfactant, indeed influence on physicochemical properties resulting in the viscoelasticity and their micro-structures.¹⁶⁻¹⁹ However, the comprehensive understanding seems not to be achieved due to laborious preparation of the surfactants with different counter-ions for ionic surfactant. In the present case, the laborious works can be overcome by using different kinds of acids. Thus I examine the systematic counter-ion effects and its correlation to the order of Hofmeister series.

The structure of this dissertation is shown in the following flowchart:



Chapter 2 THEORY

The hydrophilic-hydrophobic nature of amphiphilic molecules leads to their self-assembly into a variety of structures in aqueous media. Micelles are one of the main types of structure formed by the association of amphiphiles. They consist of a core of hydrophobic chains shielded from contact with water by hydrophilic head groups, which may be ionic or nonionic. Micelles can either be spherical or extended into ellipsoidal or rod-like shape. This depends on numerous features of surfactants and their surrounding environments. In this chapter, one shall understand the mechanism of aggregation, whereby short- and long-range interaction will be manifested. In addition, driving forces in the course of phase transitions will be explained theoretically.

2.1 MICELLIZATION

To consider the self-assembly, we should necessarily treat thermodynamics subjective to unimer (unassociated molecule) and assembly.^{4,20} According to the equilibrium thermodynamics for a molecular system forming an assembly structure in a solution, chemical potentials of identical chemical species involved in various assemblies must be equal one another. This can be formulated as follows:

$$\mu = \mu_1^0 + kT \log X_1 = \mu_2^0 + \frac{1}{2}kT \log \frac{1}{2} X_2 = \mu_3^0 + \frac{1}{3}kT \log \frac{1}{3} X_3 = \dots \quad [2.1]$$

that is,

$$\mu = \mu_N = \mu_N^0 + \frac{k_B T}{N} \log \frac{X_N}{N} \quad N = 1, 2, 3, \dots \quad [2.2]$$

In Eq. [2.1], the first equation corresponds to *monomer*, the second *dimer*, and the third *trimer*. μ_N is the average chemical potential per molecule in the aggregate with N molecules, μ_N^0 the standard specific chemical potential of μ_N , X_N the molecular concentration (mole fraction or volume fraction) in the aggregate. Surfactant molecules kinetically exchange from micelles to bulk phase and vice versa, whereby the exchange velocities can be expressed with their kinetic constants, k_1 and k_N .

$$\text{Association velocity} = k_1 X_1^N$$

$$\text{Dissociation velocity} = k_N \left(\frac{X_N}{N} \right)$$

At equilibrium (both the velocities reach to constants), the velocity ratio K is given by

$$K = \frac{k_1}{k_N} = \exp \left[- \frac{N(\mu_N^0 - \mu_1^0)}{k_B T} \right] \quad [2.3]$$

This equation is reformed into more convenient one.

$$X_N = N \left[X_1 \exp \left(\frac{\mu_1^0 - \mu_N^0}{k_B T} \right) \right]^N \quad [2.4]$$

The essential condition of aggregation of the surfactant molecules is that $\mu_N^0 < \mu_1^0$ at arbitrary N . If the potentials were identical between the molecules over the different

assembly states, μ_N^0 should have been constant, therefore Eq. [2.4] is

$$X_N = NX_1^N \quad \mu_1^0 = \mu_2^0 = \mu_3^0 = \dots = \mu_N^0$$

From $X_i < 1$, X_N must be less than X_i . This means that all the molecules are present as the monomer.

As seen in Eq. [2.4], X_i approaches to $\exp[-(\mu_i^0 - \mu_N^0)/k_B T]$ with increasing surfactant concentration, in other words, X_i cannot exceed this potential energy. The monomer concentration then becomes unchanged. This concentration is used to be called *critical micelle concentration (CMC)*. In general, the critical concentration is defined as,

$$(X_1)_{crit} = CMC \approx \exp\left(-\frac{\mu_1^0 - \mu_N^0}{k_B T}\right) \quad [2.5]$$

At the CMC, many physical properties exhibit abrupt changes as illustrated in Figure 2.1. Some of these are colligative properties such as osmotic pressure or ionic conductivity. Other techniques are sensitive to changes in the dynamics of molecules at the CMC. The representative method, surface tension, will be described in detail in the following chapter.

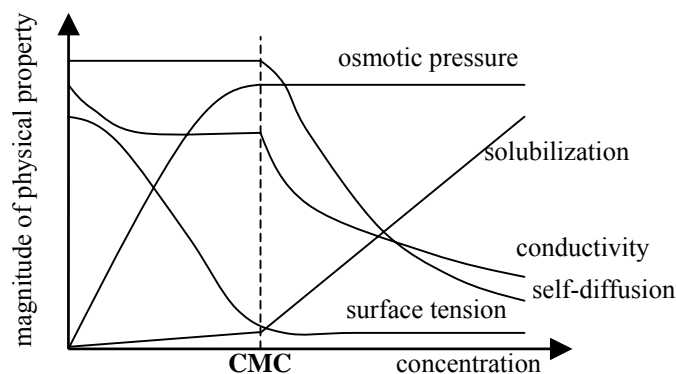


Figure 2.1. Physical properties exhibit a discontinuity near to the critical micellar concentration (CMC).

2.2 KRAFFT TEMPERATURE

In order to utilize efficiently the surfactant, one is necessary to know the concept of Krafft temperature corresponding to the solubility of hydrated surfactants. The schematic diagram is represented in Figure 2.2. In fact, the Krafft temperature is defined as the intersection of the solubility curve and the CMC curve. It may be assumed that complete mixing of molecules occurs below the saturation concentration of molecular dispersion and that the micellar molecules can be treated as if they were perfectly arranged. Thus, the solubility below the Krafft point and the CMC can be explained by the concept of the regular solution. The solubility of the surfactant dramatically increases above the CMC. The reason that the solubility does not increase vertically beyond the Krafft point is that the Krafft point rises slightly with increase in counter-ion concentration, and that the association number of the micelle is not infinite.²¹

The Krafft temperature usually increases as the alkyl chain length increases.²² However, the increase is not regular but displays an odd-even effect.²³ Also the head

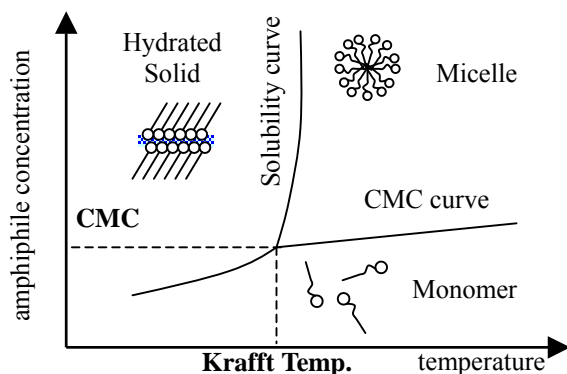


Figure 2.2. Schematic representation of Krafft Temperature.

group and the surrounding counter-ion influence on the Krafft point,²⁴ whereas there are no general trends for the counter-ion dependence. Addition of inorganic salt typically raises the Krafft point for ionic surfactants solutions due to counter-ion condensation,²⁵ while it is not the case for zwitterionic surfactants solutions.²⁶ And many other co-solutes decrease the Krafft point of surfactant.²⁷ If the solubility of a surfactant is very low it will clearly not be operative in various applications. Since a longer-chain surfactant is generally more efficient, there is commonly a delicate compromise in the design of surfactants. Attempts to lower the Krafft point had mainly been directed towards the conditions in the solid state. The surfactants with a lower Krafft point can be developed by structural coordination; chain branching in the alkyl chain,²⁸ introduction of an unsaturated bond in the alkyl chain,²⁹ alternating the alkyl chain with the siloxane chain,³⁰ and so on.³¹ Thus the developments are generally based on making the packing condition in the solid state less.

2.3 COLLOIDAL FORCES

2.3.1 VAN DER WAALS FORCES

The famous theory of colloidal stability due to Derjaguin, Landau, Verwey and Overbeek (DLVO theory) contains two ingredients: a repulsive double-layer force calculated via the Poisson-Boltzmann equation and an attractive van der Waals force. The van der Waals force contains several contributions. One is the quantum mechanical dispersion interactions (London dispersion force). A second term arises from the thermally averaged dipole-dipole interaction (Keesom term) and a third contribution comes from dipole-induced-dipole interactions (Debye term). The van der Waals force operates between both apolar and polar molecules and varies rather little between different materials, *i.e.* compared to the double-layer force, which can change by orders of magnitude upon addition of small amounts of salt.³² The most straightforward way to calculate the van der Waals force is by assuming that the total potential is given by the sum of potentials between pairs of molecules, *i.e.* the potential is said to be pairwise additive—this is usually called the Hamaker approach.³³ The resulting potential depends on the shapes of the colloidal particles and on their separation. In the case of two spheres separated in vacuum by a distance D (Figure 2.3) the non-retarded potential energy is

$$F_{vdW} = -\frac{A}{6D} \frac{R_1 R_2}{(R_1 + R_2)} \quad [2.6]$$

where A is the Hamaker constant and given by the following equation:

$$A = \pi C \rho_1 \rho_2 \quad [2.7]$$

C is the coefficient concerning in the inter-atom pair potential, ρ_1 and ρ_2 the number densities of particle 1 and 2 in unit volume. The Hamaker constant of most condensed phase is found in the range $0.4-4 \times 10^{-19}$ J.

The assumption of pairwise additivity is not entirely correct and a more rigorous theory has been presented by Lifshitz *et al.*²⁰ The mathematical formalism of the Lifshitz theory is rather involved and in order to fully utilize the approach the knowledge of the frequency-dependent dielectric permittivity for all frequencies is needed. This method assumes that the interacting particles and the dispersion medium are all continuous; *i.e.* it is not a molecular theory, but involves the quantum theory.

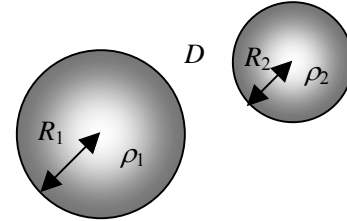


Figure 2.3. Sketch of two dispersed particles.

2.3.2 ELECTRIC DOUBLE-LAYER FORCES

We now consider the electrical potential around a charged colloidal particle in solution. A particle that is charged at the surface attracts counter-ions, *i.e.* an ionic atmosphere is formed around it. These tend to segregate into a layer adjacent to the layer of surface charges in the colloid particle. Since van der Waals forces between identical species of particles are always attractive, it would have seemed that the dissolved particles coagulate one another and precipitate as solid mass out of the solution, if van der Waals force alone were operative. However, it must not occur, because the particles dispersed in solution with large permittivity such as water are charged commonly, resulting in hindrance of coalescence by electrostatic repulsion. Surface charge originates from two processes; (1) ionization or dissociation of a functional group on the surface, (2) ionic adsorption (bond) onto the non-charged surface from solution. Thus an electric double layer is created.

In the diffuse double layer model, the ionic atmosphere is supposed to consist of two regions. Close to the colloid particle, counter-ions tend to predominate due to strong electrostatic forces. Ions further away from the particles are assumed to be organized more diffusely, according to a balance of electrical forces and those resulting from random thermal motion. In this outer region, the concentration of counter-ions thus decreases gradually away from the surface. For the Stern-Helmholtz model, another single layer is formed over the surface. This layer and the inner layer are termed Helmholtz layer and Stern layer, respectively (Figure 2.4). Inside of both the layer, potential is changed proportionally, which is

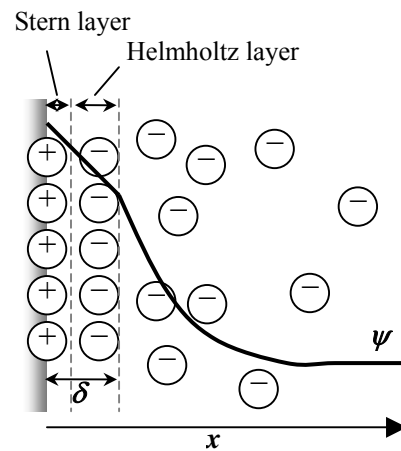


Figure 2.4. Stern-Helmholtz double layer model.

expressed by the following equation.

$$\psi = \frac{4\pi\sigma_e\delta}{\varepsilon_\delta\varepsilon_0} \quad [2.8]$$

ψ is potential, σ_e the charge density, δ the thickness of the Stern and Helmholtz layers, ε_δ and ε_0 the permittivity in the Stern-Helmholtz layer and of vacuum, respectively.

The diffuse double layer or the outer diffuse region away from Helmholtz layer can be described by the Gouy-Chapman equation, which is a solution of the Poisson-Boltzmann equation for a planar diffuse double layer.

$$\text{Poisson-Boltzmann Eq.:} \quad \frac{d^2\psi}{dx^2} = -\frac{ze\rho_0}{\varepsilon_r\varepsilon_0} \exp(-ze\psi/k_B T) \quad [2.9]$$

$$\text{Gouy-Chapman Eq.:} \quad \psi = -\frac{4k_B T}{e} \tanh\left(\frac{e\psi_0}{4k_B T}\right) \exp(-\kappa_D x) \quad [2.10]$$

where x the distance from the middle of two planes, z the counter-ion valency, e the electron charge, ρ_0 a normalization constant with the dimension of density, ε_r the relative permittivity of solution. κ_D is given as follows,

$$\kappa_D = \left(\frac{e^2 \sum_i c_i z_i^2}{\varepsilon k_B T} \right)^{1/2} \quad [2.11]$$

The quantity $1/\kappa_D$ has dimensions of length and it called the Debye screening length. In the case of $ze\psi_0/(k_B T) \ll 1$, *i.e.* for a system where the thermal diffusion energy $k_B T$ is much dominant rather than the surface potential ψ_0 and/or the electrolyte is weakly charged, then the potential simplifies to

$$\psi = \psi_0 \exp(-\kappa_D x) \quad [2.12]$$

This equation is known as Debye-Hückel equation. When $ze\psi_0/(k_B T) \gg 1$, the potential at arbitrary position x can be obtained from the equations [2.8] and [2.10].

2.3.3 DLVO THEORY

DLVO theory consists of the above forces. The total interaction energy is formulated by sum of the two contributions. Differing from the electric double layer force, The van der Waals potential is not much sensitive to the concentration of electrolyte and pH, whereby it can be considered to be constant. The van der Waals attraction would be greater than the double layer repulsion whenever the distance between two particles or planes is enough small, because the attraction increases exponentially with decreasing distance, while the repulsion increases rather slowly. The relationship of both the forces exhibits as a function of distance (D) in Figure 2.5. In the case of strongly charged particles,

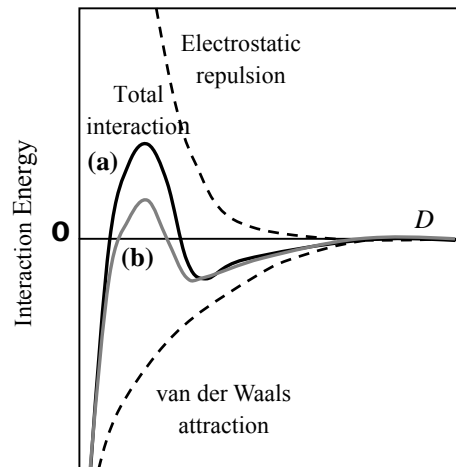


Figure 2.5. Schematic representation of DLVO interaction versus distance profile. (a)→(b): decreasing surface potential (*e.g.* added salt).

the repulsion over long range works out, as a consequence, an energy barrier appears commonly in the distance from 1 to 4 nm. The energy barrier allows the particles not to approach each other. Then the colloid particles settle down at the minimum, *i.e.* keep a constant distance away from one another. This is kinetically stable. On the other hand, reduction of the charge density or potential suppresses the energy barrier (Figure 2.5 (a)→(b)), resulting in coagulation and/or flocculation. The colloidal system therefore is unstable.

2.3.4 HYDRATION FORCE

The hydration force between the amphiphilic surfaces is proposed firstly by Langmuir.³⁴ A charged or zwitterionic surface immersed in aqueous solution results in one or several well-defined layers of water molecules hydrating the surface in the same way as a dissolved ion has a hydration shell. Pushing two such surfaces together results in a dehydration and could be anticipated to be accompanied by a repulsive hydration force. The hydration force often exceeds the DLVO force in the short range and prevents from coalescence of bilayer, vesicle, biomembrane. This is the background to the notation of repulsive hydration forces.

Very strong short-ranged repulsive forces have been found to act between lipid bilayers.³⁵ The range is somewhere between 10 and 30 Å and the repulsion is found to decay exponentially with separation.^{36,37} Similarly, repulsive forces between solid mica surfaces are reported from experiments using surface apparatus.³⁸ Repulsive hydration forces seem to exist both between neutral and charged surfaces. Despite the fact that the mica surfaces in the force apparatus are rigid and the bilayer systems studied have a certain flexibility, there is surprisingly good agreement between the two techniques. The repulsive forces between mica surfaces have also been seen in other solvent.

These experiments have given rise to a surprisingly wild flora of theoretical explanations. Structural or H-bonding polarization at the surface has been suggested as the cause for the repulsion. Bilayer undulations and image charge interactions have also been put forward as possible mechanisms. Recently, it has been suggested that the lipids protrude out into the solvent and this protrusion is limited when two surfaces approach and a repulsive force appears. The mechanism is akin to the idea of undulation forces. The difference lies mainly in the range of the fluctuations. The original undulations model invoked long wavelength undulation, while in the protrusion model the ‘undulations’ are molecular in range.

2.4 SELF-ASSEMBLY STRUCTURES

The preceding section interpreted the thermodynamic treatment on the micellization. This self-assembly structure is not demonstrated by spherical micelle solely; the assembly consisting of some molecules can be modified favorably into different structures. The variable functions are concentration, temperature, pressure, and so on. Then, spontaneously the molecules arrange or distribute in a preferable aggregate-form according to their minimum free energy. In this section, various factors determining the morphologies will be introduced.

2.4.1 FORMULATION OF MODEL FOR FREE ENERGY

Contributions to the free energy μ^0 fall into two classes, bulk and surface terms. It

is well established that for most amphiphiles their hydrocarbon interiors in micelles and bilayers are in a liquid-like state above 0 °C.^{4,39,40} Hence the bulk free energy per amphiphile, g , will be a function only of temperature T and the number of carbon atoms n . Surface contributions are of two kinds: (1) those arising from the attractive hydrophobic or surface tension forces, and (2) from opposing repulsive forces, in main of electrostatic origin. Since the hydrocarbon interior exists in a liquid-like state, we expect that the attractive force contribution can be well represented by an interfacial free energy per unit area of aggregate γ , where γ is close to 50 mJ/m² characteristic of the liquid hydrocarbon-water interface. This value has been shown to be essentially the surface tension of water minus the dispersion energy contributions at the water-hydrocarbon interface.⁴¹ Thus the contribution of the attractive interfacial tension force to μ^0 is written as γa , where a is the area occupied per amphiphile.

The repulsive surface terms are much more difficult to handle. The shape, size, orientation of charged head groups, surface charge density, specific ionic adsorption, unknown dielectric constant of the surface region, certain occurrence of Stern layers and associated discreteness of charge effects all conspire to inhibit any rigorous analysis.^{4,40,42} Despite the apparent intractability of the problem, the various approaches suggest that all of these complications can be subsumed by simple phenomenological forms. Thus, a repulsive energy contribution which varies as a constant/ a has been shown by Tanford⁴² to give a realistic description of micelle size and CMC.

If these assumptions are granted, the free energy μ^0 per amphiphile in the aggregate is

$$\mu^0 = \gamma a + \frac{\text{const.}}{a} + g \quad [2.13]$$

Following the concept of the opposing force, the attractive and repulsive forces should be balanced at an optimal distance. Here the distance is denoted by the area of head group a , which is called optimal surface area (a_0). a_0 is given by the minimum free energy, *i.e.* $\partial\mu_0/\partial a = 0$ in Eq. [2.13].

2.4.2 PACKING CONSTRAINTS

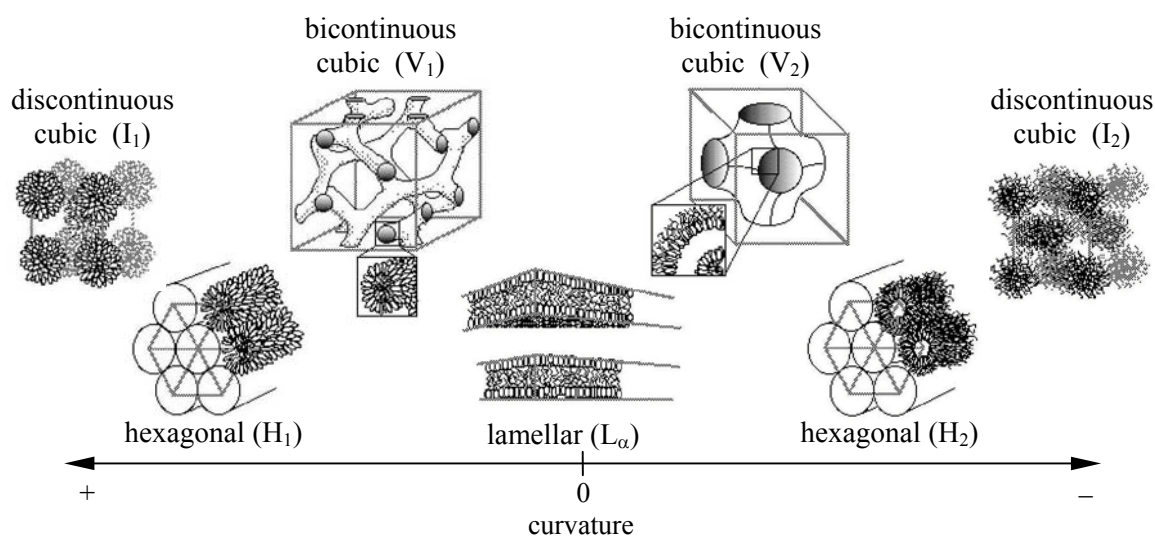


Figure 2.6. Various self-assembly structures and their correlation with interfacial curvature.

It is well-defined that the chemical structure of surfactant determines the aggregate structure. The remarkable dependence is that lipids with two alkyl chains form vesicle rather than micelle even at the low concentration. It is therefore clear that packing constraints must be invoked for a proper treatment of self-assembly, otherwise, in the absence of any such restrictions, spherical micelles will always be thermodynamically favored over other shapes. Since μ^0 is almost identical for all structures, a structure consisting of the minimum aggregation number is entropically favorable. On contrary, the small structure leads to $a > a_0$, resulting in energetic disadvantage. Thus, it will be necessary to consider the available shape and size of aggregates consistent with $a = a_0$.

The packing properties of amphiphiles in micelle can be described by geometry. Israelachivili *et al.*⁴³ proposed the dimensionless packing parameter, $v/(a_0 l_c)$, using the optimal surface area a_0 , volume of hydrophobic chain v , and the critical chain length l_c . Here it is assumed that the hydrophobic chains are in liquid state and incompressible. The series of the structures relative to the packing parameter are shown in Figure 2.6.

Now let us consider an amphiphile of surface area a and oil pool volume v in a micelle where the local radii of curvature are R_1 and R_2 . The packing equation is formulated by referring to Figure 2.7.

$$v/a = l \left[1 - \frac{l}{2} \left(\frac{1}{R_1} + \frac{1}{R_2} \right) + \frac{l^2}{3R_1 R_2} \right] \quad [2.14]$$

This equation is exact for spherical surfaces ($R_1 = R_2$), cylindrical surfaces ($R_2 = \infty$) and planar surfaces ($R_1 = R_2 = \infty$), and holds to a high degree of approximation, with an error of not more than 1 %, for surfaces of arbitrary curvature.

2.4.3 BILAYER STRUCTURES

The bilayer structures can be classified into three groups in terms of their physical properties; classical stacked lamellae (L_{ah}), vesicle (L_{al}), and multi-connected sponge phase (L_3). These structures have been observed in numerous phase diagrams, and often appear in the vicinity of one another. This is the reason why their packing constraints are approximately consistent.

The L_{ah} phase at rest is sketched by the several monolayers stacked along the direction normal to the layer. This phase is visually transparent or a little turbid, and shows optical birefringence under polarization. The one-dimensional periodic structure is characterized by means of the scattering methods⁴⁴; the periodicity assigns to $(1/2)^n$ decay according to the Bragg equation. The interlayer spacing, *i.e.* hydrophobic layer + water layer determines the physical features. Typically the water-swollen lamellar phase exhibits the iridescent coloration phenomena depending on the thickness of the

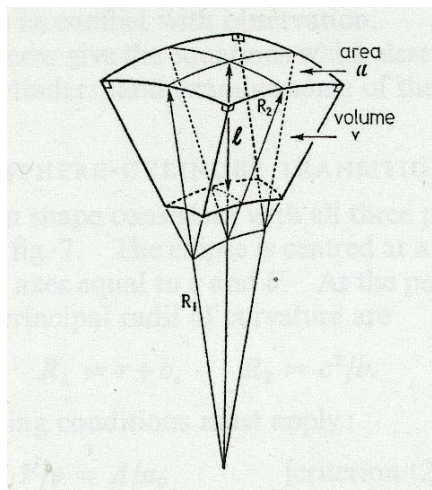


Figure 2.7. Local curvature. R_1 and R_2 are the local radii. l is the hydrophobic length.

interlayer distance.⁴⁵⁻⁴⁷

Vesicles can be imagined as lamellar micelles bent around and enclosed in a sphere, leaving an aqueous solution inside the sphere and one outside. The structure of the surfactant needed to form such structures is that the size of the hydrophobic group is nearly the same size as the effective size of the hydrophilic group. This is expressed as the above packing constraint, $v/(a_0l_c) \sim 1$. However, the packing theory cannot permit to interpret satisfactorily the bent structure because the packing constraints between planar lamellae and vesicle are almost same. Thus one must take a *bending modulus* into account. Besides well-known systems in which double-chain surfactants produce vesicles, many different kinds of systems lead to vesiculation under an appropriate condition.⁴⁸⁻⁵⁰ One of the remarkable systems is the composite of two surfactants with distinct charge signs. In these systems, the mixing reduces the net charge density on the head group, resulting in formation of vesicle, while in empirical fact vesiculation takes place in the vicinity of the neutral composition. It is thus proposed that the bilayers must possess a net charge in order to form vesicles.

This bilayer structure gives different properties with the L_{ch} phase. Addition of water cannot swell vesicles beyond certain limited size. Instead vesicles are dispersed in water like conventional micelles. Then, dilution may induce to a phase transition, from concentrated vesicle (multilamellar vesicle: MLV) to diluted vesicle (unilamellar vesicle: ULV). Vesicle thus shows various macroscopic aspects. Depending on their sizes, the appearances are to be turbid or transparent, and the birefringence is variable as well.

L_3 (sponge phase) consists of a multiply connected bilayer structure that divides a solvent into two interwoven labyrinths, which is called bicontinuous structure. The schematic figure and the microscope image are shown in Figure 2.8. This phase is commonly observed in the vicinity of L_{ch} phase as well as vesicles,⁵² and regardless of their microscopic resemblances the topological distinctions result in further different macroscopic properties. L_3 phase is optically transparent at rest and generally flows freely with constant viscosity. However, the very dilute sponge phases exhibit a transient birefringence when shaken, which suggests a shear-induced transition to a lamellar state.^{53,54}

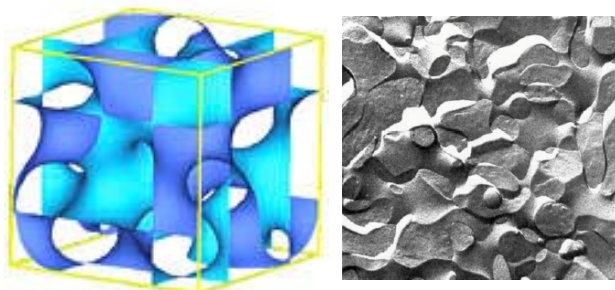


Figure 2.8. L_3 (sponge) phase. The bar length on the right figure corresponds to 10 nm. The microscope image was quoted from Ref. [51]

2.4.4 INTERFACIAL CURVATURE AND ELASTIC MODULUS

The differential geometry of surfaces is applied to the model for interfacial curvature of a continuous surfactant film. A surface can be described by two fundamental types of curvature, mean and Gaussian curvatures. Both can be defined in terms of the principal curvatures $c_1 = 1/R_1$ and $c_2 = 1/R_2$. The mean curvature is

$$H = \frac{c_1 + c_2}{2} \quad [2.15]$$

and the Gaussian curvature is defined as

$$K = c_1 c_2 \quad [2.16]$$

Conventionally the signs of the radii of curvature are defined to be positive if the surface points outwards.

The elastic free energy density associated with curvature of a surface contains, for small deformations, the sum of contributions from mean and Gaussian curvature. It is given approximately by

$$f_{\text{curvature}} = f_{\text{mean}} + f_{\text{Gaussian}} = \frac{1}{2} \kappa (2H - c_0)^2 + \kappa' K \quad [2.17]$$

c_0 is the spontaneous curvature, i.e. twice the equilibrium mean curvature for the case of zero Gaussian curvature, $c_0 = c_1 = 2H_{\text{eq}}$, $c_2 = 0$. The quantities κ and κ' are the elastic moduli for mean and Gaussian curvatures respectively, and have units of energy.

The above three classes of bilayer phases are easily explained, to a first approximation, in terms of membrane bending elasticity. For a symmetric bilayer the bending energy per unit area can be reformulated from Eq. [2.17] to⁵⁵

$$f = \frac{1}{2} \kappa 2H^2 + \kappa' K \quad [2.18]$$

The spontaneous curvature is omitted because of the symmetry. The bending energy of vesicle would be regarded as the energy required to create a vesicle from planar bilayer, i.e. $4\pi(2\kappa + \kappa')$. The energy from planar bilayer to sponge phase is correspondent to $-4\pi\kappa'$, which arises from creation of passages connecting parallel bilayers.⁵⁶ The contributions of both the moduli to these bilayer phases can be mapped as a primitive phase diagram in Figure 2.9.

Each modulus can be controlled by several methods. For the aggregates, the individual surfactant molecular structure strongly affects on the moduli. And, rather than the hydrophobic moiety of surfactant molecule, the hydrophilic one is superior to work out the curvature energy. In fact, surface

charge is a particularly powerful and adaptable means of influencing κ and κ' . Its effect on the bending elastic moduli of normal bilayers depends on two controllable parameters, the charge density on the membrane surface and the Debye length of the aqueous medium. The electrical contribution to κ is positive, while that to κ' is negative. For high surface charge densities and low salt concentrations, the bending moduli can be expressed as follows.⁵⁷

$$\kappa_{el} = \frac{1}{2\pi} \frac{k_B T}{l_B \kappa_D} \quad [2.19]$$

$$\kappa'_{el} = -\frac{\pi}{6} \frac{k_B T}{l_B \kappa_D} \quad [2.20]$$

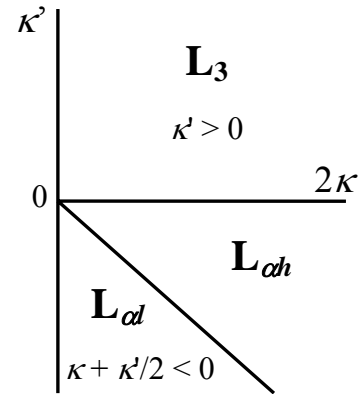


Figure 2.9. Primitive phase diagram of bilayer phases as governed by the bending rigidity, κ , and the Gaussian modulus, κ' .

l_B is the Bjerrum length, $e^2/(4\pi\epsilon_0\epsilon_r k_B T)$. Under these conditions, one might have important implication for spontaneous vesiculation,⁵⁸ with which the experimental results are in fairly well agreement.^{50,59}

2.4.5 WORM-LIKE MICELLE

The micelles cannot transform suddenly into a mesophase with changing intensive or extensive quantities like temperature and concentration. In the micellar phase, spherical micelles in the vicinity of CMC would grow up gradually with increasing concentration (although micelles composed of certain surfactants may not be spherical even at CMC). The micellar growths are accompanied before phase transition to a liquid crystal with a structural periodicity. In the intermediate concentration region, there may be a preference for two-dimensional (sheet-like) or one-dimensional (worm-like) assemblies, depending on surfactant geometry and the presence of additives like co-surfactant and salt. The isotropic disordered phase, which consists of an entangled mass of flexible worm-like objects, leads to the viscoelasticity and shear birefringence,⁶⁰ while the solution still flows along shear stress. For the worm-like micelle, one can envisage that small spherical micelles at low concentration undergo uniaxial growth to make rod micelles as the volume fraction of amphiphile is increased. At some length scale, these rods become flexible and behave as polymer. Its statistics and dynamics actually resemble to polymer solutions, however there are distinctions in terms of structural deformation. The aggregate is easily broken (scission) and recombined repeatedly,⁶¹ while polymer cannot be done in such a way. Nevertheless, if the scission energy of a micelle (the energy required to create two end-caps from a semi-infinite cylinder) is large enough, then the semi-flexible wormlike micelles are compatible with the polymer solution, and entangled with one another, at relatively low total volume fractions of surfactant. Figure 2.10 illustrate various length scales. These scales are intrinsic for polymer, while controllable for worm-like micelle, and determine the macroscopic properties of the solution *e.g.* viscosity.

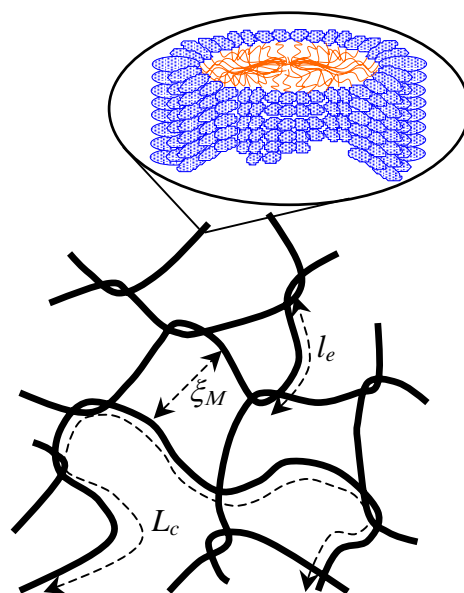


Figure 2.10. Schematic representation of entangled worm-like micelles with relevant length scales: contour length L_c , entanglement length l_e , and mesh size ξ_M .

2.5 PHASE TRANSITION

2.5.1 CONCENTRATION-INDUCED PHASE TRANSITION

As had been implied in the former sections, phase transitions can be induced by changing several parameters. In the dilute micellar solution, micelles undergo uniaxial or biaxial growth with increasing concentration, resulting from energetic preference. The process in the course of micellar growth may specify the type of lyotropic liquid

crystal neighboring the micellar solution at low surfactant concentration. Oetter *et. al* showed the relationship between the interfacial tension on the micelle-bulk surface and the liquid crystal structure; regardless of the interfacial tension measurements in the micellar solutions at low surfactant concentration, the values classify definitively into different liquid crystals at high concentration.⁶² One can recognize from Eq. [2.13] that the attractive free energy strictly relate to the interfacial tension. It is furthermore necessarily emphasized that the optimal head group area is the most critical parameter. Increment of concentration causes hydration on the surfactant hydrophilic moiety to reduce, resulting in the suppression of repulsive force between not only aggregates also head groups. As a consequence, the higher the concentration, the higher the packing constraint is. Thus the concentration-dependent phase transition arises from the suppressed head group area, and this interpretation is confirmed well by numerous phase diagrams.

2.5.2 EFFECTS OF ADDITIVES

In the case of the presence of an additive in surfactant solution, the aggregate structure depends strongly on the character of the additive. Solubilizes such alcohols and alkanes enable inner micelle to modify and to give rise up to the inner volume. If the additive has polarity (*i.e.* forming hydration bonds with water or hydrophilic part of surfactant), the interfacial curvature is reduced upon addition of the additive. On contrary, a non-polar alkane is solubilized in the deep core of micelle, the curvature then comes to be more positive. Often the polar additives are termed *co-surfactant*, which potentially forms no itself aggregate, while cooperates with an amphiphile as if the additives were hydrophobic surfactant. The cooperative surfactants introduce the negative curvature change due to the moderate head group repulsion, besides relax the elasticity of surfactant film. This softness of surfactant film plays a significant role in microemulsion⁶³ and lamellar⁶⁴ morphologies.

When inorganic salts are dissolved in surfactant solution, each dissociated species re-build up the double-layer on the charged micelle surface according to their charge signs. For the ionic surfactants, the interaction force is dominantly electrostatic, while for the nonionic surfactants the effect of added salt is much more complicated; their chemical species affect the water structure, resulting in hydration of the surfactant head groups. This effect is well-known as *salting-in* and *salting-out*. For both phenomena, the anionic specie rather than the cationic one influences the water structure, *i.e.* the salting-out anions such as Cl⁻ prevent from hydration, while the salting-in ones like SCN⁻ promote to hydrate the head group. Hofmeister expressed such the anion property in the sequent series⁶⁵:



The left side in the series corresponds to the salting-out or lyotropic salt and the right side the salting-in or hydrotropic salt. These effects had been observed by experimental measurements of cloud point,⁶⁶ CMC,⁶⁷ and stability of liquid crystal.⁶⁸ The ionic surfactant, on the other hand, has strong electrostatic interaction with its opposite charge ion. The anionic species of salt has remarkable effects compared to the cationic one as mentioned above, *i.e.* one finds that the cationic surfactant systems would show different properties dependent on the kind of the chemical species. Then the Hofmeister series implies the distinct meaning. The salting-in anion breaks the water structure, suggesting that water do not dissolve preferably the ion into itself, however, the salting-

out anion can be dissolved in water because of making up the water structure. These can be explained by the binding degree of the cationic head group of surfactant and the anion. Namely the salting-in anions refer to the anion bound highly with the surfactant head group, and the others are that bound loosely. Here the anions with high and low binding degrees are called hydrophilic and hydrophobic counter-ions, respectively. As derived from the names, these counter-ions make the surfactants hydrophilic or hydrophobic, *e.g.* the surfactant with a hydrophobic counter-ion forms much larger aggregates than that with a hydrophilic counter-ion.⁶⁹

2.5.3 TEMPERATURE-INDUCED PHASE TRANSITION

Temperature may be the most effective intensive factor on the phase transition in the surfactant chemistry field. As with the melt solid or crystal, the liquid crystal phases have their melting points, here indicating the order-disorder transition. Such the phase transitions are denoted by symmetry changes, *i.e.* by transformation in orientational and translational ordering in the system. For instance, a phase transition from the lamellar phase to the micellar phase is defined by the break of translational order in one dimension. The layered structure is characterized by a periodic alternation in density or composition.

The temperature at which phase separation occurs at low surfactant concentration is called the *cloud point*. On heating the solution may start to scatter light strongly in a well-defined temperature range. It becomes cloudy. The isotropic solution region is bordered towards higher temperatures by a lower consolute curve (Figure 2.11), above which there is a phase separation into one surfactant-rich and one surfactant-poor solution. The minimum in the lower consolute curve is termed LCST (lower critical solution temperature). The onset of phase separation is manifested by a cloudiness of the solutions, and further increasing temperature induces the visible phase separation into two phases. This would be determined by the Gibbs free energy. If ΔG_m for the blend is less than that of the components, then the system is completely miscible. If, however, there is a temperature at which ΔG_m is greater than that of two coexisting phases, then phase separation will occur. Below T_c , ΔG_m for a mixture is always less than that for the pure components, so a homogeneous phase (1Φ) is stable.

Phase separation on heating is typically observed for aqueous solutions of nonionic surfactants.^{21,52} This originates from demixing of surfactant molecules and water, *i.e.* dehydration. A few cationic surfactant solutions also show lower consolute behavior.^{70,71} High concentration of salt can cause cationic surfactant solution to separate into two immiscible phases. This phenomenon, originally termed coacervation, has been investigated since 1940s and was first observed for mixtures of the cationic surfactant with salts such as potassium thiocyanate (KSCN) and potassium chloride (KCl).^{72,73} The phase separation is of the upper consolute behavior, which shows phase

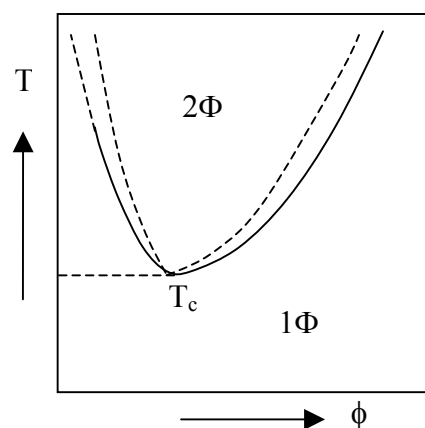


Figure 2.11. Lower critical solution temperature (LCST, T_c). 1Φ and 2Φ refer to the isotropic phase and two-phase. T is temperature, ϕ the concentration or volume fraction of surfactant.

separation on cooling. Clouding phenomena strictly relates to infinite micelle growth, resulting in the macroscopic scattering light. Therefore, the smaller micelles exist below the cloud temperature, the higher the cloud point is observed. The hydrophilic surfactants, whose chemical structures are manipulated by their hydrophilic and hydrophobic chains, thus have relatively high cloud temperature,⁷⁴ especially for the ionic surfactants without salt clouding phenomena seldom appears. The topological variation in the course of clouding had been argued using different models to date.^{75,76} Recently it was demonstrated by the electron microscope that the spherical micelles transform to branched micelles via cylindrical structure on elevating temperature.⁷⁷ In any case, the spontaneous curvature of micelle should be reduced with approaching critical temperature.

2.5.4 SHEAR-INDUCED PHASE TRANSITION

Recently, it has been observed that lyotropic lamellar phases under steady shear flow present different orientations. Shear force induces a hydrodynamic instability; a lamellar phase exposed under certain shear stress is of *kinetically* stable at its steady state, whereas is not of *thermodynamically* stable at rest. The lamellar orientations were drawn in the dynamic phase diagram (Figure 1.2) by Diat *et. al.*, who developed the theoretical description of the shear-induced phase transition. At very low shear rates and high surfactant concentrations, the membranes are mainly parallel to the flow with the smectic director parallel to the velocity gradient direction (region I in Figure 1.2).

In this state a lot of defects or dislocations would persist in the two directions perpendicular to the director,⁷⁸ which is presumably similar to the thermotropic systems. At higher shear rates or for more dilute systems, a new state appears where the smectic layers form multilayer spherical droplets of well-defined size, controlled by the shear rate, ranging typically from 10 μm to less than 1 μm (region II). At even higher shear rates, the membranes orient parallel to the flow with the smectic director parallel to the gradient of the velocity direction. This state has some resemble patterns with the first orientation but no defects remain in the direction of the flow (region III).

The bilayer structures are stabilized dominantly by the electrostatic interaction between charged membranes and the undulation introduced by Helflich.⁷⁹ This undulation force seems to be destabilized by shear flow. At very low shear rate, the system flows by moving dislocations and is very viscous but Newtonian. For the intermediate shear rates, the sample is forced to move faster and the dislocation cannot follow anymore. The fact that the plate movements are faster than the rate of displacement of the dislocations creates a pressure perpendicular to the layer and the lamellar bilayers develop undulation instability. These dislocations forbid the system to flow and instead the system bifurcates to another orientation which consists of small spheres rolling on each other in order to allow the flow to proceed. Therefore the shear stress would be correlated with the sphere size. Diat *et al.* have observed a relation between the size R , of lamellar droplets in an onion phase and the applied shear rate, $\dot{\gamma}$:

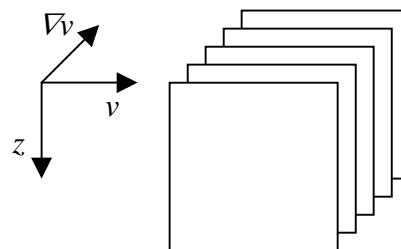


Figure 2.12. Orientation of lamellar sheets in shear flow. v and ∇v represent the directions of the flow and the velocity gradient, respectively.

$R \sim 1/\sqrt{\dot{\gamma}}$.^{10,80} They calculated the characteristic size of the onions by balancing two forces: an elastic one, f_{el} , and the viscous force f_{vis} as follows⁸¹:

$$f_{el} = \frac{4\pi(2\kappa + \kappa')}{d} \quad [2.21]$$

$$f_{vis} = \eta R^2 \dot{\gamma} \quad [2.22]$$

The elastic force corresponds to one required to maintain a lamellar phase with a size R , and the viscous force is one experienced in a flow. d is the repeating distance of bilayer, η the viscosity, $\dot{\gamma}$ the applied shear rate. According to the balance of the equations [2.21] and [2.22], the equilibrium size for the steady state can be calculated,

$$R = \sqrt{\frac{4\pi(2\kappa + \kappa')}{\eta d \dot{\gamma}}} \quad [2.23]$$

This theoretical view agrees fairly with the empirical results.

van der Linden *et. al*, furthermore, addressed the volume fraction dependence on the onion size.⁸² They used another balance between the Laplace pressure and the local shear stress during shear. The difference in curvature of the droplet surface with respect to its surroundings would imply, during shear, a surface stress, equal to the Laplace pressure, $4\sigma_{eff}/R$, where σ_{eff} refers to the effective surface tension of the droplet. The surface stress due to the curvature of the surface, created at a certain shear rate $\dot{\gamma}$, balances the shear stress, $\eta \dot{\gamma}$. One then finds for the onion diameter

$$R = \frac{4\sigma_{eff}}{\eta \dot{\gamma}} \quad [2.24]$$

Essentially σ_{eff} can be described by the product of the bending elasticity and compression modulus. For the case of non-charged or highly charge-screened system, the compression modulus B is given by⁸³

$$B = \frac{9\pi^2(k_B T)^2 d}{64\kappa d_w^4} \quad [2.25]$$

$d = \delta + d_w$, with δ and d_w represent the thickness of the bilayer and the water layer, respectively. One thus can formulate the effective surface tension using Eq. [2.25] and a geometric relationship, $d_w = \delta(1-\phi)/\phi$.

$$\sigma_{eff} \sim \left(\frac{\phi}{\delta}\right)^2 \quad [2.26]$$

Hoffmann and Rehage, on the other hand, found out an analogous phase transition, $L_3 \rightarrow L_{oh}$, under shear,⁸⁴ and their group had experimentally explored it.⁸⁵ Cates and Milner, furthermore, theoretically studied the $L_3 \rightarrow L_{oh}$ transition in the presence of shearing on the basis of a physical picture that the transition in a lyotropic system also belongs to the category of the fluctuation-induced first-order transition.⁸⁶ They predicted the decrease in the first-order nature of the transition with an increase in the shear rate, based on the idea that symmetry-breaking shear field suppresses the origin of the first-order nature, *i.e.* large fluctuation effects associated with the degeneracy of the possible orientations of the ordered state. It is well-known that the sponge phase becomes birefringent once the shear field is exposed,⁸⁷ and recently Yamamoto *et. al* showed experimentally the sponge-lamellar phase transition under shear.⁸⁸ In the sponge phase, shear flow tears off selectively the passage of the

membrane that is not along the flow direction, if it is strong enough. And the sponge phase starts to have anisotropy with an increase in the shear rate. This may lead to the shortening of the characteristic length of the system.⁸⁹ When the shear rate becomes sufficiently strong to erase all the passages, the characteristic length would be equal to that of the lamellar phase, and thus the shear-induced phase transition takes place. The sponge-lamellar phase transition should be first-order thermodynamically because of the symmetry difference between these phases, while the order of phase transition increases upon addition of shear flow. This could be due to the contribution of the flow mechanics instead of the thermodynamics.

Chapter 3 EXPERIMENT

3.1 INGREDIENTS

3.1.1 SURFACTANTS

In the present study, two types of surfactants are used, and their chemical structures are shown in Figure 3.1. These surfactants are termed “*amphoteric surfactant*”, since their hydrophilic head groups (-N(CH₃)O, -N(CH₃)₂O) vary from nonionic- to cationic-form with regard to the bulk pH. They therefore have advantageous properties such as their compatibility with all other classes of surfactants, non-sensitivity to hard water, and stability in both acidic and basic conditions. Such charge signs of zwitterionic surfactants can be quantitatively described by using the dissociation constant.



The dissociation constant determines the composition of the cationic and nonionic species in the system, that is, pH-variation introduces the mixture of two surfactants at arbitrary ratio. At higher concentration than CMC, where surfactant molecules are

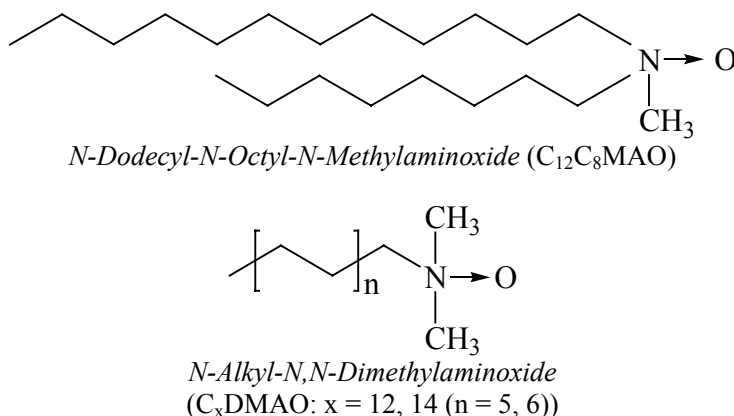


Figure 3.1. Chemical structures of different surfactants.

present as monomer or micelle, two different dissociation constants arise from each favorable ionization degree of monomer and micelle. The introduction of charges is more favored on the micelle surface than to the monomer in solution.⁹⁰⁻⁹²

Recently it was discovered by Maeda *et al.* that aminoxide surfactants construct the hydrogen bond between charged head groups,⁹³ as schematically depicted in Figure 3.2. The hydrogen bond is expected to decrease the area per head group and the apparent bonded dimers would behave as if they were double chain amphiphiles. On the single chain aminoxide surfactants, several marked effects of the protonation have been thoroughly examined over some decades,⁹⁰⁻¹⁰⁰ while another surfactant, C₁₂C₈MAO, has been hardly reported on its physicochemical properties.

To my knowledge, the double-chain aminoxide surfactant would not have been ever exploited to date. The series of the surfactants were provided from Clariant GmbH,

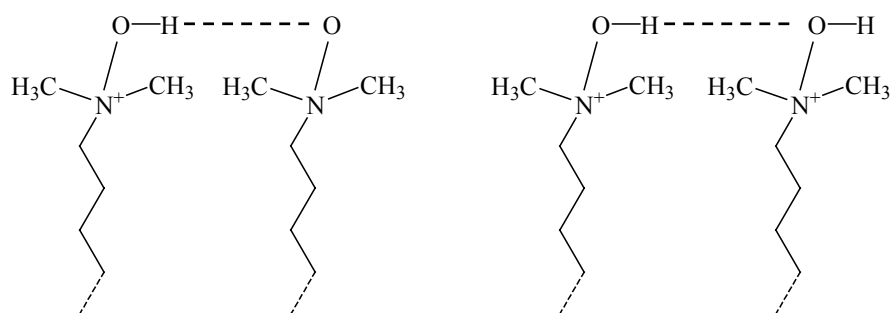


Figure 3.2. Schematic representations of the hydrogen bonds: between the nonionic and the cationic head groups (left), and between two cationic head groups (right).

and they were washed twice with acetone and recrystallized. The purity was verified in terms of its melting point. The common double-chain surfactants, for instance, lecithin, AOT (sodium bis-(2-ethylhexyl)sulfosuccinate),¹⁰¹ and N,N-dialkyl-N,N-dimethylammonium bromide,¹⁰² tend to form a bilayer structure even at low surfactant concentration according to their packing restrictions. Therefore, C₁₂C₈MAO is expected not to be out of the conventional tendency. It should be noteworthy, however, that the head group is aminoxide having the potential short-range interaction, hydrogen bond.

The product specifications for each surfactant are summarized in the following table. The original products were refined twice with acetone and recrystallized.

Table 3.1. Specifications for each surfactant, molecular weight (M_w) and supplier of each product.

Surfactant		M_w [g/mol]	Supplier
N-Dodecyl-N-Octyl-N-Methylaminoxide	C ₁₂ C ₈ MAO	327.62	Clariant GmbH
N-Alkyl-N,N-Dimethylaminoxide	C ₁₂ DMAO	229.40	Hoechst GmbH
	C ₁₄ DMAO	257.46	
	OleylDMAO	311.54	

3.1.2 ACIDS

The present study utilized various kinds of acids, which are listed up in Table 3.2. Their intrinsic properties are also shown in the table. All the chemicals belong to the strong acid whose pK_a is considerable low. pK_a is expressed by the instructive equation.

$$pK_a = pH + \log \frac{[HA]}{[A^-]} \quad [3.2]$$

A refers to the conjugate base.

The radii of ions, r , are those in solid states, which were obtained by the diffraction measurements.¹⁰³ The accuracy is ≤ 0.0005 nm for the monoatomic ions and ≤ 0.001 nm for polyatomic ions. The quantity Δr is the thickness of the first hydration shell,¹⁰⁴ given by:

$$\Delta r = \left[\frac{45d^3|z|}{r} + r^3 \right]^{1/3} - r \quad [3.3]$$

where d is the diameter of a water molecule, equal to 0.276 nm, and z the ionic valency.

Hydration numbers of ions are defined by different operational methods: diffraction experiment or computer simulation,^{105,106} compressibility method,¹⁰⁷ hydration shell model,¹⁰⁸ and Stokes volume.¹⁰³ Here the hydration numbers were quoted from ones obtained by the Stokes volume method. This method employs the conductivities of the solutions. The “ionic Stokes radii” are formulated by:

$$r_{Stokes} = 9214|z|\lambda^\infty \quad [3.4]$$

The unit of r_{Stokes} is in pm. λ^∞ is the conductivity at infinite dilution in $\text{cm}^2/(\Omega \cdot \text{equiv})$. The numerical coefficient pertains to 298.15 K and incorporates the viscosity of water. Then the Stokes radii must be corrected in order to yield acceptable sizes of the ions in solution, and the correction can be performed empirically as follows:

$$r_{corr} = 214 + 0.427r_{Stokes} \quad [3.5]$$

The hydration number (N_h) can be calculated using further correction of a packing factor $k_p = 0.888$ in terms of the ionic “Stokes molar volume”.

$$N_h = \left[k_p N_A \frac{4\pi}{3} r_{corr}^3 - V^\infty \right] / V_w \quad [3.6]$$

N_A is the Avogadro number, V^∞ and V_w are the ionic limiting standard molar volume at infinite dilution and the molar volume of water, respectively.

The last column includes the standard Gibbs free energies ΔG°_{hyd} of hydrated ions from the elements in the standard state, *i.e.*, transferring from the ideal gas phase to the infinite dilute aqueous solution.^{103,109} The net Gibbs free energy of the aqueous ions is given by

$$\Delta G^\circ_{hyd}(\text{ion}) = \Delta G^\circ_f(\text{ion, aq}) + z(467.2) - \Delta G^\circ_f(\text{ion, g}) \quad [3.7]$$

ΔG°_f is the standard Gibbs free energy of the hydrated ion based on $\Delta G^\circ_f(\text{H}^+, \text{aq}) = 0$. The notations in parentheses indicate the state of the ion; aq = aqueous, g = gas. The second term is complement factor in order to convert from the relative (based on $\Delta G^\circ_f(\text{H}^+, \text{aq}) = 0$) to the absolute Gibbs free energies of formation of the aqueous ions, and the value is given by using the standard Gibbs free energy of hydration of the hydrogen ion, $\Delta G^\circ_{hyd}(\text{H}^+) = -1056 \pm 6 \text{ kJ/mol}$.^{108,110}

For the multicharged ions, the first-, second-, and/or third-dissociation can

Table 3.2. Acidities and ion properties for different anionic species at 25 °C.

Name	Structure	Configuration	pK _a	r [nm]	Δr [nm]	N _h	ΔG [°] _{hyd} [kJ/mol]
sulfate	SO ₄ ²⁻	tetrahedral	1.99	0.230	0.0432	5.3	-1090
carbonate	CO ₃ ²⁻	planar	10.33	0.178	0.0754	7.1	-479
dihydrogen phosphate	H ₂ PO ₄ ⁻		2.15	0.200	0.0335	2.6	-473
acetate	CH ₃ COO ⁻	irregular	4.74	0.244	0.0200	1.1	-389
formate	HCOO ⁻	planar	3.75	0.202	0.0327	1.1	-382
chloride	Cl ⁻	spherical	~ -7	0.181	0.0425	3.9	-363
bromide	Br ⁻	spherical	~ -9	0.196	0.0352	3.4	-328
nitrate	NO ₃ ⁻	planar triangle	~ -2	0.199	0.0339	3.0	-311
thiocyanate	SCN ⁻	cylindrical	-1.85	0.249	0.0189	0.2	-275
perchlorate	ClO ₄ ⁻	tetrahedral	~ -10	0.242	0.0205	2.6	-227
trifluoroacetate	CF ₃ COO ⁻		0.67±0.2				

cooperate in solution. The specific quantities corresponding to each dissociation degree are listed up for reference in Table 3.3.

Table 3.3. Acidities and ion properties for multicharged anions at 25 °C.

Name	Structure	pK_a	r [nm]	Δr [nm]	N_h	ΔG_{hyd}° [kJ/mol]
sulfate	HSO_4^-	$pK_{a1} = -6.22$	0.190	0.0379	0.8	-335
	SO_4^{2-}	$pK_{a2} = 1.99$	0.230	0.0432	5.3	-1090
carbonate	HCO_3^-	$pK_{a1} = 6.36$	0.156	0.0584	1.8	-368
	CO_3^{2-}	$pK_{a2} = 10.33$	0.178	0.0754	7.1	-479
phosphate	H_2PO_4^-	$pK_{a1} = 2.15$	0.200	0.0335	2.6	-473
	HPO_4^{2-}	$pK_{a2} = 7.21$	0.200	0.0594	10.4	-
	PO_4^{3-}	$pK_{a3} = 12.34$	0.238	0.0560	7.9	-2773

The properties of aqueous solutions depend to a large extent on the effects of the solutes on the structure of the solvent, water. Water is a highly structured liquid,¹¹¹ and many interactions are governed by the energetics of the formation and destruction of this structure. The introduction of a solute from outside into water is accompanied by the creation of a cavity, against the cohesive forces due to the structure, to accommodate the solute, before any direct solute-water interactions take place. The structure of the water in the vicinity of the solute, however, is affected by its presence, and some solutes (ions) are water structure breakers whereas others are water structure makers. This breaking or making is indirectly related to the hydrophobicity or hydrophilicity of the solute. The structure of water can be described quantitatively by a change in the average number of hydrogen bonds in which a water molecule participates, ΔG_{HB} .¹¹² Empirically, ΔG_{HB} seems to be related to the structural entropy, S_{str} , of the ions.

$$\Delta G_{HB} = -0.14 - 8.2 \times 10^{-3} S_{str} \quad [3.8]$$

The structural entropy, in turn, is obtained from a model according to¹¹³:

$$S_{str} = \Delta S_{hyd}^\circ - [a + b \cdot r] - Az^2(r + \Delta r)^{-1} [(\Delta r/r)\varepsilon'^{-2}(\partial\varepsilon'/\partial T)_p + \varepsilon^{-2}(\partial\varepsilon/\partial T)_p] \quad [3.9]$$

ΔS_{hyd} is the absolute molar entropy of hydration. The second term derives from the cavity formation, obtainable for neutral solutes with the same radius r as that of the ion, with $a = -22$ and $b = -0.600$ in J/(K·mol). The coefficient in the third term is $A =$

Table 3.4. ΔG_{HB} for different anions.

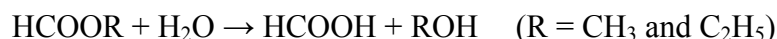
Name	Structure	ΔG_{HB}
carbonate	CO_3^{2-}	0.28
acetate	CH_3COO^-	0.12
dihydrogen phosphate	H_2PO_4^-	-0.1
sulfate	SO_4^{2-}	-0.21
formate	HCOO^-	-0.33
chloride	Cl^-	-0.61
nitrate	NO_3^-	-0.68
bromide	Br^-	-0.8
thiocyanate	SCN^-	-0.82
perchlorate	ClO_4^-	-1.01
trifluoroacetate	CF_3COO^-	

$N_A e^2 / 8\pi\epsilon_0 = 7.0 \times 10^{10}$ J·(nm)/mol, where e is the unit charge ($= 1.60218 \times 10^{-19}$ C), ϵ_0 the relative permittivity of vacuum ($= 8.85419 \times 10^{-12}$ C²/(J·m)). ϵ' is the relative permittivity of water in the first hydration shell, where dielectric saturation takes place, and $\epsilon' = 1.58$ and $(\partial\epsilon'/\partial T)_p = -1.0 \times 10^{-4}$ K⁻¹ are to be used. The values of ϵ , the relative permittivity of pure water, and its isobaric temperature derivative, $(\partial\epsilon/\partial T)_p$, are 78.4 and -0.3595 K⁻¹, respectively, at 25 °C. Table 3.4 exhibits the ΔG_{HB} values for each anion.

Ions in the range of $-0.1 \leq \Delta G_{HB} \leq 0.1$ are to be considered as borderline, neither significantly breaking nor making water structure. $\Delta G_{HB} \leq -0.1$ indicates to be structure breakers, ΔG_{HB} is higher than 0.1 for structure makers.

3.1.3 ESTERS

An ester is hydrolyzed into a carboxylic acid and an alcohol in solution. The hydrolysis reaction of methyl (or ethyl) formate produces formic acid and methanol (or ethanol).



The hydrolysis is occurred in the course of two different chemical reactions on the basis of the acidity or basicity of medium. Intermediates are formed during both the reaction processes. In spite of the presence of the intermediates, the hydrolysis reaction should be of the first order, which has been verified experimentally. The hydrolysis rate constant for esters could be determined by conductivity or pH measurements, since a typical reaction is stoichiometric.

3.2 PHASE STUDY

3.2.1 SINGLE PHASES

To understand a surfactant system, the phase study is one of significant methods. For the concentrated surfactant system, one can observe different types of aggregate structures as functions of the concentrations of additives such as co-surfactant, salt and oil, and even of the surfactant itself. The phase behavior would inform us of their properties involving interactions between them. Each associating structure can be identified by several experimental methods. The simple distinctions of liquid crystals are optical anisotropy and apparent viscosity. Some of liquid crystals such as lamellar and hexagonal liquid crystals show birefringence when placed between a polarizer and an analyzer which are crossed perpendicularly, since the liquid crystals are capable to rotate about the direction of light propagation. The others, on the other hand, cannot polarize light, and no light is transmitted when the polarizer and analyzer are combined.

The apparent viscosity also supports to determine a phase present; the liquid crystals prevent to flow due to their network structures when the solution is tilted or upside-down. Especially the highly networked hexagonal and cubic liquid crystals are remarkably stiff, not moving without addition of much sufficient flow stress at all. Furthermore, an elastic liquid crystal should have the yield stress,^{114,115} which traps bubbles, occurred by rigorous stirring, in the solution for a long time.¹¹⁶ One can recognize the viscoelastic micellar solutions from the flow property as well as the liquid crystals. It is well-known that the wormlike micelle exhibits the Weissenberg effect¹¹⁷ under shearing, which refers to the phenomenon that the anisotropic character of the elongated micellar solutions under flowing gives rise to additional stress components

acting along the flow direction.¹¹⁸ When the shear stress is released, the wormlike micelle itself contracts, as a consequence, macroscopic reverse-recoiling is observable.

Further structural information can be given by the scattering methods, rheology, calorimetry, microscopy, conductivity, and so on. Some of them applied to the present system will be introduced in the following sections in detail.

3.2.2 PHASE SEPARATION AND TIE LINE

Between single phases a two-phase or a three-phase lays at arbitrary temperature because of the first-order character of the phase transition. The number of phases should be obeyed by the phase rule:

$$P = C - F + 2 \quad [3.10]$$

For any point in the phase diagram, Eq. [3.10] must be operative by the number of phases coexisting (P), the number of components that make up the system (C) and the number of degree of freedom (F). The separated two or three or multi phases should be consisted of the neighboring phases, governed by the tie line. For a binary system, here referring to a water/surfactant, the tie line must be connected horizontally from one to another single phase at constant temperature. The end-points of the tie line give the compositions of the two phases in equilibrium. For a ternary system such as two surfactants/water and surfactant/water/oil, the phase behavior becomes complicated due to $F = 2$ at constant temperature. Namely, the phase rule permits to three coexisting phases. The tie line can be no longer drawn by the same way as the binary system: one would be able to determine the tie line by quantitative methods,¹¹⁹ since the relative amounts of the two or three phases are related to the lever rule along the tie line. Transitions between phases in surfactant systems are generally of the first-order, implying that there is a smaller or larger two-phase region between two single-phase regions. The two-phase region may sometimes be difficult to be found out visually, *e.g.* a two-phase consisting of two liquid crystals.

3.3 RHEOLOGY

The term ‘‘Rheology’’ derives from Greece $\rho\varepsilon'\omega$ (= flow, rheo), and would be defined as the study of deformation and flow of matter. Specifically, it is concerned with the description of mechanical properties under various deformation conditions. Dilute solutions of surfactant systems usually behave as Newtonian liquids. The viscosities of these solutions can be basis on the size and shape of aggregates, besides on the second binding force such as van der Waals, electrostatic, and hydration forces. At higher concentration, the surfactant solutions show a complicated rheological behavior. They come to be elastic and their viscosities depend on the shear time or the shear rate. Generally, the viscosity increases with the surfactant concentration, however, there are systems which are of low viscosity at high concentrations and there are other systems which show the opposite behavior. The experimentally well defined zero shear viscosity can be interpreted in terms of two independent parameters: a structural parameter, ‘‘shear modulus’’ and a dynamic parameter, ‘‘structural relaxation time’’. Both quantities must be determined separately, which had become possible through the dynamic measurement in a linear range of deformation.

3.3.1 NEWTONIAN SOLUTION

Here one can consider a coordinate system, with the x direction perpendicular to the shearing planes (Figure 3.3). A shear stress, σ , is applied to an upper plate, forcing it to move with a velocity v relatively to an infinite distance from the upper plate, $v = dx/dt$. If the displacement of a given element located at arbitrary dy is dx , the shear strain γ and shear rate $\dot{\gamma}$ are defined as

$$\gamma = \frac{dx}{dy} \quad [3.11]$$

$$\dot{\gamma} = \frac{d\gamma}{dt} = \frac{d}{dt} \left(\frac{dx}{dy} \right) \quad [3.12]$$

The Newtonian fluid is defined as the relation that the applied stress is proportional to the resulting rate of deformation or simply the resulting velocity of flow.

$$\sigma = \eta \dot{\gamma} \left(= \eta \frac{d\gamma}{dt} \right) = \eta v \left(= \eta \frac{dx}{dt} \right) \quad [3.13]$$

The proportional coefficient is the viscosity, obtained from a single measurement of the shear stress and the shear rate.

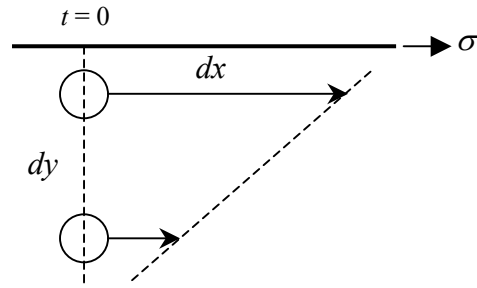


Figure 3.3. Kinematics of simple shear.

3.3.2 IDEAL ELASTIC DEFORMATION

The elastic materials such as metal, ceramic, and wood are deformed according to the Young's equation within the linear region, in which the original structure can be overcome reversibly from the deformed one. The relationship of deformation and stress is formulated using the Young Modulus E .

$$\sigma = E \frac{\Delta x}{x} \quad [3.14]$$

x and Δx are respectively the side length of a cubic and the displacement of x (see Figure 3.4). As a displacement angle with z -axis (δ) is introduced, the Eq. [3.14] is described in a convenient form.

$$\sigma = G_0 \tan \delta \quad [3.15]$$

The coefficient G_0 , equal to E in this case, is called shear modulus. Also the displacement angle is often called phase shift.

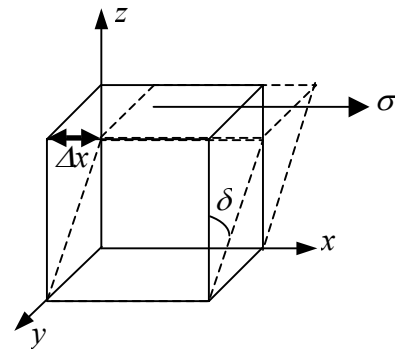


Figure 3.4. Deformation of elastic body by an applied stress.

3.3.3 VISCOELASTIC FLUID

3.3.3.1 LINEAR VISCOELASTICITY

Most surfactant solutions show flow behavior more complex than described in the sections 3.3.1 and 3.3.2. The rheological properties of these solutions can often be represented by mechanical models which, at least qualitatively, behave in an analogous manner. The basic elements of the mechanical models are an elastic spring to represent

Hookian law and a dashpot which obeys Newtonian law. Each spring element is assigned stiffness analogous to the shear modulus G_0 and each dashpot represents a viscosity η . To simplify the model, one considers that a viscoelastic surfactant solution is consisted of one spring combined with one dashpot in series. If the applied force is assumed to be analogous to the shear stress and displacement analogous to shear strain, the spring constant can be interpreted as the elastic shear modulus and the dashpot as the shear viscosity. Since real solutions generally exhibit nonlinear behavior under large deformation, such models are appropriate only for small displacements. The region, where the response of a viscoelastic material is only a function of time for all magnitudes of stress or strain, is called the linear viscoelastic regime. Figure 3.6 shows an example of the linear and non-linear regimes for a viscoelastic solution, which can be determined by variations of the rheological parameters as a function of stress or strain.

On the basis of the model in Figure 3.6, such a viscoelastic solution can be represented by linear differential equations. When a certain stress is applied to the solution, the spring stretches instantaneously, while the dashpot elongates steadily at the rate of σ/η . The total strain is the sum of the elastic strain γ_H and the viscous strain γ_N .

$$\gamma = \gamma_H + \gamma_N \quad [3.16]$$

Differentiating this equation with respect to time yields

$$\dot{\gamma} = \dot{\gamma}_H + \dot{\gamma}_N = \frac{1}{G_0} \cdot \frac{d\sigma}{dt} + \frac{\sigma}{\eta} \quad [3.17]$$

When the deformation process is suddenly stopped, the Maxwell model relaxes with a time constant τ which is given by the ratio of the viscosity and the elastic modulus. By setting $\dot{\gamma} = 0$ in Eq. [3.17], the stress relaxation can be expressed by

$$\sigma = \sigma_0 e^{-t/\tau} \quad [3.18]$$

Thus the stress relaxes exponentially to zero.

Dynamic experiments can be performed to get further information on the viscoelastic behavior of the solution. The dynamic tests enable us to obtain information

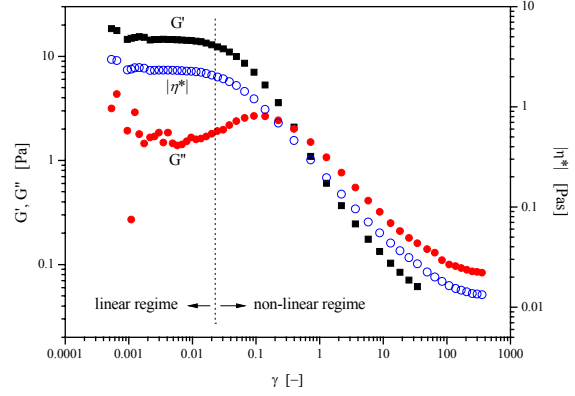


Figure 3.5. Determination of the linear regime for a viscoelastic solution. Symbols in the figure denote γ = strain, G' = storage modulus, G'' = loss modulus, and $|\eta^*|$ = complex viscosity.

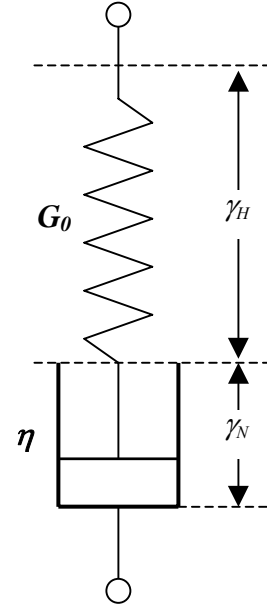


Figure 3.6. Schematic representation of Maxwell model

on the equilibrium state of the surfactant solution without ruining supermolecular internal structures. In general, a sinusoidal deformation or strain is applied to the solution. If the material obeys Newtonian law, the stress will lead the strain by 90° and for an elastic solid the shear stress will be in phase with the shear strain (Figure 3.7). For viscoelastic materials, therefore, it is expected that the phase difference between stress and strain would be between 0 and 90° .

The response of the Maxwell model to the periodic change of frequency ω consists of a sinusoidal shear stress σ which is out of phase with the strain by the phase shift δ . The shear stress is made up of two components; the first component is in phase with the deformation and the second one is out of phase with the strain. From these quantities, the storage modulus G' and the loss modulus G'' can be calculated according to the equations

$$G' = \frac{\hat{\sigma}}{\hat{\gamma}} \cos \delta \quad G'' = \frac{\hat{\sigma}}{\hat{\gamma}} \sin \delta \quad [3.19]$$

where $\hat{\sigma}$ and $\hat{\gamma}$ indicate the amplitudes of the shear stress and of the deformation. It is convenient to express the periodically varying function in terms of the complex viscosity η^* , the magnitude of which is defined as

$$|\eta^*| = \frac{(G'^2 + G''^2)^{1/2}}{\omega} \quad [3.20]$$

The behavior of the Maxwell material under harmonic oscillations can be obtained from the equations

$$G'(\omega) = G_0 \frac{\omega^2 \tau^2}{1 + \omega^2 \tau^2} \quad [3.21]$$

$$G''(\omega) = G_0 \frac{\omega \tau}{1 + \omega^2 \tau^2} \quad [3.22]$$

It is seen that for $\omega\tau \gg 1$, G' approaches a limiting value which is identical with the shear modulus G_0 . Under such experimental conditions the model behaves as an elastic body. At low frequencies $\omega\tau \ll 1$, G' becomes proportional to ω^2 . This region is called the terminal zone and the Maxwell model behaves as a liquid.

3.3.3.2 NON-LINEAR VISCOELASTICITY

For a non-Newtonian liquid, the value of apparent viscosity (η_{app}) depends on the shear stress or shear rate. The relationship between shear rate and shear stress is different for different systems. The flow properties are shown in Figure 3.9. Non-Newtonian behavior can arise from many different mechanisms, some of which are

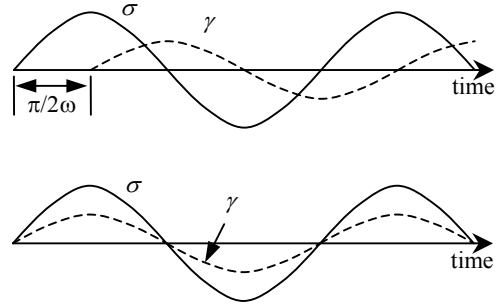


Figure 3.7. Phase difference between stress (σ) and strain (γ) for Newtonian solution (top) and for an elastic body (bottom).

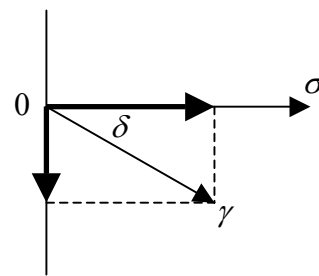


Figure 3.8. Complex number plane of stress (σ), strain (γ), and phase shift (δ) for a viscoelastic solution.

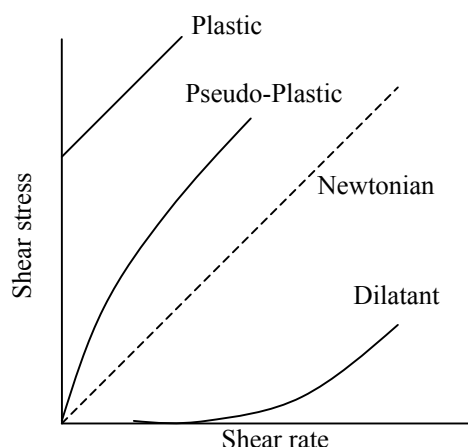


Figure 3.9. Different relationships between shear rate and shear stress for the stationary state

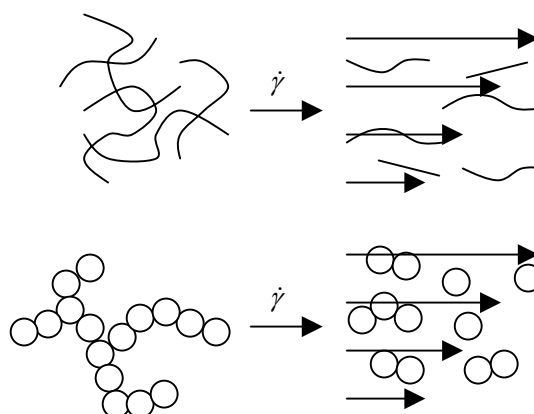


Figure 3.10. Examples of the shear-thinning.

illustrated in Figure 3.10. For dilute systems, shear-thinning can be due to flow orientation of the particles or the change in conformation of the polymer molecules or elongated micelles. Thus, when the shear rate is larger than the rate of thermal reorientation of the particles, they will be aligned in the flow direction. For concentrated systems, shear-thinning appears when the shear rate is larger than the rate of build-up of the equilibrium supra-particulate structures. For a shear-thinning or pseudo-plastic system, η_{app} decreases with increasing shear rate; plastic liquids are characterized by a finite yield value, *i.e.* a minimal yield stress needed before they start to flow.

Characteristic viscosities can be observed in some of the systems. This is a case of shear-thinning behavior. At low shear rates there exists a region where the viscosity value is constant. The value is termed the limiting viscosity η_0 at zero shear rate. At intermediate shear rates there is a non-linear region where the viscous resistance falls with increasing shear rate. Another constant value of the apparent viscosity is found at very high shear rates. The term η_∞ is called the limiting viscosity at infinite shear rate. Under these conditions, anisometric particles are aligned in the streaming solutions or a supermolecular network structure has been destroyed by the shearing forces.

Some of models had been proposed in the non-linear behavior of the viscoelastic solution. Nonlinear viscoelastic models of the differential type, such as the Phan-Thien Tanner model,¹²⁰ White-Metzner model¹²¹ and Giesekus model¹²² were used to predict the steady shear, oscillatory shear and transient shear properties of surfactant aggregates. The Phan-Thien Tanner model and the Giesekus model were used in eight modes to fit the relaxation modulus accurately. The White-Metzner model gave the best prediction for the steady shear properties. The Phan-Thien

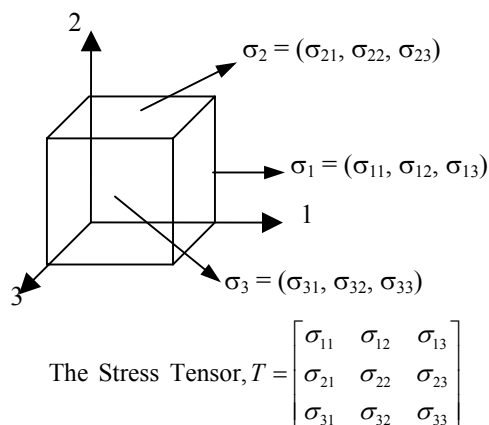


Figure 3.11. The definition of the stress tensor in terms of force components acting on the faces of a cube.

Tanner model and the Giesekus model predicted the transient shear viscosity and the transient first normal stress coefficient better than the White-Metzner model. A consistent prediction of all the experimental data could not be obtained using a single model.¹²³ The key effect on the non-linear behavior seems to be Weissenberg effect, describing the anisotropic character of the flowing solution. It is convenient to express the mechanical anisotropy of the flowing solution by the first normal stress difference $N_1(\infty, \dot{\gamma})$ and the second normal stress difference $N_2(\infty, \dot{\gamma})$.

$$N_1(\infty, \dot{\gamma}) = \sigma_{11}(\infty, \dot{\gamma}) - \sigma_{22}(\infty, \dot{\gamma}) \quad [3.23]$$

$$N_2(\infty, \dot{\gamma}) = \sigma_{22}(\infty, \dot{\gamma}) - \sigma_{33}(\infty, \dot{\gamma}) \quad [3.24]$$

where σ_{11} , σ_{22} , σ_{33} are components of the three dimensional stress tensor (Figure 3.12). For a non-Newtonian liquid, in general, these normal stresses are nonzero¹¹¹.

It can be shown that, for most viscoelastic solutions, there exists a simple correlation between dynamic and steady-state shear flow characteristics, so-called Cox-Merz rule.¹²⁴ In a first approximation, the complex viscosity $|\eta^*|$ at a certain frequency ω gives the same information as the steady-state value of the shear viscosity η at the corresponding shear rate $\dot{\gamma}$. The good agreement between both the viscosities has been reported in polymer solutions¹²⁵ and worm-like surfactant solutions.¹²⁶ The Cox-Merz rule however is usually not reliable for more complex structured fluids, such as liquid crystalline polymers, concentrated colloidal dispersions, or gels. Experimental data show that the non-equivalence between the complex viscosity curve in oscillatory flow and the simple shear viscosity curve.^{127,128} Manero *et al.* explained the departure from the Cox-Merz rule that the steady shear curve is governed by a larger relaxation time than that of the complex viscosity.¹²⁹ For the worm-like micelle system, the steady shear viscosity and the oscillatory viscosity in the intermediate shear rate or oscillation range can be given by

$$\eta(\dot{\gamma}) = \frac{G_0}{\dot{\gamma}} \left(\frac{\tau_\infty}{\tau_S} \right)^{1/2}, \quad \tau_\infty \dot{\gamma} \ll 1 \quad [3.25]$$

$$|\eta^*(\omega)| = \frac{G_0}{\omega}, \quad \tau_R \omega \ll 1 \quad [3.26]$$

Three time constants, τ_∞ , τ_S , τ_R , indicate the characteristic time at high deformation rates ($= \eta_\infty/G_0$), the structural relaxation time, and the retardation time, respectively. To comply with the Cox-Merz rule, it is necessary that τ_S equals to τ_∞ . When $\tau_S > \tau_\infty$, the shear viscosity is shifted downwards with respect to the complex viscosity. At high frequencies, the complex viscosity approaches to a specific asymptote.

$$|\eta^*(\omega)| \rightarrow G_0 \tau_R \quad [3.27]$$

This implies that $\tau_R = \tau_\infty$ permits to the Cox-Merz rule at high frequency or shear rate. The Maxwell model with the single relaxation time would follow the Cox-Merz rule, however, the relaxation mode of a real system is governed by some independent time constants arising from different motions at each time scale.¹³⁰⁻¹³²

3.3.2 EQUIPMENTS

The rheological measurements were performed by a Haake RS600 with a cone-plate sensor and a Haake RS300 with a double-gap cylinder sensor. The sensor systems are described in Table 3.5 and Figure 3.12. The sensor systems can be used properly

according to the viscosity of solution: RS600 for highly viscous liquids and RS300 for low viscous liquids (< 100 mPas). Temperature in the measuring system can be controlled to an accuracy of ± 0.1 °C by a thermo-controller (Haake TC 81) for RS600 and by an ethylene glycol circulator with an accuracy of ± 0.5 °C for RS300. The measurements are operated by the software, Haake RheoWin Job Manager, and data on the measurements are analyzed by Haake RheoWin Data Manager.

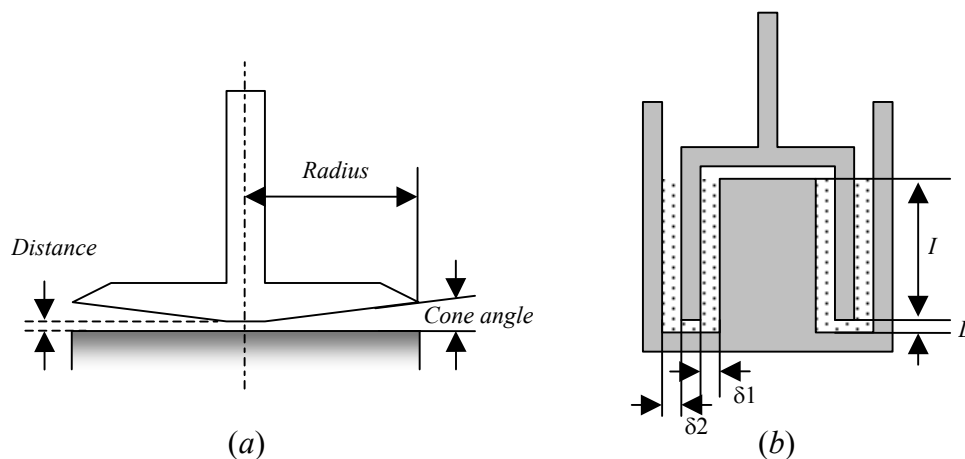


Figure 3.12. Sensor systems; (a) cone-plate geometry, (b) double gap cylinder geometry.

Table 3.5. Geometrical information on the Cone-Plate sensor and the Double Gap Cylinder Sensor.

Sensor	Radius [mm]	Cone angle [deg.]	Distance [mm]
Cone-Plate	30 ± 0.01	1	0.052

Sensor	Gap $\delta 1$ [mm]	Gap $\delta 2$ [mm]	Length I [mm]	Distance D [mm]
Double Gap Cylinder	0.25	0.3	55 ± 0.006	5.1

3.4 SURFACE TENSION

The cohesive forces between molecules down into a liquid are shared with all neighboring atoms. Those on the surface have no neighboring atoms above themselves, and exhibit stronger attractive forces upon their nearest neighbors on the surface. This enhancement of the intermolecular attractive forces at the surface is called surface tension. The surface tension is expressed in units of dyn/cm or mN/m. Since the surface tension is equivalent to a surface free energy, the surface tension can also be expressed in energy units, erg/cm² or mJ/m².

In aqueous systems, an additive can affect the

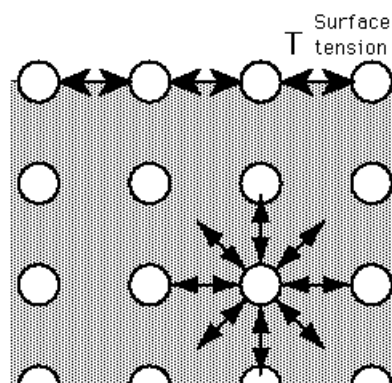


Figure 3.13. Image of the cohesive forces for the bulk molecules and the surface molecules.

surface tension in three different ways. Organic water-soluble materials, such as ethanol, normally decrease the surface tension monotonically with increasing concentration. Surfactants, on the other hand, show a very large reduction in surface tension at very low concentrations up to the critical micelle concentration (CMC), whereupon the surface tension is practically constant. This large reduction is due to a strong adsorption of the surfactants at the liquid-air surface. At concentration higher than the CMC, all additional surfactant will form new micelles, thus keeping the surfactant monomer activity (concentration) more or less constant. Electrolytes normally increase the surface tension. The reason is that the electrolytes are depleted from the surface, *i.e.* there is a negative adsorption of the ions at the surface.

3.4.1 GIBBS ADSORPTION ISOTHERM

The adsorption isotherm, come out by Gibbs, is basis on all adsorption processes at the liquid-air surface. Initially, the relationship between the surface tension (σ_s) and the chemical potentials (μ_i) of components is derived from

$$d\sigma_s = -\sum_i \Gamma_i d\mu_i \quad [3.28]$$

Γ_i is the surface excess concentration of i component. At equilibrium in terms of the concentration between the surface and bulk phase, Eq. [3.28] is substituted using $d\mu_i = RTd\ln a_i$ to

$$d\sigma_s = -RT\sum_i \Gamma_i d\ln a_i \quad [3.29]$$

a_i is the activity of i component in the bulk phase. In the case of sufficiently diluted solution, the activity of solvent and the activity coefficients of solutes are regarded as constant, and a_i then can be replaced by its molar concentration C_i . For nonionic surfactant/water mixture, Eq. [3.29] can be simply expressed as

$$d\sigma_s = -RT\Gamma_1 d\ln C_1 \quad [3.30]$$

For ionic surfactants, one has to take into account the fact that there is a counter-ion associated with the surfactant and that the surface as a whole must be electrically neutral. Thus Eq. [3.30] is reformulated by

$$d\sigma_s = -RT(\Gamma_1^+ d\ln C_1^+ + \Gamma_1^- d\ln C_1^-) = -2RT\Gamma_1 d\ln C_1 \quad [3.31]$$

Assuming monolayer adsorption, one realizes that the adsorbed amount is inversely proportional to the cross-sectional area per adsorbed molecule, a_s . The relationship can be shown to be as follows:

$$a_s (\text{nm}^2/\text{molecule}) = \frac{10^{14}}{N_A \Gamma_1} \quad [3.32]$$

where Γ_1 is expressed in mol/cm^2 .

3.4.2 EQUIPMENTS

The surface tension measurements were carried out by a Lauda tensiometer TE 1C (Du Noüy ring method) equipped with a thermo-controller. In this method, a ring is pulled through the liquid-air surface and the maximum downward force directed to the ring is measured. The calibration was always performed using a standard ring before each measurement, and an identical sample was measured repeatedly more than three cycles. The deviation from the average surface tension was set below 0.2 mN/m in one cycle of the measurement; if the actual deviation exceeded 0.2 mN/m, the measurement

was automatically continued until the surface tension less than 0.2 mN/m was attained.

3.5 INTERFACIAL TENSION

The interfacial tension is defined as the surface tension between two immiscible liquids such as water/oil. The interfacial tension therefore substantially depends on the properties of two phases. A surfactant can reduce the interfacial free energy, resulting in enhancement of mixing two insoluble materials. The interfacial tension would be related directly to the solubilization capacity and the aggregate structure. In fact, the surfactant aggregate in aqueous solution makes itself phase separation consisting of the hydrophobic oil pool and the bulk water phase as demonstrated in Figure 3.14. Generally, the interfacial tension of a given liquid surface is measured by finding the force across any line on the surface divided by the length of the line segment. The interfacial tension thus becomes a force per unit length which is equal to the energy per surface area as well as the surface tension. Let us consider an oil droplet in water phase. The curved surface leads to a pressure difference between the water phase and the oil phase. The pressure inside the droplet on the concave side of the surface is expected to exceed the pressure on the convex side. The pressure difference (Δp) can be expressed by Young-Laplace equation:

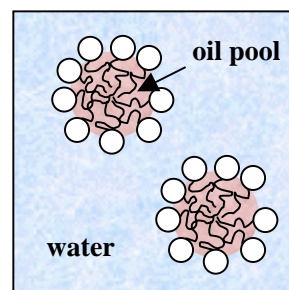


Figure 3.14. Micro-phase separation between the micelle oil pool and the bulk water phase.

The interfacial tension thus becomes a force per unit length which is equal to the energy per surface area as well as the surface tension. Let us consider an oil droplet in water phase. The curved surface leads to a pressure difference between the water phase and the oil phase. The pressure inside the droplet on the concave side of the surface is expected to exceed the pressure on the convex side. The pressure difference (Δp) can be expressed by Young-Laplace equation:

$$\Delta p = \frac{2\sigma_l}{R} \quad [3.33]$$

The general form is

$$\Delta p = \sigma_l \left(\frac{1}{R_1} + \frac{1}{R_2} \right) \quad [3.34]$$

σ_l is the interfacial tension, R_1 and R_2 are the principal radii of curvature of the interface.

3.5.1 SPINNING DROP METHOD

This method is used to apply to systems that the surface tension values are very low, $\sigma_l < a$ few mN/m. A small drop of a sample is injected inside a thin capillary tube in which an immiscible liquid is filled. The tube is then spun with a high speed and the interfacial tension is calculated from the angular speed of the tube and the shape of the drop using the following equation.

$$\sigma_l = A(r_d \times 0.4)^3 v^2 \Delta\rho \quad [3.35]$$

A is the corrective constant, r_d the radius of the drop, v the angular speed of the tube, $\Delta\rho$ the density difference between the drop and the continuous phase.

3.5.2 PENDANT DROP METHOD

The pendant drop method involves the determination of the profile of a drop of one liquid suspended in another liquid at mechanical equilibrium.¹³³ The profile of a drop is determined by the balance between gravity and surface forces. The correlation

can be formulated on the basis of the Young-Laplace equation by

$$\sigma_l = \frac{gD_e^2\Delta\rho}{H} \quad [3.36]$$

g is gravity, D_e the equatorial diameter of the drop, H the correction factor which is related to the shape factor of the pendant drop.

The liquid is injected from a needle into an immiscible liquid so that it forms a drop on the tip of the needle. The drop is then optically observed and the interfacial tension is calculated from the size and shape of the drop. The drop is captured by a CCD camera, and its size can be evaluated relative to the needle diameter.

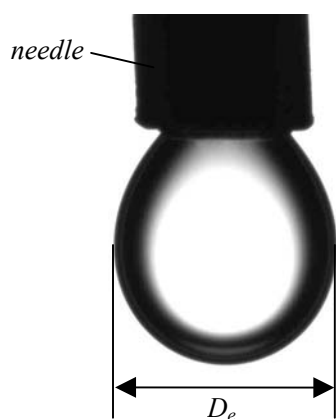


Figure 3.15. Image of the pendant drop.

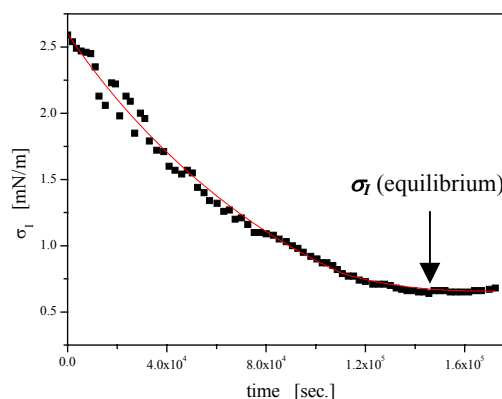


Figure 3.16. Change of the interfacial tension (σ_l) with time.

3.5.3 EQUIPMENTS

The spinning drop method was performed by means of a spinning drop interfacial tensiometer (KRÜSS) equipped with a thermocontroller. Decane was used as continuous phase. The rotating speed was controlled up to 4000 rpm.

The pendant drop measurements were carried out with a commercial apparatus (Dataphysics, OCA20) equipped the CCD camera with a resolution of 752×582 pixel. The needle with 0.9 mm in diameter was used. The performance of the camera is 25 pictures/second.

3.6 MICROSCOPE

3.6.1 POLARIZED MICROSCOPE

Polarized light microscopy is a useful method to generate contrast in birefringent specimens and to determine qualitative and quantitative aspects of crystallographic axes present in various materials. The beautiful kaleidoscopic colors displayed by specimens under crossed polarizers arise as a result of the interference between light waves passing through the specimen.

The polarized light microscope is designed to observe and photograph specimens that are visible primarily due to their optically anisotropic character. In order to accomplish this task, the microscope must be equipped with both a polarizer, positioned in the light path somewhere before the specimen, and an analyzer (a second polarizer),

placed in the optical pathway between the objective rear aperture and the eyepiece tube or camera port.

The specific liquid crystals exhibit their own textures under polarization.¹³⁴ The textures are referred in the several literatures.

3.6.2 TRANSMISSION ELECTRON MICROSCOPE

A transmission electron microscope, TEM, works much like a slide projector. A projector shines a beam of light through (transmits) the slide, as the light passes through it is affected by the structures and objects on the slide. These effects result in only certain parts of the light beam being transmitted through certain parts of the slide. This transmitted beam is then projected onto the viewing screen, forming an enlarged image of the slide.

TEMs work the same way except that they shine a beam of electrons (like the light) through the specimen (like the slide). Whatever part is transmitted is projected onto a phosphor screen for the user to see. A more technical explanation of a typical TEMs working is as follows;

1. The "Virtual Source" at the top represents the electron gun, producing a stream of monochromatic electrons.
2. This stream is focused to a small, thin, coherent beam by the use of condenser lenses 1 and 2. The first lens (usually controlled by the "spot size knob") largely determines the "spot size"; the general size range of the final spot that strikes the sample. The second lens (usually controlled by the "intensity or brightness knob" actually changes the size of the spot on the sample; changing it from a wide dispersed spot to a pinpoint beam.
3. The beam is restricted by the condenser aperture (usually user selectable), knocking out high angle electrons (those far from the optic axis, the dotted line down the center).
4. The beam strikes the specimen and parts of it are transmitted.
5. This transmitted portion is focused by the objective lens into an image.
6. Optional Objective and Selected Area metal apertures can restrict the beam; the Objective aperture enhancing contrast by blocking out high-angle diffracted electrons, the Selected Area aperture enabling the user to examine the periodic diffraction of electrons by ordered arrangements of atoms in the sample

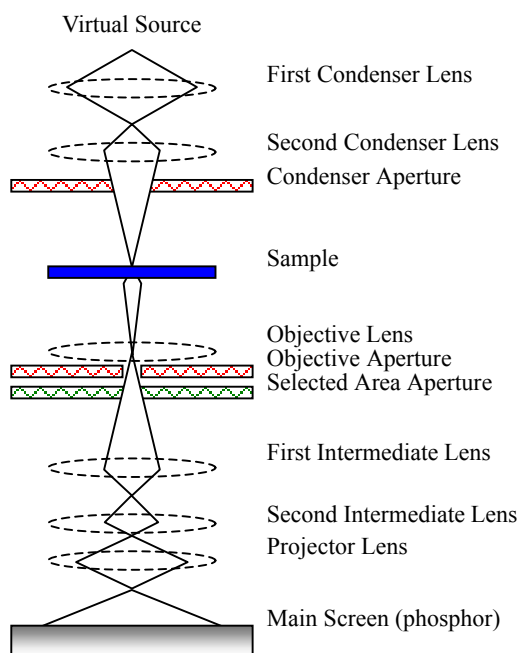


Figure 3.17. Schematic representation of the electron microscope

7. The image is passed down the column through the intermediate and projector lenses, being enlarged all the way.
8. The image strikes the phosphor image screen and light is generated, allowing the user to see the image. The darker areas of the image represent those areas of the sample that fewer electrons were transmitted through (they are thicker or denser). The lighter areas of the image represent those areas of the sample that more electrons were transmitted through (they are thinner or less dense).

3.6.2.1 FREEZE FRACTURE

The freeze fracture technique is performed in the following procedure.

- ♦ **Freezing** : Cells are quickly frozen in liquid nitrogen (-196 °C), which immobilizes cell components instantly.
- ♦ **Fracturing** : The specimen is fractured on a cooled specimen table (-100 °C) under vacuum ($< 2 \times 10^{-6}$ mbar) with aid of the liquid nitrogen cooled microtome (-180 °C).
- ♦ **Etching** : Surface ice is removed by a vacuum.
- ♦ **Shadowing** : A thin layer of carbon is evaporated vertically onto the surface to produce a carbon replica. The surface is shadowed with a metal vapor such as platinum or tungsten.
- ♦ **Cleaning** : Organic material is digested away by acid, leaving a replica.

3.6.2.2 CRYOGENIC PREPARATION

The cryogenic preparation is performed by means of the ice-embedding (bare-grid) method as follows.

- ♦ The mesh with a pair of tweezers used for reparation is made hydrophilic by glow discharge.
- ♦ A drop of the solution containing the fine specimen is placed onto the tweezers with a copper TEM grid.
- ♦ The tweezers is set up on a rapid freezing device.
- ♦ The mesh is splitted so that a thin film of liquid is formed on the micro grid.
- ♦ The mesh is immediately plunged into a coolant such as liquid ethane. A thin film of amorphous ice forms and preparation of the frozen specimen embedded in ice is completed.

3.6.3 EQUIPMENTS

The polarized microscope observations were carried out with a polarizing microscope (Standard Pol 16 of Zeiss, Germany) equipped a hot stage (Mettler FP 82). The samples were put on a glass plate and covered with a glass cover. In order to orient a liquid crystal, alternatively, some of the samples were filled in the capillary tubes of a layer thickness of 0.3 mm.

3.7 DIFFERENTIAL SCANNING CALORIMETRY

The differential scanning calorimeter measures the amount of energy (heat) absorbed or released by a sample as it is heated, cooled, or held at a constant temperature. Typical applications include determination of melting point temperature

and the heat of melting; measurement of the glass transition temperature; curing and crystallization studies; and identification of phase transformations.

The measurement of thermal effects in a Tian-Calvet type microcalorimeter is done by two fluxmeters (one on the measurement side and one on the reference side), each of which measures the thermal power exchanged constantly between the experimental vessel and the calorimetric unit.

The main difference in comparison to the DSC technique with a flat plate probe is that the Tian-Calvet type fluxmetric probe envelopes the sample and is therefore capable of measuring almost all the exchanges between the vessel and the unit, a characteristic that gives this device a clear advantage in terms of both the quantity of the measurement and their sensitivity (capacity to measure very weak effects).

When two fluxmeters start to be heated, the computer will plot the difference in heat flow against temperature. That is to say, the heat absorbed by the object is plotted against temperature. The heat flow at a given temperature is shown in units of heat, q , supplied per unit time, t . The heating rate is temperature increase ΔT per unit time, t .

$$\frac{\text{heat}}{\text{time}} = \frac{q}{t} = \text{heat flow} \quad [3.37]$$

$$\frac{\text{temperature increase}}{\text{time}} = \frac{\Delta T}{t} = \text{heating rate} \quad [3.38]$$

The heat capacity, C_p , is supplied by dividing the heat flow q/t by the heating rate $\Delta T/t$.

$$\frac{q/t}{\Delta T/t} = \frac{q}{\Delta T} = C_p = \text{heat capacity} \quad [3.39]$$

For the surfactant systems, mostly, the phase transition would be of the first-order. This means that when it reaches to be at a specific transition temperature, the temperature would not rise until all the materials have been transformed. This also means that the furnace is going to have to put additional heat into the object in order to transform into another structure and keep the temperature rising at the same rate as that of the reference probe. This extra heat flow during transformation shows up as a more or less dip in the DSC plot as heat is absorbed by the materials. The heat required during transition can be calculated by integrating the area of this dip. The transition enthalpy, ΔH , is given by

$$\Delta H = \int_t^{t+\Delta t} \frac{q}{t} dt = \int_{T_1}^{T_2} C_p dT \quad [3.40]$$

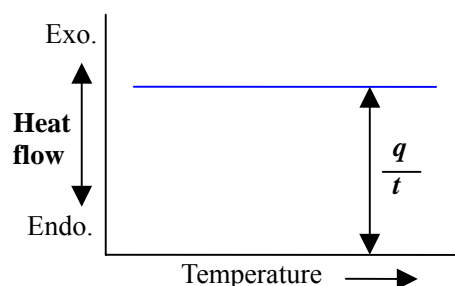


Figure 3.18. DSC plot against temperature.

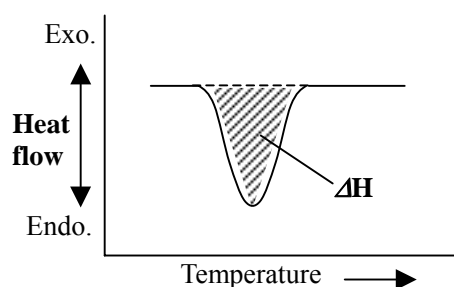


Figure 3.19. Endothermic peak of DSC curve.

3.7.1 EQUIPMENTS

The DSC measurements were carried out with a micro DSC III (SETARAM, France) equipped with a water-cooling thermostat. To avoid steam condensation in the calorimetric wall, especially at low temperature, a constant sweeping of dry nitrogen was circulated during the measurements. The available temperature range is in 0 ~ 120 °C. A standard batch vessel, made of Hastelloy C276, was used throughout the present experiments. The vessel is composed of a cylinder of 6.4 mm of internal diameter and useful height equivalent to 19.5 mm for the sample. The useful volume for the sample is equal to 1 cm³. The sample is filled in the vessel, and closed with a stopper with a rubber o-ring. The reference solution (solvent) was weighted as exactly same amount as the sample solution. The temperature sweep rate was fixed at 0.2 K/min. Before each measurement, the onset temperature had been kept for more than 10 min. in order to stabilize the temperature. The results were monitored by a combined computer with the SETARAM software.

3.8 CONDUCTOMETRY

The fact that a certain substance called electrolyte conducts electricity over its solution directly proves the presences of independent mobile ions. The electrical conductivity can be measured by using conductive cells and an electrical circuit. The electrical resistance of the electrolyte solution is related to the cross-section area of electrode, A , and the distance between two electrodes, l .

$$R = \rho_R \frac{l}{A} \quad [3.41]$$

where ρ_R is the resistivity, referring to the resistance of the cell per area and with unit length. The relationship can be rewritten by

$$\frac{1}{R} = \kappa \frac{A}{l} \quad [3.42]$$

κ is the conductivity.

3.8.1 EQUIPMENT (CONDUCTIVITY)

Conductivity measurements were performed with an Automatic Precision Bridge (Wayne Kerr B905) and a glass electrode (WTW LTA/S). The cell constant was calibrated on every measurement by KCl aqueous solution (7.47458 g/kg-water, $\kappa = 1.2852$ S/m).

3.9 pH-METRY

pH meters measure the H⁺ concentration (the pH) of solutions using an ion sensitive electrode. An ion-selective electrode will ideally respond to only one specific ion, though in reality there is always some degree of interference from other ions in solution. A typical pH probe is a combination electrode, which combines both the glass and reference electrodes into one body. The bottom of a pH electrode balloons out into a round thin glass bulb. The pH meter is best thought of as a tube within a tube. The inside tube (the inner tube) contains an unchanging saturated potassium chloride (KCl) and a 0.1M hydrochloric acid (HCl) solution. Also inside the inner tube is the cathode

terminus of the reference probe. The anodic terminus wraps itself around the outside of the inner tube and ends with the same sort of reference probe as was on the inside of the inner tube. Both the inner tube and the outer tube contain a reference solution but only the outer tube has contact with the solution on the outside of the pH probe by way of a porous plug that serves as a salt bridge.

3.10 DENSIMETRY

The oscillating U-tube density meter is based on the principle of a U-tube which has a resonant frequency f that is inversely proportional to the square root of its mass, M .

$$f = \frac{1}{T} = \frac{1}{2\pi} \sqrt{\frac{c}{M + \rho \cdot V}} \quad [3.43]$$

T is the period, c the constant, ρ the density, V the volume of the tube. V is given; the density of the liquid sample filled into the U-tube is calculated from its resonant frequency.

$$\rho = A(T^2 - B) \quad [3.44]$$

$$A = \frac{c}{4\pi^2 V}, \quad B = \frac{4\pi^2 M}{c}$$

One can as well calculate the density using the density of a reference.

$$\rho_1 - \rho_2 = A(T_1^2 - T_2^2) \quad [3.45]$$

3.10.1 DENSITY OF SURFACTANT

Since all the surfactant used in the present study are solid at room temperature, the densities of the surfactant aqueous solutions with different composition were measured. The weight fraction of the surfactant aqueous solution (W_S) is proportional to the reciprocal of the density ($1/\rho$).

$$\frac{1}{\rho} = \frac{1}{\rho_w} + \left(\frac{1}{\rho_s} - \frac{1}{\rho_w} \right) W_S \quad [3.46]$$

where ρ_s and ρ_w are the densities of surfactant and water, respectively. According to Eq. [3.46], the density of the pure surfactant (at $W_S = 1$) is obtained by extrapolation. In this case, we assume that the density of the surfactant is unchanged at the constant temperature even if a phase transfers to another one, *i.e.*, the density in the solution is identical to that in the liquid crystal, and the system is incompressible.¹³⁵

3.10.2 EQUIPMENTS

The density measurements were carried out by using a Anton Paar Densimeter (DMA 40, Austria) with a temperature-controlled thermostat. The densities were calculated by the hand-made software.

3.11 SMALL ANGLE X-RAY SCATTERING

Small angle x-ray scattering (SAXS) is a technique for studying structural features of colloidal size. It is performed by focusing a low divergence x-ray beam onto

a sample and observing a coherent scattering pattern that arises from electron density inhomogeneities within the sample. Since the dimensions typically analyzed are much larger than the wavelength of the typical X-ray used (1.54Å, for Cu), dimensions from tens to thousands of angstroms can be analyzed within a narrow angular scattering range. This angular range or pattern is analyzed using the inverse relationship between particle size and scattering angle to distinguish characteristic shape and size features within a given sample.

3.11.1 INTERFERENCE AND SCATTERING

In Figure 3.20, a plane incident wave traveling in the direction specified by the unit vector S_0 is scattered by the particles located at two points, O and P. A detector is placed in the direction specified by the unit vector S at a distance far from these scattering centers. If the scattering is coherent and there is no phase change on scattering, the phase difference $\Delta\phi$ between the two waves scattered at O and P and arriving at the detector depends only on the path length difference δ_p between the two rays:

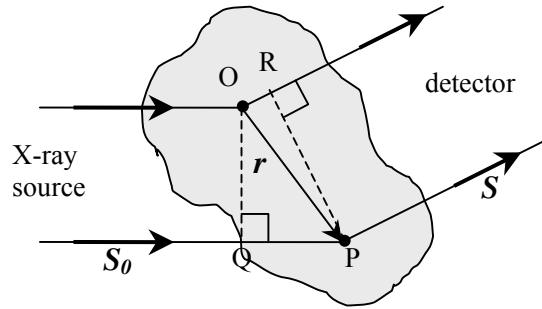


Figure 3.20. Geometry of the path length difference.

$$\Delta\phi = \frac{2\pi\delta_p}{\lambda} \quad [3.47]$$

Designating the position of the second scattering relative to the first as r , we have $QP = S_0 \cdot r$ and $OR = S \cdot r$, and therefore the phase difference is

$$\Delta\phi = \frac{2\pi}{\lambda}(S_0 \cdot r - S \cdot r) = -2\pi s \cdot r \quad [3.48]$$

where s is defined as

$$s = \frac{S - S_0}{\lambda} \quad [3.49]$$

The vector s is referred to as the unit scattering vector, and it completely characterizes the scattering geometry: the incident and scattering beam directions and the wavelength. Its magnitude is related to the scattering angle 2θ by

$$|s| = s = \frac{2}{\lambda} \sin\left(\frac{\theta}{2}\right) \quad [3.50]$$

Then the scattering vector q is defined as

$$q = \frac{2\pi}{\lambda} \cdot s = \frac{4\pi}{\lambda} \sin\left(\frac{\theta}{2}\right) \quad [3.51]$$

The scattering intensity at every scattering angle, in general, can be expressed by the sum of the phase differences at all scattering points.

$$I(q) = I_e \Phi(q) = I_e |f(q)|^2 = I_e \sum_k b_k |\exp(-iq \cdot r_k)|^2 \quad [3.52]$$

Here I_e is the scattering ability per electron, $\Phi(q)$ the scattering function of particle, $f(q)$ the scattering amplitude, b_k the scattering ability at the point k .

In more detail, for the aggregate system, the scattering intensity could be described in terms of the electron density difference between the solvent and the aggregate core. Let us assume that the scatter occupies a volume V_s , and that the suspending medium has a volume $V - V_s$. The total volume occupied by the sample is V . For a given orientation of q , the amplitude $f(q)$ of the sample is

$$f(q) = \int_{V_s} \rho_e(r) \exp(iq \cdot r) dV + \rho_{e0} \int_{V-V_s} \exp(iq \cdot r) dV \quad [3.53]$$

where $\rho_e(r)$ and ρ_{e0} are the electron densities of the scatter and the medium. This equation can be written by

$$f(q) = f_s(q) + f_M(q)$$

$$f_s(q) = \int_{V_s} [\rho_e(r) - \rho_{e0}] \exp(iq \cdot r) dV \quad [3.54]$$

$$f_M(q) = \rho_{e0} \int_V \exp(iq \cdot r) dV$$

$f_M(q)$ is the amplitude of a scatterer with a uniform density. Commonly, $f_M(q)$ would be expected to be negligible at all observable values of q compared to $f_s(q)$, since the diameters of the scatterers that can be studied by small-angle scattering are rarely greater than a few tenths of a micrometer, resulting in that a conventional equipment cannot permit to measure intensity. As a consequence, the observable amplitude $f(q)$ can be given by the second equation of Eqs. [3.54] with the effective electron density ($\rho_e(r) - \rho_{e0}$).

3.11.2 SCATTERING FROM LAMELLAR STRUCTURE

Let us consider an ideal two-phase lamellar structure (see Figure 3.21) consisted of two layers (here assigning phase (a) and (b)) with different layer thicknesses and scattering length densities. The scattering length density profile $\rho_L(x)$ in the stack of such parallel lamellae can be written as¹³⁶

$$\rho_L(x) = \rho_u(x) * z(x/d) \quad [3.55]$$

$\rho_u(x)$ is the scattering length density distribution within a single period for x between 0 and d ,

$$\rho_u(x) = \rho_b + (\rho_a - \rho_b) \Pi(x/d_a)$$

$$\Pi(x/d_a) = \begin{cases} 1 & \text{for } |x| < 1/2 \\ 0 & \text{for } |x| > 1/2 \end{cases} \quad [3.56]$$

$\Pi(x)$ is the step function. And $z(x/d)$ represents a one-dimensional lattice of period $d (= d_a + d_b)$. By taking the absolute square of the Fourier transform of $\rho_L(x)$ in Eq. [3.55], the intensity of scattering in one-dimension $I_1(q)$ is obtained as

$$I_1(q) \propto |F(q)|^2 z(dq/2\pi) \quad [3.57]$$

$F(q)$ is the structure factor. The lattice factor $z(dq/2\pi)$ expresses the fact that the square of the Fourier transform of $z(x/d)$ is itself a lattice of period $2\pi/d$ (in q) in reciprocal

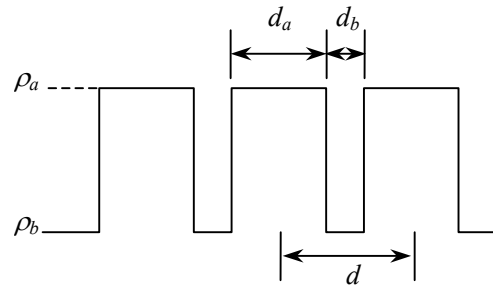


Figure 3.21. Scattering length density profile in the direction perpendicular to the lamella plane in the ideal two-phase lamellar system.

space. With $\rho_u(x)$ given by Eq. [3.56], we obtain

$$|F(q)|^2 = (\rho_a - \rho_b)^2 \frac{4}{q^2} \sin^2\left(\frac{d_a q}{2}\right) \quad [3.58]$$

Eqs. [3.57] and [3.58], together, state that Bragg peaks occur at a series of q values satisfying $dq/2\pi = n$ or $q = 2\pi n/d$ (n is the order of reflection), and that the height of the n th order peak is proportional to $\sin^2(\pi n \phi_a)/n^2$, where $\phi_a (= d_a/d)$ is the volume fraction of phase (a).

3.11.3 SCALING LAW

Since data on scattering measurements is dealt with in the reciprocal space, the structural information is reflected in the opposite q range: the scattering at the large q value gives information in terms of the relatively microscopic structure, and small q refers to the large structure. For small-angle scattering, we can classify ordinarily into three regions as shown in Figure 3.22. In the small q range, the dimension of aggregate or particle can be evaluated by the Guinier law.¹³⁷ The size of a particle, irrespective of whether it is geometrically well defined or irregular in shape, can be conveniently characterized by its radius of gyration according to the Guinier law.

For many of the particles having well-defined, simple geometric shapes, it is possible to calculate the intensity curve from Eq. [3.53] without any approximation. These different shapes can be identified simply by the power law of intensity decay in the intermediate q range.

$$I(q) \sim q^{-\alpha} \quad [3.59]$$

The exponent α is equal to 4 for sphere (three dimensional), 2 for thin disks (two dimensional), and 1 for thin rods (one dimensional), and is thus seen to reflect the dimensionality of the object.

At further large q , the scattering intensity is reflected by a surface fractal of aggregates. Porod proposed for the ideal two-phase model that the scattering intensity should decrease as $\sim q^{-4}$ in the large q range, and moreover that the proportionality constant should be related to the total area S of the boundaries between two phases in the scattering volume.¹³⁸ In other words, as $q \rightarrow \infty$,

$$I(q) \rightarrow \frac{2\pi(\Delta\rho_e)^2 S}{q^4} \quad [3.60]$$

where $\Delta\rho_e$ is the electron density difference. This power law indicates that the surface of aggregate is smooth, and if the decay is more than -4, it is likely that the boundaries between the two phases would be indistinct.¹³⁹

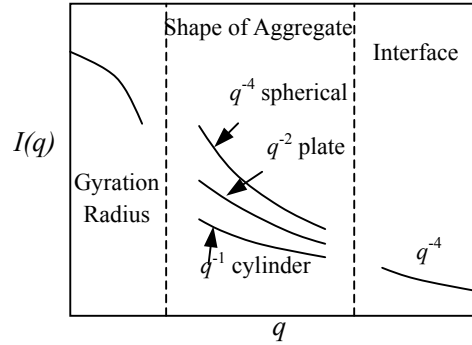


Figure 3.22. Different scattering ranges and the corresponding structural informations.

3.11.4 EQUIPMENTS

The schematic construction of small angle X-ray scattering used in the present study is drawn in Figure 3.23. The X-ray source (CuK_α ray, $\lambda = 0.154 \text{ nm}$) is generated on impact of electron, emitted by an electron gun (tungsten filament), at a target metal (Cu). The filament is maintained at a high negative voltage (*ca.* 30 kV) under high vacuum. The generated X-ray is collimated through the slit and the block collimation system, and irradiates the capillary-type sample holder made from glass (diameter = 1 mm). The scattering radiation is counted by the one-dimensional detector. The distance of the sample holder – detector is 41.4 cm.

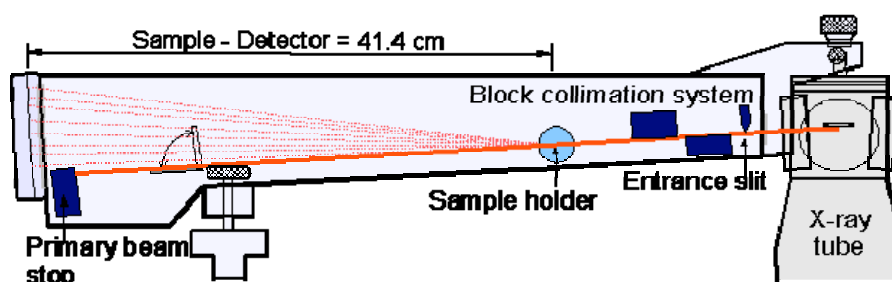


Figure 3.23. Schematic representation of X-ray apparatus.

3.12 DYNAMIC LIGHT SCATTERING

The dynamic light scattering (DLS) methods only provide information about the “long-wavelength” properties of the system. Complementary techniques such as gamma ray (QEGS), X-ray (SAXS), and neutron scattering (SANS) methods provide information on a much shorter wavelength scale. Typical ranges for the wave vectors accessible by these various scattering methods are described in Table 3.6.¹⁴⁰ To illustrate how these scattering techniques provide complementary information about a system, the combined light scattering and SAXS studies by Schaefer et al. on aggregated silica particles are given in Figure 3.24.¹⁴¹ The power law -2.1 for the scattered light intensity indicates that the aggregates are fractal objects. At the short wavelength regime

Table 3.6. Scattering methods and their corresponding scattering vector (q) range.

Method	q -range (cm^{-1})
DLS	$5 \cdot 10^4 \sim 4 \cdot 10^5$
SAXS	$2 \cdot 10^6 \sim 4 \cdot 10^7$
SANS	$7 \cdot 10^5 \sim 9 \cdot 10^6$
QEGS	$1 \cdot 10^7 \sim 1 \cdot 10^9$

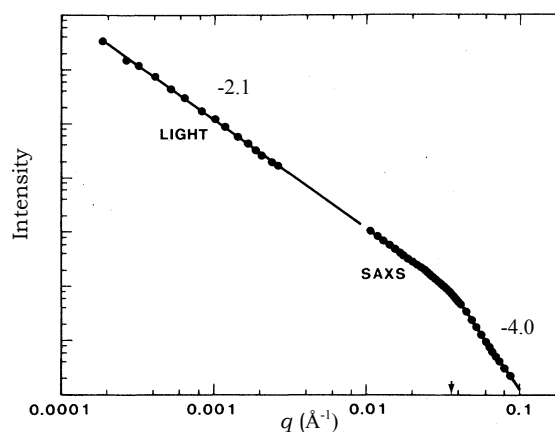


Figure 3.24. Combined light scattering and small-angle X-ray scattering from colloidal silica. (Ref. 135)

accessible to SAXS, the power law -4.0 indicates that the monomer units that make up the aggregate remains intact. Thus DLS is available to measure the particle and its size-distribution in the range of less than submicron, 1 nm ~ 5 μm.

3.12.1 PRINCIPLE

The dynamic light scattering measures electric field correlation function accompanied with concentration fluctuation of a solute particle. This method accordingly provides information about the dynamic structure of the particles in view of fluctuation. Now let us define the following two correlation functions under a given scattering electric field E_S :

$$g^{(1)}(q, \tau_{ret}) = \frac{\langle E_S^*(t) E_S(t + \tau_{ret}) \rangle}{\langle |E_S(t)|^2 \rangle} \quad [3.61]$$

$$g^{(2)}(q, \tau_{ret}) = \frac{\langle |E_S^*(t)|^2 |E_S(t + \tau_{ret})|^2 \rangle}{\langle |E_S(t)|^2 \rangle^2} \quad [3.62]$$

where τ_{ret} is the retardation time, $g^{(1)}(q, \tau_{ret})$ and $g^{(2)}(q, \tau_{ret})$ are the first- and second-normalized self-correlation functions, respectively. On the basis of heterodyne method, $g^{(2)}(q, \tau_{ret})$ can be expressed by

$$g^{(2)}(q, \tau_{ret}) = 1 + C |g^{(1)}(q, \tau_{ret})| \quad [3.63]$$

C is the constant. The self-correlation function $g^{(2)}(q, \tau_{ret})$ is in principle obtained from correlation of intensities $I(t_a)$ at a given time $t = t_a$ and $I(t_a + \tau_{ret})$ at a give retarded time $t = t_a + \tau_{ret}$.

$$g^{(2)}(q, \tau_{ret}) = \frac{\langle I(t_a) \cdot I(t_a + \tau_{ret}) \rangle}{\langle I(t_a) \rangle^2} \quad [3.64]$$

The blanket $\langle \rangle$ represents the average. The particle continually moves from one to another due to the Brownian motion at a speed dependent on the particle size. The self-correlation function indicates the degree of superposing particle as a function of time, as depicted in Figure 3.25. Therefore, $g^{(2)}(q, \tau_{ret})$ regresses with time because superposition of the identical particle is less and less with movement of the particle.

For the case of monodisperse system, $g^{(1)}(q, \tau_{ret})$ should be a single exponential curve, formulated by using the decay constant Γ' .

$$g^{(1)}(q, \tau_{ret}) = \exp(-\Gamma \tau_{ret}) \quad [3.65]$$

Furthermore, Γ' gives the translational diffusion coefficient D_{diff} by the following

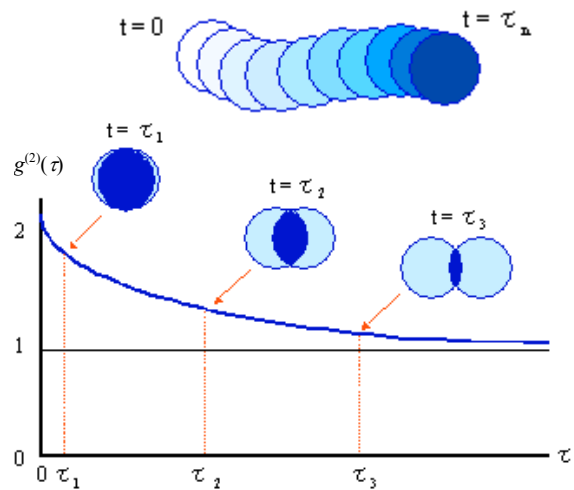


Figure 3.25. Schematic representations of the Brownian motion (above) and self-correlation function (below).

equation.

$$\Gamma = q^2 D_{diff} \quad [3.66]$$

$$q = \frac{4\pi n_D}{\lambda} \sin\left(\frac{\theta}{2}\right) \quad [3.67]$$

where n_D is the refractive index of solvent, λ the wavelength of incident beam, θ the scattering angle. Finally one can calculate the hydrodynamic radius R_H from D_{diff} according to the Einstein-Stokes equation.

$$R_H = \frac{k_B T}{6\pi\eta_0 D_{diff}} \quad [3.68]$$

k_B is the Boltzmann constant, T the absolute temperature, and η the viscosity of solvent. On the other hand, for a polydisperse system, the correlation function Eq. [3.65] can be replaced by

$$g^{(1)}(q, \tau_{ret}) = \frac{\int G(\Gamma) \exp(-\Gamma \tau_{ret}) d\Gamma}{\int G(\Gamma) d\Gamma} \quad [3.69]$$

$G(\Gamma)$ refers to distribution of the decay constant. This calculation informs not only the individual particle size but the size distribution.

3.12.2 EQUIPMENT

A Brookhaven BI-9000 AT digital correlator was employed for the dynamic light scattering measurements. A He-Ne laser of wavelength 632.8 nm served as light source, and all samples were measured at 90° scattering angle. Temperature was kept at 25 °C with an equipped water-circulator.

Chapter 4 C₁₂C₈MAO/HCl SYSTEM

INFLUENCE OF PREPARATION ROUTE ON LYOTROPIC MESOPHASE

In this chapter, the effect of preparation route on the morphologies of L_α phases is discussed using the double-chain surfactant, N-Dodecyl-N-Octyl-methylaminoxide (C₁₂C₈MAO). The preparation routes in priori are described as follows:

1. **Normal preparation:** samples at various protonation degrees are mixed well at room temperature which is above their Krafft points.
2. **Thermal treatment:** samples at given protonation degrees are heated above their specific temperature (cloud temperature) with mixing, and then cooled down to room temperature without stirring.
3. **Shear force removal:** C₁₂C₈MAO emulsion is protonated by adding a given amount of an ester, formic acid methyl ester (HCOOCH₃), that hydrolyzes in aqueous medium after the addition, resulting in the formation of composite aggregates at a finite time corresponding to the hydrolysis reaction.

4.1 NORMAL PREPARATION: EQUILIBRIUM PROPERTIES

4.1.1 PHASE SEQUENCE

Figure 4.1 shows the phase sequence of ternary C₁₂C₈MAO-HCl-water system as a function of HCl amount (*X*). The surfactant concentration is fixed at 100 mM, and temperature is at 25 °C. The binary system, C₁₂C₈MAO and water, forms a visually separated two-phase (2Φ) with no birefringence (Figure 4.2). The non-protonated surfactant seems not to be miscible in water and to form any aggregates in such a large amount of water. The small amount of added HCl, however, helps the solubility of C₁₂C₈MAO in water; the increasing *X* induces the phase transition 2Φ (no birefringence

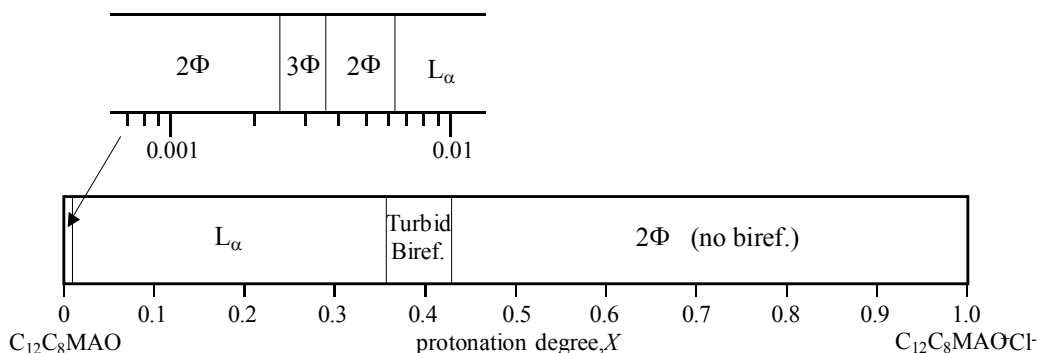


Figure 4.1. Phase diagram of C₁₂C₈MAO-HCl-water system at 25 °C. The C₁₂C₈MAO concentration is kept at 100 mM, and protonation degree indicates $X = [\text{HCl}]/[\text{C}_{12}\text{C}_8\text{MAO}]$.

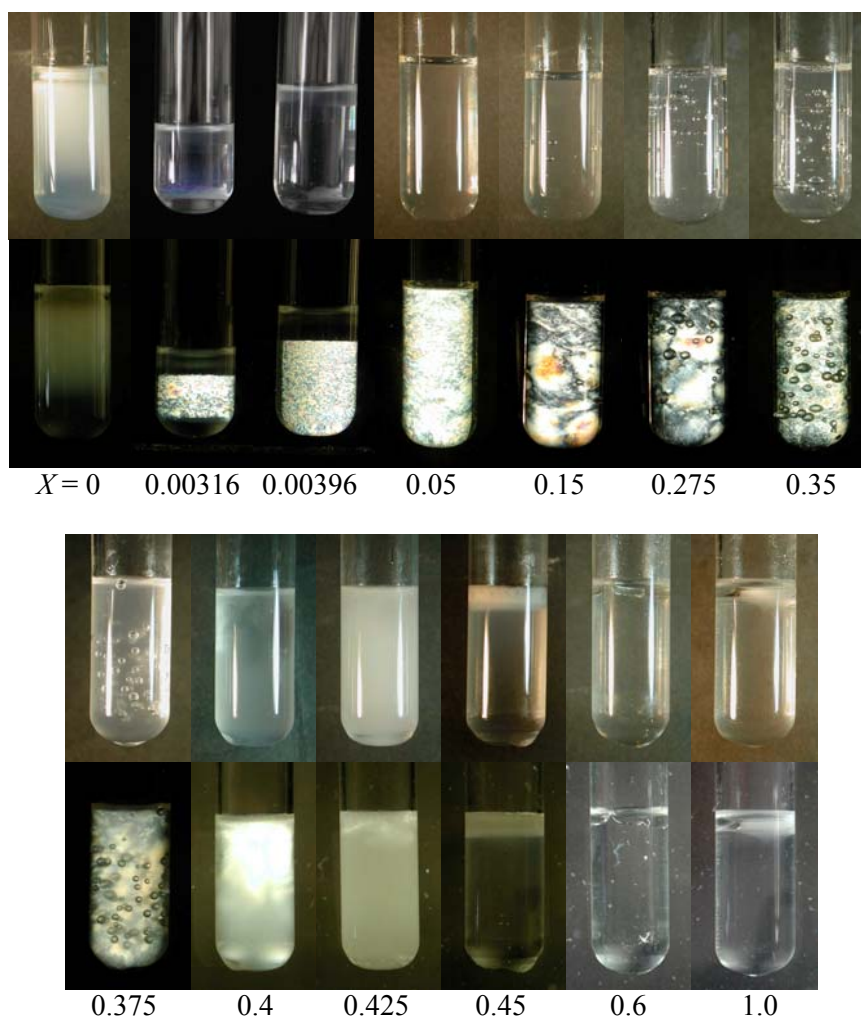
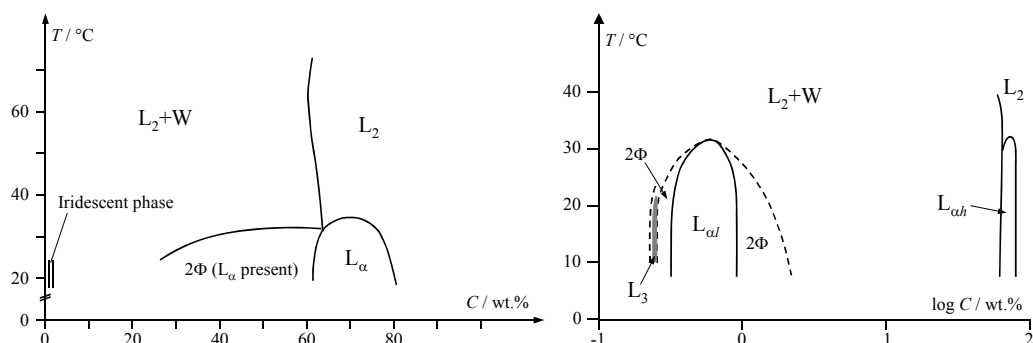


Figure 4.2. Sample appearances at different X s in Figure 4.1. The above and below photographs were taken without and with polarizers, respectively.

in both phases) $\rightarrow 3\Phi$ (a birefringent phase sandwiched between two no-birefringent phases) $\rightarrow 2\Phi$ (birefringent and no-birefringent phases) \rightarrow lamellar phase (birefringent L_α) as seen in Figure 4.2. In other words, the mixture of two analogous, $C_{12}C_8MAO$ and $C_{12}C_8MAOH^+Cl^-$, at an appropriate ratio enables water to contain between bilayers. Further addition of HCl then causes the bilayer structure to be unstable, *i.e.* the single L_α phase turns to the turbid two-phase, which shows still light scattering between the polarizers. At protonation degree more than 0.45, the solutions become again the separated two-phases, and at $X = 1$ a L_α phase is no longer formed in the solution: the appearance of the solution is similar like oil and water phases.

To understand the different two-phase regions at the low and high protonation degrees, the two extreme protonation degrees, for $X = 0$ and 1, phase diagrams were drawn up (Figure 4.3). Figure 4.3 (a) is that at $X = 0$ with different temperature, and (b) refers to that at $X = 1$ at a fixed temperature (25 °C). In the system of $C_{12}C_8MAO$ /water, one can observe various phases; the stacked L_α phase is present in the high concentration region, and, on the other hand, the two-phase region is observable in the

(a) $C_{12}C_8MAO$ /water system



(b) $C_{12}C_8MAOH^+Cl^-$ /water system (25 °C)

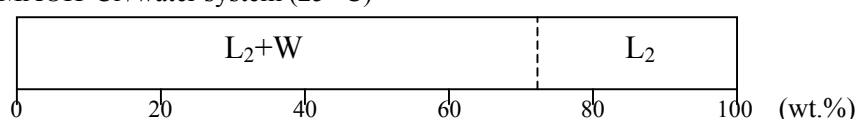


Figure 4.3. Phase behaviors of (a) $C_{12}C_8MAO$ /water system and (b) $C_{12}C_8MAOH^+Cl^-$ /water system at 25 °C as a function of each surfactant concentration. For (a), the phase diagram on the left hand was drawn in linear scale of concentration, and that on the right hand done in logarithm scale. Each notation indicates as follows: L_2 -reverse micellar solution, L_α -lamellar phase, L_3 -sponge phase, W-excess water phase. The L_α phase is classified into the stacked lamellar phase ($L_{\alpha h}$) and the vesicle phase ($L_{\alpha l}$).

low concentration region. The L_α phase transforms to the reverse micelle (L_2) sensitively with temperature. One should note that there is a transparent and colorful phase isolated from the two-phase (Iridescent phase or $L_{\alpha l}$, Figure 4.4). According to the phase rule, it is found that the phase diagram would be abnormal because the tie line should be parallel to the concentration axis under a fixed atmosphere pressure in the binary system. From my visual inspection, however, the phases between $L_{\alpha l}$ and $L_{\alpha h}$ could not be identified and the phase boundaries were drawn simply by macroscopic homogeneity. This abnormal phase behavior would arise from the presence of small quantity of the cationic $C_{12}C_8MAO$. Aminoxide surfactants are charged slightly by hydrogen ion dissociated from water,¹⁵ as a consequence, the tie line could not be followed by the phase rule. Figure 4.5 shows the photographs of moderately protonated $C_{12}C_8MAO$ solutions ($X = 0.17$) at different concentrations. The appearances are definitely different from the above two systems at $X = 0$ and 1; the strong birefringence is weakened with dilution, whereas even at 10 mM (~ 0.3 wt.%) the birefringence was observed under agitation. Figure 4.3 (b) was drawn roughly, while the simple phase sequence was observed. At the high concentration, the protonated surfactant produces a transparent fluid phase, generally assigning to the reverse micellar phase (L_2). The structure is that the hydrophilic groups orient toward inside of the micelle and the hydrophobic alkyl chains do toward outside, *i.e.* the curvature of micelle interface is



Figure 4.4. Iridescent phase. The $C_{12}C_8MAO$ concentration is 60 mM.

Figure 4.5 shows the photographs of moderately protonated $C_{12}C_8MAO$ solutions ($X = 0.17$) at different concentrations. The appearances are definitely different from the above two systems at $X = 0$ and 1; the strong birefringence is weakened with dilution, whereas even at 10 mM (~ 0.3 wt.%) the birefringence was observed under agitation. Figure 4.3 (b) was drawn roughly, while the simple phase sequence was observed. At the high concentration, the protonated surfactant produces a transparent fluid phase, generally assigning to the reverse micellar phase (L_2). The structure is that the hydrophilic groups orient toward inside of the micelle and the hydrophobic alkyl chains do toward outside, *i.e.* the curvature of micelle interface is

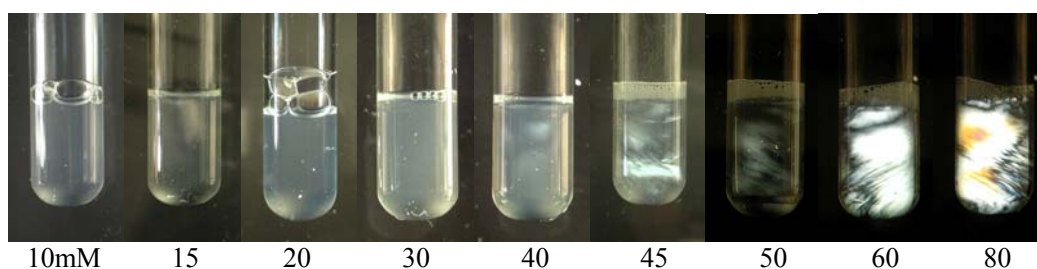


Figure 4.5. Photographs of C₁₂C₈MAO/H⁺Cl⁻ mixture (*X* = 0.17) at different concentrations. Temperature is 25 °C.

negative. Any lyotropic mesophases could not be observed with dilution in this system; L₂+water phase were formed in the wide concentration range below 70 wt.% C₁₂C₈MAOH⁺Cl⁻. These three concentration-sequences allow us to create a rough ternary phase diagram as drawn in Figure 4.6. This diagram elucidates that the phases between L_{al} and L_{ah} in C₁₂C₈MAO/water system involve at least one of the bilayer structures. On the other hand, the phase sequence in Figure 4.1 remains unclear, *i.e.* it is indicative that the protonated form of the surfactant is more hydrophobic than the unprotonated one, and this behavior is found not to be common in any surfactant systems.¹⁴²

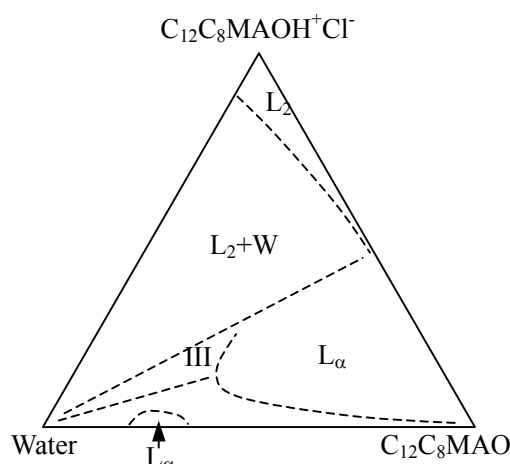


Figure 4.6. Ternary phase diagram of C₁₂C₈MAO/C₁₂C₈MAOH⁺Cl⁻/water system at 25 °C. III refers to three-phase.

4.1.2 pH AND CONDUCTIVITY MEASUREMENTS

The results of pH and conductivity measurements are shown in Figure 4.7. For both the measurements, the samples were agitated at a constant shear rate during the measurement by a magnetic stirrer. In the same figure the pH values of hydrochloric

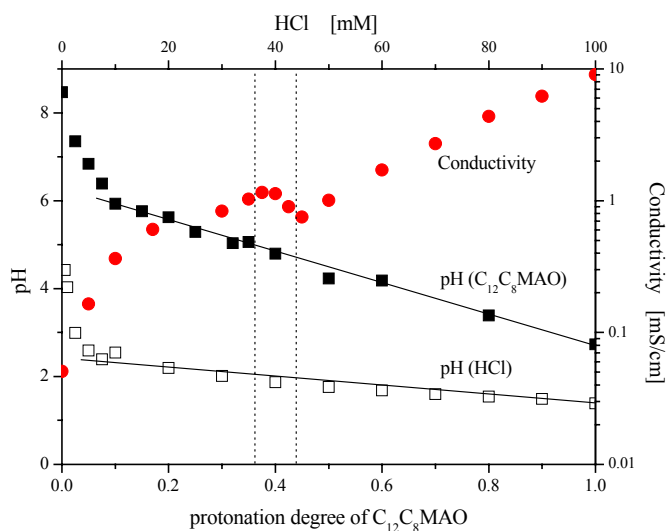


Figure 4.7. pH and conductivity measurements. The C₁₂C₈MAO concentration is fixed at 100 mM, and temperature is 25 °C. The square symbols indicate the pH-values of C₁₂C₈MAO/HCl solution (■) and HCl alone solution (□). The circle symbol (●) indicates the conductivity of C₁₂C₈MAO/HCl solution.

acid (HCl) alone solutions are also plotted with its concentration. pH decreases steeply with increasing HCl content in the low HCl concentration, then goes down gently. The conductivity, on the other hand, shows apparently the phase boundaries at which L_α turns to two-phase upon addition of HCl. Entirely the conductivity increases stoichiometrically with the amount of HCl, however, for different phases, the electrically conductive features seem to be different, as had been found in some literatures.^{143,144} The initial, steep increase in the conductivity at low protonation degree is in good agreement with the pH measurement, suggesting that the free hydrogen ions transfer rapidly from the micelle surface to the bulk phase and vice versa. Beyond $X = 0.1$ the conductivity increment inclines downwards and reaches to a maximum at $X = 0.35$. At this X , the transparent, birefringent L_α phase comes to be turbid although the birefringence is still observable (Figure 4.2). The conductivity then decreases with increasing X up to 0.45, and again begins to increase logarithmically with X . In the range from $X = 0.1$ to 0.35, the H^+ species would be condensed on the aggregate surface, resulting in reduction of the mobility of H^+ . Beside the change in the conductivity must be considered in views of the formed aggregate structure. If a continuous oil phase is present, the charge carriers cannot be passed through the oil medium. This interpretation might be reasonable for the fact that the conductivity decreases with X in the turbid, birefringent phase (intermediate phase between L_α and 2Φ). After the phase transition to 2Φ (L_2+W), the increase in the conductivity is mainly due to the H^+ dissolved in the separated water phase.

From pH data in Figure 4.7, the free hydrochloric ion concentration $[H^+]$ and pK_a at each X were calculated using the following equations and plotted in Figure 4.8.

$$pK_a = pH + \log \frac{(1-\alpha)}{\alpha} \quad [4.1]$$

$$\frac{[H_S^+]}{[H_H^+]} = pH(HCl) - pH(C_{12}C_8MAO/HCl) \quad [4.2]$$

α is the protonation degree of $C_{12}C_8MAO$, $[H_S^+]$ and $[H_H^+]$ are the proton concentration in the $C_{12}C_8MAO/HCl$ solution and the HCl alone solution, respectively. The dissociation constant K_a decreases gradually with X in the L_α region, and the slope of decreasing K_a becomes greater at the phase boundary of L_α and 2Φ . Similarly the ratio $[H_S^+]/[H_H^+]$ increases dramatically in the 2Φ region compared to the L_α phase. These

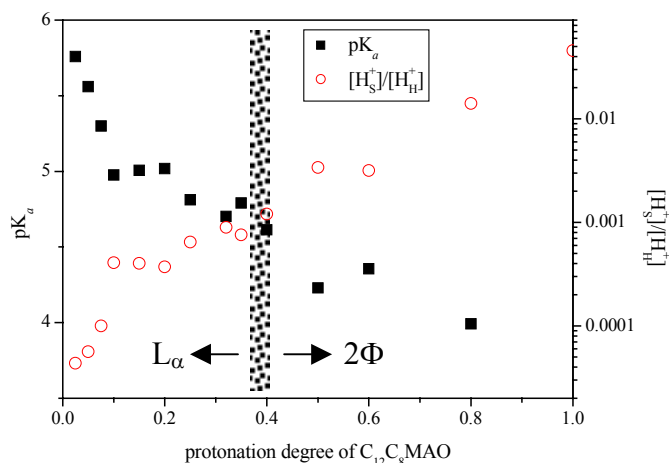


Figure 4.8. Changes in pK_a (■) and the ratio of proton concentration in the $C_{12}C_8MAO/HCl$ system to that in HCl alone solution ($[H_S^+]/[H_H^+]$, ○) with protonation degree at 25 °C. The $C_{12}C_8MAO$ concentration is fixed at 100 mM.

changes demonstrate that the mole fraction of free H⁺ increases with X , that is, the protonation of C₁₂C₈MAO is considerably suppressed upon excess addition of H⁺.

4.1.3 RHEOLOGICAL PROPERTIES OF L_α PHASE

Over the L_α phase, the rheological measurements were performed under the linear deformation from frequency (f) = 0.01 to 10 Hz. Figure 4.9 illustrates these rheograms at different protonation degrees at 25 °C. Most of the rheograms show the typical behavior of a viscoelastic fluid with a yield stress: both moduli are almost independent on frequency in the measuring range, the storage modulus G' is by a factor of 10 higher than the loss modulus G'' . The viscosity shows no plateau anymore; it decreases double-logarithmically with increasing frequency in the whole frequency range which appears in typical vesicle systems.¹⁴⁵⁻¹⁴⁷ The G' values at $f = 1$ Hz are plotted as a function of protonation degree in Figure 4.10. G' abruptly increases up to $X = 0.15$, and afterwards remains constant until the phase transition takes place. This

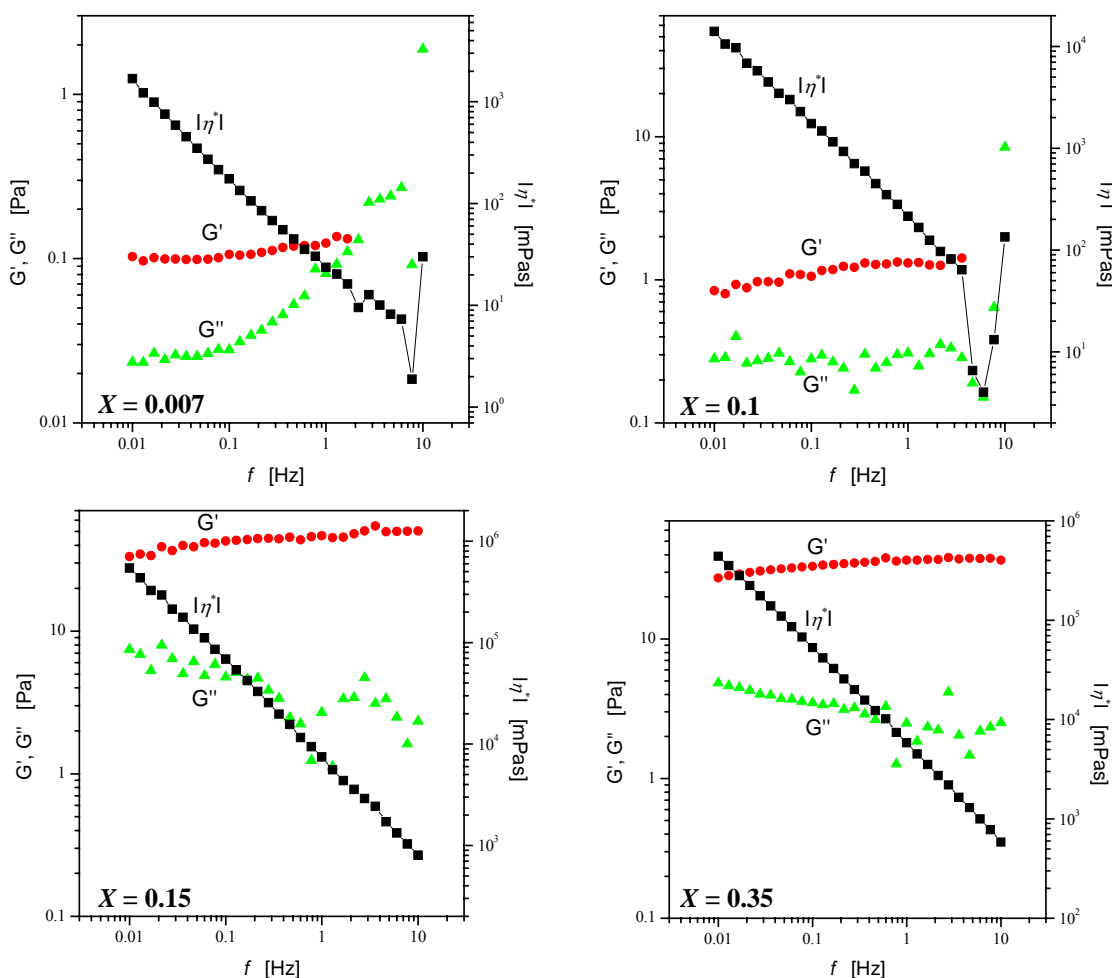


Figure 4.9. Dynamic rheological measurements for the L_α solutions at different protonation degree (X) in the C₁₂C₈MAO system at 25 °C. The C₁₂C₈MAO concentration is fixed at 100 mM. The various symbols refer to the rheological parameters, ● : storage modulus, ▲ : loss modulus, ■ : complex viscosity. The measuring frequency range is 0.01~10 Hz.

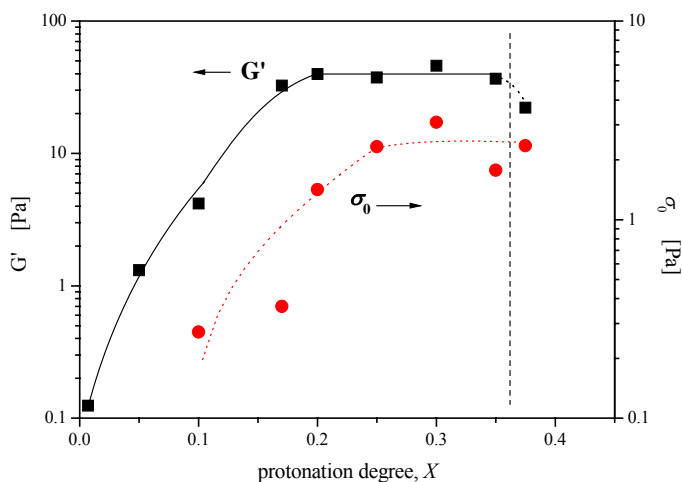


Figure 4.10. Changes in the storage modulus (G' , ■) and the yield stress (σ_0 , ●) for the L_α solutions at different protonation degrees (X) in the $C_{12}C_8MAO$ system at 25 °C. The $C_{12}C_8MAO$ concentration is fixed at 100 mM.

phenomena is similar to the previous result in the tetradecyl-dimethylaminoxide ($C_{14}DMAO$)/tetradecyl-trimethylammonium bromide ($C_{14}TMABr$) system¹⁴⁸: the moduli G' were found to increase with increasing charge density up to 10 % of ionic surfactant and then remained constant on further increase of the charge density. It could be argued that the shear modulus G' is determined by the osmotic compression modulus which is related to the osmotic pressure of the system.¹⁴⁹ This quantity can be calculated from the concentration gradient of ions present between two surfaces by solving the Poisson-Boltzmann equation. As for the present system, the protonation of $C_{12}C_8MAO$ head group leads to condensation of counter-ions around the aggregate surface, consequently, to the osmotic pressure. This counter-ion distribution on the surface however can interpret interaction between the particles solely, while in fact intra-particle interaction as well influences the modulus G' . The intra-particle, *i.e.* inter-molecular interaction affects the vesicle size and polydispersity. If G' is determined by the relaxation of multilamellar spherical droplets,¹⁵⁰

$$G' \sim \frac{\sigma_{\text{eff}}}{R} \quad [4.3]$$

where σ_{eff} is the effective surface tension (see “Chapter 2”) and R is the radius of the spheres. The size contribution to the modulus was also correlated with the volume fraction of the vesicle phase by Kevelam *et al.*,¹⁵¹ who proposed that the vesicles were sterically stabilized such as the hard sphere model.¹⁵² The hard sphere model or the correlation of the volume fraction, however, cannot explain the increase in G' with protonation in the present system at all, because the surfactant concentration is kept constant and the volume fraction of vesicles is almost unchanged over any protonation degrees.

Non-linear measurements were carried out for the samples at different protonation degrees. The yield stresses (σ_0) given by steady shear-stress curves are shown in Figure 4.10. The σ_0 changes with X in the similar way to G' . The yield stress proves the densely packed vesicle phase¹⁵³ and prevents from rising up air-bubbles in the solutions as found in Figure 4.2 where the bubbles had been trapped for more than one year. Shear thinning behavior can be observed for most of the L_α solutions in both the dynamic and static measurements (Figure 4.11). For the low X , The shear thinning given by the steady shear measurement is not coincident with that by the dynamic

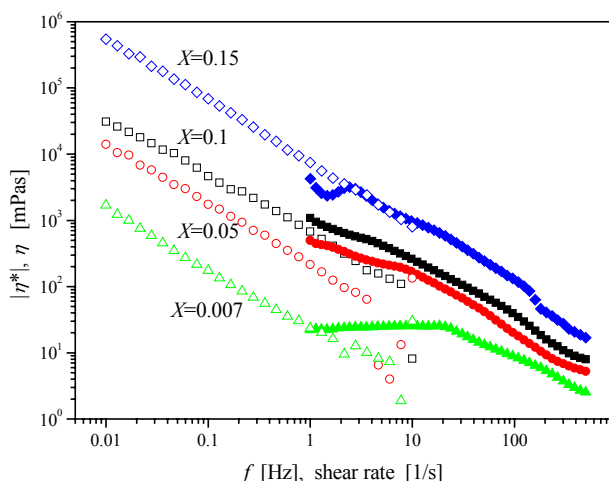


Figure 4.11. Examinations of the Cox-Merz rule for the $C_{12}C_8MAO/HCl$ solutions at different X at 25 °C. The surfactant concentration is fixed at 100 mM. The open and filled symbols indicate the complex viscosity $|\eta^*|$ measured by the oscillatory experiment and the apparent viscosity η obtained by the steady shear measurement.

measurement, especially at $X = 0.007$ the relaxation processes of the two measurements are completely distinct from one another. This deviation from the Cox-Merz rule would arise from the flow property under an applied stress. The solution at $X = 0.007$ have no yield stress and shows a viscous property at high frequency range in Figure 4.9, therefore the elastic deformation would not occur any more. With increasing protonation degree, the two shear thinning experiments come to obey the Cox-Merz rule, suggesting that the time constants of both the measurements are equal. These mechanical properties would interpret the change in the L_α morphologies with protonation. The L_α solutions at low X can be expected to consist of the stacked bilayer structure on the basis of the quite low yield stress and the different relaxation modes between the steady flow and oscillatory flow. As mentioned above, the sufficiently high σ_0 and the structural deformation coincident between the two experiments unambiguously reveal the presence of vesicle at high X .

Numerical multilamellar vesicle (MLV) phases are ready to transform to other L_α morphologies under shearing. This dynamic phenomenon had been documented well by Roux *et al.* over a few decades.^{10,80,154,155} The present system was no exception concerning this phenomenon, and addition of excess stress beyond the intrinsic yield stress forces the vesicles to deform along the applied flow direction. It was recognized from the simple steady shear (stationary shear) measurements that there were some steps during the morphological transition as seen in Figure 4.12 and 14: Region I (persistence of non-flow, yield stress) → Region II (stress reduction) → Region III (stress plateau) → Region VI (shear thinning). Changes in the shear stresses σ for the samples at various X are shown as a function of shear rate $\dot{\gamma}$ in Figure 4.12. All of the solutions exhibit step increments of the stresses up to each specific yield stress with shear rate as shown in Figure 4.13. Beyond the yield stress, however, the deformation processes are different depending on the protonation ratio; for any samples, a definitive peak appears at certain $\dot{\gamma}$ dependent on X , and the quasi-Newtonian flow can be seen at much higher $\dot{\gamma}$. After the maximum stresses, the stresses at $X < 0.1$ decrease gently with shear rate and keep constant, while for the samples with higher protonation ratio, $X > 0.17$, the stress curves are almost independent on shear rate and suddenly drop down in ~ 3 Pa at around 250-300 1/s. However, in the vicinity of the phase boundary ($X = 0.35$),

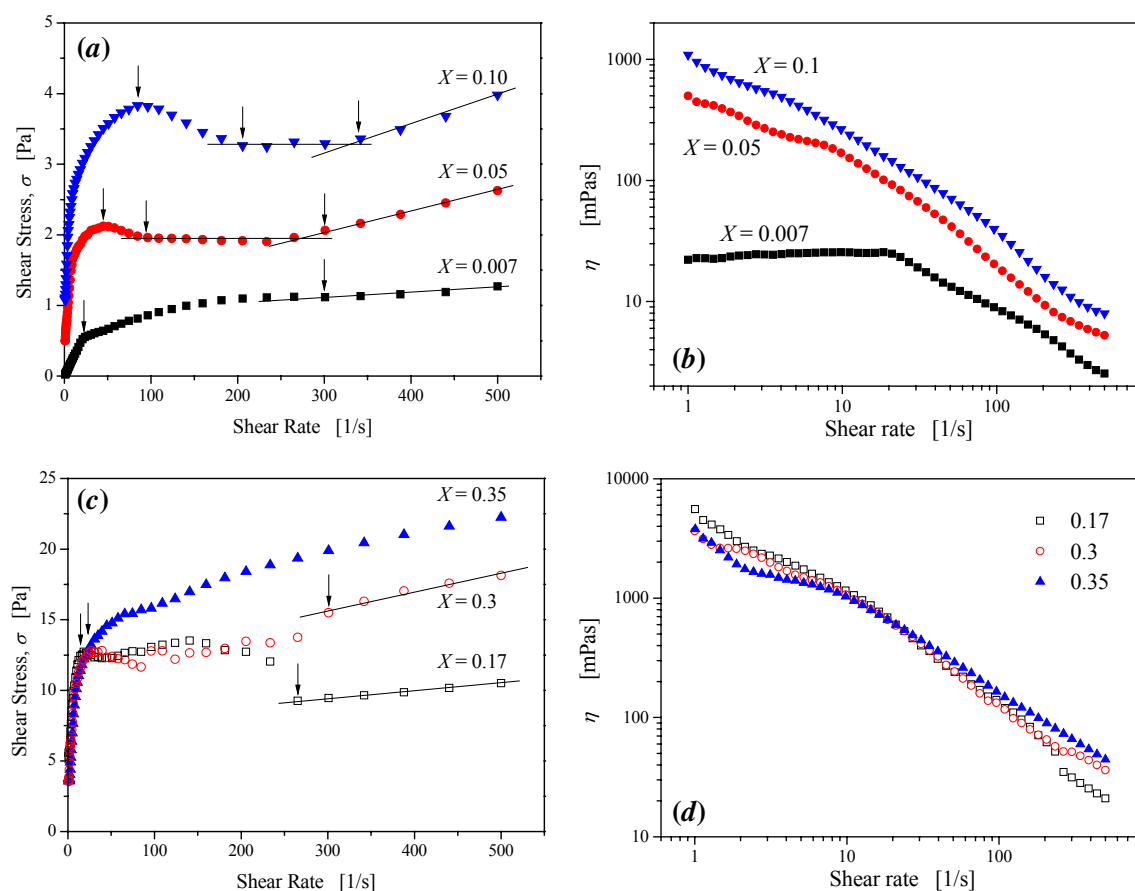


Figure 4.12. Steady shear rheograms of the shear stress σ versus shear rate $\dot{\gamma}$ (a, c) and the apparent viscosity η versus $\dot{\gamma}$ (b, d) for the $C_{12}C_8MAO/HCl$ aqueous solutions at different X at 25 °C. The surfactant concentration is fixed at 100 mM. Each symbol refers to as follows: ■ - $X = 0.007$, ● - 0.05, ▼ - 0.10, □ - 0.17, ○ - 0.30, ▲ - 0.35. The arrow marks indicate the critical shear rates at each transition point.

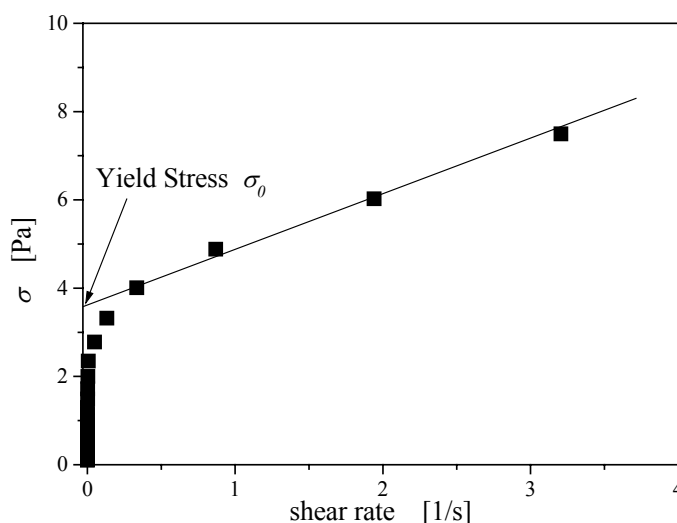


Figure 4.13. The plot of the shear stress (σ) versus shear rate in $C_{12}C_8MAO/HCl$ system at 25 °C. The surfactant concentration and protonation degree are 100 mM and $X = 0.3$.

there are no peak and no fluctuation of the curve over the whole measuring shear range, and it can be found thus that a typical $\dot{\gamma}$ - σ rheogram for the Bingham fluid appears. For

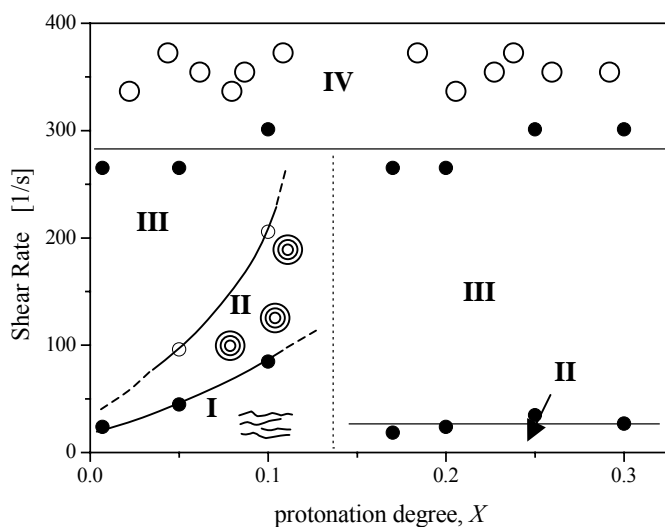


Figure 4.14. Dynamic phase diagram as a function of protonation degree X in $C_{12}C_8MAO/HCl$ system at 25 °C. The surfactant concentration is fixed at 100 mM. The notations represent the different phases with their characteristic rheological properties referring to Figure 4.12: I – stacked bilayer form with the yield stress, II – multilamellar vesicle form, III – transformation region from multilamellar to unilamellar vesicle, IV – unilamellar vesicle.

the $\dot{\gamma}$ - η rheograms, the shear thinning can be observed, but the slopes of the shear vary in the corresponding ranges of shear rate. As demonstrated in the previous papers, the abnormal stress profiles would be explained by the shear-induced phase transition. According to the dynamic phase diagram proposed by Roux *et al.*,¹⁰ the defected planar lamellar phase transforms to the oriented lamellar phase along the flow direction via the spherical vesicle and the coexistence phase (vesicle + oriented lamellae) with increasing shear rate. Here the transition sequence with shear should be reviewed necessarily, because in the present system the layer thickness was ~ 52 nm from SAXS measurement which is so large that the shear-induced transition would not take place anymore if the dynamic phase diagram could precisely predict the phase state. To identify the dynamic phase state at high shear rate $\dot{\gamma} \sim 300$ 1/s, the slope of shear thinning is compared with the previous data. The stacked bilayer and the multilamellar vesicle can be described empirically by their characteristic power laws of $\dot{\gamma} \propto \sigma^x$. The stacked bilayer morphology regardless of the defect presence corresponds to an exponent $x \sim 1$, and an exponent for the multilamellar vesicle is $x \sim 0.2$.^{80,156} Cates *et al.* reported the shear thinning behavior with an exponent $x \sim 0.4$ for the multilamellar vesicle in the AOT/brine system.¹⁵⁷ The slopes at various X s are summarized in Table 4.1. Every exponent x is much less than that of the stacked bilayer structure, and in the most case the power laws lay between those of the two L_α morphologies. This namely suggests that the L_α morphology can be the small unilamellar vesicle. The difference between the x values at each protonation degree might result from the difference of the capable minimum size of the vesicles under shear because the surfactant at different degree of protonation should have the corresponding aggregate size.

The solutions at lower X seem to follow the above transformation: the shear thickening and the plateau after the peak top correspond to respectively the vesicle formation and the coexistence phase. At

Table 4.1. Power laws of shear thinning, $\dot{\gamma} \propto \sigma^x$, at different protonation degrees X .

protonation degree, X	exponent x
0.007	0.2442
0.05	0.4805
0.10	0.4420
0.17	0.1968
0.20	0.3504
0.30	0.3082
0.35	0.2193

higher X , however, the shear thickening region does not appear because the solutions consist already of the vesicles, thus the coexistence region (stress plateau) alone could be observed. Over the entire X range, the shear thinning with a constant slope occurs at high shear rate. I plotted three characteristic points, the peak top, the intersection between the shear thickening and the plateau, and the transition point to the shear thinning region, as a function of X in Figure 4.14. It can be seen that the morphologies of the solutions clearly change with not only shear rate but also the composition X . The upper boundary (III→IV) is almost constant within accuracy of the measurement. On the other hand, it appears that the transformation boundaries, I→II and II→III shift to the higher shear rate with X for the solutions at lower X . The phases I and II are stabilized as regards with the applied shear stress and instead the phase III is suppressed. On the other hand, at $X > 0.1$, the II→III boundary is almost unchanged with X .

When the solution at $X = 0.17$ is diluted with water, the dynamic diagram in Figure 4.15 shows a dependence on a bilayer volume fraction (ϕ_L , see Appendix A.1: Calculation of Volume Fraction) as well as the other systems reported to date. This figure would prove that a morphology formed at each shear rate is defined well for the solutions at different X . The phase boundary between regions III and VI shifts gradually toward lower shear rate when ϕ_L decreases, while the shear rate required for the phase transition from region II to III is mostly independent on the concentration in the studied ϕ_L range. Thus in our system the dynamic phase transition is observable at definitive shear rates. In the above results, however, there is a contradiction against the phase diagram drawn by Roux that the morphological transitions at the specific shear rates are governed by a bilayer mass fraction or volume fraction. Namely, for the present system with the variable of X , the bilayer composition should be invariant regardless of X unless the hydration number and the compression of the lipophilic moiety take into account. From Figure 4.14, it appears that the shear stability of planar bilayer is influenced greatly by protonation, but when the vesicle is constructed predominantly the vesicle deformation by shear is independent on the charge density of the head group.

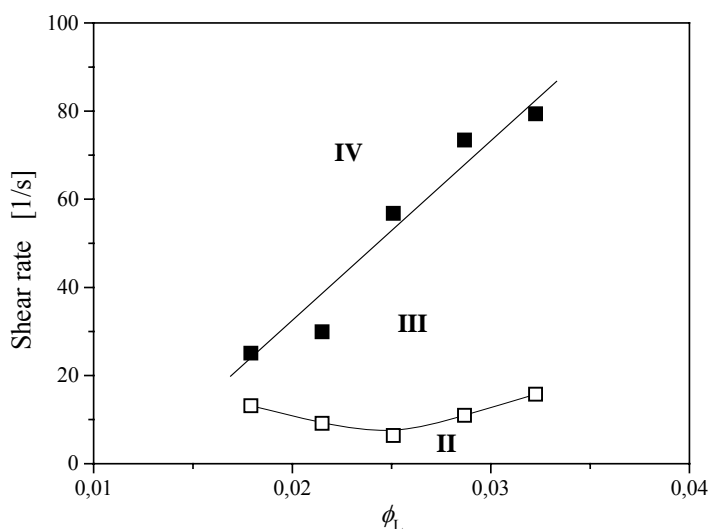


Figure 4.15. Dynamic phase diagram of the volume fraction of lipophilic group in the surfactant (ϕ_L) versus shear rate in water/ $C_{12}C_8MAO/HCl$ system at 25 °C. The symbols (II, III, IV) represent the same morphologies as those described in Figure 4.14. The protonation ratio is fixed at $X=0.17$.

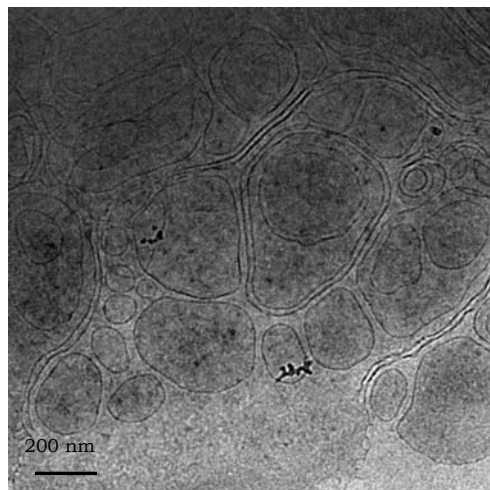
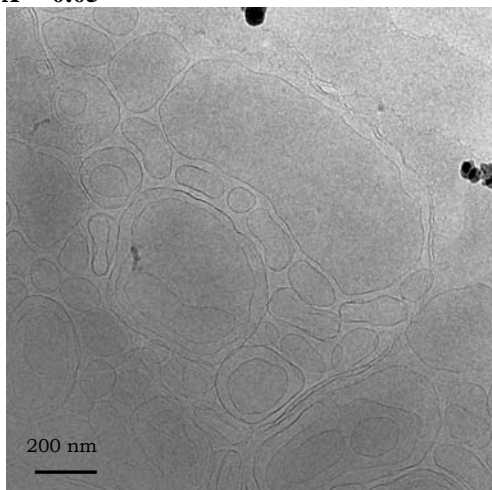
4.1.4 MICROSCOPIC OBSERVATION

The aggregate structures were confirmed directly by the electron microscope. Figure 4.16 shows the cryo-TEM micrographs at $X = 0.05$ and 0.1 . The micrographs at $X = 0.05$ exhibit the large aggregates of which the scale is *ca.* 400 nm or more. Every particle is very closely neighboring each other, and the particle shape seems to vary with time depending on the sterical packing. One can observe that the membranes are deformed and fluctuate, while the interlayer spacing is constant. In the micrographs at $X = 0.1$, the vesicle shapes become more uniform and spherical; some aggregate sizes are smaller than those at $X = 0.05$, and each particle is away from one another. However, the other vesicles are still more than 200 nm in diameter and it can be seen that there are the concave and convex interfaces of vesicles.

Figure 4.17 exhibits the FF-TEM micrograph at $X = 0.3$. Even at this protonation degree, the vesicle size is polydisperse, whereas every vesicle is enclosed sphere and the observable maximum size is *ca.* 300 nm.

These micrographs clearly support the rheological properties: the vesicle

$X = 0.05$



$X = 0.1$

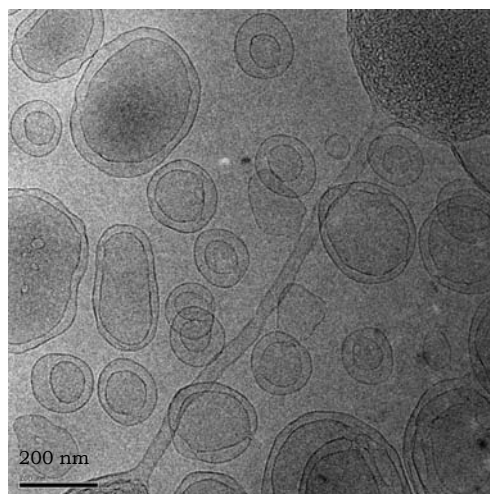
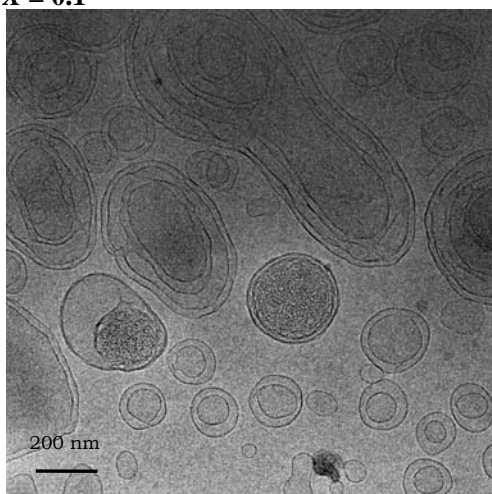


Figure 4.16. Cryo-TEM micrographs for the $C_{12}C_8MAO/HCl$ solutions at $X = 0.05$ (top) and 0.1 (bottom). The bar length is correspondent to 200 nm.

formation and the morphological transformation with protonation degree. The charge density can control the vesicle size, polydispersity, distance between particles, furthermore the fluctuation of membrane.

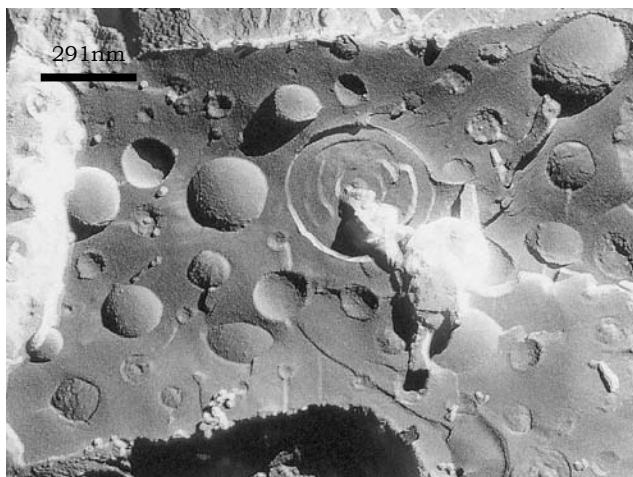


Figure 4.17. FF-TEM micrograph at $X = 0.3$ in $C_{12}C_8MAO/HCl$ system. The bar length corresponds to 291 nm.

4.1.5 SYNERGISM

Single-chain aminoxide surfactants show synergism by mixing another chemical species such as an anionic and/or a cationic surfactant¹⁵⁸ and even its homologous surfactant.¹⁵⁹ The effect can be observed in terms of the viscosity,^{159,160} CMC,^{158,161} surface tension¹⁶² and so on. In the double-chain aminoxide surfactant studied at present, synergism has not been reported to my knowledge. And it either can or cannot occur because some mixing surfactant systems have no such effect owing to the geometrical hindrance of interaction between the head groups of two different surfactants.¹⁶³ $C_{12}C_8MAO$ has no side-chain in the vicinity of its head group, instead the bulky hydrophobic chains, which may interrupt interaction of nonionic and ionic head groups.

To verify synergism, the surface and interfacial tension measurements were carried out with a function of protonation degree at room temperature. The $C_{12}C_8MAO$ concentration was kept at 1 mM, which is sufficiently higher than its CMC (refer in Figure 4.19). Figure 4.18 shows the surface tension at the variety of X . The surface tension is almost unchanged with protonation and increases slightly at $X = 0.9$ and 1.0.

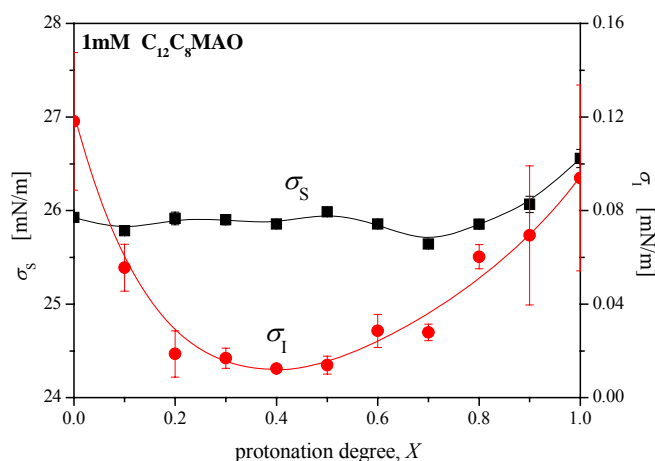


Figure 4.18. Surface and interfacial tension measurements for the $C_{12}C_8MAO/HCl$ solutions at different X at room temperature. The surfactant concentration is fixed at 1 mM. The interfacial tension was measured against decane.

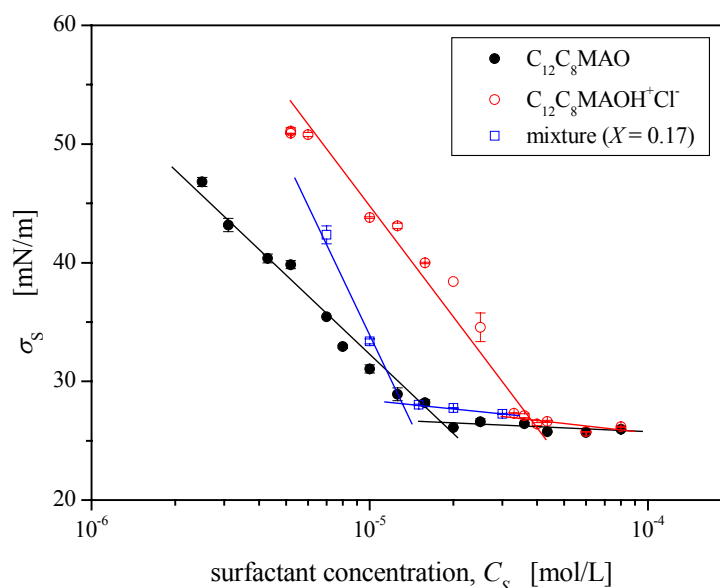


Figure 4.19. Adsorption isotherms of $C_{12}C_8MAO$, $C_{12}C_8MAOH^+Cl^-$, and their mixture ($X = 0.17$) at room temperature.

The increment of surface tension is only 0.7 mN/m. In Figure 4.19, adsorption isotherms of $C_{12}C_8MAO$, $C_{12}C_8MAOH^+Cl^-$, and their mixture ($X = 0.17$) are illustrated.

These isotherms give some parameters concerning the adsorption properties of the surfactant, which are listed up in Table 4.2. $\partial\sigma_s/\partial(\log C_s)$ is the slope of the isotherm in the vicinity of CMC, exhibiting the efficiency of adsorption onto the air-water surface. The CMC of $C_{12}C_8MAOH^+Cl^-$ is approximately two times as large as that of non-protonated $C_{12}C_8MAO$. This tendency is general: the hydrophilic surfactant has relatively higher CMC in comparison to the hydrophobic one. The mixture, however, has lower CMC, indicating that there is more or less synergism. The change in $\partial\sigma_s/\partial(\log C_s)$ is noticeable: the mixture much more preferably adsorbs onto the air-water surface, suggesting interaction between two analogous.

Furthermore, the interfacial tension (against decane) demonstrates that synergism appears in the mixture system (Figure 4.19). Its minimum can be found in the range from $X = 0.2$ to 0.5 . This regime is in reasonable agreement with the constant G' regime in Figure 4.10. Reminding Eq. [4.3], one can estimate the vesicle size R with the assumption that the effective surface tension σ_{eff} is substituted by the interfacial tension σ_i . The calculated sizes are summarized in Table 4.3, and exceed considerably those observed by TEM. This correlation apparently suggests that the increasing modulus cannot be determined by reduction of the interfacial tension due to synergism. The depression of the vesicle size would be generally considered to cause the smaller vesicles to pack densely in a

Table 4.2. Adsorption properties of the various surfactants at room temperature.

	CMC [mM]	$\partial\sigma_s/\partial(\log C_s)$
$C_{12}C_8MAO$	0.0178	-23.101
$C_{12}C_8MAOH^+Cl^-$	0.0373	-27.783
Mixture ($X = 0.17$)	0.0123	-57.92911

Table 4.3. Calculation of the vesicle radius at different X using Eq. [4.3].

X	G' [Pa]	σ_i [mN/m]	R [nm]
0.1	4.184	0.0556 ± 0.0100	13279 ± 2397
0.3	46.01	0.0169 ± 0.0043	366.4 ± 93.5

unit volume, as a consequence, the solution has highly elastic property according to the hard sphere model. The model however unlikely can be applied to this case as mentioned above: TEM shows that the distance between the vesicles increases with protonation, that is, protonation induces simultaneously a repulsive interaction between the vesicles. This repulsive force arises from diffuse double layer of counter-ion on the vesicle surface upon addition of the charge, resulting in the osmotic pressure toward the midplane of two aggregate surfaces as sketched in Figure 4.20. The osmotic pressure P_{osm} arises up the Young modulus B following the approximation, $B \sim P_{\text{osm}}$,¹⁶⁴ and, as a result, the storage modulus is elevated as dominating compressibility with a theoretical formulation.¹⁶⁵

$$G' = \frac{B}{2(1+n_p)} \quad [4.4]$$

n_p is the Poisson number.

4.1.6 INTERLAMELLAR SPACING BETWEEN THE BILAYER

The layer thickness of the L_α phase was measured for the differently protonated

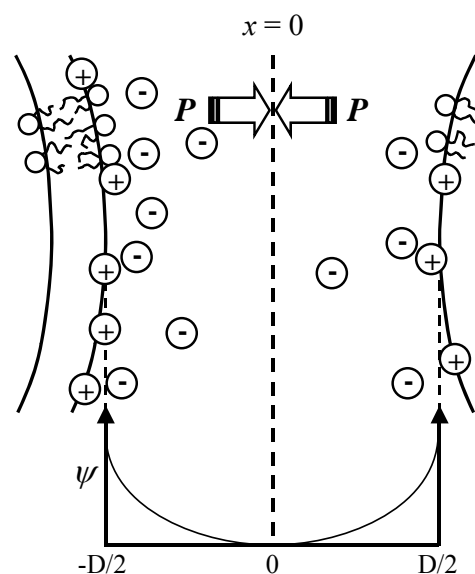


Figure 4.20. Osmotic pressure (P) acting on the midplane ($x = 0$) between two ion-condensed membrane. Ψ indicates the chemical potential.

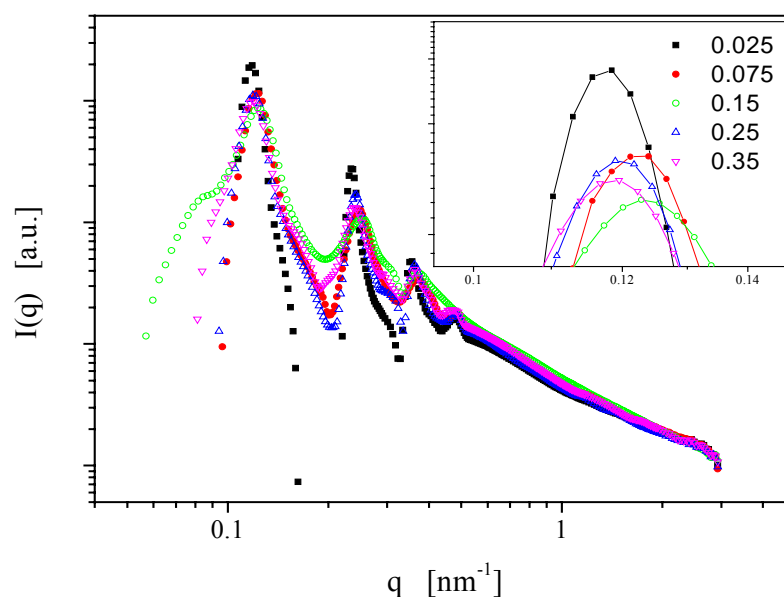


Figure 4.21. SAXS spectra for the $C_{12}C_8MAO/HCl$ solutions at different X at room temperature. The surfactant concentration is fixed at 100 mM.

samples by SAXS. The scattering spectra are shown in Figure 4.21. The correlation peaks assign to the bilayer structure according to the Bragg law, $q_1:q_2:q_3:q_4 = 1:2:3:4$. The interlayer spacing (d) corresponding to the first peak is in fairly good agreement with the thickest spacing in the TEM micrographs, where one can observe the thinner spacing, ~ 20 nm, corresponding to the second X-ray peak. Figure 4.22 shows a plot of the interlayer spacing against protonation degree. The d -value firstly decreases with increasing X , and increases passing through the minimum. The interlayer spacing is expressed with the thicknesses of the surfactant layer (d_s) and the water layer (d_w) (see in Figure 4.23) as follows:

$$d = d_s + d_w \tag{4.5}$$

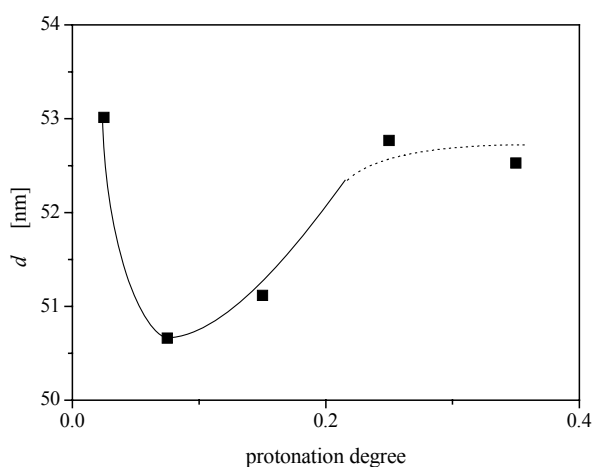


Figure 4.22. Change in the interlayer spacing d as a function of protonation degree (X).

Therefore, the thickness of d_s can be derived from the surfactant spacing. Let us consider membrane fluctuation at certain constant temperature. The surfactant membrane is stabilized by thermal fluctuation (Figure 4.24). The fluctuation can be enhanced or suppressed by temperature, concentration, and additives, of which some harden the membrane. Increase in the charge density on the membrane surface leads to the stiffer membrane, resulting in suppression of the membrane fluctuation. If the domain size of the lamellae would be constant, a contour length of the lamellae should be longer with decreasing fluctuation. Since the amount of water contained in the bilayer remains unity, the thickness of water-layer then would be compressed on lowering fluctuation. The increase in the charge density, therefore, can be expected to decrease monotonically the interlayer spacing. On the other hand, it was recognized from the interfacial tension measurements that the two surfactants, $C_{12}C_8MAO$ and $C_{12}C_8MAOH^+Cl^-$, have the head group interaction, synergism. The synergism effect does not allow water molecules to penetrate into the hydrophilic surfactant layers, as a consequence, water can be squeezed out of the surfactant layers. Furthermore, the short-range interaction would affect freedom of the hydrophobic

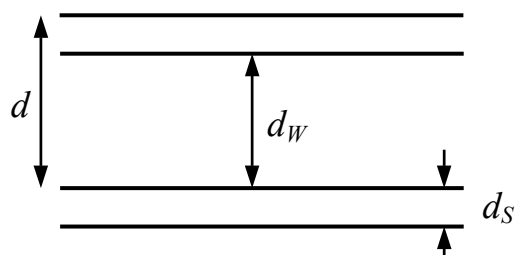


Figure 4.23. Interlayer spacing (d) between the bilayer. d_w and d_s represent the spacings of water and surfactant layers, respectively.

chains in the aggregate core, in other words, the shrinkage of the effective cross-sectional area occupied per molecule induces to the stretching hydrophobic chain. The net thickness of the surfactant layer is related geometrically with the volume fraction of the surfactant ϕ_s in the L_α phase.

$$\phi_s = \frac{d_s}{d} \tag{4.6}$$

Since the volume fraction ϕ_s is maintained constant, d_s changes proportionally with the measured d . Thus the above two effects can be illustrated in Figure 4.25, and the measured interlayer spacing shows the minimum due to the decreasing d_w and asymptotes the following maximum due to the increasing d_s .

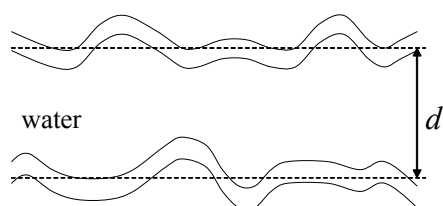


Figure 4.24. Schematic representation of thermal fluctuation of the membrane. d is the average interlayer spacing.

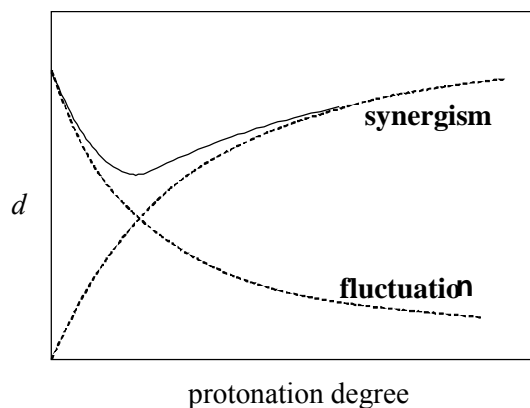


Figure 4.25. Influences of synergism and fluctuation on the interlayer spacing d with protonation.

4.1.7 ION CONDENSATION

The above results prove that the micelle surfaces are condensed by the added ion species. The thickness of the electric double layer is condensed upon addition of salt. Figure 4.26 shows a change in the storage modulus G' with NaCl concentration in water/ $C_{12}C_8MAO/HCl/NaCl$ system at 25 °C, where the surfactant concentration and the protonation degree are fixed at respectively 100 mM and $X = 0.17$. The modulus decreases exponentially with NaCl concentration. The manner of G' decay with the salt

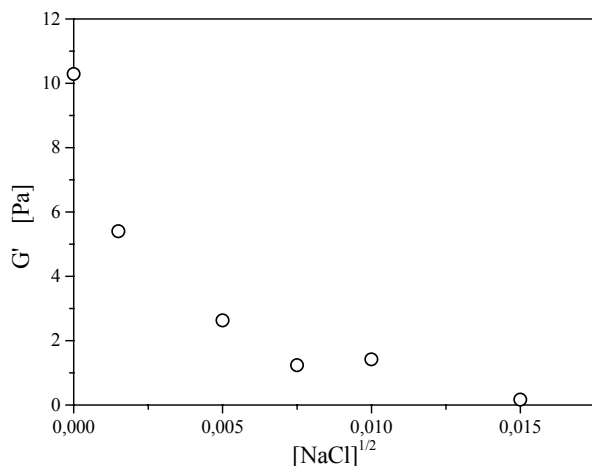


Figure 4.26. A plot of the storage modulus G' as a function of square root NaCl concentration ($[NaCl]^{1/2}$) in water/ $C_{12}C_8MAO/HCl/NaCl$ system at $X = 0.17$ at 25 °C. The surfactant concentration is fixed at 100 mM.

concentration is distinct from the previous result¹⁴⁸: G' is reciprocally proportional to the square root of NaCl concentration for the vesicle solution. The ionic atmosphere around the aggregates is indeed a main contribution to the decreasing G' . The diffusion electric double layer should be compressed by the added salt, as a consequence, the long-range repulsion force decreases with increasing salt concentration. But it seems not to be only due to the electrostatic contribution. Visually the sample becomes turbid with increasing NaCl concentration while still showing birefringence between the polarizers. This refers to coagulation of the vesicles, by which such a large vesicle can scatter the visible light (Figure 4.27). The coagulation should reduce the elasticity of the system on the basis of Eq. [4.3], of which the effective surface tension (σ_{eff}) would cause G' to decrease upon addition of the salt likewise. Further addition of NaCl leads to phase separation (Figure 4.27 (c)) which seems to consist of the surfactant phase and water. The phase separation would arise from depressed solubility of C₁₂C₈MAO in water due to the salting-out effect.

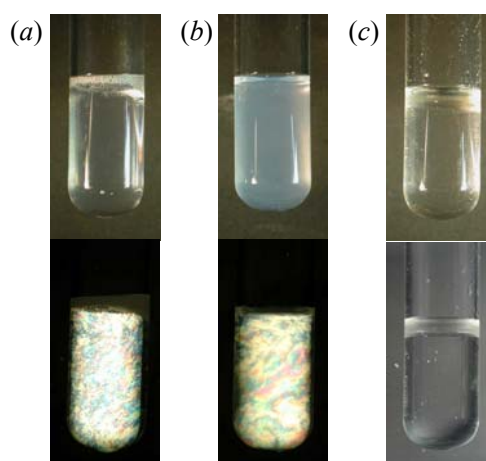


Figure 4.27. Sample appearances in water/C₁₂C₈MAO/HCl/NaCl system at 25 °C. The NaCl concentrations are (a) 0.005, (b) 0.05, (c) 0.5 wt.%. The surfactant concentration and protonation degree remain constant at 100 mM and $X = 0.17$.

The phase behaviors of different counter-ion systems were also investigated under the condition same as the HCl system (Figure 4.28); the C₁₂C₈MAO concentration is 100 mM and the protonation degree is 0.17. The phase sequences of bromide Br⁻ and formiate HCOO⁻ are similar to that of HCl: the L_{α} phase transforms to the separated two-phase with increasing protonation degree. The phase boundary solely depends on the counter-ion, and shifts to low protonation degree as the following sequence:



The order is compatible with well-known Hofmeister series. And these ionic features can be described by their interaction with the charged head group. Figure 4.29 shows a relationship of the hydration entropy ΔS_{hyd} and the protonation degree at the phase boundary. The hydration entropy was obtained from $\Delta S_{hyd} = S(\text{ion, aq}) - S(\text{ion, g})$, where $S(\text{ion, aq})$ and $S(\text{ion, g})$ are the absolute entropies in aqueous medium and

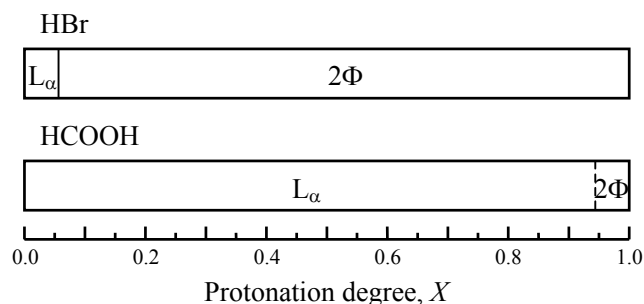


Figure 4.28. Phase sequences for the different acids, bromic acid (HBr) and formic acid (HCOOH), in C₁₂C₈MAO/water system at 25 °C. The surfactant concentration is fixed at 100 mM.

gaseous phase, respectively. The phase boundaries for the different counter-ions (X_C) have a linear relationship with their hydration entropies. The higher hydration entropy enhances counter-ion diffusion in the bulk phase, resulting in more effective protonation

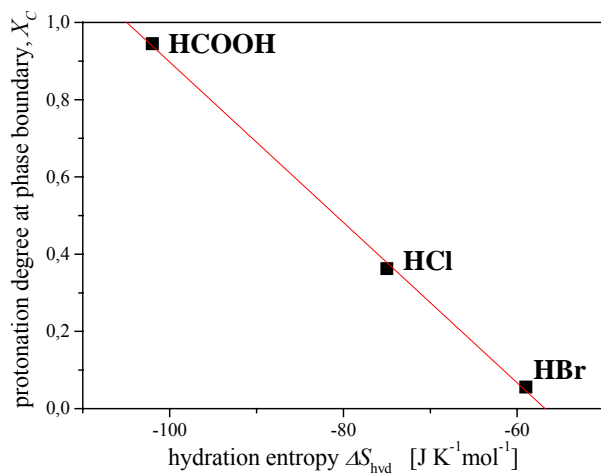


Figure 4.29. Relation between the protonation degree at each phase boundary X_C and the hydration entropy ΔS_{hyd} for the different acids in 100 mM $C_{12}C_8MAO$ system at 25 °C.

of $C_{12}C_8MAO$. It is thus conceivable that the vesicle stability definitively relates to the ion condensation on the vesicle surface.

4.2 THERMAL TREATMENT

4.2.1 CLOUDING PHENOMENON

This process is subject to so-called clouding phenomenon. In generally, this phenomenon is observed in various nonionic surfactant systems such as a polyoxyethylene type surfactant.⁵² Some of these systems exhibit a phase transition, $L_1 \rightarrow L_1 + \text{water} \rightarrow L_\alpha \rightarrow L_3$ (sponge phase) $\rightarrow L_2$ (reverse micelle), with increasing temperature, indicating to be relative to the bending modulus. In the present system, also, such a phase separation with temperature was observed at lower X . Figure 4.30 exhibits the phase diagram of protonation degree versus temperature in water/ $C_{12}C_8MAO/HCl$ system. The clouding phenomenon was observed up to $X = 0.15$,

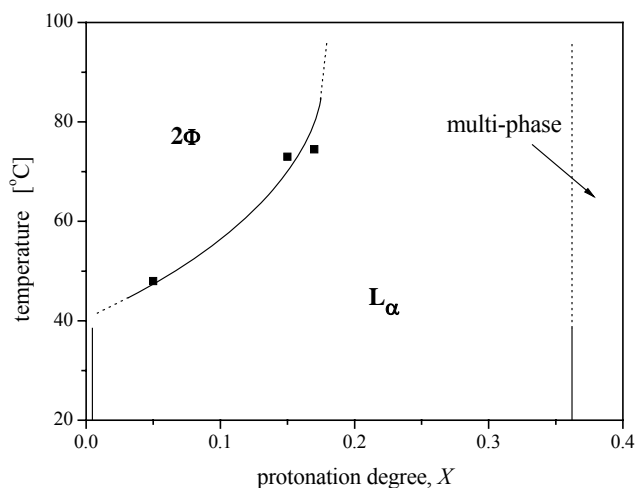


Figure 4.30. Phase diagram of water/ $C_{12}C_8MAO/HCl$ system as a function of temperature. The surfactant concentration is fixed at 100 mM. The notations, 2Φ and L_α represent respectively two-phase and lamellar phase.

hereafter the clouding temperature would lay above 100 °C. The clouding temperature is rising up with increasing protonation degree, which is compatible with general tendency that the clouding temperature increases with the hydrophilicity of surfactant.^{74,166} Figure 4.31 shows the appearances of the samples prepared by different ways between the polarizers. Sample (A) was prepared by the normal way in the previous section 4.1, *i.e.* the sample was simply mixed at room temperature. Sample (B) was exposed at a temperature higher than the specific phase separating temperature, ~ 80 °C, and stirred through cooling from the high temperature. Sample (C) was heated until the temperature same as Sample (B) but cooled down without shearing. The concentration and composition for all the samples are fixed at 100 mM and $X = 0.17$, respectively. The bubbles breaking out through shearing were removed by centrifugation; all the samples were centrifuged at 1000 rpm in about 10 minutes. The photographs demonstrate that the scattered light intensity is reduced and the color becomes monochromatic by the thermal treatment. This would be dependent on alignment¹⁶⁷ and the interlayer spacing⁴⁷ concerning the L_α domain.

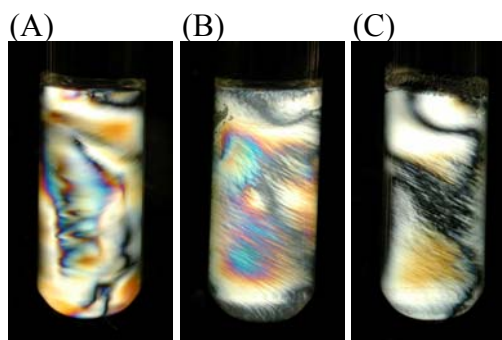


Figure 4.31. Appearances of the samples prepared through the different preparation routs: (A) normal preparation (Section 4.1), (B) heating and cooling with agitation, (C) heating and cooling without shear. The surfactant concentration and protonation degree are 100 mM and $X = 0.17$.

4.2.2 RHEOLOGICAL PROPERTIES

The rheograms for the samples prepared through the different preparations (A), (B), and (C) are shown in Figure 4.32. The measurements were carried out using an identical solution, *i.e.* the heating and cooling processes were conducted in the rheometer. Therefore it should not be taken into account that the even tiny shear force

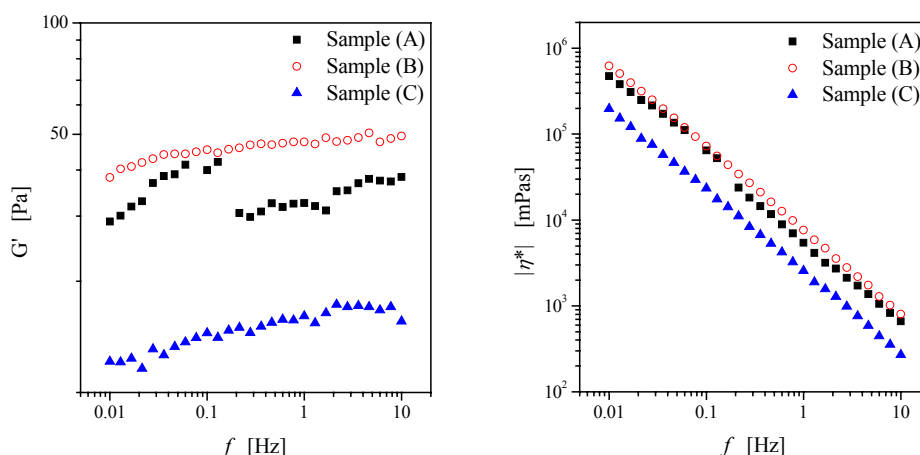


Figure 4.32. Influences of the preparations (A, ■), (B, ○), and (C, ▲) on the rheological parameters, storage modulus G' (left) and complex viscosity $|\eta^*|$ (right), in 100 mM $C_{12}C_8MAO/HCl$ ($X = 0.17$) aqueous solutions at 25 °C.

generated throughout the experimental procedure would influence on the aggregate structure, consequently the rheological properties. The shear moduli for all the samples are almost independent on frequency, and the complex viscosities represent the shear thinning with a slope ~ -0.97 . This indicates that any solutions consist of the L_α morphologies as confirmed by birefringence in Figure 4.31. In Table 4.4, the storage modulus (G' , $f = 1$ Hz), the complex viscosity ($|\eta^*|$, $f = 1$ Hz), and the yield stress (σ_0) are compared between the samples (A), (B) and (C). Samples (A) and (B) have the higher viscoelastic property than Sample (C); G' and $|\eta^*|$ of Sample (C) are half or one-third of those of Sample (A) and (B). Moreover, for Sample (C), σ_0 could not be measured by the cone-plate system in the same stress-controlled range as Sample (A) and (B). The yield stress also attempted to be found out by the sweep measurement of shear rate – stress (σ), whereas the significant break point, corresponding to the yield stress, could not be observed as shown in Figure 4.33. The behavior of Sample (C) thus seems to be a viscous fluid. On the basis of weaker birefringence and lower viscoelasticity, it can be plausible that Sample (C) composed of the stacked bilayer morphology or even large vesicular one. It is also of interest that Sample (B) has the higher viscoelastic properties than Sample (A). This would be due to contribution of the vesicle size, which may be explained by the similar procedure to the finely-dispersed emulsion using the phase inversion method.¹² The mechanism is essentially related to the interfacial tension. The interfacial tension at the phase inversion point reaches to the minimum,¹⁶⁸ where the emulsion turns to the microemulsion consisting of well-defined bicontinuous structure.¹⁶⁹ The shear force could tear the bicontinuous structure apart, and the dispersions would be smaller and smaller depending on the applied shear force because the interfacial tension is quite low. In turn, the mechanism can be manipulated in the present case because the clouding phenomenon originates from the similar structural modification.⁷⁷ The high

Table 4.4. Comparison of the rheological parameters, storage modulus G' (1 Hz), complex viscosity $|\eta^*|$ (1 Hz), and yield stress σ_0 , for the L_α solutions prepared by the different routs. The surfactant concentration and protonation degree are kept at 100 mM and $X = 0.17$.

Sample	G' [Pa]	$ \eta^* $ [mPas]	σ_0 [Pa]
(A)	32.58	5453	0.366
(B)	47.67	7626	0.9093
(C)	16.1	2569	-

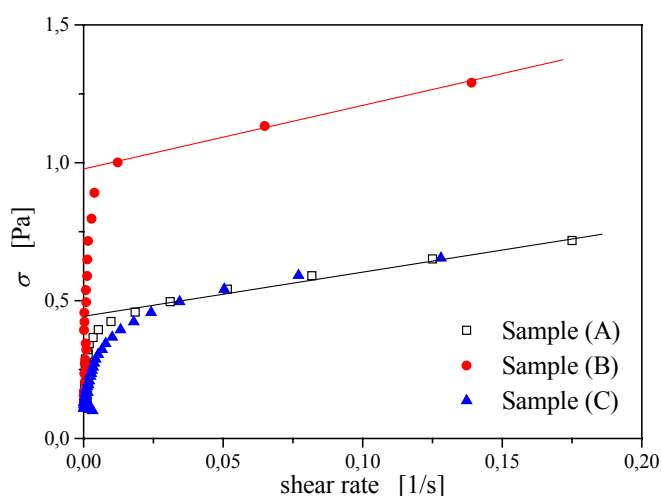


Figure 4.33. Sweep curves of the stress (σ) – shear rate for the samples differently prepared through preparations (A, \square), (B, \bullet), and (C, \blacktriangle). The surfactant concentration and protonation degree are 100 mM and $X = 0.17$.

yield stress value of Sample (B) implies that there exists much densely packed vesicles. The temperature-induced structural modification, however, did not occur at higher protonation degree than $X = 0.2$ where the phase separation with rising temperature does not take place in the measurable temperature range.

Changes in the complex viscosity and the transmittance of Sample (A) are shown as a function of temperature in Figure 4.34. Both $|\eta^*|$ and the transmittance drop steeply down at around 72 °C, referring to the phase separation. The viscosity decreases by a factor of 10^3 , which clearly demonstrates that the viscoelastic structure arising from the densely packed multilamellar vesicles are ruined through the phase separation. Thus it is evident that the vesicle structure is ready to modify into another L_α structure by controlling shear and temperature, while the modification requires the temporarily breaking-down of the vesicle structure.

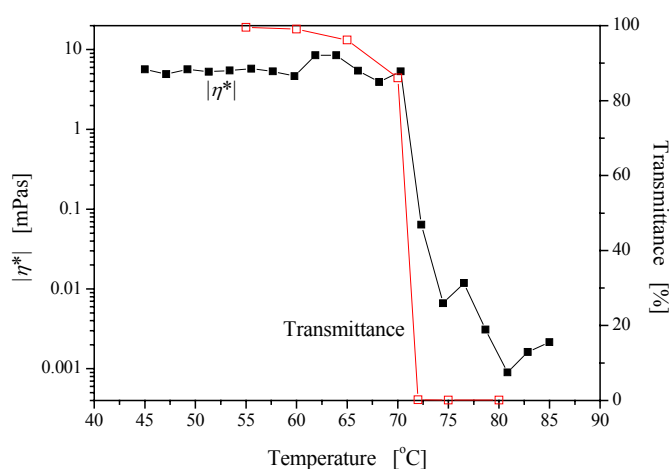


Figure 4.34. Changes in the complex viscosity ($|\eta^*|$, ■) and the transmittance (□) with temperature. The surfactant concentration and protonation degree are 100 mM and $X = 0.2$.

The dependence of protonation degree on the temperature-induced structure modification was studied for the series of samples with different X using rheology. Figure 4.35 shows the plot of the storage modulus G' against protonation degree for the samples before and after heating. The annealed samples were prepared in the measuring cell of the rheometer under no shear. As mentioned in the previous section 4.1, G'

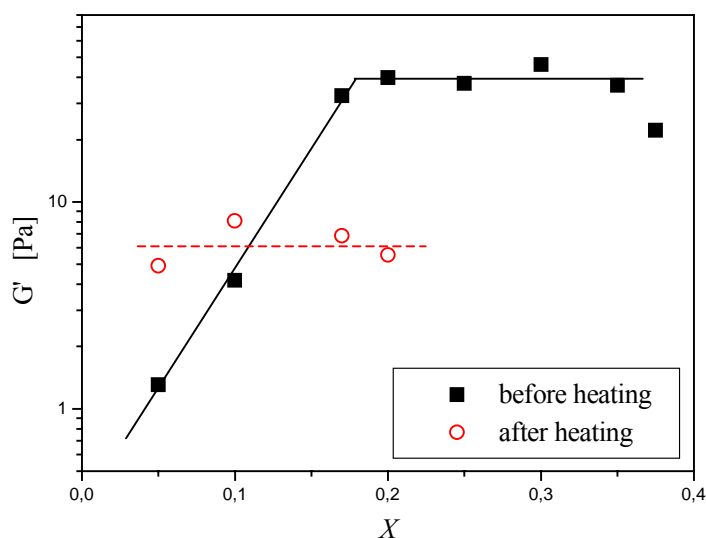


Figure 4.35. Plots of the storage modulus G' versus protonation degree X for the samples before (■) and after heating (○) in $C_{12}C_8MAO/HCl$ ($X = 0.17$) system at 25 °C. The surfactant concentration is kept at 100 mM.

increases monotonically with protonation degree in the low X range, and levels off at $X = 0.17$, remaining constant up to the phase boundary. The heated samples, on the other hand, show the different change in G' ; the modulus is almost independent on the charge density of the system, namely, the resulting morphology could be the same over the studied X range. Although the formed structure after heating was speculated to be the stacked L_α before, the storage moduli in fact increase by the thermal treatment at $X = 0.05$ and 0.1 where the large multilamellar vesicles are present (see Figure 4.16). The upwards deviation of G' at low X would result from an experimental error; in the course of elevating temperature, more or less water is inevitable to evaporate from the sample solution although the measuring system had been covered with the plastic cover and retained under constant vapor pressure as far as possible, whereas certainly the absolute G' values of upwards deviation at low X seem to be so much small that it would be unnecessary to account for the experimental error. At high X , rather, it is noteworthy that G' remarkably decreases by heating, and the modulus after heating is one order smaller than that before heating. Provided the aggregate structure at $X = 0.05$ is identical in spite of the thermal history, the invariant G' with protonation degree after heating elucidates that their structure can be the flat bilayer structure or such the large vesicle as seen in the cryo-TEM micrographs in Figure 4.16.

4.2.3 THERMAL QUANTITY AND PHASE TRANSITION

The enthalpic change accompanied with the clouding phenomenon on heating is scanned by DSC (Figure 4.36). The composition is again fixed at $X = 0.17$. Two cycles were performed in the same temperature range. Continuously the second cycle was followed after the first measurement, *i.e.* the solution used in the second cycle is the same state as Sample (C). The DSC profiles in both the first and second cycles show the characteristic endothermic peaks, 71.5 – 74 °C, corresponding to the phase separation temperature, which is in good agreement with the results obtained from the transmittance measurement and the rheometry. In detail the endothermic peak consists of two transition peaks: the former one may be pre-transition accounting for $L_\alpha \rightarrow L_1/L_\alpha$, and the latter is $L_1/L_\alpha \rightarrow L_1/L_2$. If so, the intermediate transition $L_1/L_\alpha \rightarrow L_1/L_\alpha/L_2 \rightarrow L_1/L_2$ should appear. However, one cannot recognize it from the DSC profile, and it is likely that the scanning rate is too fast to detect the transition. The phase transition was visually observed, but the three-phase temperature could not be identified. In the measuring temperature range, any other definitive peaks do not appear. Between the first and second cycles, the magnitude of the transition enthalpy (ΔH) is apparently different: 35.6 J/mol for the first cycle, 14.1 J/mol for the second cycle as shown in Table 4.5. To confirm the reproducibility and the reliance, the solution at $X = 0.15$ was measured under the same condition. As well as $X = 0.17$, the solution at $X = 0.15$ gives the similar results; the peak tops are correspondent between two cycles, and the peak area is shrunk in the second cycle. The corresponding enthalpies are 72.6 J/mol for the first cycle and 14.9 J/mol for the second cycle, respectively. In turn the variations of the heat capacity on cooling were measured, but there is no significant difference between the first and second cooling processes at both $X = 0.17$ and 0.15 . The enthalpy difference suggests that the heated solution has different chemical properties such as the hydration number. The major origins of the phase separation would be water-surfactant interaction and micellar branching. The representative nonionic surfactant, polyoxyethylene glycol, depresses the interaction with water on heating, resulting in

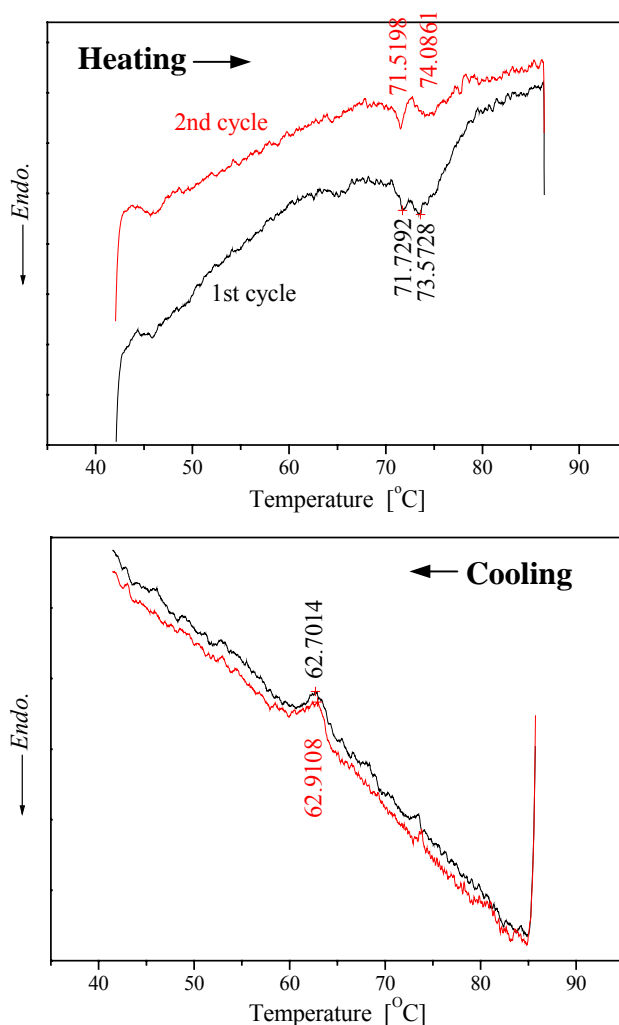


Figure 4.36. DSC profiles of two temperature cycles on heating (left) and cooling (right) in $C_{12}C_8MAO/HCl$ ($X = 0.17$) system. The surfactant concentration is kept at 100 mM. The heating and cooling rates are kept at 0.2 °C/min.

dehydration.^{170,171} The surfactant then makes itself rearrange, as a consequence, the aggregate structure transforms into a favorable form with lower curvature. Kjellander^{172,173} proposed that micelle growth alone is insufficient to cause phase separation, and a recent theory¹⁷⁴ and experiment⁷⁷ suggest that the driving force for phase separation is the entropic attraction between network junctions. This network structure results from the energy cost of the end-cap. The dominant attractive force between aggregates thus introduces the phase separation into surfactant-rich and surfactant-poor phases. The primary structure in our system at these compositions is multilamellar vesicle, therefore, the mechanism of the phase transition may differ somewhat from that of the micelle-two phase transition. However, this explanation would be able to apply for our system, because the separated phase in our system does not consist of flocs of aggregated vesicles (no macroscopic birefringence)¹⁷⁵ and addition of the charged $C_{12}C_8MAO$ permits to rise up the clouding temperature, that is relevant directly with the aggregation number and the attraction force. The DSC profiles prove as follows: the deviation of heat quantities between two cycles results from the formation of different aggregate structures. It is conceivable that the depression of ΔH

in the second cycle is compensated by depression of the hydration number or the entropic energy cost accompanied with the structural modification. This means that at 25 °C the heated solution retains a structure formed above the clouding temperature. This speculation agrees well with the results from the rheology.¹⁷⁶ Such an irreversible structural transition was found in a vesicle system by Oberdisse *et al.*,¹⁷⁷ while the mechanism remains unclear.

Table 4.5. Transition enthalpies in the first and second cycles at $X = 0.17$ and 0.15 in $C_{12}C_8MAO/HCl$ system. The surfactant concentration is kept at 100 mM.

	ΔH in first cycle (J/mol)	ΔH in second cycle (J/mol)
$X=0.17$ (Heating)	35.65	14.05
$X=0.17$ (Cooling)	3.67	4.03
$X=0.15$ (Heating)	72.57	14.94
$X=0.15$ (Cooling)	6.06	9.73

4.2.4 MICROSTRUCTURE CHANGE

The structural change on heating was monitored by means of SAXS. The solutions managed to be inserted into the capillary tube, especially the non-shear sample was set herein just after heating: the cloudy solution was inserted and cooled down to room temperature in the capillary tube. During this procedure, the complete non-shear would be unable to be achieved because temperature inside the capillary (*ca.* 20 °C) is uncontrollable, which can lead to the friction between the capillary wall and the solution, even internal friction of the solutions arising from temperature distribution. Therefore the data obtained will be interpreted qualitatively, and the reproducible results solely are to be dealt with.

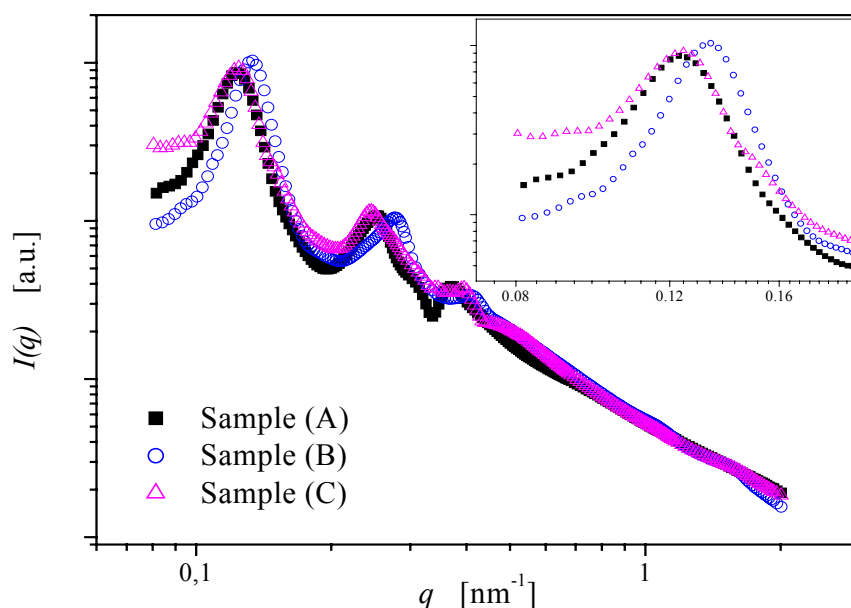


Figure 4.37. SAXS spectra for the solutions prepared through the different procedures in $C_{12}C_8MAO/HCl$ ($X = 0.15$) system. The surfactant concentration is kept at 100 mM.

Figure 4.37 shows X-ray spectra for Samples (A), (B), and (C) at $X = 0.15$. For all the samples, the identical solution was used, *i.e.* the solutions required for each measurement were taken out of the stock solution. The composition thus should be the same. The measuring time duration is about 17 hours, which seems to be sufficient to reform the L_α phase from the turbid phase. For all the samples one can observe three significant peaks, whose ratio is $q_1:q_2:q_3=1:2:3$, assigning again to the L_α morphologies. The scattering curves are coincident one another in the high q range, indicating the same interface structure. However, it is remarkable that the scattering intensity deviates as $q \rightarrow 0$ dependent on the preparation processes: Preparation (B) causes the intensity to go downwards relative to Preparation (A), and Preparation (C) contrarily gives rise to it. Note that the absolute intensities for every sample are almost the same over the q range. The scattering intensity $I(q)$ is proportional to the particle density per unit volume, n_p , and a product of the form factor $P(q)$ and the structure factor $S(q)$, *i.e.*¹⁷⁸

$$I(q) \propto n_p \cdot P(q)S(q) \quad [4.7]$$

The asymptotic form factor $P(q \rightarrow 0)$ can be considered as unity. The scattering intensity at $q \rightarrow 0$, as a consequence, is expressed by a function of the structure factor, in other words, the inter-aggregate interaction. Particle interference shows that $I(q)$ infinitely approaches to 0 as $q \rightarrow 0$. It can be expected therefore that the dimension of inter-vesicle varies with the preparation routes. If the same dimension of vesicles are dispersed in the medium for all the solutions, the number density decreases in the following order: Sample (C) < Sample (A) < Sample (B). The structure factor $S(0)$ relates to isothermal osmotic compressibility B , giving¹⁷⁹

$$S(0) = n_p k_B T B \quad [4.8]$$

For the case of a hard sphere system, $S(0)$ is represented by the Carnahan-Starling expression¹⁸⁰:

$$S(0) = \frac{(1 - \Phi)^4}{(1 + 2\Phi)^2 - 4\Phi^3 + \Phi^4} \quad [4.9]$$

where Φ is the effective volume fraction of the hard sphere. In the present case, however, the volume fraction of the bilayer and the charge density remain constant, and the water layer thickness is unchanged via thermal treatment. Thus the void fraction between particles plays a significant role, and increasing vesicle size then would be inevitable in order to expand the void volume. As seen in Figure 4.38, $S(0)$ steeply decreases in the range from $\Phi = 0.01$ to 0.5, where the present system exists, $\Phi \sim 0.47$. Assuming that all neighboring vesicles in unit volume are fused, the volume fraction becomes $\Phi = 0.31$, then $S(0)$ rises up to *ca.* 0.1.

This change in $S(q)$ explains well the rheological properties of the different solutions. The structure factor can be related to the shear modulus G' because $S(0)$ expresses the compressibility in the system.

$$G' \sim \frac{kT}{S(0)} \quad [4.10]$$

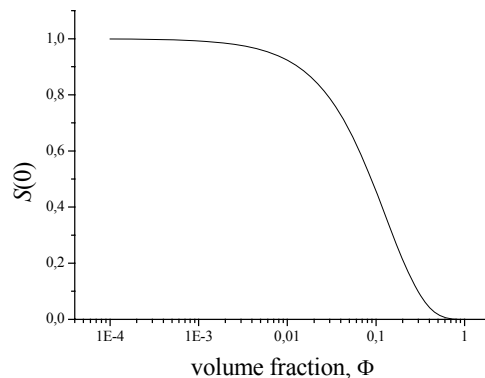


Figure 4.38. $S(0)$ curve dependent on volume fraction Φ (from Eq.[4.9]).

Qualitatively the order of the magnitude of G' corresponds to that of $S(q)$. Thus the SAXS measurements fairly agree with the above speculation from the rheology and DSC measurement.

4.3 CHEMICAL REACTION

4.3.1 PROTONATION WITH TIME

In recent years we have invented and investigated the protonation method using a chemical reaction for the several systems.^{145,181-184} The method had been served for the bilayer structural modification from L_3 to L_{oh} ; the general route of sample preparation (applied shear force) derives vesiculation, while the kinetic reaction that protonates the bilayer creates the planar lamellar morphology. The reaction that is used for the protonation is the hydrolysis reaction of methyl formiate $HCOOCH_3$ to formic acid and methanol. Formic acid is a strong enough acid to protonate alkylaminioxides, and methanol in small concentrations has hardly an effect on mesophases.¹⁸¹ The present work attempted to produce a non-shear L_{oh} from the two-phase at $X = 0$ using the chemical reaction in order to recognize the influence of shear history on the lamellar morphologies. The rate constant of the reaction is in a very convenient range so that the ester can be mixed with the starting phases and the protonation can proceed in times between minutes and a day depending on the conditions like temperature, pH, and concentration. The two-phase sample was homogenized with ultrasonication, and we had seen no phase separation in the sample for at least one day. Figure 4.39 exhibits sample appearances with time. $HCOOCH_3$ was added to the emulsion so as to set at the mole ratio $[HCOOCH_3]/[C_{12}C_8MAO] = 0.17$, that is, the vesicle phase should be present if enough shear force is exposed to the solution as observed in the previous sections. The milky solution changes into a transparent one gradually with time, finally reaches to a clear single phase. The birefringence is a little bit weaker than that of the stirred solution and seems to be heterogeneous after three hours. This may be due to the creaming up of the bilayers formed by protonation within this time scale. However the

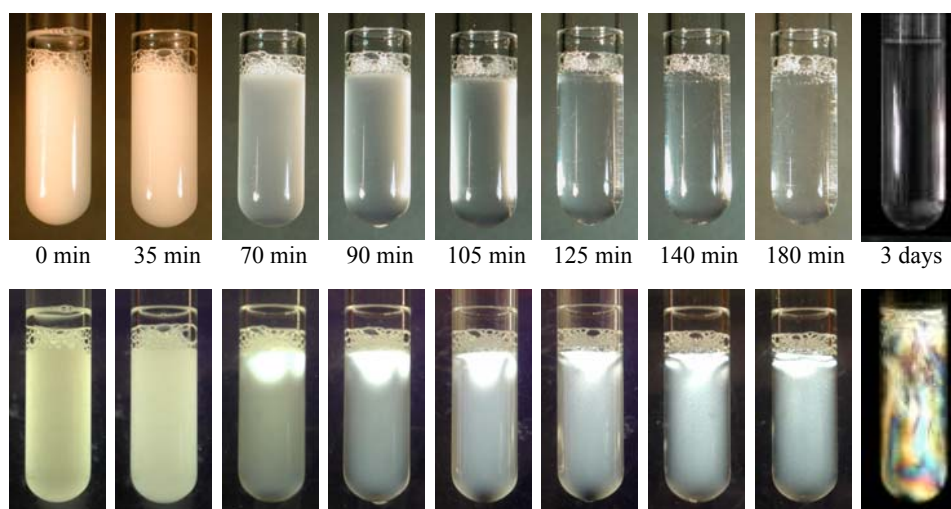


Figure 4.39. Change in the sample appearance of $C_{12}C_8MAO/HCOOCH_3$ ($X = 0.17$) solution with time at 25 °C. The surfactant concentration is 100 mM.

solution becomes completely transparent and homogeneously birefringent around three days after addition of the ester. Thus it is concluded that the chemical reaction is accomplished over at least three days in the surfactant present system.

4.3.2 MICROSOCPY

To demonstrate the aggregate structure produced by the chemical reaction, the microscope observations were performed by using the polarized microscope and FF-TEM. In the course of the experiments, the samples were inevitably affected somewhat by shear force. However the micrographs in Figure 4.40 show typical lamellar textures: (a) oily-streak texture, (b) focal conic texture, (c) Malta-cross texture. There are certainly different textures observed in the identical solution, but which properly depends on the position where the textures were observed. The micrograph (a) was found out around the center of the solution, on the other, (b) and (c) were observed in the vicinity of solution edge. On the microscope measurements, the cover glasses were not used because of avoided shear force, while the solution drop spontaneously spread over the glass plate more or less. The spreading, *i.e.* shear flow results in vesiculation from the lamellar sheet as seen in Figure 4.40 (b) and (c). The micrograph of the sheared solution under no polarized light is shown in Figure 4.40 (d). The picture exhibits finely dispersed and densely crowded droplets. The sample does not give any

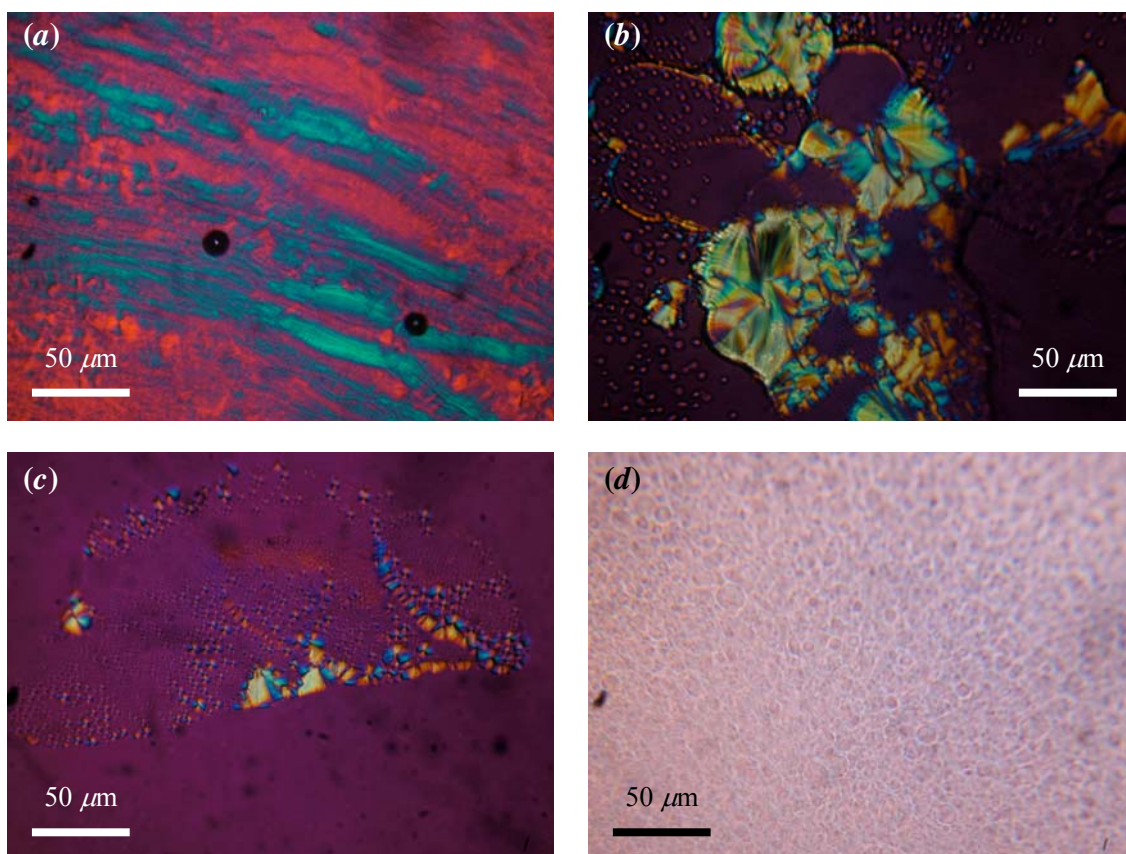


Figure 4.40. Microscope observation of the lamellar phases in $C_{12}C_8MAO-HCOOCH_3$ (a, b, and c) and $-HCl$ (d) solutions. The micrographs represent the different lamellar textures; (a) oily-streak, (b) focal conic, (c) Malta-cross textures. The sample (d) was prepared under shearing at room temperature, and the photograph was taken without the polarizers.

texture microscopically under polarized light due to the much small dimension of aggregate. Therefore, it is evident that the chemical reaction induces to the stacked L_α morphology. And it is also noted that the tiny shear flow would be enough to roll up the lamellar sheets.

The FF-TEM image is shown in Figure 4.41. In the image, in fact, one would be difficult to seek out the spherical vesicles, instead can observe the several lamellar layers. The domain size is greatly distinct compared to the sheared solution (Figures 4.16 and 17). These microscopic observations manifest that the large size of aggregate beyond expectation is formed by this procedure.

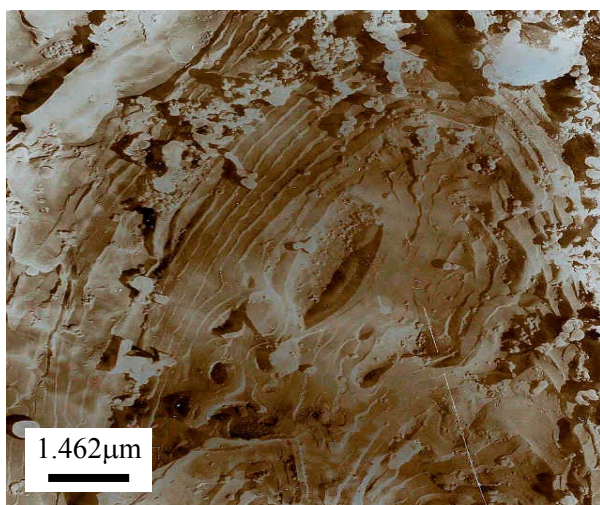


Figure 4.41. FF-TEM image of the $C_{12}C_8MAO/HCOOCH_3$ solution ($X = 0.17$) prepared by means of the chemical reaction. The surfactant concentration is 100 mM.

4.3.3 RHEOLOGICAL PROPERTIES FOR NON-SHEARED SOLUTION

One recalls the preparation of the non-shear solution; the test solution was prepared inside of the double-gap system in the rheometer. Every chemical was weighted exactly at $X = 0.17$ and the solution had left for three days before the

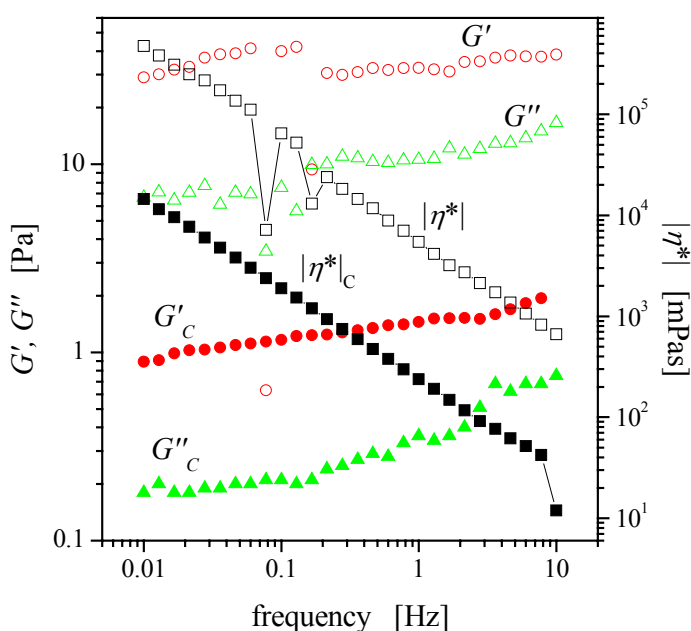


Figure 4.42. Dynamic rheological measurements for two solutions prepared by the normal preparation route (hollow symbols) and using the chemical reaction (filled symbols) at 25 °C. The subscript “C” indicates the chemical reaction sample. The surfactant concentration and protonation degree are fixed at 100 mM and $X = 0.17$.

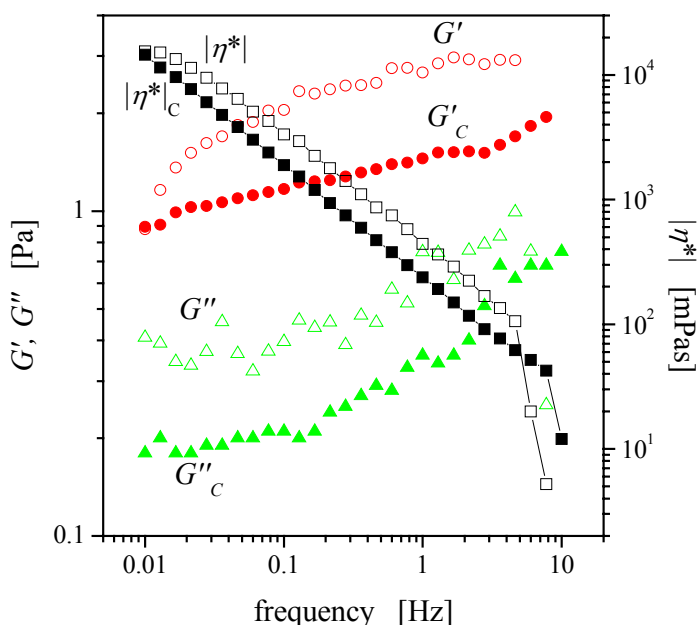


Figure 4.43. Dynamic rheological measurements for two solutions prepared by thermal treatment without shear (hollow symbols) and using the chemical reaction (filled symbols) at 25 °C. The subscription “C” indicates the chemical reaction sample. The surfactant concentration and protonation degree are fixed at 100 mM and $X = 0.17$.

measurements. Figure 4.42 shows the rheogram in the linear regime as a function of frequency. Apparently the rheogram is similar to that of the sheared sample in Figure 4.8, whereas the moduli, G' and G'' , and the complex viscosity $|\eta^*|$ decreases by a factor of 10 by removing pre-shear from the system. The viscoelasticity of the sample subject to the chemical reaction is surprisingly further lower than that of the heated, non-sheared sample (Figure 4.43).

The steady shear measurement in Figure 4.44 demonstrates that the applied shear induces to phase transitions from the bilayer structure (L_{ah}) to the unilamellar vesicle

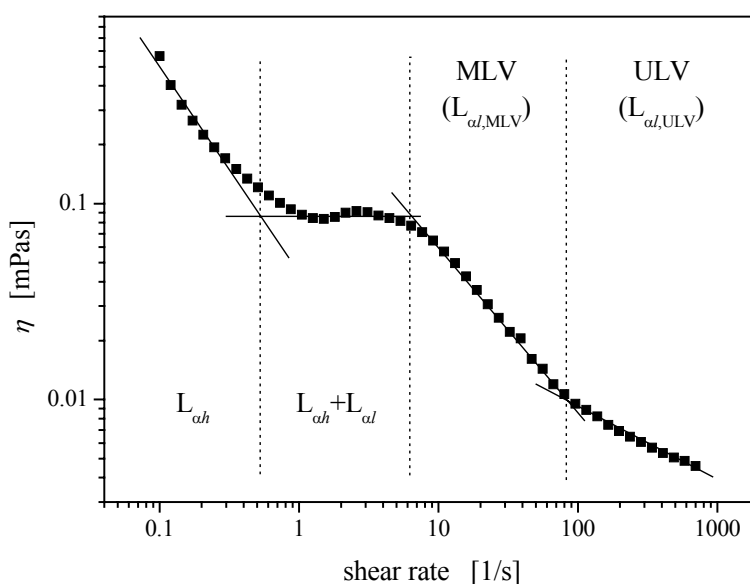


Figure 4.44. Steady shear measurement for the solution produced by using the chemical reaction at 25 °C. The surfactant concentration and protonation degree are fixed at 100 mM and $X = 0.17$. Each notation indicates as follows: L_{ah} - stacked lamellae, $L_{al,MLV}$ - multilamellar vesicle, $L_{al,ULV}$ - unilamellar vesicle.

(ULV, $L_{al,ULV}$) via the multilamellar vesicle (MLV, $L_{al,MLV}$) with increasing shear rate.¹⁸³ Their characteristic slopes of shear thinning manifest the phase transition points. Furthermore one can observe a plateau range between L_{ah} and $L_{al,MLV}$, which would be correspondent to the coexistence regime of their structures or transformation regime. It is found thus that the transition from L_{ah} and $L_{al,MLV}$ is of first-order.

Figure 4.45 represents the irreversible morphology transition in the non-linear regime. In this figure, one can divide into four regimes where different power laws hold: (1) the shear thinning with the slope = -0.866, (2) the viscosity plateau, (3) the shear thinning with the slope = -0.689, and (4) the shear thinning with the slope = -0.464. The first shear thinning in the first shear cycle can be principally due to the formation of ordered bilayer structures being aligned in the flow direction.^{185,186} The initial shear thinning is quite pronounced, which could be understood that the layers orient normal to the flow direction.¹⁸⁷ When shear rate exceeds a critical shear rate ~ 0.5 1/s, the plateau is observed. This could be explained by the fact that at this point some of the bilayers start to close themselves. However, the formation of vesicles would cause the shear thickening as referred to Ref. [183]. Again the shear thinning occurs at the shear rate = 3.4 1/s where most of the bilayers form the closed structure and behave in the same way as the L_{al} phase. For the first cycle, the measurement stopped at an intermediate shear rate and the shear rate was decreased down to the starting point. Upon reduction of the shear rate, no reversibility for the viscosity values is observed and the viscosity is about one order of magnitude larger than that of the non-sheared phase, suggesting that the vesicles formed once are quasi-stable. Then, when the shear rate increases again (second

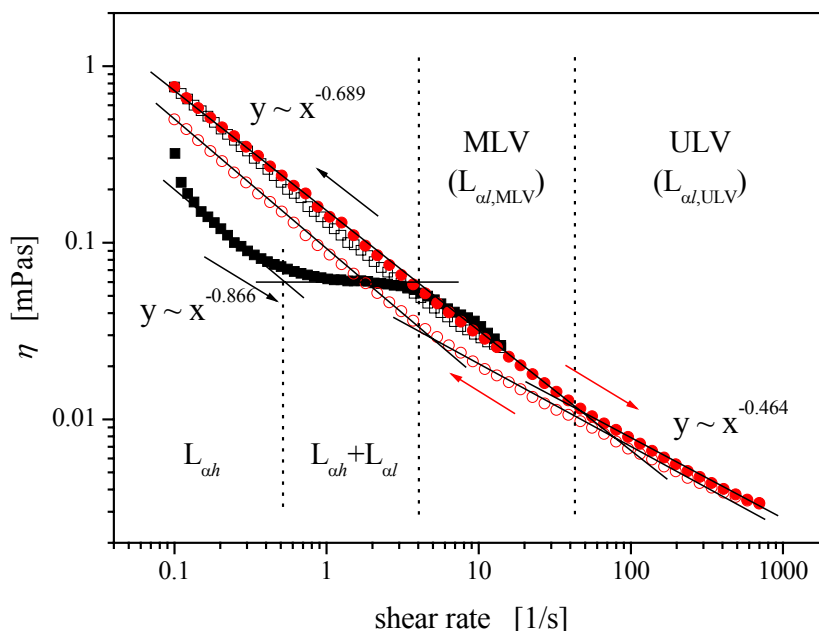


Figure 4.45. Shear history effect on the lamellar morphologies in $C_{12}C_8MAO/HCOOCH_3$ system at 25 °C. The surfactant concentration and protonation degree are fixed at 100 mM and $X = 0.17$. The square (\blacksquare, \square) and circle symbols (\bullet, \circ) represent respectively the first- and second-cycle of measurements. The solid and hollow symbols are in the shear up-stream and down-stream. Each notation indicates as follows: L_{ah} - stacked lamellae, $L_{al,MLV}$ - multilamellar vesicle, $L_{al,ULV}$ - unilamellar vesicle.

cycle), the viscosity decreases in the same way as the viscosity change with decreasing shear rate in the first cycle. The shear thinning in this regime would result from the deformation or rupture of vesicles. Further high shear rate causes another orientation corresponding to the unilamellar vesicle (ULV) as with the transformation observed in Figure 4.14. The transition point could be the breaking point of the straight lines with the different power laws at the shear rate ~ 50 1/s. The morphological transition however takes place in different manner: the transition from MLV to ULV seems to be of second-order. Since such a weak first-order transition may disappear under strongly shearing,⁸⁸ particularly in the non-linear regime, the steady shear measurement was repeated more carefully. Figure 4.46 shows the $\eta - \dot{\gamma}$ and $\sigma - \dot{\gamma}$ curves in the system same as above, where the time durations at each steady shear are prolonged up to 30 minutes. This figure clearly demonstrates that the MLV-ULV transition is of first-order while the coexistence region is narrowly limited. After the maximum shear rate in the second cycle (Figure 4.45), the viscosity profile was measured again with the decreased shear rate. The transition point from ULV to MLV is observed at a critical shear rate, so that the transition is reversible and it can be mentioned that the multilamellar vesicles are stable morphology at rest. However the breaking points between up- and down-streams of shear rate are inconsistent. From Figure 4.46, the MLV-ULV transition is of very weak first-order, hence, the inner energy of vesicles supplied by shearing could not be dissipated instantaneously even at less than the corresponding shear rate. As a consequence, the inconsistency between up- and down-streams of shear flow would appear.

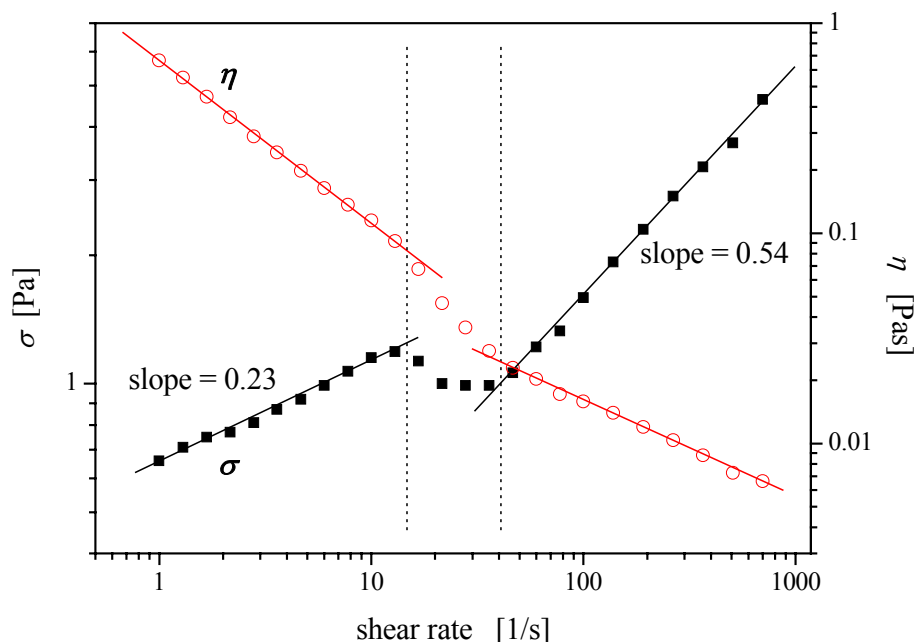


Figure 4.46. Changes in the shear stress σ (■) and the apparent viscosity η (○) with shear rate in $C_{12}C_8MAO/HCOOCH_3$ system at 25 °C. Each shear rate was retained for 30 minutes. The surfactant concentration and protonation degree are fixed at 100 mM and $X = 0.17$.

Chapter 5 C_xDMAO SYSTEM

EFFECT OF COUNTER-ION ON AGGREGATE STRUCTURE

5.1 AGGREGATE STRUCTURE AND ZERO-SHEAR VISCOSITY

5.1.1 C₁₄DMAO MICELLE

100 mM C₁₄DMAO aqueous solution consists of small micelles at 25 °C, and the small micelle is growing up with its concentration until 30 wt.%, at which the L₁ phase turns to the nematic phase and at further high concentration to the hexagonal phase.¹⁸⁸ The phase behavior would inform us that the micelle tends to elongate uniaxially with the concentration. X-ray measurements were performed for the series of different concentrations in the binary C₁₄DMAO/water system. The desmeared scattering intensities are shown in Figure 5.1. The scattering intensities are normalized by each concentration c and optical constant K . The optical constant K is calculated by the following equation.

$$K = N_A \left[\frac{n_e}{M_S} - \frac{v_S \rho_{0,e}}{N_A} \right]^2 \quad [5.1]$$

where N_A is the Avogadro number, n_e the electron number per molecule, M_S the monomolecular weight of surfactant, v_S the partial specific volume, and $\rho_{0,e}$ the electron density of solvent. From the scattering intensity at $q \rightarrow 0$, it appears that the molecular weight of micelle increases with concentration. The scattering intensities decay with a power law of -1, $I(q) \sim q^{-1}$, implying that the cylindrical particle is present in the binary

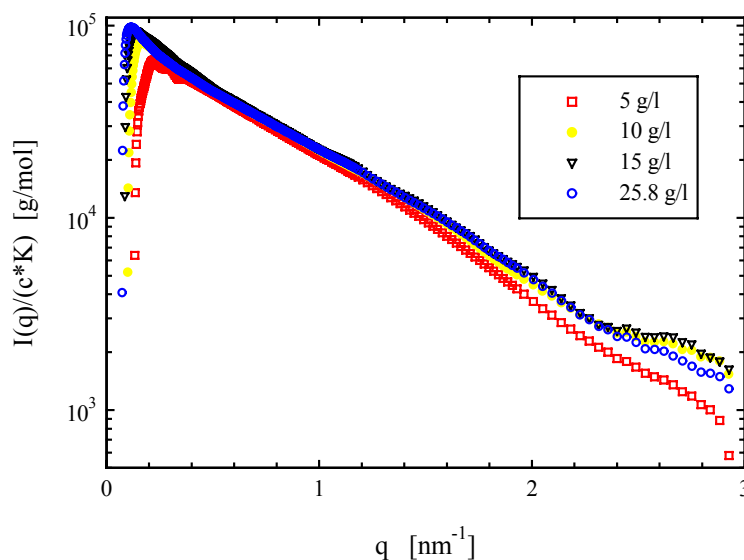


Figure 5.1. Desmeared scattering intensities normalized to concentrations and optical constant for the different concentrations in binary C₁₄DMAO/water system.

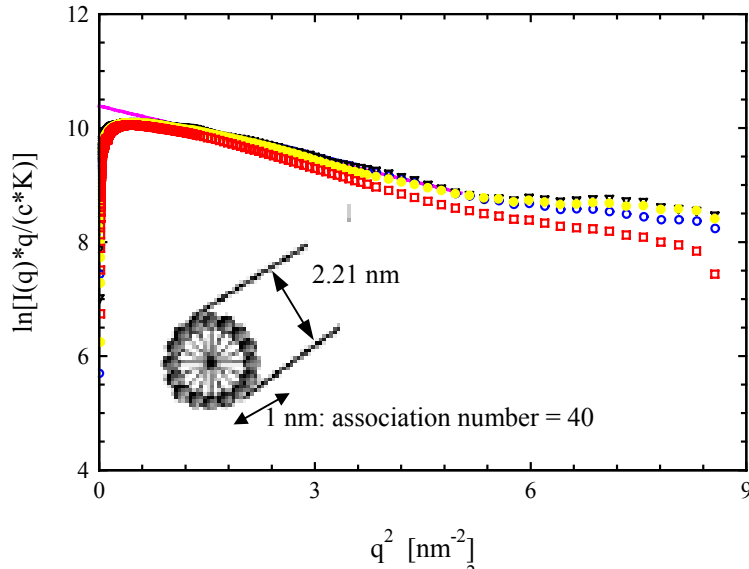


Figure 5.2. Plots of $\ln[I(q)*q/(c*K)]$ versus q^2 . The slope and the slice give the radius of gyration R_G and the molecular weight per unit length M_L .

system. In Figure 5.2, $\ln[I(q)*q/(c*K)]$ is plotted against q^2 . This plot allows for calculations of the the cylinder radius r_c and the molecular weight per unit length M_L .

$$I(q) = \frac{M_L}{q} \pi c K \exp\left[-\frac{R_G^2 q^2}{2}\right]^2 \quad [5.2]$$

R_G is radius of gyration for cross-section, gives r_c by $r_c = \sqrt{2}*R_G$. The molecular weight per unit length (nm) is 10459 g/(mol.nm) and radius of gyration in cross-section is 0.78 nm, *i.e.*, geometrical diameter in cross-section is 2.21 nm. The molecular weight corresponds to 40 association number per nanometer, which value shows no concentration dependence. According to the Guinier law,¹³⁷ furthermore, the length of the cylinder (L_c) can be calculated by using r_c and radius of gyration ($R_{G,L}$) for the length L_c ,

$$R_{G,L}^2 = (r_c^2/2) + (L_c^2/12) \quad [5.3]$$

The computed length L_c is about 11 nm, which agrees well with data obtained by the neutron scattering method.¹⁸⁹

Figure 5.3 gives the semilogarithmic plot of population against the hydrodynamic radius R_H measured by the dynamic light scattering. The average diameter is 6.45 nm and fairly monodisperse, which is comparable to the reported value.¹⁹⁰

The C₁₄DMAO micellar solution at 100 mM has interaction of inter-aggregate to some extent, while the solution behaves like a Newtonian fluid

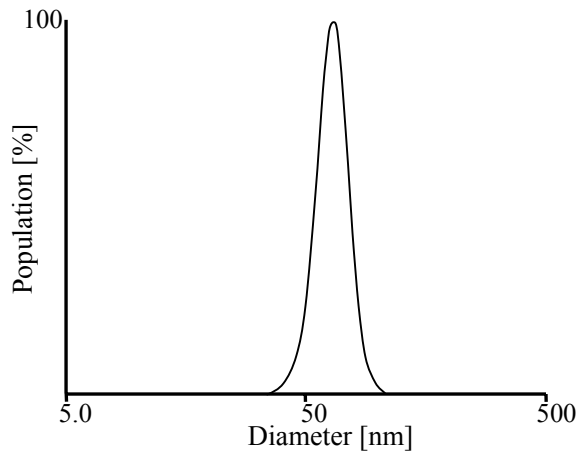


Figure 5.3. Hydrodynamic radius and its polydispersity in 100 mM C₁₄DMAO/water system at 25 °C.

(Figure 5.4). The viscosity η remains constant with shear rate $\dot{\gamma}$, and the stress σ increases proportional to $\dot{\gamma}$. The change in the zero-shear viscosity η_0 is plotted as a function of the C₁₄DMAO concentration (C_s) in Figure 5.5. It can be seen that η_0 begins to increase dramatically at $C_s \sim 200$ mM, which often refers to the onset of entanglement of wormlike micelles. And the power law of the slope is $\eta_0 \propto C_s^{-5.22 \pm 0.6}$.

Table 5.1. Various scales of cylindrical micelle formed in 100 mM C₁₄DMAO/water system.

R_G [nm]	r_c [nm]	L_c [nm]	R_H [nm]
0.78	1.105	~11	3.225

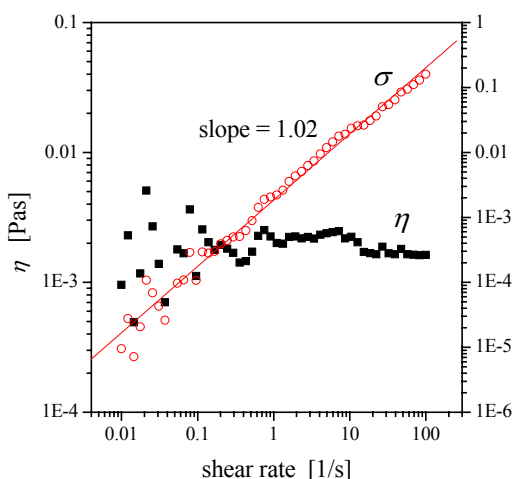


Figure 5.4. Steady shear measurement in 100 mM C₁₄DMAO/water system at 25 °C. The viscosity η and the stress σ are plotted as a function of shear rate.

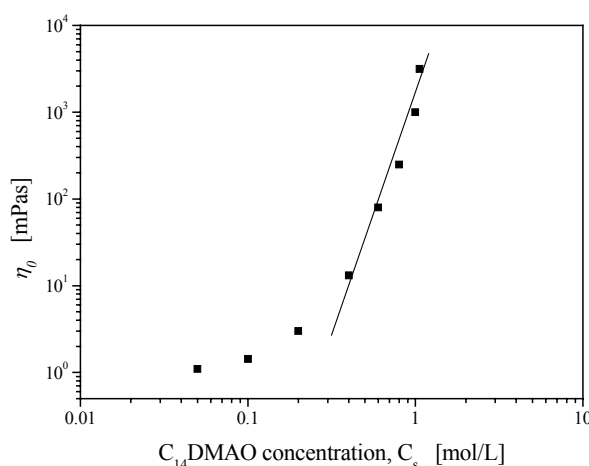


Figure 5.5. Change in the zero-shear viscosity η_0 with the C₁₄DMAO concentration at 25 °C.

5.1.2 PROTONATION OF C₁₄DMAO

5.1.2.1 MICELLAR PHASE

As interpreted in Chapter 4, the double-chain aminoxide surfactant shows synergism upon addition of HCl, meaning that the two homologue surfactants interact each other. Even in the single-chain aminoxide surfactant systems, the effect accompanied with protonation had been documented over a few decades. Firstly, monovalence counter-ion systems are tackled using the rheological measurement. Figure 5.6 shows the plots of η_0 versus protonation degree X in the different acids systems; (a) HCl and formic acid (HCOOH), (b) nitric acid (HNO₃) and bromic acid (HBr), (c) trifluoroacetic acid (CF₃COOH). The pK_a 's of every acid are sufficiently low (see Table 3.2), therefore the acids are to protonate completely the aminoxide group. The viscosity, as a result, would be attributed to their ion-pairs. The counter-ions Cl⁻ and HCOO⁻ has apparently no effect on η_0 , even η_0 decreases with protonation. In the case of Br⁻ and NO₃⁻, on the other hand, η_0 steeply increases with X and decreases passing through their maximums at around half-protonation of C₁₄DMAO. The changes in η_0 are typical synergistic effects. It is of interest that the shear thickening appears in the Br⁻ and NO₃⁻ systems, and the phenomena become remarkable with increasing protonation degree (Figure 5.7). The shear thickening have been observed in several surfactant systems, of

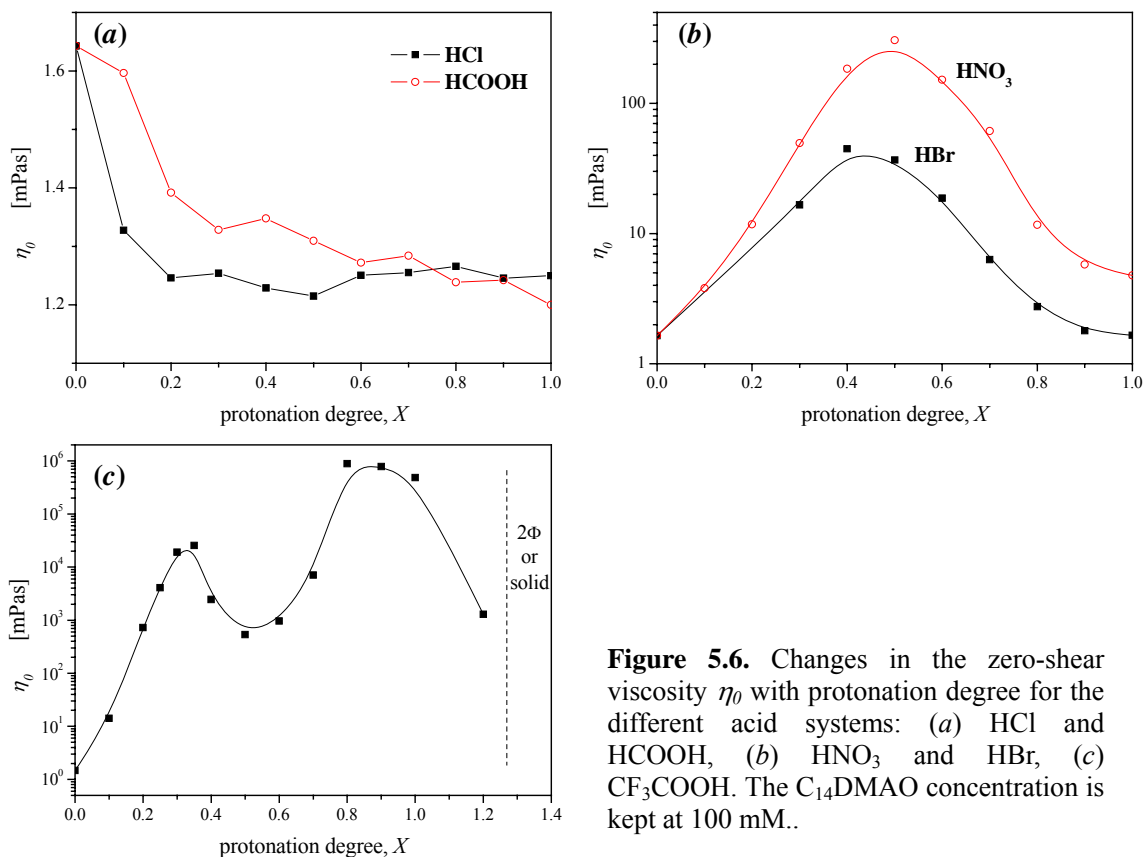


Figure 5.6. Changes in the zero-shear viscosity η_0 with protonation degree for the different acid systems: (a) HCl and HCOOH, (b) HNO₃ and HBr, (c) CF₃COOH. The C₁₄DMAO concentration is kept at 100 mM..

which most encountered in the intermediate range of surfactant concentration where the micelles start growing up.¹⁹¹⁻¹⁹³ Hoffmann *et al.* proposed a model that the shear flow induced necklace-type structures of small rods.⁸⁵ And Hu *et al.* examined the effect of NaSal concentration on the shear thickening in CTAB solution, concluded then that the increase in NaSal/CTAB ratio up to unity prolongs the micellar lifetime.¹⁹⁴ The bromide and nitrate ions stand between the Hofmeister series, and it is conceivable that the shear thickening is the sign that these counter-ions are more hydrophobic than Cl⁻ and HCOO⁻

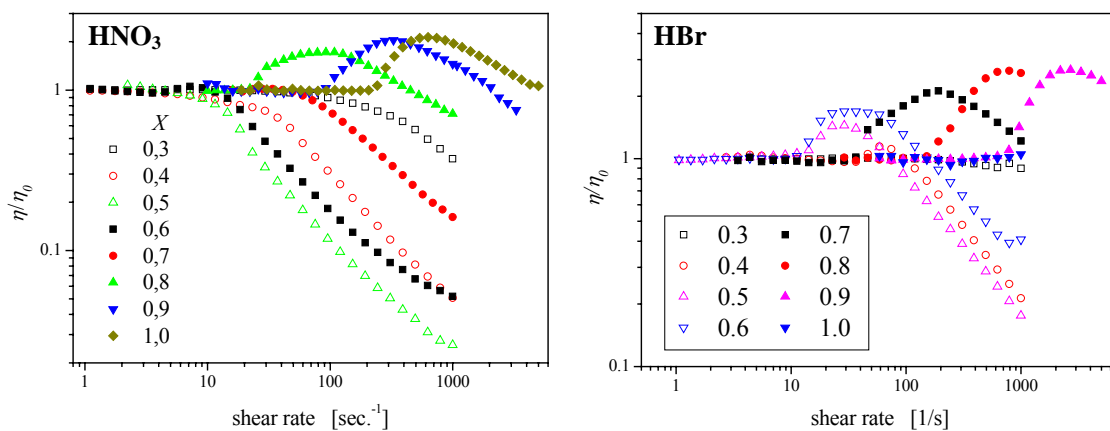


Figure 5.7. Normalized shear viscosity (η/η_0) as a function of shear rate for different protonation ratios (X) in HNO₃ (left) and HBr (right) systems at 25 °C.

, while less than SCN^- and ClO_4^- as will be shown in the next section. In the CF_3COOH system, the rheological behavior is complicated: there are two maximums in the measuring X range, and a minimum is observable at $X = 0.5$. Here I exclude the CF_3COOH system due to its complexity, while it will be discussed later with complementary experiments.

Table 5.2. pK_a values of Oxalic acid and Tartaric acid.

	pK_{a1}	pK_{a2}
Oxalic	1.23	4.19
Tartaric	2.98	4.34

Figure 5.8 shows the changes in η_0 with protonation degree in the di- and tri-valence acids systems, sulfuric acid (H_2SO_4), oxalic acid, tartaric acid, tartronic acid, and phosphoric acid (H_3PO_4). H_2SO_4 , oxalic acid, tartaric acid, and tartronic acid should act as di-valence acid in 100 mM C_{14}DMAO aqueous solution because their pK_a values are lower than that of C_{14}DMAO solution (~ 6), while H_3PO_4 would not dissociate completely and should act as mono-valence acid (Table 3.2 and 5.2). Thus, X indicates the different amounts of acids in these systems: $X = 1$ corresponds to $[\text{H}_2\text{SO}_4] = [\text{oxalic}$

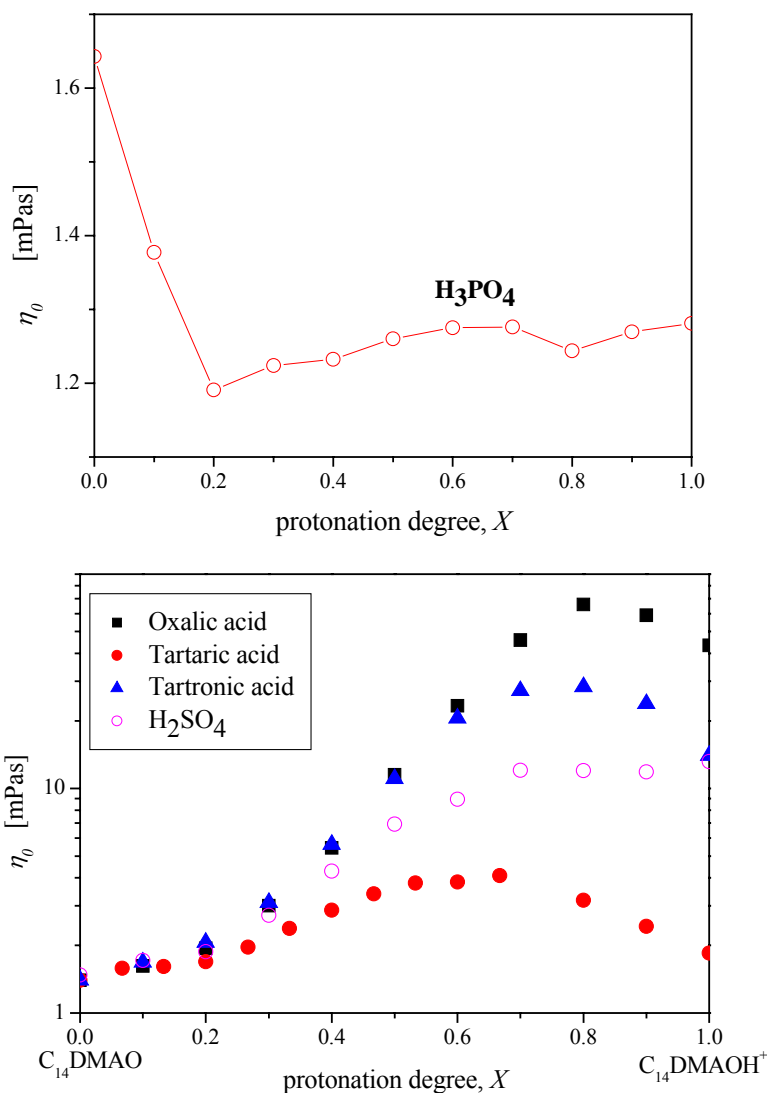


Figure 5.8. Changes in the zero-shear viscosity η_0 with protonation degree for the different acid systems: H_3PO_4 (top), Oxalic acid, Tartaric acid, Tartronic acid, H_2SO_4 (bottom). The C_{14}DMAO concentration is kept at 100 mM..

acid] = [tartaric acid] = [tartronic acid] = 50 mM, [H₃PO₄] = 100 mM. The di-valence acid should attract with two oppositely charged surfactant head groups. The electrostatic interaction may bind two molecules strongly rather than the peculiar hydrogen bonding between two head groups, such as di-valence cationic counter-ion Ca²⁺.¹⁹⁵ However, in the present case, the expectation seems not to work out remarkably, and it is likely that the monotonic increase in η_0 would arise from condensation of counter-ion onto the micelle surface. Unlikely H₂SO₄, H₃PO₄ does not affect the aggregate structure as well as HCl and HCOOH. Thus SO₄²⁻ ion may act as the more lyotropic ion than HPO₄²⁻ and even Cl⁻ in view of the rheological measurements, suggesting that this rheological behavior or the system itself might not obey the Hofmeister order. On the contrary, the H₂PO₄⁻ ion seems to stand properly in the Hofmeister series. The organic acids furthermore exhibit the different viscosity curves. The curves have their own maximums unlikely H₂SO₄, and the protonation degree at which the maximums locate are much higher than those in the HNO₃ and HBr systems. The pK_{a1} values of oxalic acid and tartaric acid are similar to that of formic acid, while their viscosity changes are definitively distinct. This would be due to effects of another carboxylic group. If so, the di-valence effect referring to Ca²⁺ is more efficiently operative in comparison to SO₄²⁻ because of their weak hydration.

5.1.2.2 FORMATION OF LAMELLAR PHASE

Figure 5.9 shows the phase diagram in C₁₄DMAO/perchloric acid (HClO₄) system. It is known that the ClO₄⁻ ion takes an extreme standing in the Hofmeister series.¹⁹⁶ It can most effectively shield positive charges. It was, however, very surprising to realize that the micellar phase (L₁) of C₁₄DMAO is already transformed into the single L _{α} phase at $X = 0.25$, that means that only one HClO₄ molecule is necessary to

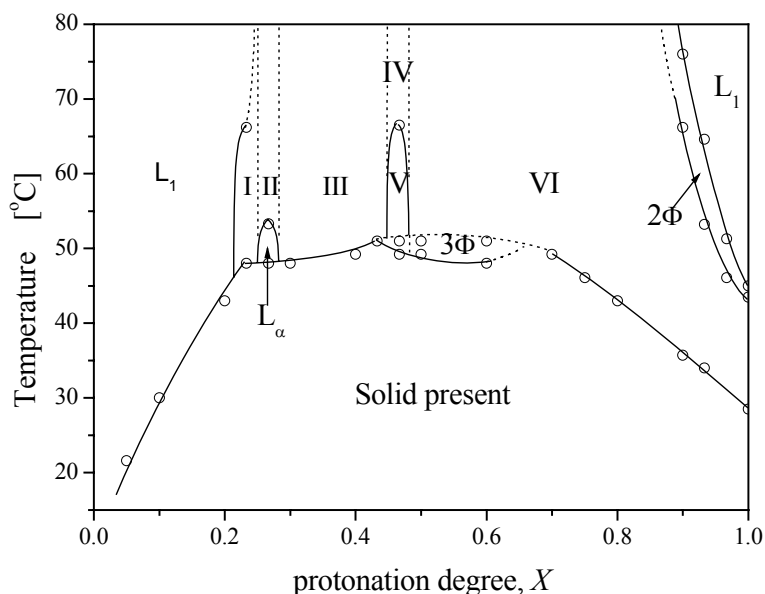


Figure 5.9. Phase diagram of water/C₁₄DMAO/HClO₄ system. The C₁₄DMAO concentration is kept at 100 mM. Notations represents as follows: L₁-micellar solution, L _{α} -single lamellar phase, 2 Φ -two phase, 3 Φ -three phase, I-L _{α} /L₁, II and III-L _{α} present (turbid), IV-L _{α} present (weak birefringence), V-L _{α} present (separated two-phase), VI-L _{α} present (turbid).

transform four C₁₄DMAO molecules from the micellar state to the bilayer state. This clearly demonstrates that the ClO₄⁻ ions have an ordering effect that extends much further than the geometrical size. However, the complete protonation leads to again L₁ phase.

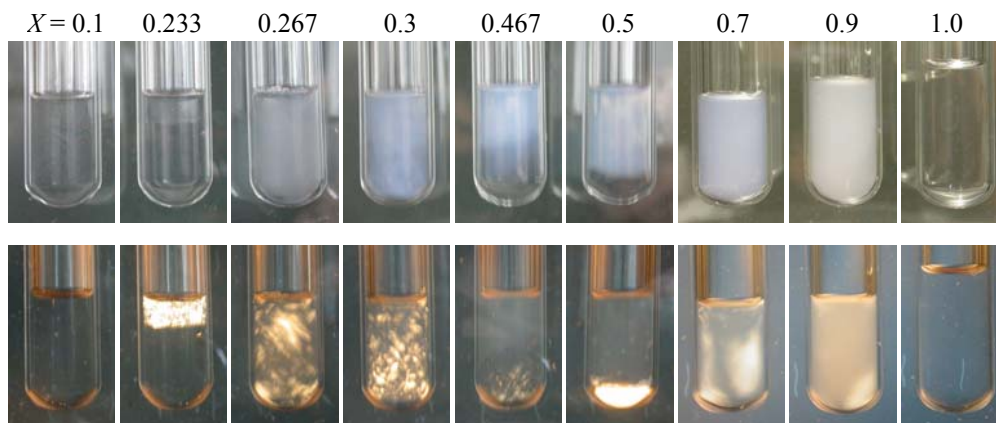


Figure 5.10. Samples of the system C₁₄DMAO/HClO₄ (Figure 5.9) with different protonation degrees in between and without polarizers.

Some pictures belonging to each phase are shown in Figure 5.10. The appearance varies with protonation degree in the L_α region: the L_α phase with strong birefringence changes to another L_α phase which are weakly birefringent and translucent. This implies that the morphology of lamellae transforms from stacked bilayer to small unilamellar vesicle with increasing charge density. It could be that the turbidity of the samples at higher X in the L_α region is due to the fact that the surfactant volume fraction is not large enough to be in the single L_α region. The phase behavior manifest thus that the synergistic effect appears definitively. And the solubility curve would suggest the unusual synergistic effect which contradicts to the eutectic phenomenon in mixture systems. In general, the melting point should be reduced by adding impurity to the pure component due to decreasing chemical potential of its solid state. This, however, is not

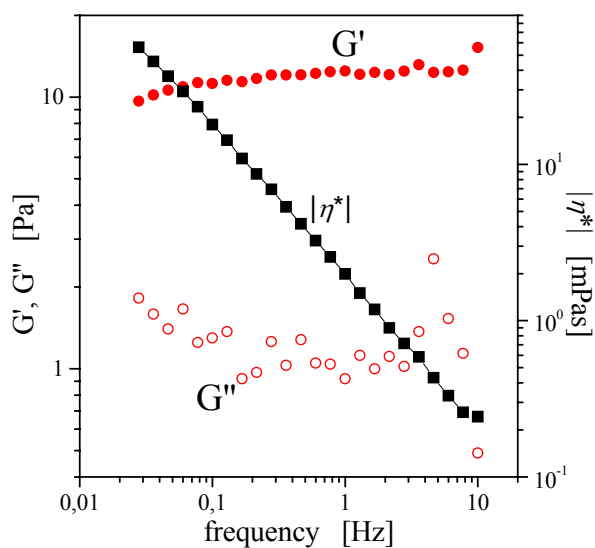


Figure 5.11. Dynamic rheograms for the L_α phase at X = 0.467 in HClO₄/C₁₄DMAO system at 60 °C. The surfactant concentration is kept at 100 mM. The symbols represent the storage modulus (●, G'), the loss modulus (○, G''), and the complex viscosity (■, |η*|).

the case in the present system. The uncommon behavior may be able to be interpreted by the mutual interaction between the protonated and non-protonated species. It is thus likely that the hydrogen bonding leads to the closely packing of the chemically different molecules in solid state.¹⁹⁷

Intuitively one would assume that increasing the charge density on the tetrahedral ClO₄⁻ ion should even better shield the charge density of the positively charged micellar structure. However, this is not the case as becomes obvious when the ClO₄⁻ ions are replaced by SO₄²⁻ ions which introduce the low viscous L₁ phase (Figure 5.7). This counter-ion properly follows the Hofmeister series rather than the charge density.

The L_α phase has viscoelasticity which implies formation of the vesicles: G' is higher by a factor of 10 than G'' and both moduli are independent on frequency (Figure 11). Figure 5.12 shows the changes in the zero-shear viscosity η_0 in the L₁ phase and the

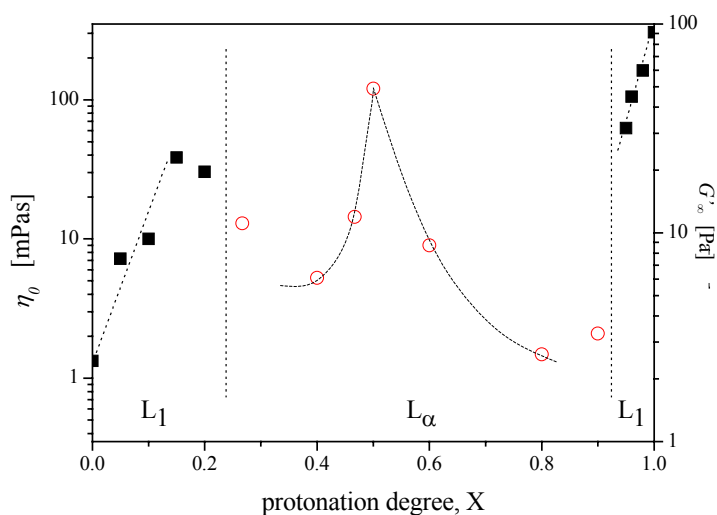


Figure 5.12. Plots of rheological parameters, zero shear viscosity η_0 (■) and shear modulus G'_∞ (○), with protonation degree in C₁₄DMAO/HClO₄ system at 60 °C. The surfactant concentration is 100 mM.

plateau modulus G'_∞ in the L_α phase as a function of protonation degree at 60 °C. In the L₁ phase at low X , η_0 increases monotonically with X and the L₁ phase transforms to the L_α phase. In the L_α phase, the zero-shear viscosity could not be observed: η_0 still increases as $\dot{\gamma} \rightarrow 0$ or $f \rightarrow 0$. Instead the plateau modulus is plotted against X . G'_∞ shows a maximum at the half protonation of C₁₄DMAO. The maximum at $X = 0.5$ cannot be described with any proper explanation because of the different L_α morphologies at these protonation degrees as expected from macroscopic observation in Figure 5.9. However, one can see a significant synergistic effect on the shear modulus. After the transition L_α → L₁, the viscosity is further rising up with protonation. This suggests that the system is still somewhat stabilized by hydrogen bonding.

Figure 5.13 demonstrates the photographs for a series of solutions at different protonation degrees in thiocyanic acid (HSCN)/C₁₄DMAO system at 25 °C. The series also produce the birefringent L_α phase, and the SCN⁻ ion locates on the right-hand side (lyotropic acid) in the Hofmeister series. The conventional lyotropic counter-ion, salicylate (Sal⁻), was verified as well. The counter-ion often induces micelle growth because of its strong condensation on the micelle surface. As a consequence, the Sal⁻ ions intensively shield the surface charge as with ClO₄⁻. In Figure 5.14, the phase sequence having their pictures is demonstrated at 25 °C. The phase sequence is

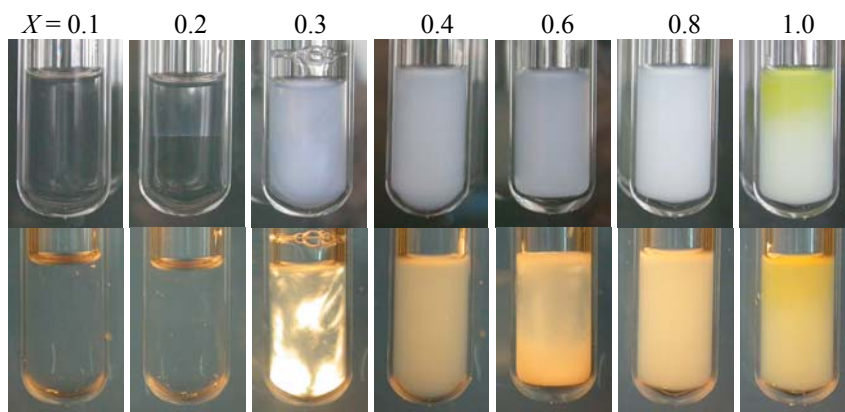


Figure 5.13. Photographs for the samples in HSCN/C₁₄DMAO system at 25 °C. The surfactant concentration is kept at 100 mM.

somehow similar to those in the HClO₄ system: the L_α phase is formed around $X = 0.25$, and brightness of birefringence is dependent on protonation degree in the L_α phase. The samples in the two-phase (2Φ) between the L₁ and L_α phases shows much noticeable birefringence, while their rheograms and SAXS spectra are indicative to be two phases present (Figure 5.15 and 5.16). In comparison to the single L_α phase, the rheogram in 2Φ shows the frequency-dependence of G' and G'' , and their variation cannot be explained by using any models proposed to date. The SAXS spectrum furthermore clarifies the presence of another aggregate structure besides of the L_α phase: the peaks (q_1, q_2) correlate to the Bragg reflection of bilayer, while the broadened peak (q_3) cannot accord to the Bragg sequence. The significant broadened peak could be attributed to the neighboring L₁ phase. The rheological parameters (η_0 , G'_{∞} , and yield stress (σ_y)) are plotted with protonation degree in Figure 5.17. The viscosity dramatically increases by a factor of 10³ with X in the L₁ region and decreases a bit beyond a maximum before the phase transition to 2Φ. In the 2Φ region, η_0 increases again with protonation, and the

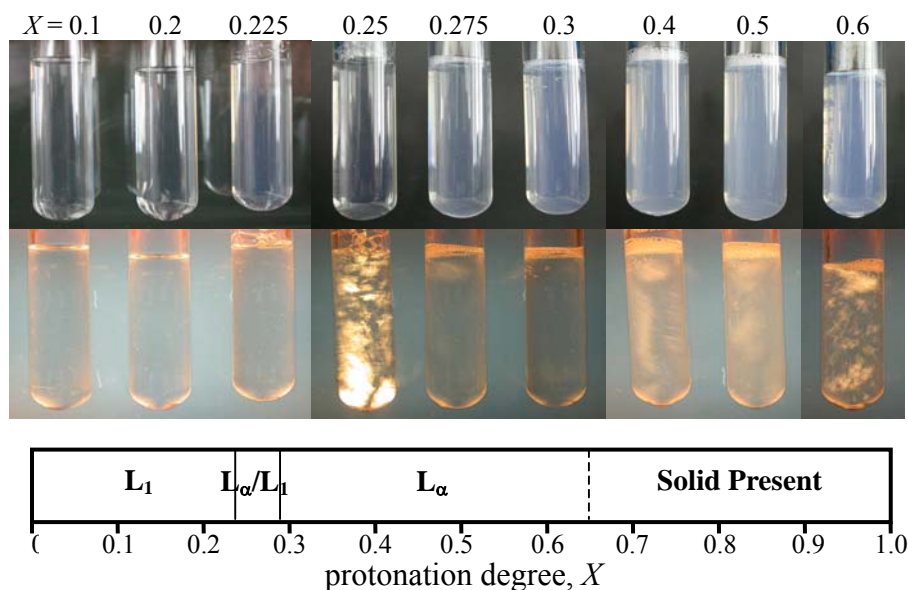


Figure 5.14. Phase sequence and the sample appearances corresponding X in HSal/C₁₄DMAO system at 25 °C. The surfactant concentration is kept at 100 mM.

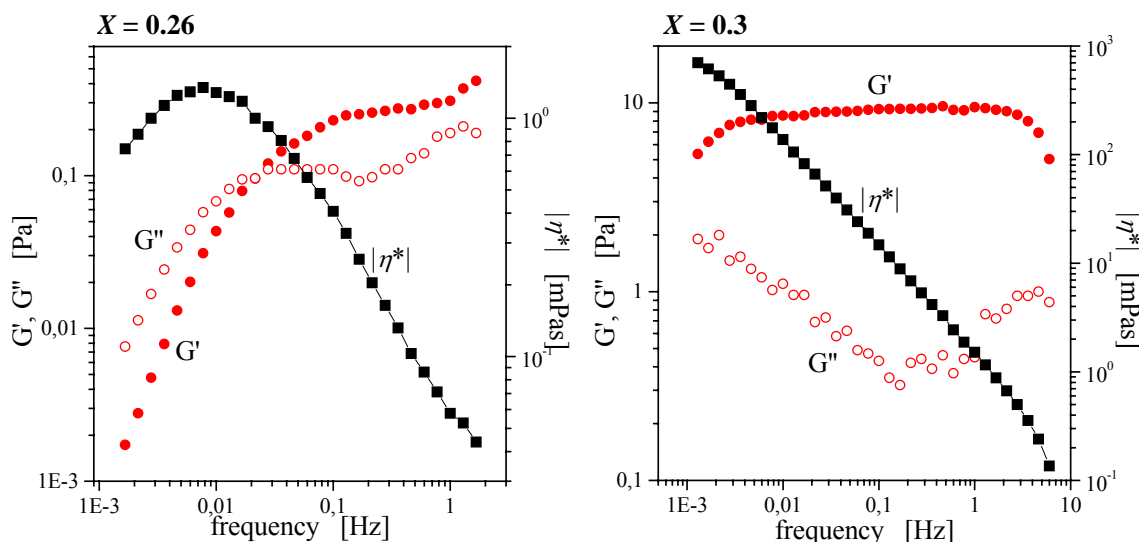


Figure 5.15. Rheograms for the sample at $X = 0.26$ (2Φ , strong birefringence) and 0.3 (L_α) in HSal/ C_{14} DMAO system at 25°C . The surfactant concentration is kept at 100 mM .

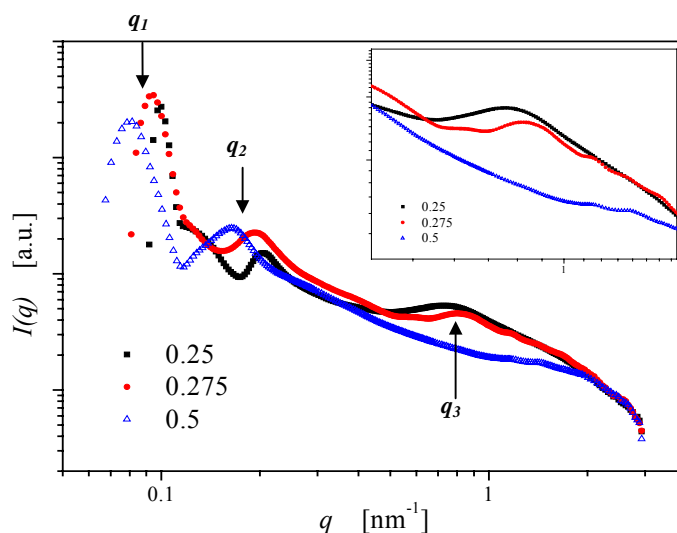


Figure 5.16. SAXS spectra at different proto-nation degree, $X = 0.25$ (2Φ , \blacksquare), 0.275 (2Φ , \bullet) and 0.5 (L_α , Δ), in HSal/ C_{14} DMAO system. The surfactant concentration is kept at 100 mM .

plateau modulus G'_∞ and the yield stress σ_y come to appear. Then G'_∞ and σ_y give rise continuously up to the phase boundary of 2Φ - L_α and become independent on the charge density. The highly elastic property supposes the vesicle formation, and the less birefringence could be due to the unilamellar vesicle present. It should be noted that the solubility of the mixture of C_{14} DMAO/ C_{14} DMAOH⁺Sal⁻ in aqueous medium rises up with increasing amount of C_{14} DMAO, that is incompatible with the phase behavior in the HClO₄ system (Figure 5.9). The bulky head group may interrupt the more ordered structure in solid state such as cholesterol surfactants¹⁹⁸ and benzyl surfactants.¹⁹⁹

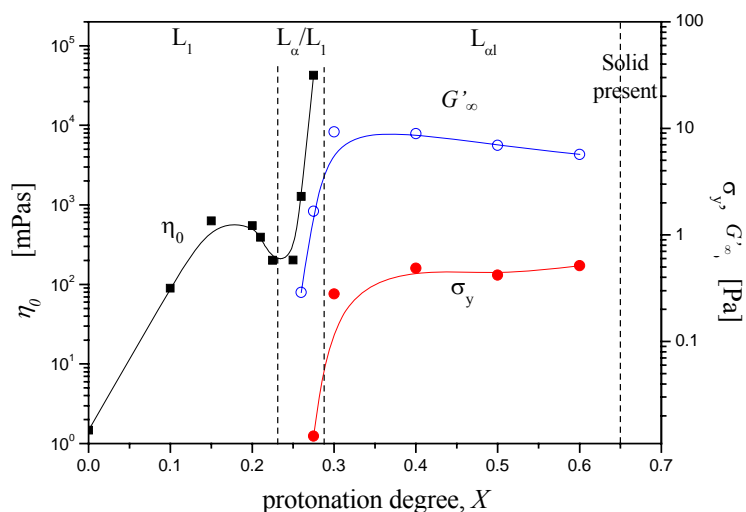


Figure 5.17. Changes in rheological parameters, zero-shear viscosity (η_0 , ■), plateau modulus (G'_{∞} , ○) and yield stress (σ_y , ●), as a function of protonation degree X in HSal/C₁₄DMAO system. The surfactant concentration is kept at 100 mM.

5.1.2.3 HYDRATION AND VISCOELASTICITY

In order to explain the above results more clearly, two factors, acidity and hydration of ion-pair, should be focused on. In Figure 5.18 the maximum η_0 and the corresponding X are plotted as functions of respective hydration free energy ΔG_{hyd} and pK_a for some of the acids. The unknown hydration free energies such as organic acids were estimated by the following equation:

$$\Delta G_{hyd} = n \cdot \Delta G_{hyd}(\text{COOH}) + m \cdot \Delta G_{hyd}(\text{OH}) + l \cdot \Delta G_{hyd}(\text{CH}) \quad [5.4]$$

n , m , and l are the numbers of carboxyl group, hydroxyl group, and methylene group in the molecule. $\Delta G_{hyd}(\text{COOH})$, $\Delta G_{hyd}(\text{OH})$, and $\Delta G_{hyd}(\text{CH})$ are the molar hydration free energies of these functional groups. $\Delta G_{hyd}(\text{COOH})$ refers to that of formic acid, -382 kJ/mol because its hydration energy seems to be mainly attributed to the hydrophilic functional group. $\Delta G_{hyd}(\text{OH})$ and $\Delta G_{hyd}(\text{CH})$ then correspond to -25.95 and -1.06 kJ/mol, respectively.²⁰⁰ According to Eq. [5.4], ΔG_{hyd} values for each organic acids are given as follows: -764 kJ/mol for oxalic acid, -818.02 kJ/mol for tartaric acid, -791.01 kJ/mol for tartronic acid.

It seems that the pK_a values have no correlation with the locations of protonation degrees at their maximum viscosities. In this figure, the second pK_a for the divalence acids is adopted, while it is certainly unambiguous whether the usage of pK_{a2} can be properly compared with other monovalence acids because of their incomplete dissociation in the range of acidic pH. An annoying issue in evaluating protonation degree in the present study is that the proton dissociation constant K_{AO} of aminoxide micelle is not constant but increases with X . One may expect that pK_{AO} changes from about 6.0 for $X = 0$ to about 3.5 for X greater than 0.9 on the basis of the titration curve for C₁₄DMAO in water.⁹² It seems that protonation of aminoxide by the second carboxyl group of dicarboxylic acids is not easy in the range of high degree of ionization. It can be mentioned therefore that the protonation degrees corresponding to the viscosity maxima for the carboxylic acids are significantly smaller than the corresponding X values shown in Figure 5.8.

On the other hand, one can see some linear relationships between the hydration free energy and the maximum viscosity, which seems to be classified into two groups. The figure manifests that the maximum viscosity can be well interpreted for the series

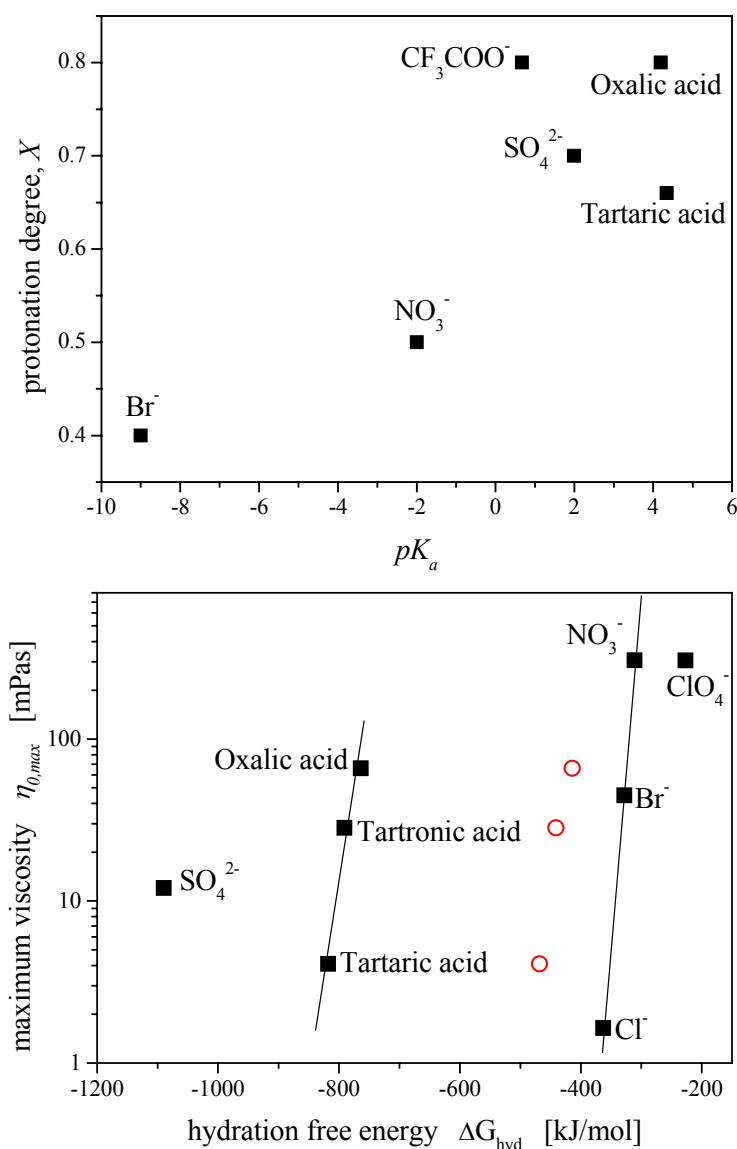


Figure 5.18. Plots of pK_a vs. protonation degree at the corresponding maximum viscosity (left), and hydration free energy ΔG_{hyd} vs. maximum viscosity $\eta_{0,max}$ (right). The hydration free energies of each dicarboxylic acid were calculated by different formula for monovalent (○) and divalent forms (■).

of monovalence anions solely by the hydration free energy. Recently, importance of dispersion force in the phenomena related to the lyotropic series has been reported by Ninham and Yaminsky²⁰¹ and the theory has explained the negative adsorption of ions at air/water interface, though with a reservation about the sign of the surface potential²⁰². However, this theory involves the ion valency and cannot interpret the effect of ion radius, that is, hydration energy on the dispersion force. And the other recent paper showed that addition of $MgClO_4$, $NaClO_4$, Na_2SO_4 had no influence on the rotational dynamics of water molecules outside the first solvation shells of the ions²⁰³. The water structure however would be destroyed or made up predominantly by hydration feature outside the first shell covering the ion. Here it is evident from the results that the hydration free energy manipulates the effect of ion on the viscosity. As well, the

divalence anions except for SO_4^{2-} show that the viscosity changes straightforwardly with ΔG_{hyd} . This seems to be due to their analogous chemical structures. It would be considered that the exception, SO_4^{2-} , must not be included in the series of the dicarboxylic acids because of their distinct acidities. As described above, the second carboxyl group may not be dissociated at high X due to the presence of aminoxide surfactant, as a consequence, the acids behave like a monovalence acid even at their protonation degrees corresponding to the viscosity maxima. If so, the plots for the dicarboxylic acids shift toward the higher ΔG_{hyd} . The recalculated ΔG_{hyd} values are -414.21 kJ/mol for oxalic acid, -468.23 kJ/mol for tartaric acid, -441.22 kJ/mol for tartronic acid, that are plotted (\circ) in Figure 5.18. Even if the extreme case is taken, it appears that the dicarboxylic acids are not in the same order as the monovalent acids. Regarding the deviate $\Delta(\Delta G_{\text{hyd}})$ between the series of monovalent acids and the dicarboxylic acids, the electrostatic force in the mutual interaction between micelles and counter-ions mainly would be attributed within the framework of Gouy-Chapman diffuse double layer model. It is evident according to the Schulz-Hardy rule that the divalent ion is superior to the monovalent one in terms of adsorption onto the micelle surface. This would preferably restrain diffusion of ions, namely, result in less hydrophilicity of counter-ion.

The sulfate ion, however, clearly differs from the situations of organic counter-ions. The low pK_{a2} indicates that HSO_4^- dissociates into H^+ and SO_4^{2-} in the entire protonation range. As well as the dicarboxylic acids, indeed, the dominant electrostatic interaction can be considered, but SO_4^{2-} seems to be isolated from any other ions in the $\eta_{0,\text{max}}-\Delta G_{\text{hyd}}$ map (Figure 5.18). It would be necessary for the viscosity evolution in the SO_4^{2-} system to be reviewed in comparison to the other systems, in order to interpret the SO_4^{2-} location in the map. NO_3^- ion could be reasonable to do it because of their structural resemblance. As seen in Figure 5.6 and 5.8, the η_0 changes are totally different: for the NO_3^- system the pronounced maximum lies at the half protonation of C_{14}DMAO and η_0 symmetrically decreases with either increasing or decreasing X , while addition of SO_4^{2-} monotonically gives rise to η_0 . When the absolute η_0 values at different X 's are compared, NO_3^- is greater than SO_4^{2-} at $X = 0.5$, and vice versa at $X = 1.0$. At high protonation degree the electrostatic contribution is thus expected to outweigh other conceivable effects on η_0 : (1) the dispersion force in the interaction between micelles and counter-ions, (2) hydrophilicity of counter-ions, and (3) entropy change of counter-ions accompanying the adsorption onto micelles. At $X = 0.5$, on the other hand, the electric term is considered not to be effective much as the other contributions. The dispersion interaction is more repulsive for sulfate than nitrate since the dielectric constant of micelle core ($\epsilon_m = 2$) is much lower than that of water ($\epsilon_w = 78.5$).¹⁶ The hydrophilicity is taken as the free energy of hydration ΔG_{hyd} , 1090 kJ/mol for SO_4^{2-} and 311 kJ/mol for NO_3^- . Thus the two factors (1) and (2) favor nitrate rather than sulfate. Factor (3) is specific to the solution of no added salt. Chemical potential of counter-ions is expressed as a function of the concentration. Since the number of sulfate ions is half of that of nitrate ions at a given value of X , the entropy difference would be estimated as $RT \ln 2 \sim 17$ kJ/mol. This effect will give a small contribution. In summary, the viscosity maximums originate from the different driving forces for NO_3^- and SO_4^{2-} , and it can be considered therefore that SO_4^{2-} ion would be excluded largely from the series of hydration energies of the anions.

The above description would favor to explain the divalent anion characteristics

from the principal viewpoint of the electrostatic interaction between micelles and counter-ions. Although the essential electrostatic contribution had been rationalized herewith for the divalent ions, there is still a doubt on the sequence of the four divalent anions, *i.e.* discrimination of sulfate from the dicarboxylic anions. As for these anions, the dispersion force and hydrophilicity would be main factors, and here one should carefully verify ionic atmosphere surrounding micelles. The ideal situation permits all the theoretical treatments including thermodynamics and quantum mechanics, and it is then likely that the viscosity maximum can be determined by water affinity of counter-ion. On the other hand, non-ideality often arises from the finite volume of ion. SO₄²⁻ ion has a small hydration radius (~ 0.230 nm) compared to the other divalent anions. With a hypothesis of incompressibility, one can formulate additivity of volumes of each functional group as follows.

$$V_t = m \cdot V(\text{CHOH}) + n \cdot V(\text{COOH}) \quad [5.5]$$

where V_t is volume per molecule, $V(\text{CHOH})$ and $V(\text{COOH})$ the volumes of the corresponding functional groups, and m and n the numbers of CHOH and COOH in a molecule, respectively. The volumes per molecule for each dicarboxylic acid are summarized in Table 5.3. Supposing that the molecule is spherical form in aqueous

Table 5.3. Volumes (V_t), radii (r), cross-sectional areas (S) for dicarboxylic anions.

	V_t nm ³	r nm	S nm ²
Oxalate	0.0690	0.254	0.203
Tartarate	0.0866	0.274	0.237
Tartronate	0.0778	0.265	0.220

medium, the effective radius and cross-sectional area can be computed. The effective area of sulfate ion is 0.166 nm², which is further smaller than those of the dicarboxylic acids (Table 5.3). The nonionic C₁₄DMAO molecules are closely associated in micellar form at a given concentration, the head group area occupied per molecule is approximately 0.17 nm² given by the SAXS measurement. The other monovalent anions have compatible sizes with sulfate, or even smaller. Therefore the smaller anions can be distributed somehow ideally within the double layer according to the Poisson-Boltzmann

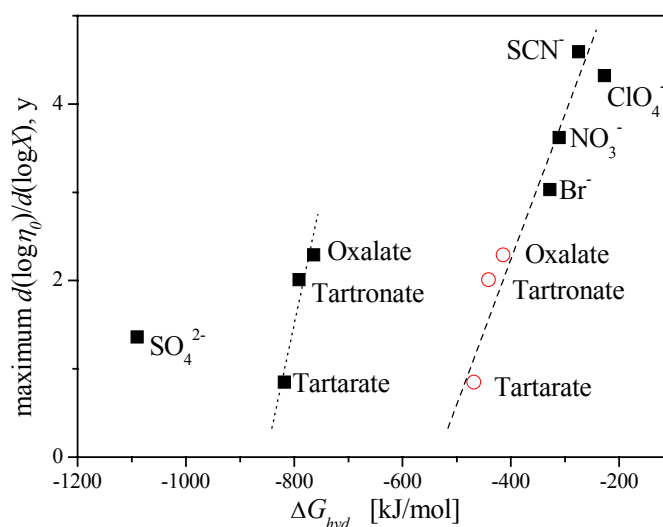


Figure 5.19. Plots of power law of $\eta \propto X^y$ against hydration free energy ΔG_{hyd} for different anions in 100 mM C₁₄DMAO solution. The hydration free energies of each dicarboxylic acid were calculated by different formula for monovalent (○) and divalent forms (■).

equation. On the other, the dicarboxylic anions would suffer from the excluded volume effect in the vicinity of the adsorbed micellar surface owing to their bulky structures, and the steric hindrance acts repulsively as the supplementary dispersion force.

In addition, the initial micellar growth with protonation is evaluated between the different counter-ions systems by the scaling law of η_0 , $\eta_0 \propto X^y$. The indices of the power laws are plotted in Figure 5.19 and summarized in Table 5.4. The indices decrease in accordance with the free energy of hydration likely $\eta_{0,max}$. Although the scaling law would have somehow temperature influence, the order mostly follows the Hofmeister series. The dicarboxylic acids are again regarded as two ionized forms, monovalency (○) and divalency (■). For the series of monovalent ions including the dicarboxylates, the micelle growth can be fairly described by ΔG_{hyd} . The micelle elongation would be due to both characteristic synergism and counter-ion property as far as the specific case of aminoxide surfactant. In view of stoichiometry, the synergistic effect gives an equivalent contribution to evolution of η_0 for the different monovalent acids. Unlikely evaluation of $\eta_{0,max}$, the magnitude of the scaling law can be interpreted by hydrophilicity of counter-ions alone because it is obtained from the difference between the quantities of states at given X values. There exists again the extraordinary sulfate ion which seems not to be in the above case, and the increasing viscosity may be due to strong condensation onto the micelle surface.

Here it should be noted that the specific counter-ions seem not to follow the Hofmeister series. The extreme lyotropic counter-ion, for instance, perchlorate and thiocyanate ions create the lamellar liquid crystal and the counter-ions would adsorb sufficiently on the micelle surface as can be expected by ΔG_{hyd} values. However the CF_3COO^- ion cannot induce such a transformation under the present condition in spite of the highest y , although the free energy of hydration is unknown. The free energies of hydration for salicylate and trifluoro acetate can be presumed by extrapolation of the linear relationship in Figure 5.19, and they are respectively -123.24 kJ/mol for Sal^- and -15.79 kJ/mol for CF_3COO^- . One can as well calculate their ΔG_{hyd} values from additivity of functional groups in the molecule. For the case of trifluoro acetate, the substitution from methyl group to trifluoro group is taken into account, and the energy loss is ca. 2.98 kJ/mol.^{204,205} The calculated ΔG_{hyd} values are -409.68 kJ/mol for Sal^- and -386.02 kJ/mol for CF_3COO^- , which are definitively incompatible with the above estimation and other references,^{206,207} and not reasonable for the viscosity developments. This contradiction would result from the fact that their counter-ions penetrate much deeply into the surfactant layer.²⁰⁸ It is evident that a packing of molecule in aggregate determines the assembly structure and the counter-ion can control the structure. If the hydrophilic property solely plays predominant role in y , trifluoro acetate anion should induce L_α formation. In this case, however, the hydrophilic contribution involving the hydrophobic counter-ion is beyond comprehension. It is noted that CF_3COO^- has

Table 5.4. Comparison of power law index (y) between the 100 mM C_{14} DMAO solutions with the different counter-ions.

	ΔG_{hyd} [kJ/mol]	y
SO_4^{2-}	-1090	1.36
Tartarate	-818.02	0.85
Tartronate	-791.01	2.01
Oxalate	-764	2.29
Br^-	-328	3.03
NO_3^-	-311	3.62
SCN^-	-275	4.59
ClO_4^-	-227	4.32
Sal^-		6.75
CF_3COO^-		8.48

greater potential to elongate the C₁₄DMAO micelles than Sal⁻, suggesting that penetration of the bulky benzene ring in salicylic molecule energetically favors higher curvature. Thus it could be concluded that the counter-ions with especial functional groups cannot be explained by the free energy of hydration solely and behave like not so much counter-ion as short-chain co-surfactant.²⁰⁹

The shear plateau modulus G'_{∞} is furthermore compared in these systems. The maximum G'_{∞} are listed in Table 5.5. Although these limited data cannot interpret any qualitative relationships, the hydrophobicity of counter-ion tends to give rise to the shear modulus. The maximum G'_{∞} is attained at half protonation for every system except for HSal system, where there are various aggregate structures: lamellar phase for ClO₄⁻ and Sal⁻, worm-like micelle for NO₃⁻ and CF₃COO⁻. Namely it is noteworthy that the elasticity of solution does not depend on structural contribution but on counter-ion itself.

Table 5.5. Comparison of plateau modulus G'_{∞} between the 100 mM C₁₄DMAO solutions with the different counter-ions.

	ΔG_{hyd} [kJ/mol]	G'_{∞} [Pa]
NO ₃ ⁻	-311	~ 4.12
ClO ₄ ⁻	-227	48.98
Sal ⁻		9.28
CF ₃ COO ⁻		50.33

5.2 TRIFLUORO ACETIC ACID CF₃COOH

5.2.1 VISCOELASTICITY

As mentioned above, the viscosity profile with protonation degree in the CF₃COOH system was surprising and of interest. The change in η_0 , indeed, seems to be interpretable by the structural transformation with X , *i.e.* growth and decline of micelles. This transformation, however, cannot explain the second η_0 maximum at high X because the high charge density should preferably produce a smaller aggregate structure.

For different protonation degrees, the dynamic rheograms are shown in Figure 5.20. These rheograms indicate that the solutions are Maxwellian: the viscous property changes to the elastic one with increasing frequency and the characteristic time constant τ_{cross} can be referred as the crossover of G' and G'' . The crossover shifts firstly to lower frequency and then goes back toward higher frequency. It is apparent that the magnitude of the modulus at the crossover remains more or less constant in terms of X , *i.e.* one can describe a master curve as seen in Figure 5.21. n is the multiplier of frequency (normalize). According to the Maxwell equations and the normalized frequency, one can obtain the structural relaxation time τ_R in the linear viscoelastic regime. The experimental values are fairly well fitted by the model with one fitting parameter τ_R (Figure 5.21). The relaxation times are plotted as a function of X in Figure 5.22, and it could be found that the viscosities of the solutions are determined mainly by the relaxation mode of the existing worm-like micelle.

On the other hand, one can observe that the plateau modulus G'_{∞} also shows dependence of protonation. The modulus reaches maximum at $X = 0.5$ as well as HClO₄ system. The plateau modulus can be expressed as $\sim k_B T / \xi^3$, where k_B is the Boltzmann constant, T the absolute temperature, ξ is the correlation length.²¹⁰ The correlation length, relative to the entanglement length of worm-like micelle, decreases by a factor

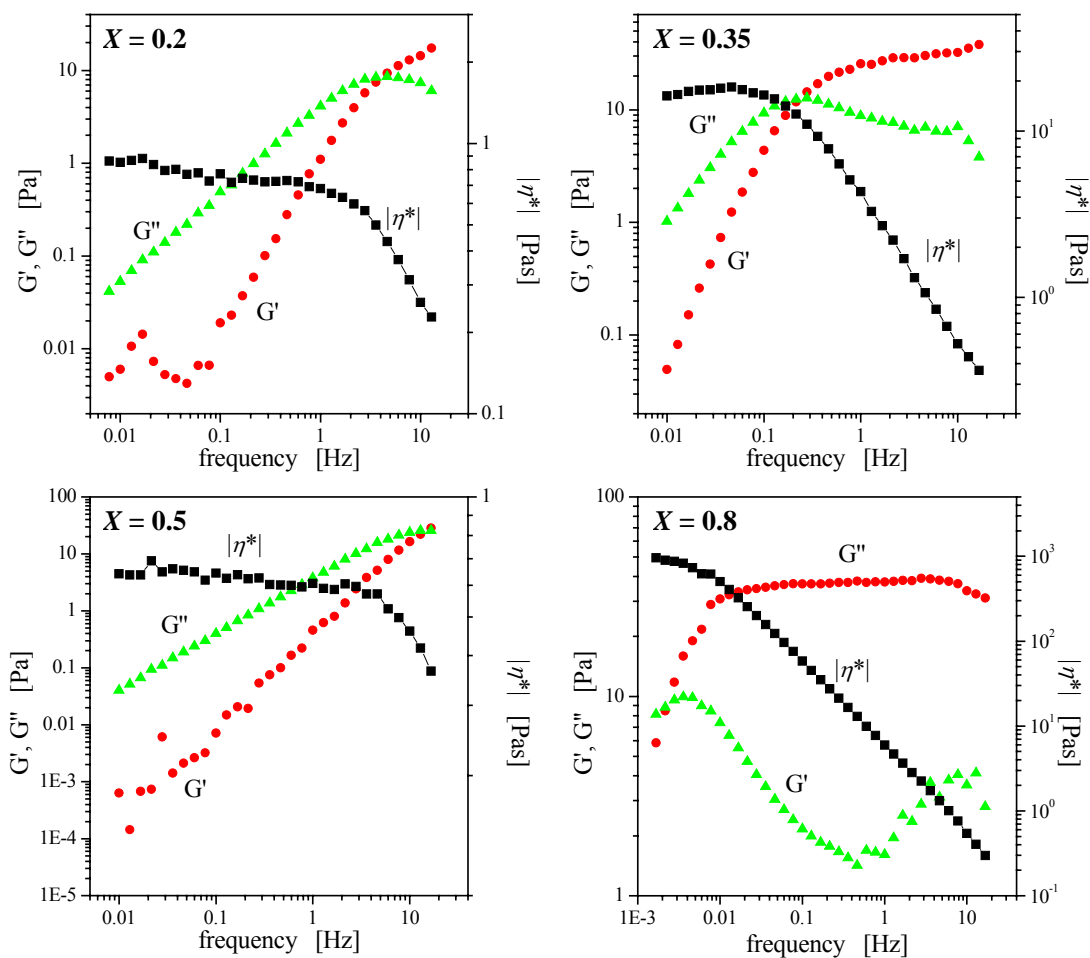


Figure 5.20. Rheograms for the solutions at different protonation degree X in $\text{CF}_3\text{COOH}/\text{C}_{14}\text{DMAO}$ system at $35\text{ }^\circ\text{C}$. The surfactant concentration is kept at 100 mM . The symbols represent respectively the storage modulus (G' , ●), the loss modulus (G'' , ▲), and the complex viscosity ($|\eta^*|$, ■).

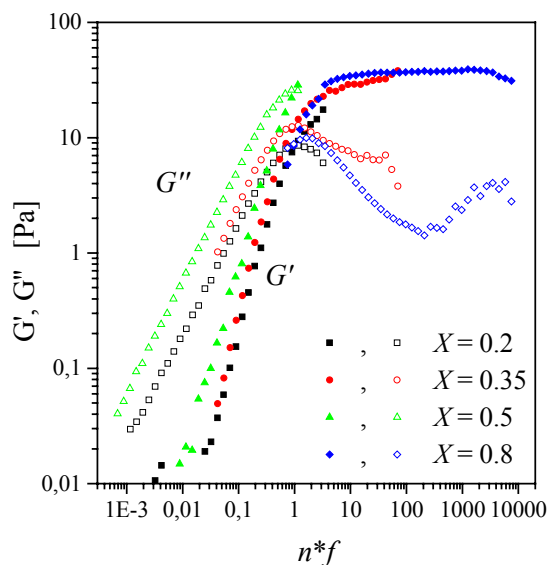


Figure 5.21. A master curve of rheological moduli, storage modulus (G' , filled marks) and loss modulus (G'' , open marks), as a function of normalized frequency n^*f in $\text{CF}_3\text{COOH}/\text{C}_{14}\text{DMAO}$ system at $35\text{ }^\circ\text{C}$. The surfactant concentration is kept at 100 mM .

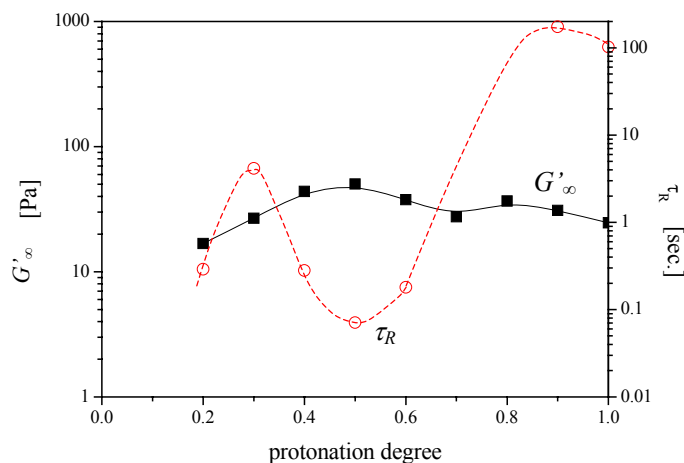


Figure 5.22. Changes in the plateau modulus G'_{∞} (■) and the characteristic relaxation time τ_R (○) as a function of protonation degree in $\text{CF}_3\text{COOH}/\text{C}_{14}\text{DMAO}$ system at 35 °C. The surfactant concentration is kept at 100 mM.

of three with increasing G'_{∞} . The constant correlation length with protonation is in contradiction with the micelle surface potential, that should increase with X . It can be therefore considered that the zeta-potential is reduced by moderate protonation. If any protonating chemical species have the same synergism effect as HCl in C_{14}DMAO system,¹⁵⁹ the hydrogen bond between the neighboring head groups can be derived in the semi-protonation regime, especially, should be remarkable at $X = 0.5$. Then it would be possible that the long-range repulsion of inter-aggregates is reduced by the characteristic hydrogen bonding. As a consequence, the correlation length decreases and the maximum G'_{∞} appears at the half protonation.

As well as the CF_3COOH system, a sodium thiocyanate (NaSCN)/HCl mixture system exhibits similar phenomenon. The mixing ratio of NaSCN/HCl is fixed at 3/7 and the proton quantity is variable, namely, X is defined as $[\text{H}^+]/[\text{C}_{14}\text{DMAO}]$. Figure 5.23 shows the change in η_0 with protonation degree at 25 °C. The viscosity maximum and minimum appear at $X = 0.4$ and 0.7 respectively, which are different from the CF_3COOH system. After passing through the minimum, η_0 increases again with X . The rheograms at different X corresponding to the critical points are shown in Figure 5.24. The rheograms are as well of Maxwellian type, whereas both moduli at high frequency are unlikely to be described by the single relaxation model. It is noteworthy that the

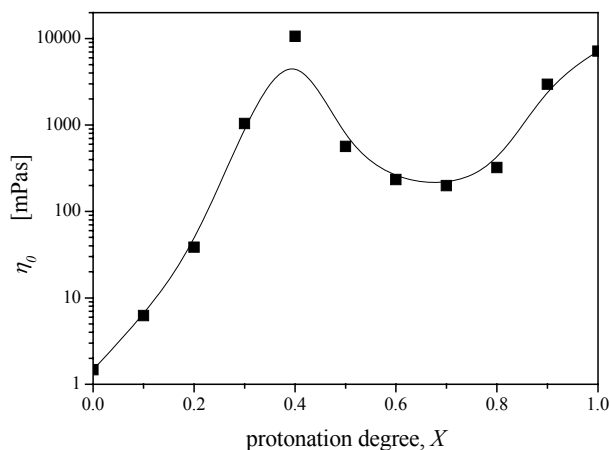


Figure 5.23. Change in the zero-shear viscosity η_0 as a function of protonation degree in $(\text{NaSCN} + \text{HCl})/\text{C}_{14}\text{DMAO}$ system at 25 °C. The ratio of NaSCN/HCl is fixed at 3/7. The surfactant concentration is 100 mM.

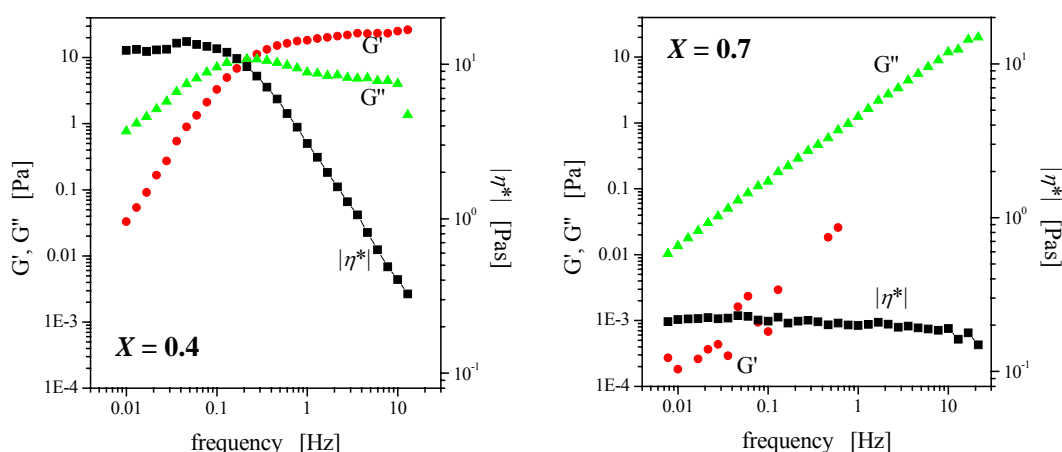


Figure 5.24. Rheograms for the solutions at different protonation degree X in (NaSCN+HCl)/C₁₄DMAO system at 25 °C. The ratio of NaSCN/HCl is fixed at 3/7. The surfactant concentration is kept at 100 mM. The symbols represent respectively the storage modulus (G' , ●), the loss modulus (G'' , ▲), and the complex viscosity ($|\eta^*|$, ■).

elastic property at $X = 0.7$ disappears especially in the high frequency regime and the complex viscosity remains constant up to $f = 10$ Hz. The viscoelasticities of NaSCN/HCl solutions also seem to be controlled by the relaxation time: the maximum and minimum τ_R are in good agreement with the corresponding η_0 . And the G'_∞ maximum locates at the equimolar ratio of non-protonated and protonated C₁₄DMAO as seen in Figure 5.25, which is the same tendency as the CF₃COOH system.

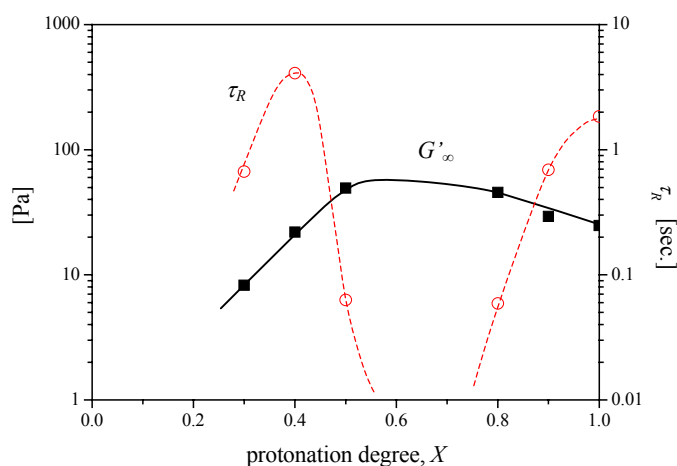


Figure 5.25. Changes in the plateau modulus G' (■) and the characteristic relaxation time τ_R (○) as a function of protonation degree in (NaSCN+HCl)/C₁₄DMAO system at 25 °C. The ratio of NaSCN/HCl is fixed at 3/7. The surfactant concentration is kept at 100 mM.

5.2.2 ADSORPTION PROPERTIES

The effects of protonation using CF₃COOH on adsorption onto the water-air surface or the water-micelle interface had been studied by means of the tensiometries. Figure 5.26 and 5.27 show respectively the adsorption isotherms at the different protonation degrees and the change in the interfacial tension with X . The isotherms demonstrate synergism definitively: the CMC is reduced by the half protonation of C₁₄DMAO, and moreover the amount of adsorption of the surfactant molecules becomes a maximum at $X = 0.5$ due to the densely packed molecules. The interaction

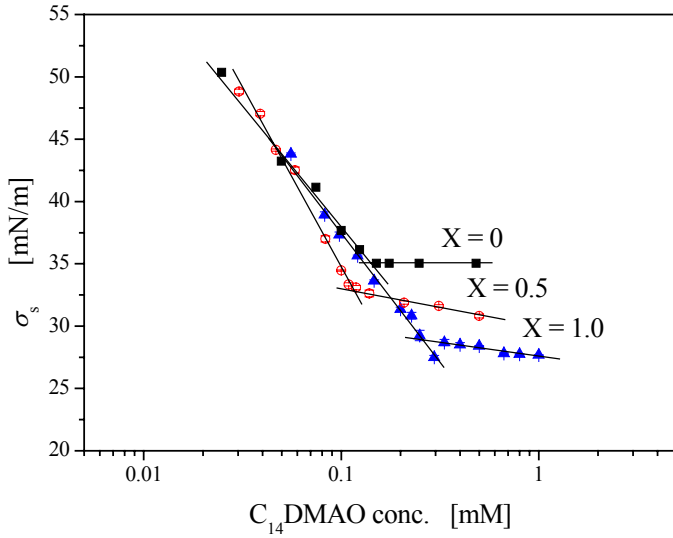


Figure 5.26. Surface tension curves for the solutions at different X 's in $\text{CF}_3\text{COOH}/\text{C}_{14}\text{DMAO}$ system.

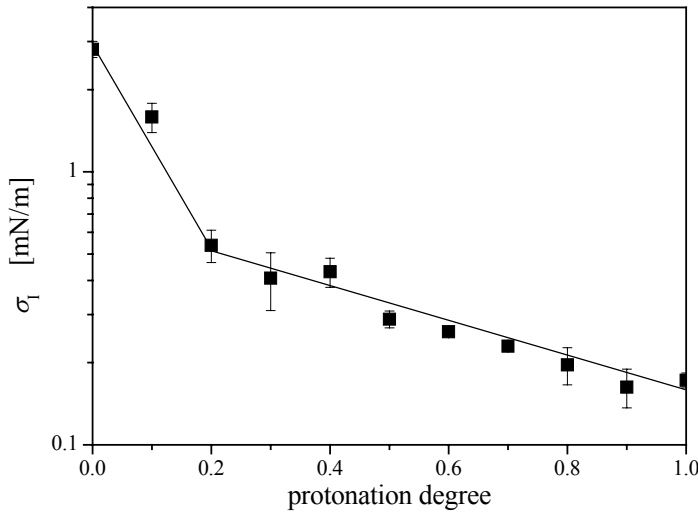


Figure 5.27. Change in interfacial tension against decane as a function of protonation degree in $\text{CF}_3\text{COOH}/\text{C}_{14}\text{DMAO}$ system. The surfactant concentration is kept at 1 mM.

between the molecules are calculated in terms of interaction parameter β , given by

$$\frac{(X_1)^2 \ln(C_1/C_1^0 X_1)}{(1-X_1)^2 \ln[C_2/C_2^0(1-X_1)]} = 1 \quad [5.6]$$

$$\ln f_1 = \beta(1-X_1)^2$$

Where X_1 and X_2 are the mole fraction of surfactant 1 and 2 at surface in the total surfactants, C_1 and C_2 the mole concentrations of surfactant 1 and 2 in the bulk phase, C_1^0 and C_2^0 the mole concentrations of surfactant 1 and 2 respectively required at a given surface tension, and f_1 the activity coefficient of surfactant 1 at surface. At $\sigma_s = 35$ mN/m, the β value at $X = 0.5$ is -1.35, and the composition of nonionic component in the surfactants is 0.495 in mole fraction. The two analogues seem to be mixed ideally on the surface. In the present case, Eq. [3.31] can be modified in the following form

$$\begin{aligned} d\sigma_s &= -RT(\Gamma_1 d \ln C_1 + \Gamma_2^+ d \ln C_2^+ + \Gamma_2^- d \ln C_2^-) \\ &= -RT(\Gamma_1 d \ln C_1 + 2\Gamma_2 d \ln C_2) \end{aligned} \quad [5.7]$$

Γ is the surface excess amount of the component, and the superscription and the subscription represent the ionic sign and the component, respectively. Eq. [5.7],

furthermore, is rewritten by $C_1 = C_2 = C$,

$$d\sigma_s = -RT(\Gamma_1 + 2\Gamma_2)d \ln C \quad [5.8]$$

The mixing composition X_1 from Eq. [5.8] permits to calculate the individual Γ_1 and Γ_2 .

$$X_1 = \frac{\Gamma_1}{\Gamma_1 + \Gamma_2} \quad [5.9]$$

And the surface area per molecule in the mixture system can be given by evolution of Eq. [3.32].

$$a_s = \frac{10^{16}}{N_A \Gamma_1} \cdot X_1 = \frac{10^{16}}{N_A \Gamma_2} \cdot (1 - X_1) \quad [5.10]$$

The results are described in Table 5.6. CMC gives a minimum at $X = 0.5$, while the average a_s calculated from Eq. [5.10] is similar to that at $X = 0$ and much smaller than that at $X = 1.0$. Provided that additivity of the head group areas for the composition holds, the a_s at $X = 0.5$ should be 0.686 nm^2 . The interacted surface area is indeed smaller than the ideal area. In view of CMC and a_s , it is conceivable that the non-protonated C_{14} DMAO is the much more hydrophobic than the protonated one as usual, while, in spite of the general synergism, the plateau surface tension decreases uncommonly with increasing X , as well as the interfacial tension σ_I (Figure 5.27).

Table 5.6. CMC and surface area occupied per surfactant molecule (a_s) at different protonation degrees in $\text{CF}_3\text{COOH}/C_{14}\text{DMAO}$ and $\text{HNO}_3/C_{14}\text{DMAO}$ systems.

CF₃COOH			
X	0	0.5	1.0
CMC [mmol/L]	0.139	0.112	0.250
a_s [nm ²]	0.471	0.495	0.901
HNO₃			
X	0	0.5	1.0
CMC [mmol/L]	0.139	0.109	0.238
a_s [nm ²]	0.471	0.567	1.06

Figure 5.28 shows the plots of σ_I versus the mixing ratio of two surfactants in the different surfactant systems. The mixture of analogues, C_{14} DMAO/tetradecyl trimethylammonium bromide (C_{14} TMABr), exhibits the upwards deviation from the ideality, while the composite of C_{14} DMAO/sodium dodecyl sulfate (SDS) creates the strong synergistic depression of

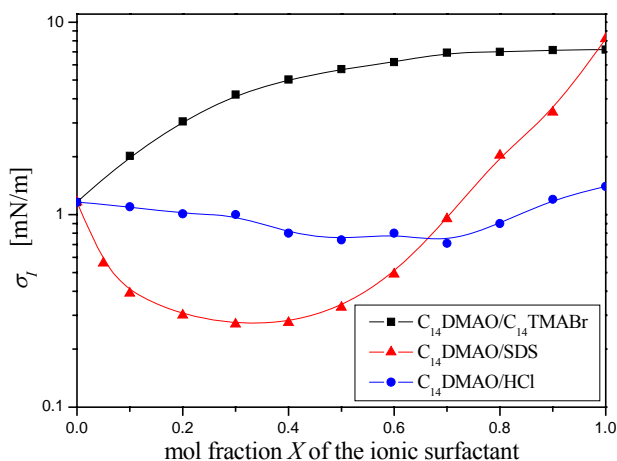


Figure 5.28. Interfacial tension against decane of the surfactant mixtures, C_{14} DMAO/ C_{14} TMABr, C_{14} DMAO/SDS, and C_{14} DMAO/HCl at 25 °C. The surfactant concentration is kept at 100 mM.

σ_7 . The synergistic phenomena, in terms of the surface or interfacial tension, can be explained by the preferable orientation of the neighboring surfactants: the charged amine group of C₁₄DMABr is surrounded by three methyl side chains which would sterically prevent the interaction between its molecules or even with other surfactants molecules. Also the ion-dipole interaction would be centered on the oxygen atom of aminoxide group, and it may be speculated that this location might lead to distortions in the structure of bound water in the neighborhood of the positive charge of the nitrogen atom of aminoxide.¹⁶⁰ The release of bound water molecules would lead to an entropy gain for the aminoxide/cationic surfactant mixtures consistent with the calorimetry data on the dodecylphosphine oxide (C₁₂PO)/dodecyl trimethylammonium bromide (C₁₂TAB) systems.²¹¹ And, on the other, SDS head group is not shielded with any attached chain and the charged sulfate anion interacts directly with the positive portion of the dipole centered on N atom. From the suppression of the cross-sectional area a_s , the present case probably can be manifested by such ion-dipole interaction, however the monotonic decreases in the surface and interfacial tensions would be necessary to involve the effect of the charge profile normal to the aggregate surface. The protonated surfactant, C₁₄DMAOH⁺CF₃COO⁻, is more hydrophobic than the non-protonated one, namely, the counter-ion is bounded strongly on the interface, and even may be immersed in the aggregates inside. Certainly, CF₃COO⁻ ions have higher affinity to an oil relative to CH₃COO⁻.^{207,212} Thus, the lyotropic acid causes simultaneously two effects on the surface potential. The complexity may relate to the viscosity curve with protonation degree.

As with, the surface and interfacial tension measurements were carried out in the nitric acid (HNO₃) system, in which one can find typical synergism of the zero-shear viscosity η_0 against protonation degree. The results are shown in Figure 5.29 and 5.30. The surface tension curves at different protonation degrees are apparently similar to those in the CF₃COOH system, and the CMC and a_s also show synergism (Table 5.6). The interaction parameter and the composition on the surface are $\beta = -1.18$ and $X_1 = 0.5121$, and the interaction between the two molecules is a little bit weaker relative to the CF₃COOH system. The concentration of the non-protonated surfactant on the surface is greater than the protonated one. This indicates that CF₃COO⁻ ion clearly

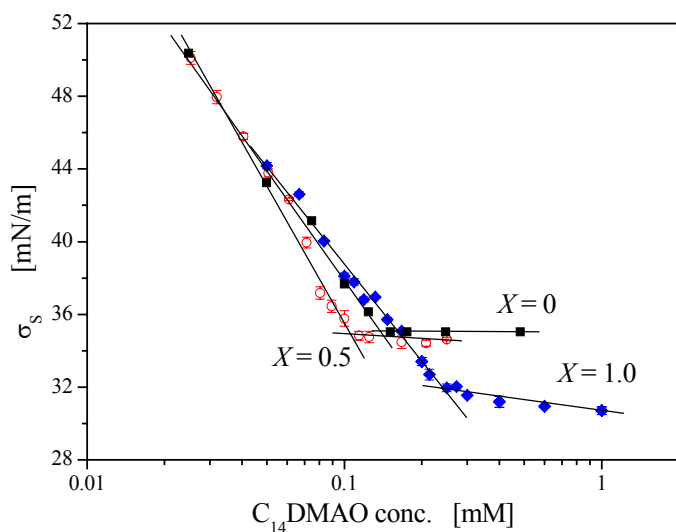


Figure 5.29. Surface tension curves for the solutions at different X 's in HNO₃/C₁₄DMAO system.

enhances C₁₄DMAOH⁺ to adsorb onto the air-water surface. Generally, the higher the hydrophobicity of one component in the mixture, the larger the interaction parameter β is. The tendency can be observed in the present system. The composition difference at the half-protonation may be related to the interaction as well. Although the surface tension decreases with increasing X for HNO₃ as well as the CF₃COOH system, σ_I exhibits a minimum around $X = 0.6$ for HNO₃ system. The behavior is remarkably different with the CF₃COOH system, and this is particular evidence that CF₃COO⁻ behaves like co-surfactant rather than counter-ion. In Figure 5.30, σ_I in the HCl system are plotted against X , and protonation with HCl also shows synergistic effect on the interfacial property. The minimum of interfacial tension curve moves to lower protonation degree when the counter-ion changes from NO₃⁻ to Cl⁻. It is likely that the composition X at the minimum interfacial tension is correlated to X_1 and β , in other words, the Hofmeister series.

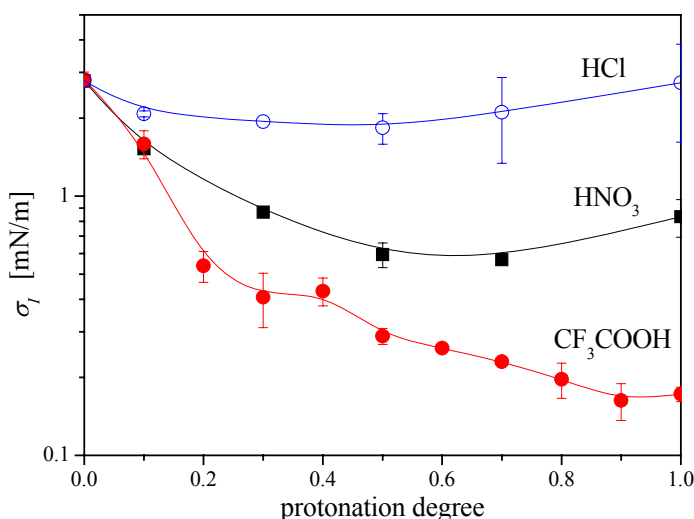


Figure 5.30. Change in interfacial tension against decane as a function of protonation degree in C₁₄DMAO/different acids systems; HNO₃ (■), HCl (○), and CF₃COOH (●). The surfactant concentration is kept at 1 mM.

5.2.3 ACTIVATION ENERGY AND INTERFACIAL TENSION

The dependence of the relaxation time on temperature was investigated for the different protonation degrees. The characteristic relaxation τ_R can be estimated by the following equation:

$$\eta_0 = G'_\infty \tau_R \quad [5.11]$$

and τ_R relates to the activation energy E_a .

$$\frac{\tau_R}{\eta_{\text{solvent}}} \propto \exp \frac{E_a}{RT} \quad [5.12]$$

where η_{solvent} is the viscosity of solvent, R the gas constant, and T the absolute temperature. A semi-logarithmic plot of $\tau_R/\eta_{\text{solvent}}$ against the reciprocal temperature $1/T$ permits to obtain the activation energy. The plots are shown in Figure 5.31 and the obtained E_a 's are given in Table 5.7. In Eq. [5.11], since the plateau modulus G'_∞ is less dependent on temperature,²¹³ the viscosities solely were measured at various temperatures (25 ~ 50 °C). There are two fundamental chemical relaxation processes that are proposed for micelles. The first, referred to as the fast process, involves the

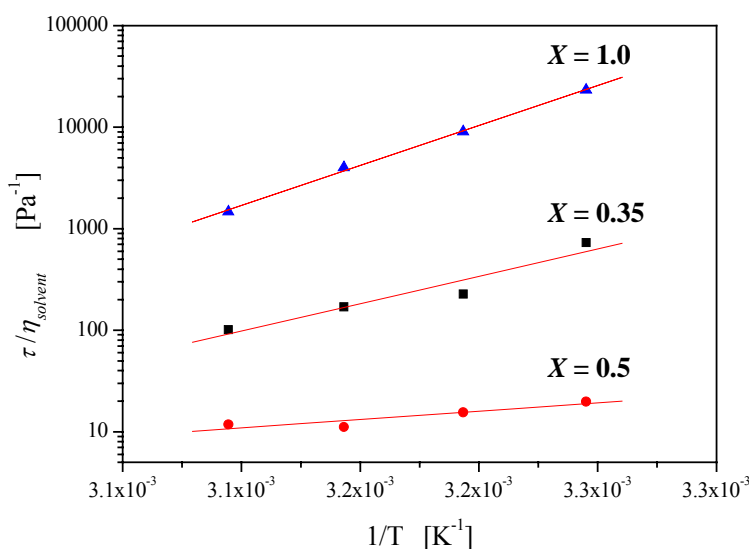


Figure 5.31. Change in the relaxation time (τ) divided by the solvent viscosity ($\eta_{solvent}$) as a function of reciprocal absolute temperature ($1/T$) at different protonation degrees in $CF_3COOH/C_{14}DMAO$ system. The surfactant concentration is kept at 100 mM.

rapid exchange of surfactant monomers with the micelle. The second, or slow process, refers to the change in micelle concentration by a stepwise process.²¹⁴ Both the process, in general, accelerate with increasing temperature,²¹⁵ and simultaneously the micelles become smaller and smaller. The activation energy thus is expected to be correlated by the scission energy of aggregates on heating, strictly to say, the energy required by the formation of a new pair of end caps.²¹⁶ The end cap energy E_e per unit volume can be expressed by the other form

$$E_e = \Delta n_e \sigma_l \cdot S = \Delta n_e \sigma_l \cdot 4\pi r_c^2 \quad [5.13]$$

Δn_e is the number of newly created end caps unit volume, σ_l the interfacial tension, S the interfacial area ($= 4\pi r_c^2$: r_c is the radius of cross-section of cylinder). Assuming that the cross-sectional diameter of micelle remains constant regardless of elongation of the micelle, one can simply estimate Δn_e using $r_c = 1.105$ nm given by the SAXS measurement (Section 5.1.1) and each interfacial tension value at the corresponding X (Section 5.2.2). The results are shown in Table 5.7. The Δn_e value at $X = 0.5$ is smaller by about a factor of 10 than those at other protonation degrees. Two structural model at $X = 0.5$ can occur from the result; (1) the structure is already small micelle at 25 °C and there is less temperature-dependence, (2) the structure has another relaxation process and is kinetically stable for temperature change. It should be noted from Figure 5.22 that the solution at $X = 0.5$ is relaxed rapidly, on the other, the correlation length is the shortest in the range of protonation.

Table 5.7. Activation energy (E_a) and the number of scission event on heating (Δn_e) at different protonation degrees in $CF_3COOH/C_{14}DMAO$ system.

X	0.35	0.5	1.0
E_a [kJ/mol]	103.0 ± 20.5	13.6 ± 4.1	150.7 ± 4.8
Δn_e [m^{-3}]	$1.68 \cdot 10^{24}$	$2.95 \cdot 10^{23}$	$5.46 \cdot 10^{24}$

5.2.4 MICROSTRUCTURE OBSERVATION

For the cryo-TEM measurements, $C_{12}DMAO$ surfactant was used in order to accomplish low viscosity of the solution at 100 mM. The change in η_0 with protonation in $C_{12}DMAO/CF_3COOH$ system is shown in Figure 5.32. η_0 approaches to a maximum at $X = 0.55$ and decreases up to $X = 0.9$, afterwards increases again with X and has a

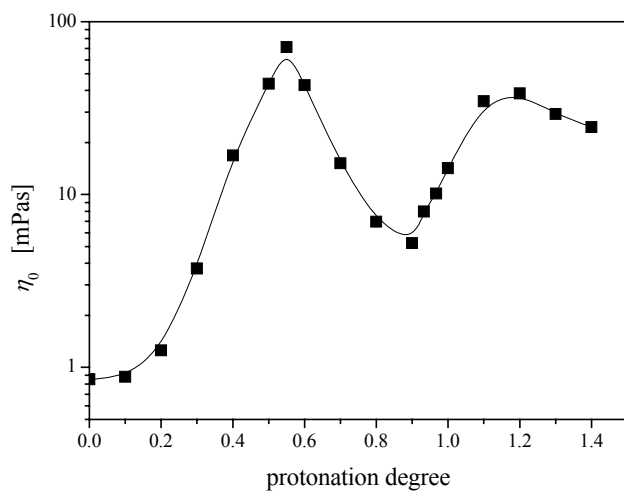


Figure 5.32. Change in the zero-shear viscosity (η_0) as a function of protonation degree in $\text{CF}_3\text{COOH}/\text{C}_{12}\text{DMAO}$ system. The surfactant concentration is kept at 100 mM.

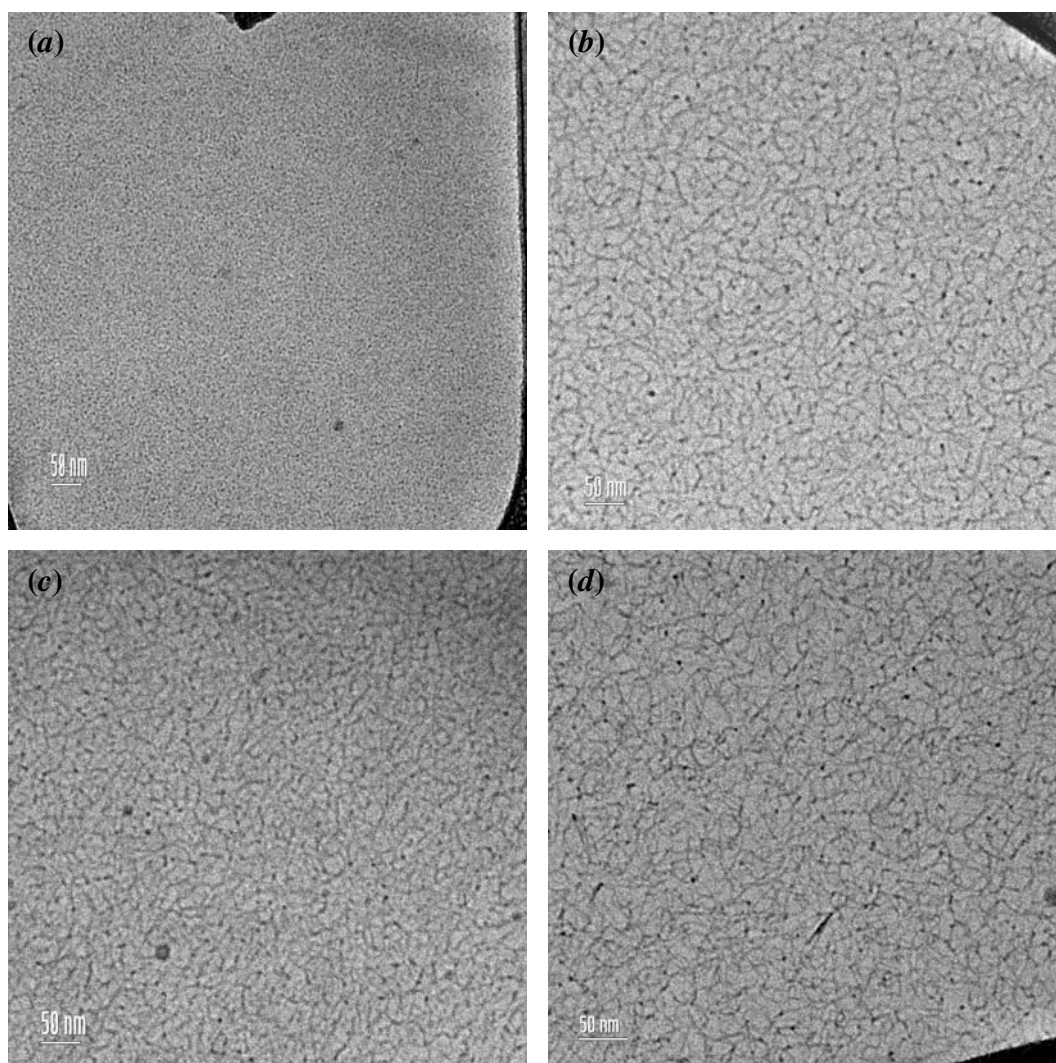


Figure 5.33. Cryo-TEM images for (a) $X = 0$, (b) $X = 0.55$, (c) $X = 0.9$, and (d) $X = 1.2$ in $\text{CF}_3\text{COOH}/\text{C}_{12}\text{DMAO}$ system. The surfactant concentration is kept at 100 mM. The magnification is the same for each image: the bar in the picture indicates 50 nm.

second maximum at $X = 1.2$. The viscosity profile is almost similar to the C₁₄DMAO system. Figure 5.33 shows the cryo-TEM micrographs at each critical X . At $X = 0$ (a), the small spherical or semi-spheroid micelles can be observed in the entire image, while protonation forms the considerably extended thread-like micelles with a number of entanglements (b, c, d). The magnification is identical between the images. Interestingly the structure at the minimum η_0 ($X = 0.9$) is not small aggregates but elongated thread-like micelles. From these micrographs, however, one cannot recognize their structural differences: all of them are flexible threads which seem to be entangled to the same extent. The link between the rheology and the micrograph can be further rationalized if they are both being driven by the same microstructural changes. Specifically, the first viscosity maximum and minimum might signify a shift from linear to branched micelles, because a connected network of branched micelles will have a lower viscosity than an entangled network of linear micelles. Appell *et al.* proposed a mechanism concerning the low viscosity of branched micelles: the mechanism of fast relaxation is by sliding the crosslinks through the micellar network as sketched in Figure 5.34(a).²¹⁷ Such a mechanism can allow for a very fluid solution and for a faster relaxation of stress than disentanglement or breaking of wormlike micelles. An analogy can be drawn here with the highly fluid L₃ (sponge) phase where an infinite multiconnected fluid membrane separates two identical subspaces of solvent. A model has been successful in describing the rheological properties of the L₃ phase in different systems, in which the relaxation of stress occurs through the simple viscous flows of the surfactant in the fluid membrane and of the solvent in its subspace.²¹⁸ On the other hand, Shikata *et al.* had proposed an alternative mechanism: the relaxation is by a ghostlike crossing (Figure 5.34(b)).²¹⁹ The equilibrium properties of the micellar network corresponds to a transient character of crosslinks so that when a micellar thread collides with another one in the network it can form a transient crosslink and the two threads separate again on the other side.

The self-assembly into aggregates of different morphologies is explained in terms of a preferred curvature for the surfactant monolayer. Elongated micelles thus correspond to locally cylindrical aggregates, their two free ends are generally thought to be closed by globular end-caps and the driving force for the micellar growth is then the difference in the free energy of surfactants in the cylindrical or globular environment; a large difference leads to longer micelles in order to diminish the number of surfactants in unfavorable globular surroundings. One can figure out another way to suppress the free ends of locally cylindrical micelles: to connect the cylinders in which case the unfavorable surroundings (the connection point) correspond to smaller curvature than the cylinder. The solution adopted by a particular system will depend on the respective energies to form globular end-caps or connection

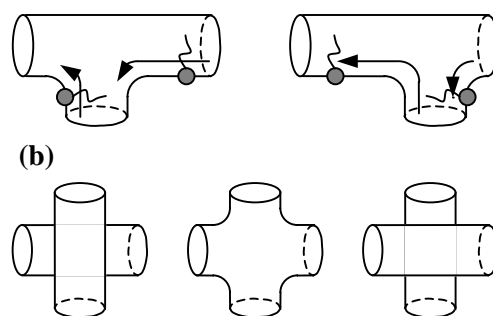


Figure 5.34. Schematic representations of (a) sliding of a crosslink along a micellar thread through the viscous flow of the surfactant molecules along the micellar network and (b) a ghostlike crossing: encounter of the two micellar threads (left) → a transient crosslink (middle) → separation of the two micellar threads (right).

points.²²⁰ The decrease in the optimal curvature of the surfactant monolayer therefore would cause the formation energy of end-caps to increase and conversely the formation energy of connection points to decrease. These mechanisms may be able to explain the phenomena occurred in the present system. The synergistic effect indeed prefers energetically the multiconnected structure to the thread-like micelle with two end-caps, since the surface area is minimized due to the operative hydrogen bonding force. The cryo-TEM pictures suggest the apparently similar structures between the various protonated samples regardless of their greatly different viscoelasticities. Certainly the cryo-TEM image cannot allow to give an insight about the three dimensional construction, as a result, one cannot discriminate that the junction of two threads is either entanglement or connection. Although the above interpretations are expected to be plausible in views of the energetic favor of the end-caps and the empirical results, the combination of the cryo-TEM image and the rheology would give another assumption. Rao *et al.* suggested that the viscoelastic solution of sodium salicylate (NaSal) and cetyl trimethyl ammonium bromide (CTAB) consists of not wormlike micelles but necklace-like chain of micellar beads.²⁰⁸ The carboxylate group attaches electrostatically with ammonium ion, on the other hand, the benzyl ring of NaSal is embedded in the non-polar micelle core. This would be supported by the fact that the viscoelasticity disappears by substituting the ortho-OH group by the meta- or para-position,²²¹ since their sites of OH group cannot be immersed much into the micelle core. The aspect may be applied to the CF₃COOH system, because the counter ion CF₃COO⁻ seems favorably to absorb onto the surface or interface as similar as the surfactant. However, this assumption would not be able to explain the viscosity decrease in the range of $X = 0.35 - 0.5$ for C₁₄DMAO and $X = 0.55 - 0.9$ for C₁₂DMAO, even in the NaSCN/HCl system. If the conjunction of spherical micelles proceeds proportionally with the amount of CF₃COO⁻, the viscosity should increase linearly.

5.2.5 SCATTERING PROFILE

The SAXS measurements are carried out in C₁₂DMAO/CF₃COOH system, and the results are shown in Figure 5.35. The spectra are not obvious due to the small difference in the electron densities between the solvent and aggregates. However one

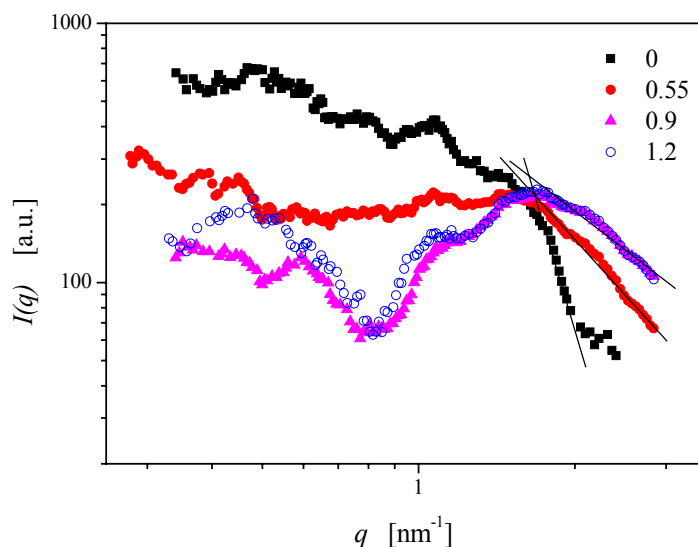


Figure 5.35. SAXS spectra at $X = 0$ (■), 0.55 (●), 0.9 (▲), and 1.2 (○) in C₁₂DMAO/CF₃COOH system.

can observe the apparent distinctions between the solutions: the scattering intensity at $q \rightarrow 0$ decreases with increasing protonation degree and decays with different power laws in the high q range. The power laws are approximately -5.9 for $X = 0$, -2.1 for $X = 0.55$, -1.4 for $X = 0.9$, and -1.5 for $X = 1.2$, indicating that the surface curvature decreases with protonating C₁₂DMAO. The intensity at low q supplies information about the inter-aggregate interaction, *i.e.* protonation induces much higher mutual interference of aggregates. It would be noteworthy that the scattering spectra at $X = 0.9$ and 1.2 are nearly superimposed one another; in fact, the spectrum at $X = 1.2$ somehow fluctuates in the intermediate q range, that implies the presence in a further well-defined ordering structure. The long-range elastic fluctuation of wormlike micelle induced by electrostatic interaction may be responsible for the decrease in the plateau modulus G'_{∞} .²²² Indeed, the increase in the charge density reduces G'_{∞} beyond $X = 0.9$, while this could not be the case and the correlation length, *i.e.* the mesh size of the network is almost unchanged. And it seems furthermore that the electrostatic interaction suppresses the elastic fluctuation. From the incoherence of the SAXS result and the rheology, it can be imagined that the viscosity increment in the range of $X = 0.9 - 1.2$ would be due to the dynamic feature of structure, strictly saying, respective relaxation modes. As described above, there are the different conceivable structures in terms of wormlike micelle. Surprisingly, the static structures at $X = 0.9$ and 1.2 are at most analogous, and one can recognize the structural change from $X = 0$ to 0.9. The SAXS spectrum at $X = 0.55$ may refer to the elongated wormlike micelle by judging from the scattering intensity at low q and the intensity decay at high q relative to $X = 0$. Further protonation would involve the coalescence of junctions of the entangled threads, resulting in formation of the branched micelle. The coupling of the identical structure and the different viscosities could be accomplished by the stress relaxation. At $X = 0.9$ corresponding to the minimum viscosity, the relaxation time would be governed by sliding of the crosslink, in other words, molecular level. At $X = 1.2$ corresponding to the second maximum viscosity, on the other hand, the breathing or the reversible scission could be mainly operative for the relaxation as indicated by much longer relaxation time. The interfacial tension also suggests that the energy cost during the scission of branched micelle is relatively lower and the scission may take place more preferably rather than the sliding of the crosslink.

5.3 CONCENTRATION VARIABLE

To explain the variation of the viscosities with protonation X , a concentration contribution to η_0 is examined in HCl, HNO₃, and NaSCN/HCl (3/7) systems at 25 °C where the viscosity profiles with X differ apparently from one to another. Figure 5.36 shows the changes in η_0 as a function of the C₁₄DMAO concentration for each system. Above the concentrations explored in the present study, the single transparent micellar phases transform to separated two phases with or without birefringence (Figure 5.37), which depends on the X value and the counter-ion. The birefringent phase at higher concentration (17.5 wt.%, $X = 0.5$) in C₁₄DMAO/HCl system is assigned to the stacked L _{α} phase by the polarized microscope as depicted in Figure 5.38. All the systems show the steep increases in the viscosities at different critical concentrations, c^* , indicating the onset of overlapping cylindrical micelles. And in some of the systems maximum viscosities (c_m, η_{0m}) are observed in the concentration ranges. Beyond the maximums,

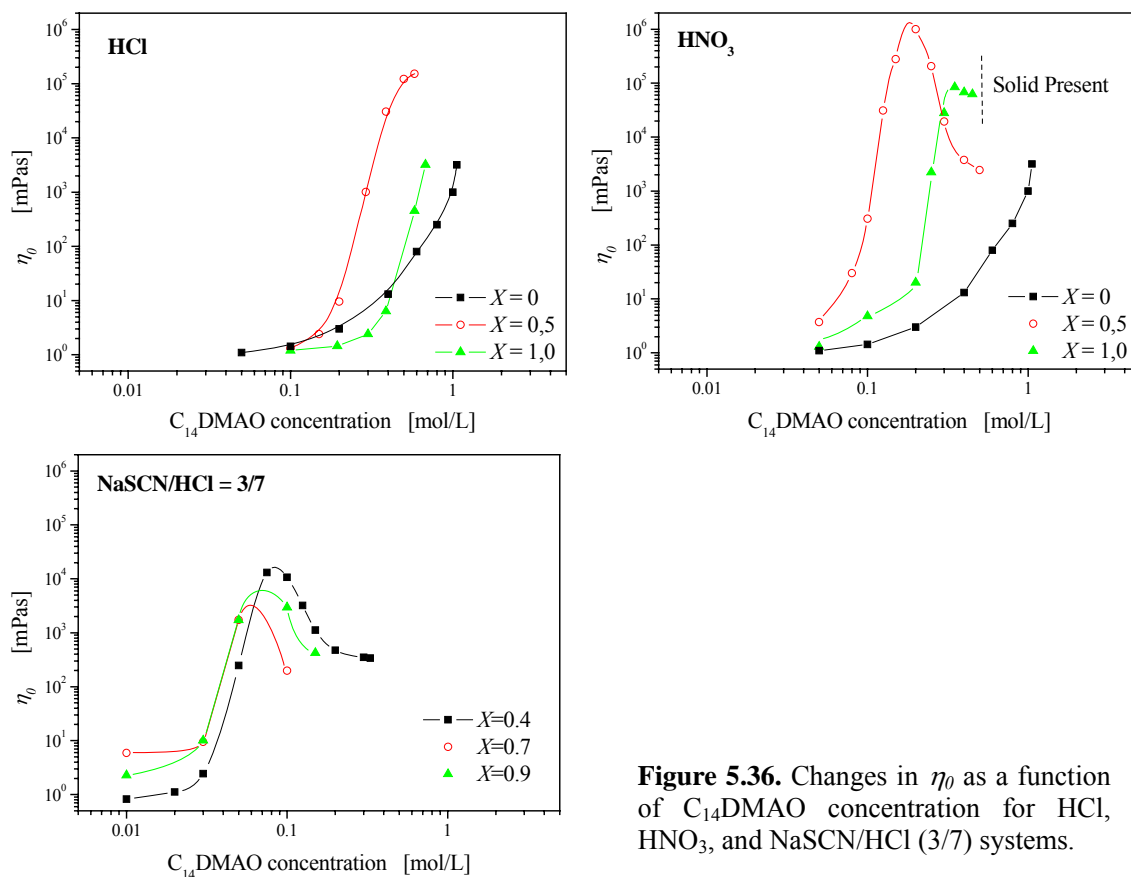


Figure 5.36. Changes in η_0 as a function of C_{14} DMAO concentration for HCl, HNO_3 , and NaSCN/HCl (3/7) systems.

intermicellar branching takes place as proved theoretically²²³ and experimentally^{176,224}. At 100 mM C_{14} DMAO in NaSCN/HCl system, it can be understood that the viscosity reduction from $X = 0.4$ to 0.7 results from the micellar branching. The slopes of the increases in the viscosities relate mainly to the micelle length and the number density of entanglements. From the above description, three parameters are dealt with in order to argue the morphologies in these systems, and these factors are summarized in Table

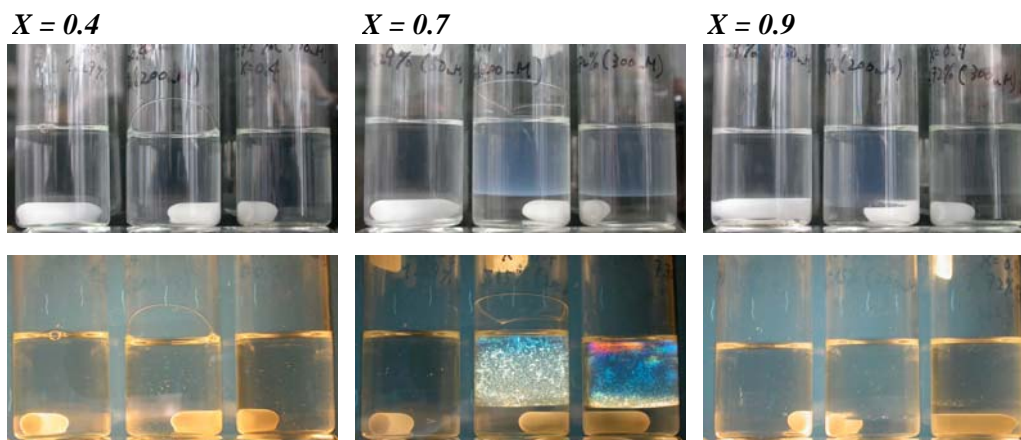


Figure 5.37. Photographs for the various concentrations of C_{14} DMAO under no polarizers (upper) and polarizers (bottom) at different X 's in NaSCN/HCl (3/7) system. Note that each photograph (different X 's) includes three samples at different concentrations, 50 mM (left), 200 mM (middle), and 300 mM (right).

5.8. In HCl system, in fact, no maximum at each X is observed in the concentration range, thus the c_m and η_{0m} are rewritten by the values at every phase boundary. All of the parameters except for $d\eta_0/dc$ show threshold values at $X = 0.5$ in HCl system. As well as the HCl system the HNO₃ system exhibits the same viscosity profiles, which are more remarkable protonation effect and well define the maxima. The variation of the parameters in HCl and HNO₃ systems can be interpreted by both concepts of synergism and micellar curvature or molecular

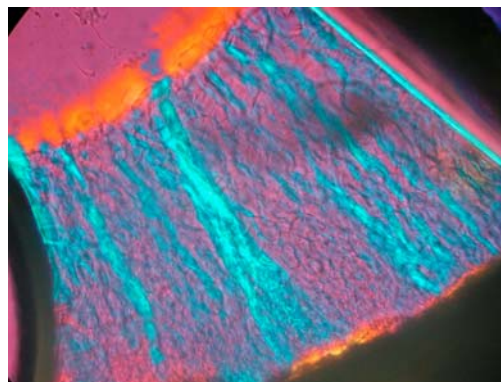


Figure 5.38. Micrographs of the solution at 17.5 wt.% ($X = 0.5$) in C₁₄DMAO/HCl system.

packing restriction. From the fact that the non-protonated C₁₄DMAO forms small globular micelles or even spheroid micelles, the intrinsic packing parameter should be less than 1/3. Thus the geometrical factor would suppress the increase in the viscosity, *i.e.* the growth of micelle. When the surfactant is protonated, the micelle is growing up proportionally with the surfactant concentration. On the basis of the conventional arguments, the opposite effect could be considered such as the comparison between SDS micelle and C₁₂E₅ one. As described above, one should take into account that the aminoxide surfactants have the lateral hydrogen bonding between hydrogen atom attached to oxygen atom and oxygen atom in neighboring two molecules. The local curvature then should be lower because the net area of the surfactant head group is compressed, resulting in elongating micelles. At $X = 1.0$ (HCl and HNO₃ systems), c^* and c_m are higher and η_{0m} is lower than at $X = 0.5$. This is simply due to the electrostatic force. On contrary to the fact that the higher electrostatic repulsion induces to the smaller micelles, it is of great interest that even at $X = 1.0$ the viscosity increases

Table 5.8. The break point of η_0 (c^*), the concentration (c_m) and the viscosity (η_{0m}) at maximum η_0 , the slope of increase in η_0 with C₁₄DMAO concentration ($d\eta_0/dc$) in HCl, HNO₃, and NaSCN/HCl (3/7) systems.

HCl

X	c^* [mol/L]	c_m [mol/L]	η_{0m} [Pas]	$d\eta_0/dc$
0	0.30	1.06	3.16	5.22 ± 0.60
0.5	0.18	0.58	152	12.17 ± 0.15
1.0	0.36	0.68	3.19	11.00 ± 0.48

HNO₃

X	c^* [mol/L]	c_m [mol/L]	η_{0m} [Pas]	$d\eta_0/dc$
0	0.30	1.06	3.16	5.22 ± 0.60
0.5	0.091	0.18	1298	16.95 ± 2.5
1.0	0.20	0.35	84	17.97 ± 2.0

NaSCN/HCl = 3/7

X	c^* [mol/L]	c_m [mol/L]	η_{0m} [Pas]	$d\eta_0/dc$
0.4	0.028	0.084	15.99	9.36 ± 0.2
0.7	0.028	0.058	2.95	10.19
0.9	0.029	0.070	5.88	10.06

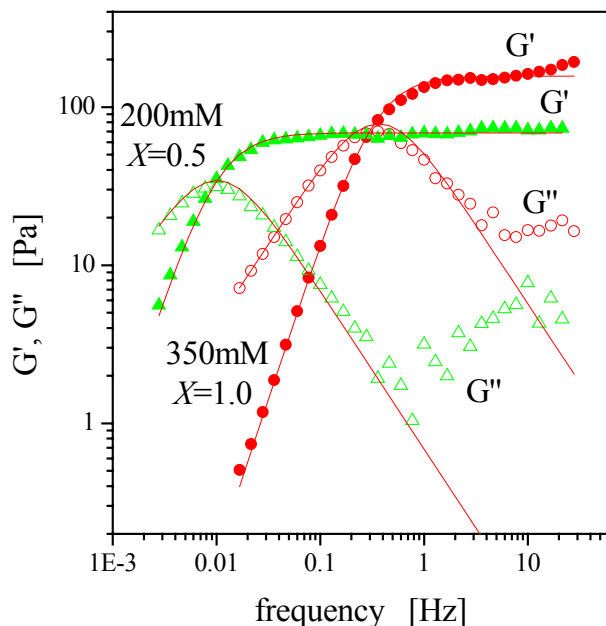


Figure 5.39. Frequency sweep measurements for the different C₁₄DMAO concentrations, 200 mM ($X = 0.5$, $\blacktriangle \triangle$) and 350 mM ($X = 1.0$, $\bullet \circ$) in HNO₃ system at 25 °C.

dramatically with the concentration, because the completely charged surfactants are unlikely to interact enough between their head groups. The results, however, suggest that the highly protonated surfactant is capable to build up the worm-like micelle in spite of the favorable spherical form. This implies that the peculiar interaction of hydrogen bonding is more dominant than the electrostatic force even at high protonation degree. The dynamic rheograms at the maximum viscosities for 200 mM ($X = 0.5$) and 350 mM ($X = 1.0$) show this in Figure 5.39. In both the systems, the Maxwell representation is fairly well fitted in the intermediate frequency range. From the diagrams, we can compute two characteristic lengths, an average micellar length (\bar{L}) and an entanglement length (l_e), using the following equations.²²⁵

$$G'_\infty \cong \frac{k_B T}{l_e^{9/5}}, \quad \frac{G''_{min}}{G'_\infty} \sim \frac{l_e}{\bar{L}} \quad [5.14]$$

where G''_{min} is the value of G'' at a “dip” in the high frequency regime. Each parameter is described in Table 5.9. The entanglement length, l_e , is shortened with protonating C₁₄DMAO, *i.e.*, the number density of entanglements is higher. It would bring about the increase in the viscosity, whereas its result opposes to the η_0 profile. On the other hand, the micelle length decreases with increasing X . This could be why the higher protonation enables the endcap energy to stabilize. The shorter micelles at $X = 1.0$ may give rise to the number of apparent entanglement because of the much denser micelles. The presence of the shorter micelles with stable end-cap energy at $X = 1.0$ is supported by no occurrence of

Table 5.9. Rheological parameters and characteristic lengths for the different compositions in HNO₃ system at 25 °C

	G'_∞ [Pa]	τ [sec.]	G''_{min} [Pa]	l_e [nm]	\bar{L} [μm]
200mM $X = 0.5$	68.6	99.0	2.24	39.2	1.20
350mM $X = 1.0$	157	2.89	15.1	29.7	0.31

branching micelles (η_0 does not decrease so much after the maximum at $X = 1.0$). The relaxation time of stress seems to be compatible with these lengths.

In NaSCN/HCl system, one can observe the definitive maximum viscosities at every X , while the protonation effect seems to be complicated because of the minimum at $X = 0.7$ concerning in c_m and η_{0m} . And the coincident c^* of the NaSCN/HCl samples at different X 's is also unexpected. The highest η_{0m} at $X = 0.4$ would originate from the same physical mechanism as the other systems. It may be conceivable that the minimum c_m and η_{0m} at $X = 0.7$ also result from the synergism. The formation of the birefringent phase with increasing concentration (Figure 5.37) implies the distinct morphologies dependent on X . Before the phase transition into the birefringence phase, thus, it is likely that the proportion of cross-links rather than of entanglements is attributed to η_0 . The increase in cross-links reduces the viscosity as referred in the highly fluid L₃ (sponge) phase where an infinite multiconnected fluid membrane separates two identical subspaces of solvent. It would be explained in terms of the end cap energy as well as HNO₃ system that η_{0m} increases with protonation degree from $X = 0.7$ to 0.9. The dynamic rheograms at each η_{0m} in Figure 5.40 manifest that the relaxation time depends not on the concentration but on the protonation degree and correlates with the threshold concentration of the saturated thread-like micelle, c_m .

Figure 5.36 and Table 5.8 mention qualitatively the effect of counter-ion on the critical concentrations. The parameters clearly depend on the Hofmeister series, thus the stronger lyotropic counter-ion causes c^* and c_m to be lower.

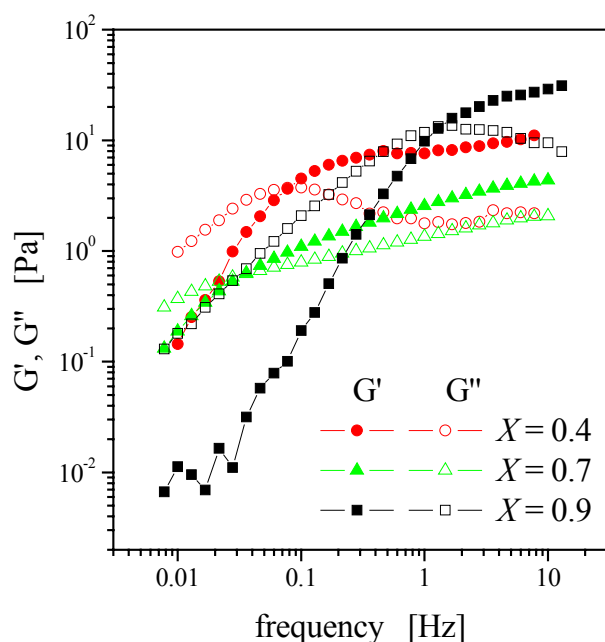


Figure 5.40. Frequency sweep measurements for the different C₁₄DMAO concentrations, 75 mM ($X = 0.4$, ●○), 50 mM ($X = 0.7$, ▲△) and 100 mM ($X = 0.9$, ■□) in NaSCN/HCl system at 25 °C.

5.3 MIXING EFFECT

5.3.1 CF₃COOH/HCOOH

The mixing effect of CF₃COOH and HCOOH had been examined in 100 mM

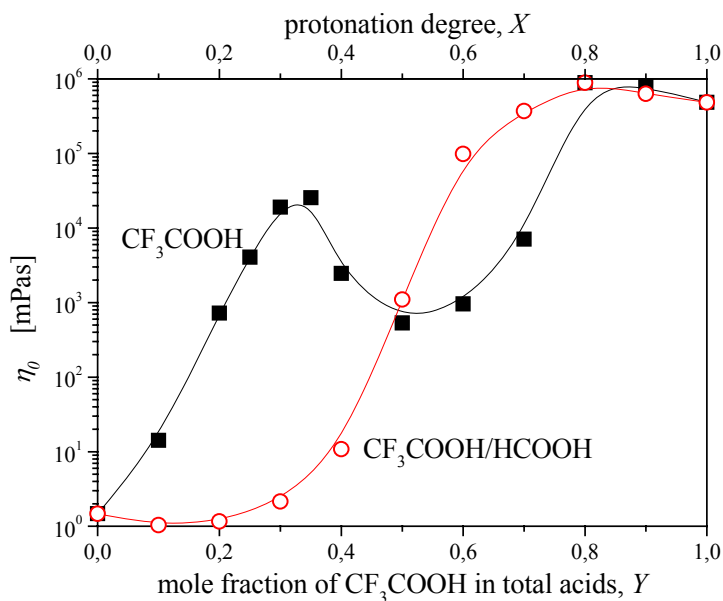


Figure 5.41. Change in the zero-shear viscosity (η_0) as a function of mole fraction of CF_3COOH in total acids (Y , \circ) for $\text{CF}_3\text{COOH}/\text{HCOOH}$ mixture system and protonation degree (X , \blacksquare) for CF_3COOH system at 35°C . The surfactant concentration and protonation degree for the mixture system are fixed at 100 mM and $X = 1.0$.

C_{14}DMAO solution at 25°C . The two acids have different influences on C_{14}DMAO micelles in terms of the viscosity. Figure 5.41 shows the viscosity evolution in two acids system. Protonation degree is fixed at $X = 1.0$, *i.e.* the surfactant is completely protonated over any studied composition. The mixing ratio of two acids is denoted by $Y = [\text{CF}_3\text{COOH}]/([\text{CF}_3\text{COOH}] + [\text{HCOOH}])$, corresponding to the horizontal axis in Figure 5.41. The figure includes the viscosity variation in CF_3COOH alone system. Both independent functions, X and Y , are regarded as a variable of CF_3COOH quantity. Their curves are definitively different: in the mixture solution, η_0 exhibits no maximum and minimum, instead, increases steeply around 1:1 mixing ratio. This curve demonstrates that HCOOH and CF_3COOH are ideally mixed and compete with one another in a sense of adsorption on the micelle surface. As seen in this graph, the viscosity of the mixture becomes higher than that of the CF_3COOH solution. The reason would be synergism of C_{14}DMAO molecules, namely, the synergistic phenomenon is limited in semi-protonation of C_{14}DMAO regardless of the ion-pair species. This curve, in addition, may give us a hint for dissolving the unclear structure at $X = 1.0$ in CF_3COOH alone system. The continuous viscosity variation thus proves a continuous structure change, in other words, the spherical micelle protonated by HCOOH is elongating with increasing CF_3COOH content. Substituting CF_3COOH by HCOOH at the half protonation $X = 0.5$ will obviously exhibit such a discrete transformation, since their single acid systems form the distinct structures at $X = 0.5$, spherical micelle for HCOOH system and branched micelle for CF_3COOH system. Figure 5.42 shows the change in η_0 with Y at $X = 0.5$. Again the viscosity of CF_3COOH alone solution is plotted in the same figure. Without misunderstanding the figure, the axes are reminded. Y (bottom axis) means the composition of two acids and $Y = 1.0$ corresponds to $X = 0.5$ for the CF_3COOH alone solution. Two curves are apparently similar, whereas they should be discriminated in view of ionic atmosphere at the micelle surface. Note that synergism between the protonated and non-protonated surfactants should be working more or less in the whole Y range, although one could not observe viscoelastic synergism in HCOOH system. Here we shall focus on the structure at $Y = 1.0$, which is expected to be a

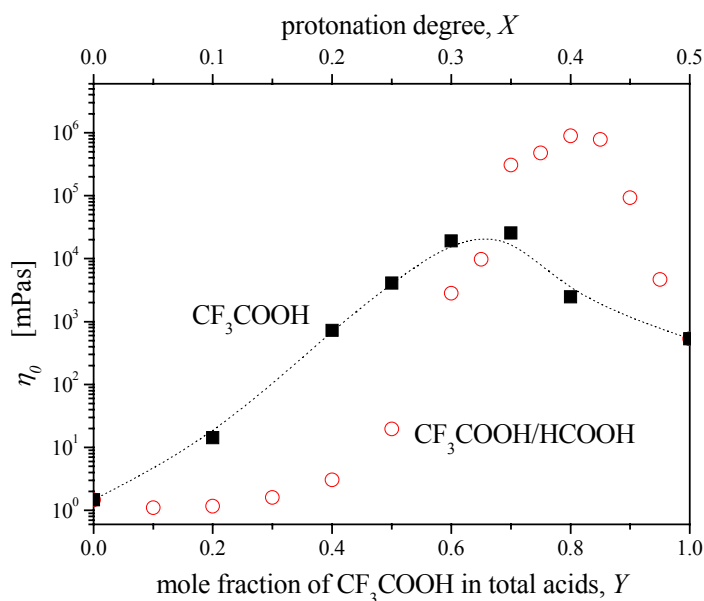


Figure 5.42. Change in the zero-shear viscosity (η_0) as a function of mole fraction of CF_3COOH in total acids (Y , \circ) for $\text{CF}_3\text{COOH}/\text{HCOOH}$ mixture system and protonation degree (X , \blacksquare) for CF_3COOH system at 35°C . The surfactant concentration and protonation degree for the mixture system are fixed at 100 mM and $X = 0.5$.

multiconnected morphology. Assuming that the spherical or thread-like micelles would disperse in aqueous media at this composition, one should observe no structural modification with Y , which refers to a continuous viscosity change. However, the viscosity gives at first rise to a maximum and then decreases with Y . This suggests that the small micelles in $\text{HCOOH}/\text{C}_{14}\text{DMAO}$ system are growing up upon addition of CF_3COOH , and the elongated micelles starts to branch at high content of CF_3COOH . The structural transformation passes through a thread-like form, which is consistent with the empirical observations and the conventional curvature theory: the micellar branching is necessary to occur as a result that the micellar elongation is saturated.

5.3.2 $\text{HClO}_4/\text{HCOOH}$

Figure 5.43 shows a phase diagram of the mixture, $\text{HClO}_4/\text{HCOOH}$, in 100 mM C_{14}DMAO aqueous solution. Protonation degree is fixed here at $X = 1.0$. The mixed acids system forms a birefringent L_α phase as well as HClO_4 alone system. In comparison to the phase diagram of HClO_4 alone system (Figure 5.9), the phase

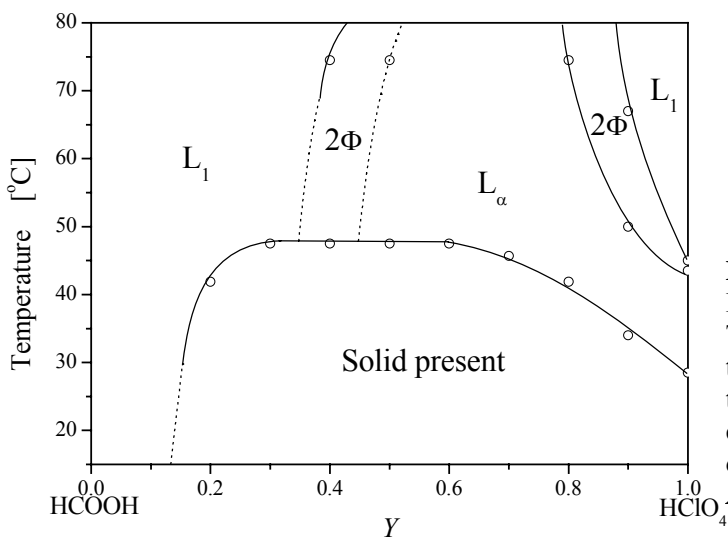


Figure 5.43. Phase diagram of $\text{HClO}_4/\text{HCOOH}$ mixture system. The horizontal axis Y represents the mole fraction of HClO_4 in total acids. The surfactant concentration and protonation degree are fixed at 100 mM and $X = 1.0$, respectively.

boundary of the L_α phase shifts to the right side, meaning that the presence of HCOOH hinders bilayer formation. This effect is consistent with $\text{CF}_3\text{COOH}/\text{HCOOH}$ system. Surprisingly, Krafft temperature is elevated with addition of HCOOH to HClO_4 so that formation of the complex solid would be uncommon in terms of the chemical potentials of these components in such a mixing system, as mentioned in Section 5.1.2.2. In the present case, however, the interpretation in Section 5.1.2.2 may not be applied to, because synergism between the head groups is not much effective due to their complete protonations of C_{14}DMAO . It can be presumed from two diagrams (Figure 5.9 and 5.43) that anti-eutectic behavior would arise from ClO_4^- counter-ion.

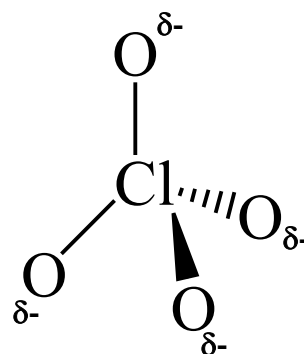


Figure 5.44. Molecular structure of ClO_4^- ion.

The tetrahedral form of ClO_4^- (Figure 5.44) leads to the homogeneous dipole moment over four oxygen atoms of its molecule. The dipole molecule is capable to interact electrostatically with four C_{14}DMAO molecules, if the hydrophobic force of C_{14}DMAO could have been ignored. Considering both the forces, one can recognize that the ClO_4^- ion interacts with the neighboring two C_{14}DMAO molecules. As a consequence, the ClO_4^- ion acts same as the synergistic hydrogen bond. Thus the presence of HCOOH would not play important role in the increment of Krafft point.

Figure 5.45 shows a phase diagram in $\text{NaClO}_4/\text{HCl}/\text{C}_{14}\text{DMAO}/\text{water}$ system, where the ratio of $\text{NaClO}_4/\text{HCl}$ is fixed at unity. It can be found from Figure 5.45 that the interesting solid stability could not be affected by the ionic strength of solution, that is, the feature of ClO_4^- ion allows the complex structure in solid state to form. And the presence of salt seems not to influence the Krafft temperatures over the X range. Above Krafft point, however, the behavior is somehow different: the L_1 phase around $X = Y = 1.0$ in HClO_4 alone system or $\text{HCOOH}/\text{HClO}_4$ system disappears in the presence of NaCl , instead the two-phase is formed. This seems to be due to the salting-out phenomenon. In these phase diagrams (Figure 5.9, 5.43, and 5.45), it is noteworthy that

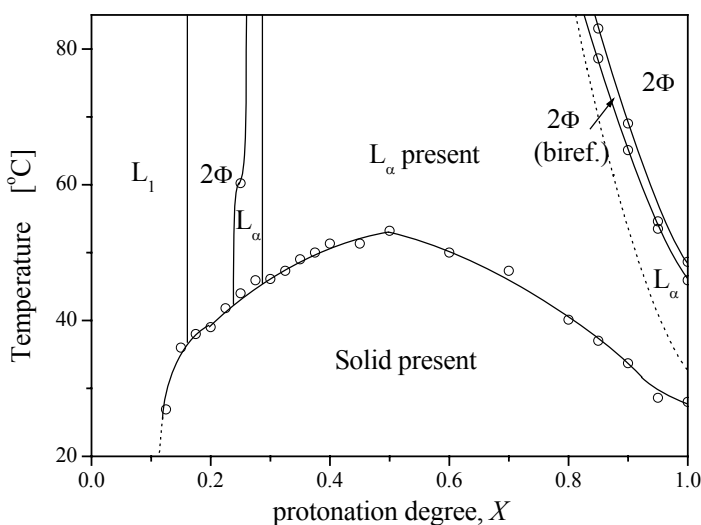


Figure 5.45. Phase diagram of $\text{NaClO}_4/\text{HCl}$ mixture system. The C_{14}DMAO concentration and the mixing ratio of $\text{NaClO}_4/\text{HCl}$ are fixed at 100 mM and unity, respectively.

the maximum Krafft points can be always observed at $X = 0.5$. The result is reasonable for the above expectation that one ClO_4^- ion produces the complex with two C_{14}DMAO molecules.

The assumption, that the tetrahedral form of ClO_4^- induces the complex, can be supported by HSCN and HSal, which bind strongly with the C_{14}DMAO head group, whereas the Krafft points in their surfactant solutions rise up monotonically with the amount of acid. This suggests that the unique phenomenon does not result from hydrophobicity but from its tetrahedral symmetry.

5.4 EFFECT OF HYDROCARBON CHAIN-LENGTH

5.4.1 L_α PHASE FORMATION

Oleyl dimethylaminoxide (OleylDMAO) has 18 hydrocarbon units, and its volume is $308.6 \text{ cm}^3/\text{mol}$. The bulky hydrophobic moiety should give the larger packing parameter than C_{14}DMAO . Furthermore the unsaturated bond in the middle of the hydrocarbon chain can introduce flexibility to itself. Kawasaki *et al.* showed vesicle formation at the half protonation of OleylDMAO with HCl.²²⁶ The phase behavior is indeed observed in the series of samples as seen in Figure 5.53, where there exists the

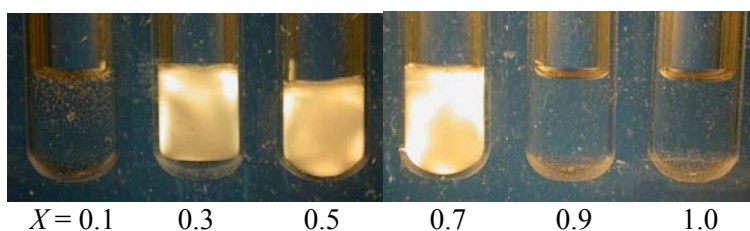


Figure 5.46. Sample appearances between the closed polarizers for different protonation degrees (X) in 100mM OleylDMAO/HCl system at 25 °C.

L_α phase in the wide protonation range. Thus it is evident that the longer chain length can effectively modify the aggregate structure even if the strongly hydrated acid is applied. Here I will extend the previous work using different monovalent acids, HCOOH, HBr, HNO_3 , and HClO_4 . For every system, the birefringent L_α phase can be formed at $X = 0.5$ (Figure 5.47). The L_α phases melt on elevating temperature, and the subsequent structures are highly viscoelastic worm-like micelle. Exceptionally the L_α -

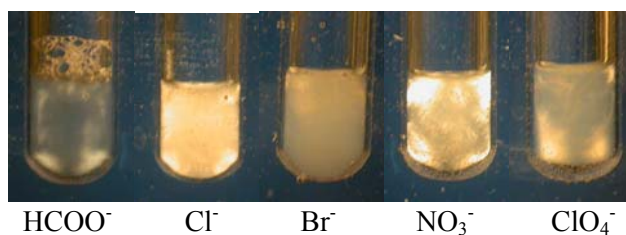


Figure 5.47. Sample appearances between the closed polarizers for different counter-ions in 100mM OleylDMAO/HCl system at 25 °C. The protonation degree is fixed at $X=0.5$.

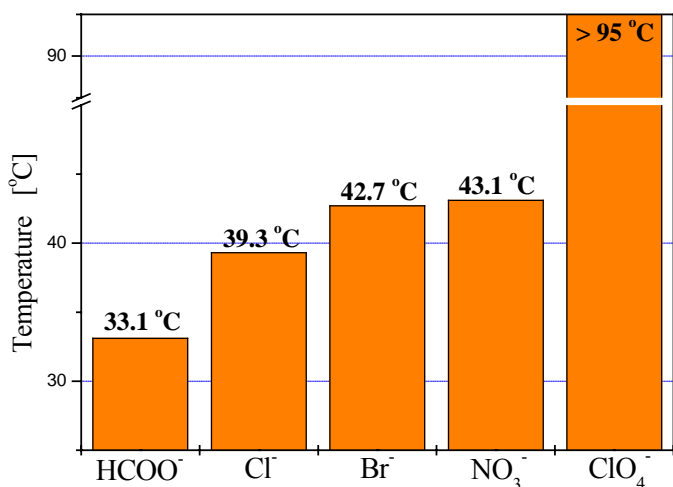


Figure 5.48. Phase transition temperatures from lamellar liquid crystal (L_{α}) to micellar solution (L_1) for different counter-ions in 100mM OleyDMAO solution at 25 °C. The protonation degree is fixed at $X=0.5$.

L_1 transition cannot be observed in the $HClO_4$ system, and the L_{α} phase is retained above 95 °C. The temperatures at which the phase transitions take place are depicted in Figure 5.48. The order of anions obeys the Hofmeister series, and surprisingly the order-disorder transition seems to be described by the counter-ion property. In Figure 5.49 the transition temperature, $T_{L_{\alpha}-L_1}$, is plotted against the free energy of hydration ΔG_{hyd} and its enthalpy ΔH_{hyd} . From the figure, one can see the linear relation between the transition temperature and ΔH_{hyd} , and it would be plausible that the thermal phase transition is attributed by ΔH_{hyd} much more than that of ΔG_{hyd} . This would be due to the entropic term in the Gibbs free energy, which cannot be sufficiently influenced by temperature change. In the previous work, it was reported that the salting-out anions caused the liquid crystal structure to be unstable, on the other, the salting-in anions built up the stable liquid crystal. The work represented the effects of the extreme anions in the Hofmeister series on stability of liquid crystal, therefore the quantitative expression was not carried out in terms of hydrophilicity of the counter-ions.

In the previous section 4.1.5, the correlation between the phase boundary of L_{α} -

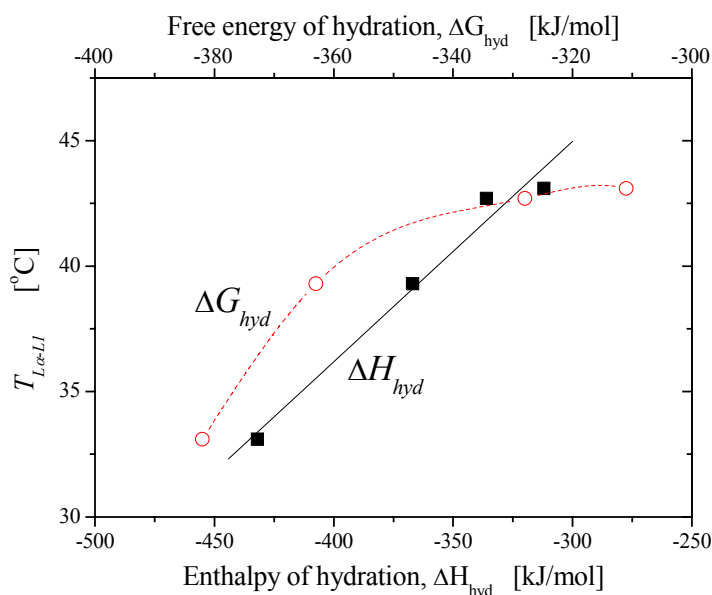


Figure 5.49. Plots of the L_{α} - L_1 phase transition temperatures $T_{L_{\alpha}-L_1}$ as functions of enthalpy ΔH_{hyd} and free energy of hydration ΔG_{hyd} in 100mM OleyDMAO solution at 25 °C. The protonation degree is fixed at $X=0.5$.

2Φ and the thermodynamical quantity was shown. For this case, entropy of hydration, ΔS_{hyd} , was used in order to mention the phase transition phenomenon. It is quite noteworthy that the phase transition induced by the charge density can be expressed by the entropy term and that induced by temperature can be determined by the enthalpy term. Addition of the charge density certainly increases entropic contribution according to the intuitive equation:

$$S = k_B \ln W \quad [5.15]$$

where k_B is the Boltzmann constant, W the dimensionless function of distribution, relating to the charge distribution on the micelle surface.

On the other, the thermal phase transition refers to the energy transfer from outside of the system, and the most cases of phase transitions on heating are endothermic. The energy absorption would be consumed by the sum of the conformational change of the hydrocarbon chains and hydration of head group or counter-ion. On the basis of the FT-IR spectroscopy measurements,^{227,228} the elevating temperature deduces the loss of the ordering hydrocarbon chain and the gain of head group hydration accompanying the gel-liquid crystal phase transition in the ionic surfactant systems. For the present system, the effect of the disordering hydrocarbon chain on the transition temperature can be considered to be constant between the solutions with different counter-ions, so that the main contribution to the transition temperature would be due to the hydration term.²²⁹ It is conceivable from the general aspect of hydration that the head group properties, for instance, charge density and head group size, determine the short-range interaction of the head group and water molecule. Hence the net hydration of the OleylDMAO head group seems to be identical at fixed protonation degree, concentration, and temperature. However, the surrounding counter-ions should affect the degree of hydration depending on the features of the counter-ions as expected from their peculiar surface areas.²³⁰ The coverage of the counter-ion over the ionic head group would prevent from water immigration onto the surface. When temperature rises up, namely, the required thermal energy is supplied to the system, the counter-ions adsorbed on the micelle are to be diffused in the bulk water phase, inducing the observed phase transition. The enthalpy of hydration was obtained from the difference of the enthalpies of ion in aqueous phase and gas phase, $H(aq.) - H(gas)$, which is definitively discriminative quantity against the enthalpy of phase transition. The experimental result however exhibits the linear relation with the hydration enthalpy, therefore it seems plausibly that the enthalpy accompanying with the phase transition can correlate proportionally with the hydration enthalpy of counter-ion.

5.5.2 RHEOLOGICAL PARAMETERS AND ΔG_{hyd}

The oscillatory measurements were carried out in the range from 0.01 to 10 Hz for the solutions with different counter-ions. Figure 5.50 and 5.51 shows the rheograms, which exhibit the distinct rheological properties even though the L_α phase is present in any systems. The hydrophilic anions ($HCOO^-$, Cl^-) and the moderate ones (Br^- , NO_3^-) produce the weakly viscoelastic lamellar phase: both moduli are almost superposed mutually, even the storage modulus (G') seems to be slightly more dominant than the loss modulus (G''). On the other hand, the much hydrophobic anion, ClO_4^- , shows highly viscoelastic L_α phase. G' is higher by the factor 10 than G'' and these moduli are independent on frequency in the measuring range. The rheogram let us speculate the vesicle formation. The G' values are plotted as a function of frequency for the different

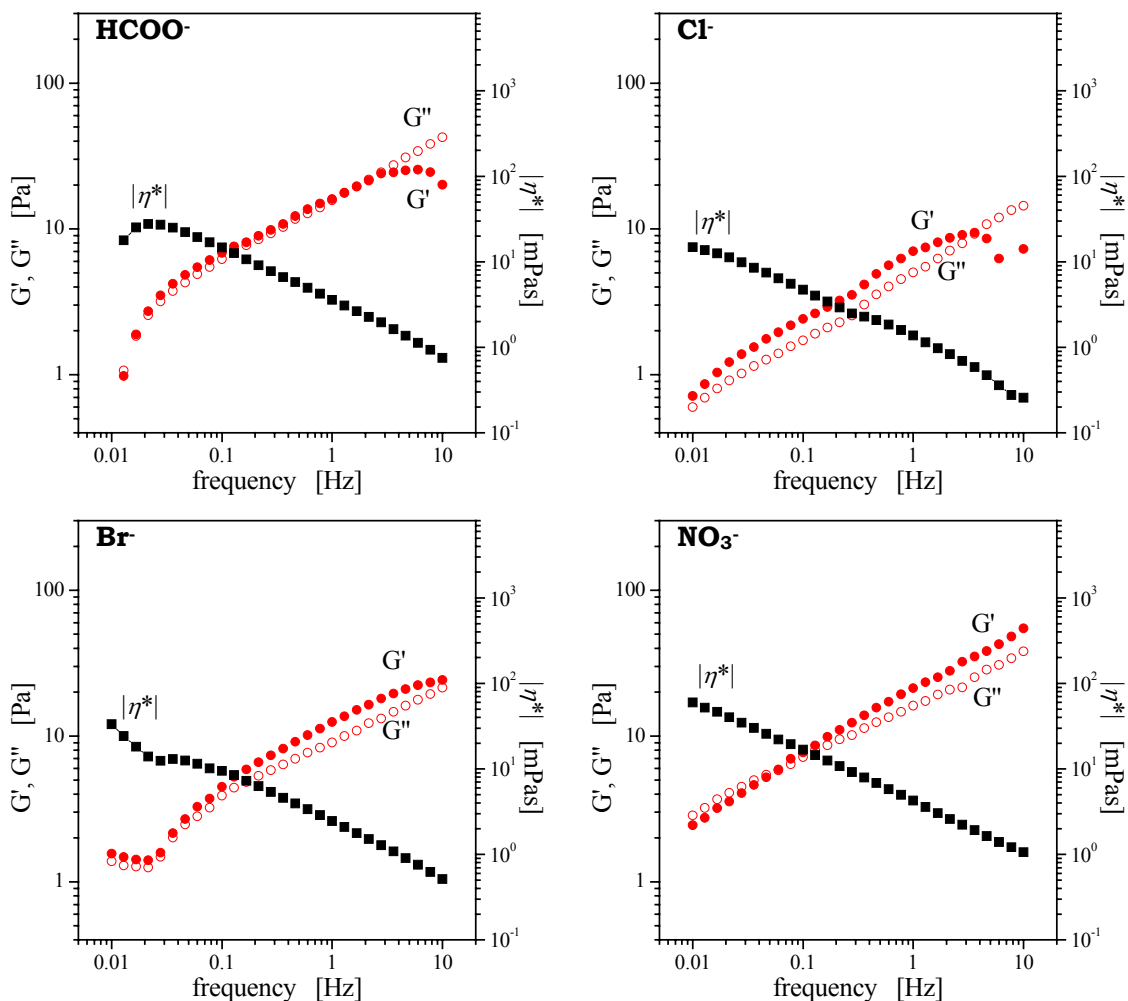


Figure 5.50. Dynamic rheograms for the different counter-ions systems at 25 °C. The symbols indicate: storage modulus (G' , ●), loss modulus (G'' , ○), complex viscosity ($|\eta^*|$, ■). The OleyDMAO concentration and the protonation degree are fixed at 100 mM and $X=0.5$.

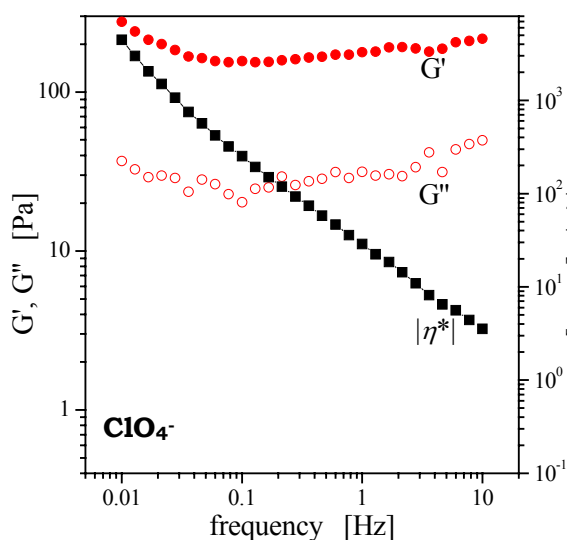


Figure 5.51. Dynamic rheograms for the ClO_4^- counter-ion system at 25 °C. The symbols indicate: storage modulus (G' , ●), loss modulus (G'' , ○), complex viscosity ($|\eta^*|$, ■). The OleyDMAO concentration and the protonation degree are fixed at 100 mM and $X=0.5$.

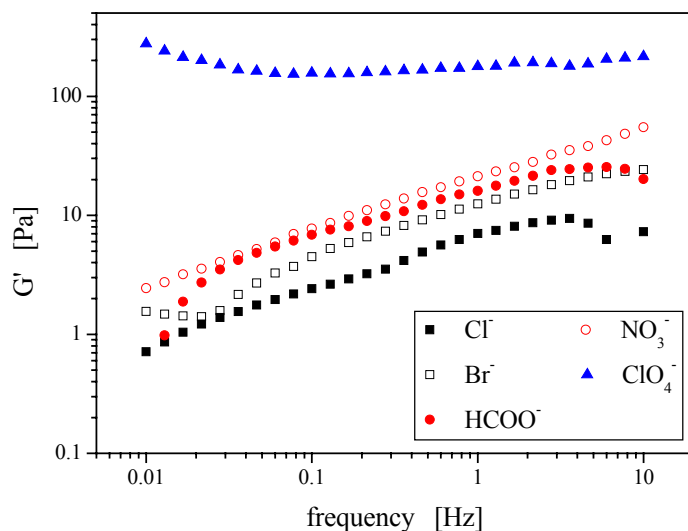


Figure 5.52. Comparison of the storage modulus (G') between the different counter-ions, Cl^- (■), Br^- (□), HCOO^- (●), NO_3^- (○), ClO_4^- (▲), at 25 °C. The OleylDMAO concentration and the protonation degree are fixed at 100 mM and $X=0.5$.

counter-ion in Figure 5.52, where it can be recognized that the counter-ion controls the elastic property. The elasticity becomes higher in the following order:

$$\text{ClO}_4^- > \text{NO}_3^- > (\text{HCOO}^-) > \text{Br}^- > \text{Cl}^-$$

The order corresponds mostly to the Hofmeister series, while cannot be described quantitatively in terms of the free energy of hydration because of the position of HCOO^- counter-ion. The ClO_4^- ion behaves completely different way to the other counter-ions, although ΔG_{hyd} of ClO_4^- is not as much difference as those of the others. As expected in the former section, the ClO_4^- ion may interact peculiarly with the head groups of surfactants, since the L_α formation can be achieved even in the C_{14}DMAO solution.

Figure 5.53 depicts the changes in the apparent viscosities (η) with shear rate in the different systems (except for the ClO_4^- ion) at 25 °C. The shear thinning typical for the L_α phase can be observed in the entire shear rate range for any counter-ions. The shear thinning behaviors are similar between Cl^- , Br^- and HCOO^- , their power indices range from -0.64 to -0.59. The HCOO^- ion, on the other, shows much less viscous flow, which may refer to the Newtonian fluid. The behavior seems to be reasonable for the

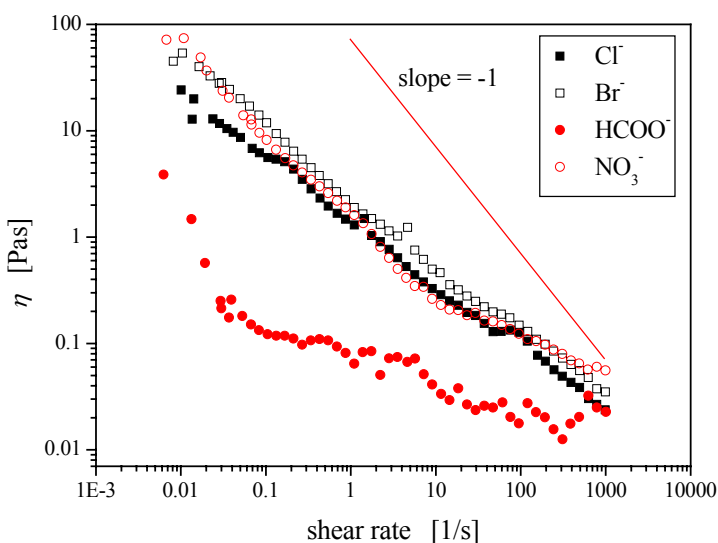


Figure 5.53. Steady shear measurements for the different counter-ions, Cl^- (■), Br^- (□), HCOO^- (●), NO_3^- (○), ClO_4^- (▲), at 25 °C. The OleylDMAO concentration and the protonation degree are fixed at 100 mM and $X=0.5$.

greater hydration feature of the HCOO⁻ ion.

Thus the rheological properties of the L_α phase are much likely to depend on the Hofmeister series or the water affinity of counter-ion. However it should be noted that the different L_α morphologies give their own viscoelastic features, therefore it should be taken for granted that there is no quantitative relation between the rheological parameters and ΔG_{hyd} . Whereas the above results would manifest that the counter-ion influences the bending moduli of lamellae.

Chapter 6 CONCLUSIONS

C₁₂C₈DMAO System

This work was to represent and interpret the properties of double-chain aminoxide surfactant, and the spontaneous or quasi-spontaneous vesicle formation could be introduced in terms of protonation of aminoxide group. The C₁₂C₈MAO aqueous solution at 100 mM consisted of two phases which were optically isotropic and low viscous. Addition of chloric acid induced a phase transition, and the following lamellar (L_α) phase was formed in the range of low protonation degree, $X = 0.007 - 0.35$. When the surfactant was protonated further ($X > 0.35$), the single L_α phase separated again into two isotropic phases. The abnormal phase sequence could be interpreted by the result that mixtures of protonated and non-protonated C₁₂C₈MAO were more surface active than each component.

The surface and interfacial measurements showed synergism of mixing two components. The interfacial tension had a minimum between the series of protonation degrees, and the critical micellar concentration (CMC) was reduced by mixing protonated and non-protonated surfactants due to the minimal surface area per molecule. This synergistic effect arised from the peculiar interaction of hydrogen bonding between protonated and non-protonated head groups. This short-range interaction would cause the C₁₂C₈MAO molecules to be more lipophilic with protonation, resulting in the phase separation at high protonation degree.

The SAXS measurements in the L_α phase also showed the synergistic effect between the head groups. The interlayer spacing of membrane at first decreased with protonation due to depressed fluctuation of the bilayer. And further protonation caused the interlayer spacing to expand due to shrinkage of the head group area with which both spacings of the water layer (d_w) and the surfactant layer (d_s) increased. These two opposing effects derived the observed minimum of the L_α interlayer spacing.

The rheological measurements and microscope observations demonstrated that the morphologies of L_α phase could be controlled by preparation routes. Shearing system was necessary to introduce the vesicle morphology in the L_α region which exhibited high viscoelasticity. It was found that the vesicles were transformed into the classical lamellar phase by the simple process of heating and cooling through the phase transition ($L_\alpha \leftrightarrow L_\alpha/L_1$) temperature. Furthermore, the classical, planar lamellar morphology could be prepared by means of kinetic protonation of the $C_{12}C_8MAO$ molecules using hydrolysis reaction. Any classical L_α phase was modified to the vesicle form under shearing, and its transformation was irreversible in terms of shear force.

C₁₄DMAO System

Various acids were treated as protonation agent in 100mM $C_{14}DMAO$ aqueous solution, and their contributions to the viscosity of solution were examined ranging $X = 0$ to 1. It was elucidated that the aggregate structure remarkably depended on the ion-pair (counter-ion) thermodynamics. According to the macroscopic properties, the counter-ions could be classified into three groups. For the Cl^- , $HCOO^-$, and $H_2PO_4^-$ ions, no remarkable structural change took place with increasing protonation. For the Br^- , NO_3^- , Oxalate, Tartarate, Tartronate, and SO_4^{2-} ions, the small micelles of $C_{14}DMAO$ grew up with protonation, which built up the highly viscoelastic solution. For the ClO_4^- , SCN^- , and Salicylate ions, the L_α phase was formed with protonation. The interfacial curvature thus followed mostly the sequence of Hofmeister series, while the sulfuric ion was completely excluded from the series because of its divalency in the studied pH-range. The viscosity change was interpreted quantitatively by the hydration free energy (ΔG_{hyd}) of counter-ion. And it was found that contribution of the monovalent counter-ion to the maximum viscosity could be described by the linear relation with ΔG_{hyd} , while the divalent counter-ions did not arrange in the same order as the monovalent ones, that could be considered to arise from (1) depressing pK_a of $C_{14}DMAO$ with

increasing amount of acid and (2) electrostatic force within the diffuse double layer. For different counter-ions, the characteristic scaling laws of viscosity evolution against X were observed. The scaling laws also obeyed ΔG_{hyd} and the dicarboxylic acids were consistent with the order of ΔG_{hyd} for monovalent acids under hypothesis that the second carboxylic group did not dissociate. Sulfate, however, could not be manipulated by ΔG_{hyd} : regardless of its strong hydrophilicity (high ΔG_{hyd}), the excess amount of SO_4^{2-} caused the micelles to grow up. The micelle growth therefore would be attributed by counter-ion condensation onto the micelles rather than hydrophilicity itself. Comprehensively it was proved that ΔG_{hyd} and the ionic valency (electrostatic force) of counter-ion played strikingly significant roles in the structural properties.

Trifluoro acetic acid CF_3COOH behaved as hydrophobic acid, however, the viscosity trend could stand in neither the sequence of ΔG_{hyd} nor the Hofmeister series. The ΔG_{hyd} expected from the experiment was -15.79 kJ/mol, but which was too small to form thread-like micelles and incompatible with the calculated ΔG_{hyd} , ~ -386.02 kJ/mol. The interfacial tension measurements suggested that the CF_3COO^- ion was incorporated into the micelle, behaving like co-surfactant. This feature complicated the viscosity change with protonation: two effects, synergism and incorporation, induced the micellar growth and the subsequent micellar branching which referred respectively to the maximum and minimum viscosities in the intermediate range of protonation degree, and then the electrostatic force dominant at high protonation degree led to the thread-like micelles with high viscosity. Over the entire X , the rheograms were fairly fitted by the Maximilian model with a single relaxation time. It was evident that the viscosity change could be controlled mainly by relaxation time. This also implied that the number density of entanglements was independent on protonation, that was visually confirmed by cryo-TEM. Synergism on mixing was also observed in the CF_3COOH system, by which the minimal CMC was obtained. The interaction parameter β indicated that CF_3COOH caused the stronger synergistic effect than HNO_3 . However, some experiments showed the successively hydrophobic $C_{14}DMAO$ with protonation. This would be due to the orientation of hydrophobic trifluoro group in the palisade layer of micelle.

The concentration dependence on the zero-shear viscosity was investigated at different protonation degrees in HCl, HNO₃, and NaSCN/HCl systems. For each system, the critical concentrations (c^*) corresponding to the onset of entanglement were observed. In addition, a maximum viscosity (η_{0m}) was defined at the corresponding concentration (c_m) in some of the systems, and beyond the maximum the viscosity decreased until a phase transition took place. This reduction of the viscosity could be explained by the saturated elongation of micelle. The threshold values, c^* , c_m , η_{0m} , in HCl and HNO₃ systems reached to their minima (c^* , c_m) and maximum (η_{0m}) at half protonation of C₁₄DMAO, suggesting the closest packing of surfactant molecules due to synergism. As a consequence, this would favor formation of lamellar liquid crystal in the high concentration range. The half protonation led to the longer micellar length and the larger number of entanglements per micelle in comparison to the other protonation degrees, resulting in the long relaxation mode.

The mixing effect of two acids was studied in CF₃COOH/HCOOH and HClO₄/HCOOH systems. When the protonation degree was kept at $X = 1$, the viscosity was determined by the quantity of either acids solely. At the fixed $X = 0.5$, however, the viscosity was promoted by substituting CF₃COOH with a small amount of HCOOH. The viscosity change represented the morphological transformation from the spherical to the branched micelle via thread-like form with increasing mole fraction of CF₃COOH. For HClO₄/HCOOH system, the phase behavior was almost similar to HClO₄ alone system. Somehow HCOOH molecules caused the L _{α} range to shrink and instead the L₁ range to extend. The solid phase showed the anti-colligative property on mixing two acids, which would be interpreted in view of the tetrahedral structure of ClO₄⁻ stabilized by conjugation.

The increasing volume fraction of hydrophobic moiety in the surfactant molecule built up the bilayer structure even using the strongly hydrated acids. The L _{α} formation was referred to synergism because the isotropic micellar phase was present on both the sides of high and low protonation degrees. The L _{α} phase melted on elevating temperature, and the subsequent L₁ phase was highly viscoelastic. The L _{α} -L₁ transition

Conclusions

temperatures for different acids were almost correlated by the enthalpy of hydration (ΔH_{hyd}). And the viscoelastic properties of the L_{α} phases were dependent on the Hofmeister series.

Chapter 7 ZUSAMMENFASSUNG

C₁₂C₈DMAO System

Bei niedrigen Konzentrationen sind die Lösungen des Tensids in Wasser zweiphasig. Beide Phasen sind optisch isotrop und niedrig viskos.

Bei Zugabe einer Säure wandelt sich eine 100 mM zweiphasige Lösung bereits bei einem niedrigen Protonierungsgrad ($X = 0 - 0.4$) in eine einphasige flüssig-kristalline L_α -Phase um. Bei Verwendung von HCl als Säure entsteht aus der einphasigen L_α -Phase bei einer Protonierung X von > 0.4 überraschenderweise wieder ein mehrphasiges System. Auch Lösungen des vollständig protonierten Tensids sind mehrphasig. Dieses überraschende Verhalten kommt dadurch zustande, daß Mischungen aus protonierten und nicht-protonierten Molekülen oberflächenaktiver sind als die beiden Komponenten.

Die Oberflächen- und Grenzflächenspannungen der $C_{12}C_8MAO$ -Lösungen durchlaufen mit zunehmender Protonierung ein Minimum. Dieses Verhalten wird als Synergismus bezeichnet und kommt durch Wasserstoffbrückenbildung zwischen den protonierten und nicht-protonierten Kopfgruppen der Verbindungen auf der Mizelloberfläche zustande. Der Synergismus bewirkt, daß die Kopfgruppen mit der Protonierung enger zusammenrücken und, daß die Lösungen von $C_{12}C_8MAO$ mit zunehmender Protonierung zunächst lipophiler werden. Das Maximum des Synergismus liegt bei $X = 0.5$.

Aber auch bei der total protonierten Verbindung existieren noch H-Brücken, was in der CMC und der Oberflächenspannung der Verbindung zum Ausdruck kommt.

Der Synergismus kommt auch in den Ergebnissen von genauen SAXS-Messungen an den L_α -Phasen zum Ausdruck. Der interlamellare Abstand der Lamellen

und die Dicke der Lamellen durchläuft mit zunehmender Protonierung der L_α -Phase durch ein schwach ausgeprägtes Minimum. Bei Aufladung der Membran unterdrückt die zunehmende elektrostatische Abstoßung die Fluktuation der Membran, was insgesamt zu einer Versteifung der Membran und zu einer Abnahme des Abstandes zwischen den Membranen führen sollte. Dieser repulsiven Wechselwirkung entgegen wirkt offenbar der Synergismus zwischen den Kopfgruppen, der zu einer Verdickung der Membran führt. Die Überlagerung der beiden Effekte ergibt offenbar das beobachtbare Minimum.

Rheologische und elektronenmikroskopische Messungen an der L_α -Phase zeigten, daß die Morphologie der L_α -Phase von der Scherbeanspruchung der Proben abhängt. Gering gescherte Proben von L_α -Phasen liegen im wesentlichen als klassische L_α -Phasen aus gestapelten Lamellen vor. Diese Phasen wandeln sich bei schwacher Scherung in mehrschalige Vesikel und bei starker Scherung in einschalige Vesikel um. Es wurde gezeigt, daß sich die klassischen L_α -Phasen durch Abkühlen der Probe von Temperaturen oberhalb des L_α/L_1 -Übergangs zur Temperatur unterhalb des L_α/L_1 -Übergangs herstellen lassen. Außerdem lassen sich klassische L_α -Phasen unter Vermeidung von Scherkräften mit Hilfe von Hydrolysereaktion erzeugen, wobei die zur Aufladung benötigten Protonen bei der Hydrolyse in der ruhenden Lösung entstehen.

C₁₄DMAO System

Im zweiten Teil der Arbeit wurden 100 mM Lösungen von C₁₄DMAO mit verschiedenen starken Säuren wie HCl, HBr, HCOOH, H₃PO₄, HNO₃, CF₃COOH, Oxalsäure, Schwefelsäure, Weinsäure, Tartronsäure, Perchlorsäure, Thiocyanensäure und Salicylsäure protoniert und die Eigenschaften der Lösungen als Funktion des Protonierungsgrades untersucht. Die rheologischen Ergebnisse aus den Systemen ergaben, daß die Gegenionen einen großen Einfluß auf die Hydrophilie und die Struktur und makroskopischen Eigenschaften der Systeme ausweisen. Nach den Ergebnissen konnten die Gegenionen in drei Gruppen aufgeteilt werden. Für die Gegenionen HCOO⁻

, Cl^- , H_2PO_4^- wurde mit zunehmender Protonierung eine Rückbildung der in der C_{14}DMAO -lösungen vorliegenden Stäbchenmizellen zu Kugelmizellen festgestellt. Für die Ionen Br^- , NO_3^- , CF_3COO^- , Oxalat, Tartrat, Tartronat, SO_4^{2-} wurde die Bildung der Stäbchenmizellen verstärkt und es bildeten sich hochviskoelastische Lösungen. Für die Gegenionen ClO_4^- , SCN^- und Salicylat bilden sich schließlich jedoch L_α -phasen. Insgesamt konnten aus den Ergebnissen die Gegenionen nach einer Reihe geordnet werden, die der Hofmeister'schen Ionenreihe entsprach. Es wurde zusätzlich versucht, einen Zusammenhang zwischen der Viskosität und der freien Hydratationsenergie (ΔG_{hyd}) für die Gegenionen quantitativ zu interpretieren. Dabei wurde entdeckt, dass der Beitrag des einwertigen Gegenions zur maximalen Viskosität durch eine lineare Relation mit ΔG_{hyd} beschrieben werden kann, während sich die des zweiwertigen Gegenions nicht auf gleicher Weise wie die des einwertigen Gegenions einordnen läßt. Diese Überlegung konnte (1) aus der Erniedrigung des pKa von C_{14}DMAO mittels Säurezugabe und (2) der elektrostatischen Kraft innerhalb der diffusen Doppelschicht abgeleitet werden. Für unterschiedliche Gegenionen wurden die charakteristischen Potenzgesetze für den Verlauf der Viskosität, aufgetragen gegen X , erhalten. ΔG_{hyd} gehorchte ebenfalls den Potenzgesetzen. Selbst die Dicarbonsäure stimmte mit der Ordnung von ΔG_{hyd} für monovalente Säuren überein, wenn man annimmt, dass die zweite Carboxygruppe nicht dissoziiert. Sulfat konnte jedoch nicht durch ΔG_{hyd} eindeutig beeinflußt werden: Unabhängig von seiner starken Hydrophilie (hohes ΔG_{hyd}), wurde durch den Überschuß an SO_4^{2-} ein Mizellwachstum verursacht. Es ist daher durchaus denkbar, dass das Mizellenwachstum eher von der Gegenionen-kondensation auf den Mizellen, als von der Hydrophilie selbst herrührt. Allgemein wurde gezeigt, dass die freie Hydratationsenergie der Gegenionen für die Struktureigenschaften eine herausragende Rolle spielen.

Trifluoressigsäure CF_3COOH , als eine hydrophobe Säure, nahm insofern eine Sonderstellung unter allen untersuchten Säuren ein, da ihr Viskositätsverlauf weder in der Reihe der ΔG_{hyd} noch in der Hofmeister Reihe eingeordnet werden konnte. Der experimentell gefundene ΔG_{hyd} -Wert von -15.79 kJ/mol, war eindeutig zu klein, um fadenförmige Mizellen zu bilden und stimmte erst recht nicht mit dem berechneten

ΔG_{hyd} -Wert von ~ -386.02 kJ/mol überein. Ein ähnlich aussergewöhnliches Verhalten zeigte auch das System mit Salicylsäure. Bei diesem Ionen muß neben dem Stand in der Hofmeister'schen Ionenreihe auch ihre Cotensideigenschaft berücksichtigt werden. Die hydrophoben Reste der Ionen (CF_3^- und Phenyl-gruppe) werden bereits in die Palisadenschicht. den Mizellen eingebaut.

Um den mit dem Protonierungsgrad einhergehenden Strukturwandel im CF_3COOH System zu verfolgen, wurden eine Reihe verschiedener Experimente durchgeführt. Über den gesamten Aufladungsbereich X wurden verschlaufte oder vernetzte Mizellen gebildet, so dass die Rheogramme gut mittels des Maxwell Modells mit einer einzigen Relaxationszeit angepaßt werden konnten. Es ist offensichtlich, dass die Viskositätsänderung hauptsächlich durch die Relaxationszeit beeinflusst werden kann. Dies deutet darauf hin, dass die Zahl der Verschlaufungen unabhängig von der Protonierung der Mizellen war, was durch die cryo-TEM-Aufnahmen bestätigt wurde. An Hand der Grenzflächenspannung, der Aktivierungsenergie der Structurrelaxationszeit und den SAXS Messungen konnte man folgern, dass sowohl die langen als auch die kurzen Relaxationszeiten sich aus dem Spaltungs- beziehungsweise Rekombinations-Prozess der verschlaufenen Mizellen einerseits und dem „sliding mode“ der verzweigten Mizellen andererseits ergeben. Im CF_3COOH System wurden desweiteren Synergismen beim Mischen beobachtet, woraus ein sehr niedriger CMC Wert resultierte. Der Wechselwirkungsparameter β deutet darauf hin, dass CF_3COOH stärkere synergetische Effekte verursacht als HNO_3 . Nichtsdestotrotz zeigte sich in einigen Versuchen, dass mit zunehmender Protonierung das $C_{14}DMAO$ hydrophob wird. Dies hing mit der Orientierung der hydrophoben Trifluoro Gruppe in der Nachbarschaft der Mizelloberfläche zusammen.

Die Konzentrationsabhängigkeit der Nullviskosität wurde bei unterschiedlichen Protonierungsgraden in HCl , HNO_3 und $NaSCN/HCl$ Systemen untersucht. Für jedes System wurden eine kritische Konzentrationen (c^*) beobachtet, die den Beginn der Bildung von Verschlaufungen der Mizellen markierte. Zusätzlich wurde in einigen Systemen eine maximale Viskosität (η_{0m}) mit der dazugehörigen Konzentration (c_m)

definiert, nach deren Überschreitung eine Abnahme der Viskosität bis zum Phasenübergang stattfand. Diese Abnahme der Viskosität konnte durch eine Sättigung des Mizellenwachstums erklärt werden. Die Schwellenwerte um c^* , c_m , η_{0m} , im HCl und HNO₃ Systemen erreichten ihre Minima (c^* , c_m) bzw. ihr Maximum (η_{0m}) im C₁₄DMAO-System bei halber Aufladung, da hier die dichteste Packung der Tensidmoleküle vorlag und so den Synergismus verstärkte. Demzufolge wurden in hochkonzentrierten Bereichen die Bildung von lamellaren Flüssigkristallen bevorzugt. Ein halb aufgeladenes System verursacht also längere Mizellen und eine größere Anzahl Verschlaufungen pro Mizelle im Vergleich zu anderen Protonierungsgraden, was zu längeren Relaxationszeiten führt. Im Gegensatz dazu existierte im NaSCN/HCl System kein eindeutiger synergistischer Effekt bezüglich der Entwicklung der Viskosität mit der Konzentration, während jedoch durch die Bildung einer L_α Phase makroskopisch ein Synergismus offensichtlich war.

Der Einfluß von Mischungen zweier Säuren wurde in den CF₃COOH/HCOOH und HClO₄/HCOOH Systemen untersucht. Bei konstantem Protonierungsgrad von $X = 1$, wird die Viskosität allein durch die Menge jeder einzelnen Säure festgelegt. Bei einer Aufladung von $X = 0.5$ wird die Viskosität jedoch hauptsächlich dadurch bestimmt, dass CF₃COOH durch etwas HCOOH ersetzt wird. An Hand der Viskositätsänderung kann man die Strukturumwandlung von kugelförmigen über fadenförmigen zu verzweigten Mizellen verfolgen, wobei der Molenbruch von CF₃COOH steigt. Für das HClO₄/HCOOH System ergab sich ein ähnliches Phasenverhalten wie für das HClO₄-Systems. HCOOH Moleküle bedingen das Schrumpfen der L_α Phase und gleichzeitig ein Anwachsen des L₁-Bereichs. Die feste Phase weist anti-kolligative Eigenschaft beim Mischen der zwei Säuren auf, was mit der tetraedrischen Struktur des ClO₄⁻ erklärt wird.

Schließlich wurde der Einfluß der Kohlenwasserstoffkettenlänge mit OleylDMAO untersucht. Der steigende Volumenbruch des hydrophoben Anteils führt selbst bei stark hydratisierten Säuren, den Packungseinschränkungen folgend, zur Ausbildung einer Doppelschicht. Die Bildung der L_α-Phase weist auf die Existenz eines

Synergismus hin. Die transparenten mizellaren Phasen waren auf beiden Seiten der L_α -phase noch vorhanden. Die L_α Phase schmolz bei Erhöhung der Temperatur und die nachfolgende L_1 Phase war hochgradig viskoelastisch. Die L_α - L_1 Übergangstemperaturen für verschiedene Säuren folgten der Hofmeister Reihe. Ein Vergleich der Plateaumodule (G'_∞) für die L_α Phase wurde für die einwertigen Säuren bei konstanter Temperatur durchgeführt. Der lineare Zusammenhang von G'_∞ und ΔH_{hyd} erinnert an den Zusammenhang zwischen $\eta_{0,max}$ und ΔG_{hyd} im C_{14} DMAO System. Es zeigt sich also klar, dass die thermischen und viskoelastischen Eigenschaften hauptsächlich durch die Hydrophilie der Gegenionen festgelegt werden.

APPENDIX

A.1 VOLUME FRACTION OF HYDROPHOBIC CHAIN

The partial molar volumes of ethylene and methylene units can be obtained by the density (ρ) measurement. Figure A.1 shows the plot of the molar volume of alkane (V) as a function of the carbon number of alkane (m). The molar volume can be given by the following equation using the molar mass (M_w):

$$V = \frac{M_w}{\rho} \quad [\text{A.1}]$$

From the linear relation, additivity of the volumes of the ethylene unit ($V(-\text{CH}_2-)$) and of the end methylene unit ($V(-\text{CH}_3)$) can be considered to hold at a constant temperature. Namely,

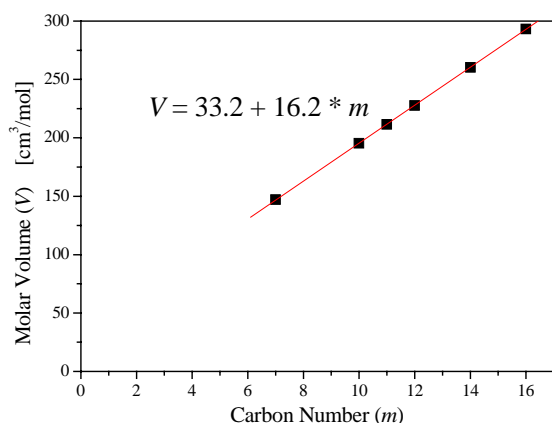


Figure A.1. Plot of the molar volume (V) against the carbon number of the hydrocarbon at 25 °C.

$$V = 2 \cdot V(-\text{CH}_3) + (m - 2) \cdot V(-\text{CH}_2-) \quad [\text{A.2}]$$

Thus the slope given in Figure A.1 corresponds to the molar volume of the ethylene, and the intersection with the vertical axis equals to $2 \cdot (V(-\text{CH}_3)) - V(-\text{CH}_2-)$. Thus the molar volumes of the ethylene and the methylene are $16.2 \text{ cm}^3/\text{mol}$ and $32.8 \text{ cm}^3/\text{mol}$, respectively, and the molar volume of the surfactant hydrocarbon chain (V_L) can be

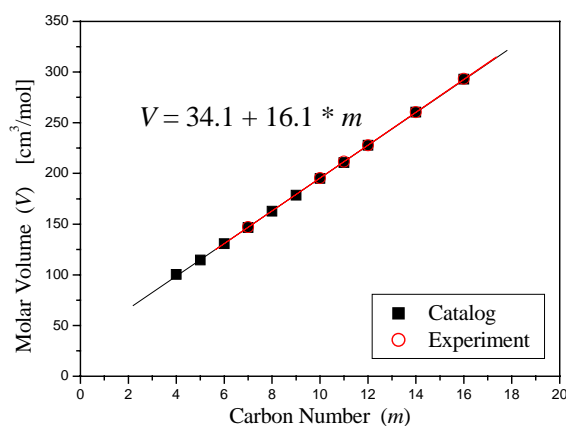


Figure A.2. Plot of the molar volume (V) calculated from catalog data against the carbon number of the hydrocarbon at 25 °C.

formulated.

$$V_L = 32.8 + 16.2 \cdot (n - 1) \quad [\text{A.3}]$$

Here the chain length of the surfactant tail is denoted as n .

The relation in Figure A.1 was confirmed by data obtainable from a chemical catalog. The catalog data is plotted in Figure A.2. These values are in good agreement with the experimental ones, and the linear relation of the molar volume and the carbon number of alkane can be observed. The small deviation can be due to the atmospheric pressure.

The above case did not consider any interaction between the alkane molecules and the reasonable equation was formulated. This would be the reason why the pure substances solely were measured. But, for the surfactant system, the aggregates are dispersed in solvent which is mostly water, then the inner core of micelle should be pressed more or less due to the curved surface. Therefore one must postulate the incompressible hydrocarbon chain for the sake of simplicity and application of Eq. [A.3]. Under this assumption, the volume fraction can be estimated simply by

$$\phi_L = \frac{V_L}{V_{system}} = \frac{M_S \cdot V_L \cdot \rho_S}{1000} \quad [\text{A.4}]$$

where ρ_S is the density of the surfactant solution at a give concentration (M_S). Note that each unit is represented by M_S in mol/L, V_L in cm^3/mol , and ρ_S in g/cm^3 .

REFERENCES

1. Beck, J. S.; Vartuli, J. C.; Roth, W. J.; Leonowicz, M. E.; Kresge, C. T.; Schmitt, K. D.; Chu, C. T. W.; Olson, D. H.; Sheppard, E. W. *J. Am. Chem. Soc.* **1992**, *114*, 10834.
2. Smith, W. V.; Ewart, R. H. *J. Chem. Phys.* **1948**, *16*, 592.
3. Tsujii, K. “*Surface Activity : Principles, Phenomena, and Application*” **1998**, p.196, Academic Press.
4. Tanford, C. “*The Hydrophobic Effect*” **1980**, Wiley, New York.
5. Derjaguin, B.; Landau, L. *Acta Physicochim* **1941**, *14*, 633.
6. Verwey, E.; Overbreek, J. Th. G. *Theory of the Stability of Lyophobic Colloids* **1948**, Elsevier, Amsterdam.
7. Bangham, A. D.; Hill, M. W.; Miller, N. G. “*Methods in Membrane Biology*” **1974**, vol.1, ch.1, E. D. Korn (Ed.), Plenum Press, New York.
8. Batzri, S.; Korn, E. D. *Biochim. Biophys. Acta* **1973**, *298*, 1015.
9. Zumbuehl, O.; Weder, H. G. *Biochim. Biophys. Acta* **1981**, *640*, 252.
10. Diat, O.; Roux, D.; Nallet, F. *J. Phys II France* **1993**, *3*, 1427.
11. Müller, I.; Xu, H. *Acta Metall.* **1991**, *39*, 263.
12. Förster, Th.; Tesmann, H. *Cosmet. Toiletries* **1991**, *106*, 49.
13. Svitova, T. F.; Smirnova, Y. P.; Pisarev, S. A.; Berezina, N. A. *Colloids and Surfaces A* **1995**, *98*, 107.
14. Photinos, P.; Saupe, A. *Physical Review A* **1990**, *41*(2), 954.
15. Maeda, H.; Kakehashi, R. *Adv. Colloid Interface Sci.* **2000**, *88*, 275.
16. Stigter, D. *J. Phys. Chem.* **1974**, *78*(24), 2480.
17. Kawasaki, H.; Imahayashi, R.; Maeda, H. *Langmuir* **2002**, *18*, 8358.
18. Saito, S.; Yukawa, M. *J. Colloid Interface Sci.* **1969**, *30*(2), 211.
19. Mukerjee, P. *Adv. Colloid Interface Sci.* **1967**, *1*, 241.
20. Israelachvili, J. N. “*Intermolecular and Surface Forces, 2nd Edition*” **1992**, Academic Press, London.
21. Shinoda, K. “*Principles of Solution and Solubility*” **1978**, Marcel Dekker, Inc., New York.
22. Yu, Z.-J.; Zhang, X.; Xu, G.; Zhao, G.-X. *J. Phys. Chem.* **1990**, *94*, 3675.
23. Shinoda, K.; Minegishi, Y.; Arai, H. *J. Phys. Chem.* **1976**, *80* (18), 1987.
24. Shinoda, K.; Hato, M.; Hayashi, T. *J. Phys. Chem.* **1972**, *76*, 909.
25. Tartar, H. V.; Cadle, R. D. *J. Phys. Chem.* **1939**, *43*, 1173.
26. Tsujii, K.; Mino, J. *J. Phys. Chem.* **1978**, *82*, 1610.
27. Glukhareva, N. A.; Pletner, M. Y. *Tenside Surf. Det.* **1996**, *33*, 315.
28. Nilsson, F.; Söderman, O.; Johansson, I. *Langmuir* **1997**, *13*, 3349.
29. Kunieda, H.; Shigeta, K.; Ozawa, K.; Suzuki, M. *J. Phys. Chem. B* **1997**, *101*, 7952.
30. Kunieda, H.; Uddin, Md. H.; Horii, M.; Furukawa, H.; Harashima, A. *J. Phys. Chem. B* **2001**, *105*, 5419.
31. Ohta, A.; Nakashima, S.; Matsuyanagi, H.; Asakawa, T. Miyagishi, S. *Colloid Polym. Sci.* **2003**, *282*, 162.
32. Israelachvili, J. N.; Adams, G. E. *J. Chem. Soc. Faraday Trans. I* **1978**, *74*, 975.
33. Hamaker, H. C. *Physica* **1937**, *4*, 1058.
34. Langmuir, I. *J. Chem. Phys.* **1938**, *6*, 873.
35. Clunie, J. S.; Goodman, J. F.; Symons, P. C. *Nature* **1967**, *216*, 1203.
36. Marsh, D. *Biophys. J.* **1989**, *55*, 1093.
37. Rand, R. P.; Parsegian, V. A. *Biochim. Biophys. Acta* **1989**, *988*, 351.
38. Franks, F. (Ed.) “*Biophysics of Water*” **1982**, Wiley, New York.
39. Wishnia, A. *J. Phys. Chem.* **1963**, *67*, 2079.

40. Stigter, D. *J. Colloid Interface Sci.* **1967**, *23*, 379.
41. Fowkes, F. M. *J. Phys. Chem.* **1972**, *66*, 382.
42. Tanford, C. *J. Phys. Chem.* **1974**, *78*, 2469.
43. Israelachvili, J. N.; Mitchell, D. J.; Ninham, B. W. *J. Chem. Soc. Faraday Trans. I* **1976**, *72*, 1525.
44. Fontell, K.; Gray, G. W.; Winsor, P. A. (Eds.) “*Liquid Crystal & Plastic Crystals*” **1974**, Vol.2, p.80-109, John Wiley & Sons. Inc., London.
45. Satoh, N.; Tsujii, K. *J. Phys. Chem.* **1987**, *91*, 6629.
46. Satoh, N.; Tsujii, K. *Langmuir* **1992**, *8*(2), 581.
47. Hoffmann, H. *Ber. Bunsenges. Phys. Chem.* **1994**, *98*, 1435.
48. Kaler, E.; Herrington, K. L.; Murthy, A. K.; Zasadzinski, J. *J. Phys. Chem.* **1992**, *96*, 6698.
49. Hoffmann, H.; Munkert, U.; Thunig, C.; Valiente, M. *J. Colloid Interface Sci.* **1994**, *163*, 217.
50. Kaler, E. W.; Murthy, A. K.; Rodriguez, B. E.; Zasadzinski, J. A. N. *Science*, **1989**, *245*, 1371.
51. Hoffmann, H.; Thunig, C.; Munkert, U.; Meyer, H. W.; Richter, W. *Langmuir* **1992**, *8*, 2629.
52. Mitchell, D. J.; Tiddy, G. J. T.; Waring, L.; Bostock, T.; MacDonald, M. P. *J. Chem. Soc., Faraday Trans. I*, **1983**, *79*, 975.
53. Pleiner, H.; Brand, H. R. *Europhys. Lett.* **1991**, *15*, 393.
54. McGrath, K. M.; Dabbs, D. M.; Yao, N.; Aksay, I. A.; Gruner, S. M. *Science* **1997**, *277*.
55. Helfrich, W. *J. Phys.: Condens. Matter* **1994**, *6*, A79.
56. Harbich, W.; Servuss, R. M.; Helfrich, W. *Z. Naturforsch.* **1978**, *a33*, 1013.
57. Lekkerkerker, H. N. W. *Physica A*, **1989**, *159*, 319.
58. Winterhalter, N.; Helfrich, W. *J. Phys. Chem.* **1988**, *92*, 6865.
59. Hauser, H. *Proc. Natl Acad. Sci. USA* **1989**, *86*, 5351.
60. Decruppe, J. P.; Ponton, A. *Eur. Phys. J. E* **2003**, *10*, 201.
61. Drye, T. J.; Cates, M. E. *J. Chem. Phys.* **1992**, *96*, 1367.
62. Oetter, G.; Hoffmann, H. *J. Disp. Sci. Tech.* **1988-89**, *9*, 459.
63. Leung, R.; Shah, D. O. *J. Colloid Interface Sci.* **1987**, *120*, 320.
64. Gradzielski, M. *Langmuir* **1998**, *14*, 6037.
65. Hofmeister, F. *Arch. Exp. Pathol. Pharmacol.* **1888**, *24*, 247.
66. Schott, H. *Colloids Surf.* **1984**, *11*, 51.
67. Atherton, A. D.; Barry, B. W. *J. Colloid Interface Sci.* **1985**, *106*, 479.
68. Iwanaga, T.; Suzuki, M.; Kunieda, H. *Langmuir* **1998**, *14*, 5775.
69. Anacker, E. W.; Ghose, H. M. *J. Am. Chem. Soc.* **1968**, *90*, 3161.
70. Warr, G. G.; Zemb, T. N.; Drifford, M. *J. Phys. Chem.* **1990**, *94*, 3086.
71. Buckingham, S. A.; Garvey, C. J.; Warr, G. G. *J. Phys. Chem.* **1993**, *97*, 10236.
72. Booi, H. L. “*Colloid Science*” **1949**, Elsevier, Amsterdam.
73. Cohen, I.; Hiskey, C. F.; Oster, G. *J. Colloid Sci.* **1954**, *9*, 243.
74. Shigeta, K.; Olsson, U.; Kunieda, H. *Langmuir*, **2001**, *17*, 4717.
75. Corti, M.; Degiorgio, V. *J. Phys. Chem.* **1981**, *85*, 1442.
76. Blankschtein, D.; Thurston, G. M.; Benedek, G. B. *J. Chem. Phys.* **1986**, *85*, 7268.
77. Bernheim-Groswasser, A.; Wachtel, E.; Talmon, Y. *Langmuir* **2000**, *16*, 4131.
78. Soubiran, L.; Coulson, C.; Sierro, P.; Roux, D. *Europhys. Lett.* **1995**, *31*, 243.
79. Helfrich, W. *Z. Naturforsch.* **1978**, *a33*, 305.
80. Diat, O.; Roux, D. *J. Phys. II* **1993**, *3*, 9.
81. Roux, D.; Nallet, F.; Diat, O. *Europhys. Lett.* **1993**, *24*, 53.
82. van der Linden, E.; Hogervorst, W. T.; Lekkerkerker, H. N. W. *Langmuir* **1996**, *12*, 3127.
83. van der Linden, E.; Dröge, J. H. M. *Physica A* **1993**, *193*, 439.

84. Rehage, H.; Hoffmann, H. *Rheol. Acta* **1982**, *21*, 561.
85. Hoffmann, H.; Hofmann, S.; Rauscher, A.; Kalus, J. *Progr. Colloid Polym. Sci.* **1991**, *84*, 24.
86. Cates, M. E.; Milner, S. T. *Phys. Rev. Lett.* **1989**, *62*, 1856.
87. Diat, O.; Roux, D. *Langmuir* **1995**, *11*, 1392.
88. Yamamoto, J.; Tanaka, H. *Phys. Rev. Lett.* **1996**, *77*, 4390.
89. Imai, M.; Nakaya, K.; Kato, T. *Eur. Phys. J. E.* **2001**, *5*, 2001.
90. Tokiwa, F.; Ohki, K. *J. Phys. Chem.* **1966**, *70*, 3437.
91. Maeda, H.; Tsunoda, M.; Ikeda, S. *J. Phys. Chem.* **1974**, *78*, 1086.
92. Maeda, H.; Kanakubo, Y.; Miyahara, M.; Kakehashi, R.; Garamus, V.; Pedersen, J. S. *J. Phys. Chem. B* **2000**, *104*, 6174.
93. Kawasaki, H.; Maeda, H. *Langmuir* **2001**, *17*, 2278.
94. Herrmann, K. W. *J. Phys. Chem.* **1962**, *66*, 295.
95. Rathman, J. F.; Christian, S. D. *Langmuir* **1990**, *6*, 391.
96. Zhang, H.; Dubin, P. L.; Kaplan, J. I. *Langmuir* **1991**, *7*, 2103.
97. Brycki, B.; Szafran, M. *J. Mol. Liq.* **1994**, *59*, 83.
98. Hoffmann, H.; Rauscher, A.; Gradzielski, M.; Schulz, S. F. *Langmuir* **1992**, *8*, 2140.
99. Panitz, J.-C.; Gradzielski, M.; Hoffmann, H.; Wokaun, A. *J. Phys. Chem.* **1994**, *98*, 6812.
100. Hoffmann, H.; Ulbricht, W. *Tenside Surf. Det.* **1998**, *35*, 421.
101. Rogers, J.; Winsor, P. A. *J. Colloid Interface Sci.* **1969**, *30*, 247.
102. Haas, S.; Hoffmann, H.; Thunig, C.; Hoinkis, E. *Colloid Polym. Sci.* **1999**, *277*, 856.
103. Marcus, Y. "Ion Properties" **1997**, Marcel Dekker, Inc., New York.
104. Krestov, G. A. "Thermodynamics of Solvation" **1991**, Ellis Horwood, New York.
105. Jeng, U.-S.; Lin, T.-L.; Tsao, C.-S.; Lee, C.-H.; Canteenwala, T.; Wang, L.-Y.; Chiang, L.-Y.; Han, C. C. *J. Phys. Chem. B* **1999**, *103*, 1059.
106. Garcia-Tarres, L.; Guardia, E. *J. Phys. Chem. B* **1998**, *102*, 7448.
107. Marcus, Y. "Ion Solvation" **1985**, Wiley, Chichester.
108. Marcus, Y. *J. Chem. Soc., Faraday Trans.* **1991**, *87*, 2995.
109. Smith, S. S.; Steinle, E. D.; Meyerhoff, M. E.; Cawson, D. C. *J. Gen. Physiol.* **1999**, *114*, 799.
110. Conway, B. E. *J. Solution Chem.* **1978**, *7*, 721.
111. Marcus, Y. *J. Solution Chem.* **1996**, *25*, 455.
112. Marcus, Y.; Ben-Naim, A. *J. Chem. Phys.* **1985**, *83*, 4744.
113. Marcus, Y. *J. Solution Chem.* **1994**, *23*, 831.
114. Munoz, J.; Gallegos, C.; Flores, V. *Tenside Surf. Det.* **1991**, *28*, 204.
115. Montalro, G.; Valiente, M.; Rodenas, E. *Langmuir* **1996**, *12*, 5202.
116. Hoffmann, H. *Adv. Mater.* **1994**, *6*, 116.
117. Weissenberg, K. *Nature* **1947**, *159*, 310.
118. Kornev, K. G.; Neimark, A. V. *J. Colloid Interface Sci.* **2003**, *262*, 253.
119. Kunieda, H.; Kanei, N.; Uemoto, A.; Tobita, I. *Langmuir* **1994**, *10*, 4006.
120. Phan-Thien, N.; Tanner, R. I. *J. Non-Newt. Fluid Mech.* **1977**, *2*, 353.
121. White, J. L.; Metzner, A. B. *J. Appl. Polym. Sci.* **1963**, *7*, 1867.
122. Holz, T.; Fischer, P.; Rehage, H. *J. Non-Newt. Fluid Mech.* **1999**, *88*, 133.
123. Dhanasekharan, M.; Wang, C. F.; Kokini, J. L. *J. Food Process Eng.* **2001**, *24*, 193.
124. Cox, W. P.; Merz, E. H. *J. Polym. Sci.* **1958**, *28*, 619.
125. Ferry, J. D. "Viscoelastic Properties of Polymer" **1980**, Wiley, New York.
126. Pflaumbaum, M.; Rehage, H.; Talmon, I. *Tenside Surf. Det.* **2002**, *39*, 212.
127. Saltero, J. F. A.; Bautista, F.; Puig, J. E.; Manero, O. *Langmuir* **1999**, *15*, 1604.
128. Saltero, J. F. A.; Puig, J. E.; Manero, O. *Langmuir* **1996**, *12*, 2654.
129. Manero, O.; Bautista, F.; Saltero, J. F. A.; Puig, J. E. *J. Non. Newt. Fluid Mech.* **2002**, *106*, 1.

130. de Gennes, P. G. *J. Chem. Phys.* **1971**, *55*, 572.
131. Doi, M.; Kuzuu, N. Y. *J. Polym. Sci. Polym. Lett. Ed.* **1980**, *18*, 775.
132. Graessley, W. W. *Adv. Polym. Sci.* **1982**, *47*, 68.
133. Emerson, Y. A.; Nicole, R. D. *Material Research* **1999**, *2*, 23.
134. Roservear, F. B. *J. Am. Oil Chem. Soc.* **1954**, *31*, 628.
135. Kunieda, H.; Shigeta, K.; Ozawa, K. *J. Phys. Chem. B* **1997**, *101*, 7952.
136. Roe, R.-J. “*Methods of X-ray and Neutron Scattering in Polymer Science*” **2000**, Oxford Univ. Press, New York..
137. Guinier, A.; Fournet, G. “*Small-angle Scattering of X-ray*” **1955**, Wiley, New York.
138. Porod, G. *Kolloid-Z.* **1951**, *124*, 83.
139. Hashimoto, T.; Fujimura, M.; Kawai, H. *Macromolecules* **1980**, *13*, 1660.
140. Schmitz, K. S. (Ed.) “*An Introduction to Dynamic Light Scattering by Macromolecules*” **1990**, p.9, Academic Press, Inc., San Diego.
141. Schaefer, D. W.; Martin, J. E.; Wiltzius, P. Cannell, D. S. *Phys. Rev. Lett.* **1984**, *52*, 2371.
142. Holmberg, K.; Jönsson, B.; Kronberg, B.; Lindman, B. (Eds.) “*Surfactants and Polymers in Aqueous Solution, 2nd ed.*” **2003**, p. 459-463, John Wiley & Sons Ltd., England.
143. Mizuno, D.; Nishino, T.; Kimura, Y.; Hayakawa, R. *Phys. Rev. E* **2003**, *67*, 061505.
144. Alibert, I.; Coulon, C.; Bellocq, A. M.; Gulik-Krzywicki, T. *Europhys.Lett.* **1997**, *39*, 563.
145. Hao, J.; Hoffmann, H.; Horbaschek, K. *Langmuir* **2001**, *17*, 4151.
146. Laughlin, R. G.; Munyon, R. L.; Burns, J. L.; Coffindaffer, T. W.; Talmon, Y. *J. Phys. Chem.* **1992**, *96*, 374.
147. Gradzielski, M.; Müller, M.; Bermeier, M.; Hoffmann, H.; Hoinkis, E. *J. Phys. Chem. B* **1999**, *103*, 1416.
148. Hoffmann, H.; Thunig, C.; Schmiedel, P.; Munkert, U. *Langmuir* **1994**, *10*, 3972.
149. Dubois, M.; Zemb, T.; Belloni, L. *J. Chem. Phys.* **1992**, *96*, 2278.
150. Versluis, P.; van de Pas, J. C.; Mellema, J. *Langmuir* **1997**, *13*, 5732.
151. Kevelam, J.; Hoffmann, A. C.; Engberts, J. B. F. N.; Blokzijl, W.; van de Pas, J.; Versluis, P. *Langmuir* **1999**, *15*, 5002.
152. Arij, A. *J. Chem. Phys.* **1978**, *69*, 1742.
153. Hoffmann, H.; Ulbricht, W. *Recent Res. Devel. Phys. Chem.* **1998**, *2*, 113.
154. Diat, O.; Roux, D.; Nallet, F. *Rhys. Rev. E* **1995**, *51*, 3296.
155. Panizza, P.; Roux, D.; Vuillaume, V.; Lu, C.-Y. D.; Cates, M. E. *Langmuir* **1996**, *12*, 248.
156. Bergenholtz, J.; Wagner, N. J. *Langmuir* **1996**, *12*, 3122.
157. Arrault, J.; Grand, C.; Poon, W. C. K.; Cates, M. E. *Europhys. Lett.* **1997**, *38*, 625.
158. Bakshi, M. S.; Crisantino, R.; De Lisi, R.; Milioto, S. *J. Phys. Chem.* **1993**, *97*, 6914.
159. Maeda, H.; Yamamoto, A.; Souda, M.; Kawasaki, H.; Hossain, K. S.; Nemoto, N.; Almgren, M. *J. Phys. Chem. B* **2001**, *105*, 5411.
160. Weers, J. G.; Rathman, J. F.; Scheuing, D. R. *Colloid Polym. Sci.* **1990**, *268*, 832.
161. Shiloach, A.; Blankschtein, D. *Langmuir* **1997**, *13*, 3968.
162. Hoffmann, H. *Prog. Colloid Polym. Sci.* **1990**, *83*, 16.
163. Hoffmann, H.; Hofmann, S.; Illner, J. C. *Progr. Colloid Polym. Sci.* **1994**, *97*, 103.
164. Leibler, S.; Lipowsky, R. *Rhys. Rev. B* **1987**, *35*, 7004.
165. Gradzielski, M.; Hoffmann, H. “*Ringed Gels: Their Structure and Macroscopic Properties*, in *The Structure, Dynamics and Equilibrium Properties of Colloidal Systems*” Bloor, D. M. and Wyn-Jones, E. (Eds.), **1990**, 427-448, Kluwer Academic Publishers, Netherlands.
166. Meguro, K.; Ueno, M.; Esumi, K. “*Nonionic Surfactants: Physical Chemistry*” Schick, M. J. (Ed.), **1987**, p.151, Marcel Dekker, New York.
167. Egger, H.; Hellweg, T.; Findenegg, G. H. *Phys. Chem. Chem. Phys.* **2003**, *5*, 3013.
168. Sottmann, T.; Strey, R. *J. Chem. Phys.* **1997**, *106*, 8606.
169. Sottmann, T.; Strey, R. *Tenside Surf. Det.* **1998**, *35*, 34.

170. Karlstrom, G. *J. Phys. Chem.* **1983**, 87, 3541.
171. Lindman, B.; Carlsson, A.; Karlstrom; Malmsten, M. *Adv. Colloid Interface Sci.* **1990**, 32, 183.
172. Kjellander, R.; Florin, E. *J. Chem. Soc., Faraday Trans. 1* **1981**, 77, 2053.
173. Kjellander, R. *J. Chem. Soc., Faraday Trans. 2* **1982**, 78, 2025.
174. Tlustý, T.; Safran, S. A.; Menes, R.; Strey, R. *Phys. Rev. Lett.* **1997**, 78, 2616.
175. Horbaschek, K.; Hoffmann, H.; Thunig, C. *J. Colloid Interface Sci.* **1998**, 206, 439.
176. Raghavan, S. R.; Edlund, H.; Kaler, E. W. *Langmuir* **2002**, 18, 1056.
177. Oberdisse, J.; Couve, C.; Appell, J.; Berret, J. F.; Ligoure, C.; Porte, G. *Langmuir* **1996**, 12, 1212.
178. Chen, S. H. *Ann. Rev. Phys. Chem.* **1986**, 37, 351.
179. Lee, Jr., C. T.; Johnston, K. P.; Dai, H. J.; Cochran, H. D.; Melnichenko, Y. B.; Wignall, G. D. *J. Phys. Chem. B* **2001**, 105, 3540.
180. Carnahan, N. F.; Starling, K. E. *J. Chem. Phys.* **1969**, 51, 635.
181. Bergmeier, M.; Gradzielski, M.; Thunig, C.; Hoffmann, H. *IL NUOVO CIMENTO* **1998**, 20, 2251.
182. Horbaschek, K.; Hoffmann, H.; Hao, J. *J. Phys. Chem. B* **2000**, 104, 2781.
183. Escalante, J. I.; Gradzielski, M.; Hoffmann, H.; Mortensen, K. *Langmuir* **2000**, 16, 8653.
184. Hao, J.; Hoffmann, H.; Horbaschek, K. *J. Phys. Chem. B* **2000**, 104, 10144.
185. Laun, H. M.; Bung, R.; Hess, S.; Loose, W.; Hess, O.; Hank, K.; Hadicke, E.; Hingmann, R.; Schmidt, F.; Lindner, P. *J. Rheol.* **1992**, 36, 743.
186. Montalvo, G.; Rodenas, E.; Valiente, M. *J. Colloid Interface Sci.* **1998**, 202, 232.
187. Berghausen, J.; Zipfel, J.; Lindner, P.; Richtering, W. *J. Phys. Chem. B* **2001**, 105, 11081.
188. Hoffmann, H.; Oetter, G.; Schwandner, B. *Progr. Colloid Polym. Sci.* **1987**, 73, 95.
189. Gorski, N.; Gradzielski, M.; Hoffmann, H. *Langmuir* **1994**, 10, 2594.
190. Gradzielski, M.; Hoffmann, H.; Langevin, D. *J. Phys. Chem.* **1995**, 99, 12612.
191. Müller, A. J.; Torres, M. F.; Saez, A. E. *Langmuir* **2004**, 20, 3838.
192. Hartmann, V.; Cressely, R. *Europhys. Lett.* **1997**, 40, 691.
193. Cressely, R.; Hartmann, V. *Eur. Phys. J. B* **1998**, 6, 57.
194. Hu, Y.; Rajaram, C. V.; Wang, S. Q.; Jamieson, A. M. *Langmuir* **1994**, 10, 80.
195. Zapf, A.; Hornfeck, U.; Platz, G.; Hoffmann, H. *Langmuir* **2001**, 17, 6113.
196. Ostwald W.; Kohler, R. *Kolloid Zeitschrift* **1927**, 43, 151.
197. Sakamoto, K. *Mol. Cryst. Liq. Cryst.* **1980**, 59, 59.
198. Lopez-Quintela, M. A.; Akahane, A.; Rodriguez, C.; Kunieda, H. *J. Colloid Interface Sci.* **2002**, 247, 186.
199. Smith, F. D.; Stirton, A. J.; Nunez-Ponzoa, M. V. *J. Am. Oil Chem. Soc.* **1963**, 43, 501.
200. Cabani, S.; Gianni, P.; Mollica, V.; Lepori, L. *J. Solution Chem.* **1981**, 10, 563.
201. Ninham, B. W.; Yaminsky, V. *Langmuir* **1997**, 13, 2097.
202. Boström, M.; Williams, D. R. M.; Ninham, B. W. *Langmuir* **1997**, 17, 4475.
203. Omta, A. W.; Kropman, M. F.; Woutersen, S.; Bakker, H. J. *Science* **2003**, 301, 347.
204. Graziano, G. *Phys. Chem. Chem. Phys.* **1999**, 1, 3567.
205. Fioroni, M.; Burger, K.; Mark, A. E.; Roccatano, D. *J. Phys. Chem. B* **2003**, 107, 4855.
206. Engel, G.; Hertz, H. G. *Ber. Bunsen-Ges. Phys. Chem.* **1968**, 72, 808.
207. Nose, A.; Hojo, M.; Ueda, T. *J. Phys. Chem. B* **2004**, 108, 798.
208. Rao, U. R. K.; Manohar, C.; Valaulikar, B. S.; Iyer, R. M. *J. Phys. Chem.* **1987**, 91, 3286.
209. Hoffmann, H.; Thunig, C.; Schmiedel, P.; Munkert, U.; Ulbricht, W. *Tenside Surf. Det.* **1994**, 31, 389.
210. Granek, R.; Cates, M. E. *J. Chem. Phys.* **1992**, 96, 4758.
211. Rathman, J. F.; Scamehorn, J. F. *Langmuir* **1988**, 4, 474.
212. Kumar, G. A.; McAllister, M. A. *J. Org. Chem.* **1998**, 63, 6968.
213. Caputo, M.-R.; Selb, J.; Candau, F. *Polymer* **2004**, 45, 231.

214. Hoffmann, H.; Nüsslein, H.; Ulbricht, W. "The Influence of Hydrophobic Counterions on The Thermodynamics and Kinetics of Ionic Micelles, in *Micellization, Solubilization, and Microemulsions*" Mittal, K. L. (Ed.), **1977**, Vol.1, p.263-289.
215. Angel, M.; Hoffmann, H.; Huber, G.; Rehage, H. *Ber. Bunsenges. Phys. Chem.* **1988**, *92*, 10.
216. Hassan, P. A.; Valaulikar, B. S.; Manohar, C.; Kern, F.; Bourdieu, L.; Candau, S. J. *Langmuir* **1996**, *12*, 4350.
217. Appell, J.; Porte, G.; Khatory, A.; Kern, F.; Candau, S. J. *J. Phys. II France* **1992**, *2* 1045.
218. Cates, M. E.; Roux, D.; Andelman, D.; Milner, S. T.; Safran, S. T. A. *Europhys. Lett.* **1988**, *5*, 733.
219. Shikata, T.; Hirata, H.; Kotaka, T. *Langmuir* **1988**, *4*, 354.
220. Khatory, A.; Kern, F.; Lequeux, F.; Appell, J.; Porte, G.; Morie, N.; Ott, A.; Urbach, W. *Langmuir* **1993**, *9*, 933.
221. Gravsholt, S. J. *Colloid Interface Sci.* **1976**, *57*, 575.
222. Schmitt, V.; Lequeux, F. *J. Phys. II France* **1995**, *5*, 193.
223. Lequeux, F. *Europhys. Lett.* **1992**, *19*, 675.
224. Khatory, A.; Lequeux, F.; Kern, F.; Candau, S. J. *Langmuir* **1993**, *9*, 1456.
225. Schubert, B. A.; Kaler, E. W.; Wagner, N. J. *Langmuir* **2003**, *19*, 4079.
226. Kawasaki, H.; Souda, M.; Tanaka, S.; Nemoto, N.; Karlsson, G.; Almgren, M.; Maeda, H. *J. Phys. Chem. B* **2002**, *106*, 1524.
227. Tian, Y. *J. Phys. Chem.* **1991**, *95*, 9985.
228. Mädler, B.; Binder, H.; Klose, G. *J. Colloid Interface Sci.* **1998**, *202*, 124.
229. Missel, P. J.; Mazer, N. A.; Benedek, G. B.; Young, C. Y.; Carey, M. C. *J. Phys. Chem.* **1980**, *84*, 1044.
230. Knock, M. M.; Bain, C. D. *Langmuir* **2000**, *16*, 2857.